The dynamics of the Hsp90 machine

studied by single molecule FRET

Dissertation

Physics Department

Technical University Munich

Philipp Wortmann

June 29, 2017

Technische Universität München
Department E22

The dynamics of the Hsp90 machine:

studied by single molecule FRET

Philipp Wortmann

Vollständiger Abdruck der von der Fakultät für Physik der Technischen Universität München zur Erlangung des akademischen Grades eines

Doktors der Naturwissenschaften (Dr. rer. nat.)

genehmigten Dissertation.

Vorsitzender:		Prof. Dr. Ulrich Gerland
Prüfer der Dissertation:	1.	Prof. Dr. Thorsten Hugel
	2.	Prof. Dr. Hendrik Dietz

Die Dissertation wurde am 29.3.2017 bei der Technischen Universität München eingereicht und durch die Fakultät für Physik am 12.6.2017 angenommen.

Abstract

Chaperones maintain the protein homeostasis in cells and furthermore allow the adaption to stress conditions, e.g. heat. The most abundant chaperone in the cell is the heat shock protein 90 (Hsp90). It chaperones a broad range of client proteins being involved in their correct folding or maturation and is therefore essential for eukaryotes. Although first characterized more than two decades ago, its function and the underlying mechanisms still remain enigmatic.

Within this thesis, three single molecule FRET (smFRET) approaches are developed and utilized to characterize the structure and the dynamics of Hsp90 and the Hsp90 machine at high spatial and temporal resolution.

The previously unresolved in solution structure of Hsp90's open conformation is resolved at 4 Å resolution by the development of a novel method for structural biology, which is based on self-consistent FRET networks. The open conformation is characterized as an highly dynamic ensemble of conformations fluctuating at the millisecond timescale including even faster local dynamics. The flat and broad energy landscape could enable the diversity of interactions characterized in prior research and provides a reasonable explanation for the variety of crystal structures that have been published.

A three-color smFRET assay is developed that yields correlated information on the conformation of Hsp90, its interaction with nucleotide and their response to other components. A weak cooperativity between Hsp90's two nucleotide binding sites is revealed and characterized. It has remained hidden in common biochemical assays before due to their limited resolution. Co-chaperones and nucleotide modulate Hsp90 at independent motifs. Thereby, they achieve a fine-tuning of Hsp90 by the interference of the affected processes. Thus, this work provides further understanding of the tightly controlled processes before the actual ATP hydrolysis step.

Finally, a biochemical tether is engineered that allows smFRET studies on the very weak interaction between Hsp90 and the co-chaperone Cdc37. Cdc37 effects on the conformational dynamics of Hsp90 partly overlap with the effects of ATP, providing further evidence of the nucleotide's role as a co-factor. The construct is the prerequisite to assess the interaction between Hsp90 and a multitude of kinases in single molecule experiments.

The results provide a much deeper insight into the underlying mechanisms that cause the effects previously observed in bulk experiments. They allow to explain the characteristics of the interaction between Hsp90 and nucleotides, co-chaperones and clients. Because ATP hydrolysis is not essential for the conformational dynamics, but would rather result in energy dissipation, its function is probably to preserve directionality in the transient association with co-chaperones and client proteins. Hsp90 – as other chaperone systems – might fulfill two chaperone functions in a cell, as a 'holder' and as a 'folder'.

The methods that have been developed within this work do not only provide the basis for further research on the diverse interactions and regulations within the Hsp90 machine, but can also be applied on other biological systems. On the foundation of this work, the in-solution structures of dynamic and flexible or badly crystallizing proteins are within reach, as well as studies on the auto-regulation and cooperativity of oligomeric ATPases, and single molecule experiments on low affinity complexes.

Publications

Some ideas and figures have appeared previously in the following publications:

Wortmann, Philipp, Markus Götz, and Thorsten Hugel: 'Cooperative nucleotide binding in Hsp90 and the underlying mechanisms'. *bioRxiv* (2017), vol. DOI:10.1101/113191

Götz, Markus, Philipp. Wortmann, S. Schmid, and T. Hugel: 'A Multicolor Single-Molecule FRET Approach to Study Protein Dynamics and Interactions Simultaneously'. *Methods in enzymology* (2016), vol. 581: pp. 487–516

Hellenkamp, Björn, Philipp Wortmann, Florian Kandzia, Martin Zacharias, and Thorsten Hugel: 'Multidomain structure and correlated dynamics determined by self-consistent FRET networks'. *Nature methods* (2017), vol. 14(2): pp. 174–180

Hellenkamp, Björn, Philipp Wortmann, Florian Kandzia, Martin Zacharias, and Thorsten Hugel: 'Determination of structural ensembles and correlated dynamics of a multi-domain protein'. *Protocol Exchange* (2017), vol. DOI:: 10.1038/ protex.2016.078

Contents

List of Figures

List of Tables

Acronyms

aa	amino acid
Aha1	activator of Hsp90 ATPase protein 1
AOTF	acousto-optical tunable filter
ADP	adenosine diphosphate
ALEX	alternating laser excitation
AMP-PNP	adenylyl-imidodiphosphate
APD	avalanche photodiode
ATP	adenosine triphosphate
ATP*	ATP-γ-(6-Aminohexyl)-imido-Atto647N
ATPγO*	ATP-γ-(6-Aminohexyl)-Atto647N
AV	accessible volume
BSA	bovine serum albumine
BIC	bayesian information criterion
Cdc37	cell division cycle protein 37
CD	circular dichroism
cryo-EM	cryo electron microscopy
CI	confidence interval
CPP	cell penetrating peptide
CTD	C-terminal domain
DNA	deoxyribonucleic acid
DTT	dithiothreitol
EMCCD	electron multiplied charge coupled device
FOV	field of view
FT	Fourier transform

FPS	fluorescence positioning system
GFP	green fluorescent protein
HILO	highly inclined laminar optical sheet
HOMO	highest occupied molecular orbit
IC	internal conversion
IPTG	isopropyl-β-D-thiogalactoside
ISC	inter-system crossing
ITC	isothermal titration calorimetry
Hsp90	heat shock protein 90
LR	likelihood ratio
LUMO	lowest unoccupied molecular orbit
MD	middle domain
MD	molecular dynamic
MLE	maximum likelihood estimator
HMM	hidden Markov model
NIR	near infra-red
NA	numerical aperture
NEF	nucleotide exchange factor
NLS	nuclear localization sequence
NTD	N-terminal domain
PF	partial fluorescence
PBS	phosphate buffered saline
PNP*	AMP-γ-(6-Aminohexyl)-PNP-Atto647N
PCR	polymerase chain reaction
PDB	protein data base
PEG	polyethyleneglycole
PIE	pulsed interleaved excitation
RC	random-coil

RMSD	root mean square deviation
RMSF	root mean square fluctuation
SAXS	small angle X-ray scattering
S/N	signal to noise
SPR	surface plasmon resonance
smFRET	single molecule Förster Resonance Energy Transfer
SR	stiff rods
TCEP	tris(2-carboxyethyl)phosphine
TIR	total internal reflection
TIRF	total internal reflection fluorescence
tta	time to absorption
UC	ultra-centrifugation
WLC	worm-like chain

CHAPTER 1

Introduction

1.1 Protein folding

Every single bacterium or cell relies on proteins to maintain its physiology and survive. Proteins fulfill a wide range of functions within a cell, from building up rigid macroscopic structures in the cytoskeleton to catalyzing reactions as biological catalysts (enzymes).

On the molecular scale, these proteins are linear chains made of 20 different amino acids connected by peptide bonds. These chains adopt a unique three-dimensional structure (i.e. the native state), which enables them to fulfill their specific functions inside a cell. The transition from a linear chain without intra-molecular contacts towards the native, biologically functioning state is called protein folding. Although the sequential sampling of

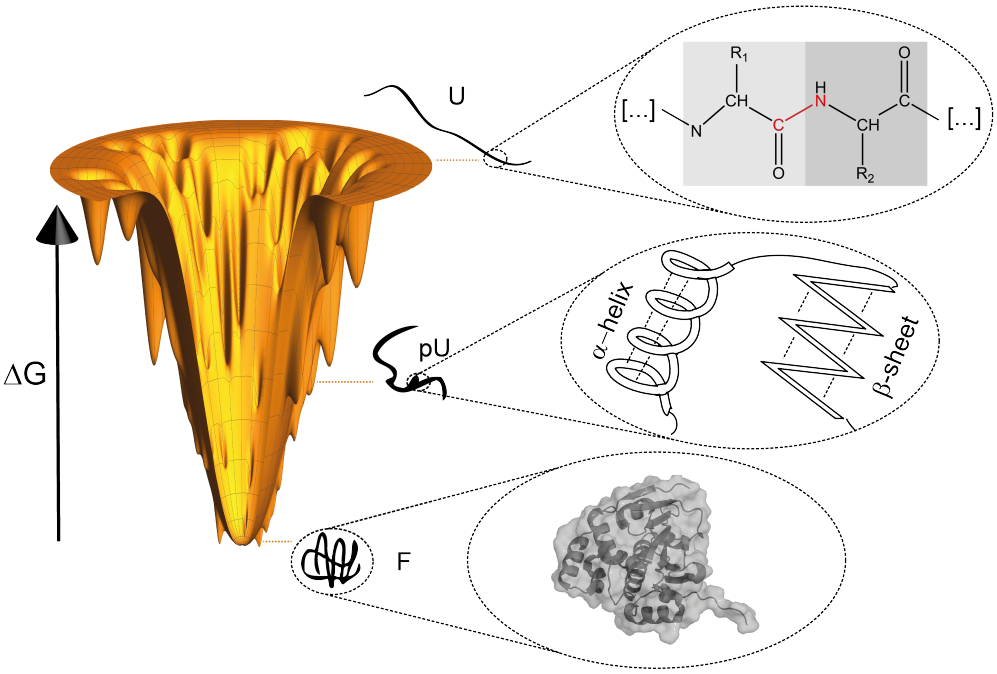

Figure 1.1: Protein folding is directed by the energy landscape of the protein. An unfolded protein (U) is a linear chain of amino acids, connected by peptide bonds (indicated in red). It forms secondary structure (such as α-helices or β-sheets) and a three-dimensional structure along its energy landscape towards the global minimum, i.e. the native, folded (F) state. Kinetically or thermodynamically stable intermediates of partially unfolded (pU) structures can appear on- or off-pathway that do not contain all specific contacts, which occur in the native state. Funnel drawn with the tool from https://oaslab.com/Downloads.html.

all possible three-dimensional conformations would consume an astronomical amount of time [5], most proteins master this process within the time of milliseconds to seconds [6].

This paradox is solved by the limited number of conformations a protein samples in reality. The protein structure is led by a microscopic trajectory along the energy landscape towards the global energy minimum (shown in Fig. 1.1). This represents the native state. Most other paths are thermodynamically or kinetically unfavorable, i.e. unlikely or slow. This process of folding is a cooperative and reversible process [7].

Nevertheless, a protein may fold into stable intermediate structures (local minima on the energy landscape) that are called off-pathway in case non-native local structures (e.g. H-bonds or salt bridges) are constituted. These structures have to break apart in order to allow the protein to fold into the fully native structure, thereby constituting an energy barrier. The complete process of folding is even complicated by the fact that, in many cases, proteins have to adopt different conformations in order to fulfill their function within a cell. This intrinsically implies the energy landscape of their structure to be rather flat, because the otherwise rigid structure would not allow such structural dynamics.

The complexity of the folding process further increases in a living cell. Here, the protein is not isolated (i.e. at ideal dilution) in an aqueous solution but experiences non-specific contacts with other macromolecules that change the energy landscape of its structure. Misfolded proteins often expose hydrophobic surfaces to their surrounding solvent. Upon contact with other misfolded proteins, this can result in an unspecific macromolecular assembly termed aggregation. Protein misfolding and aggregation are molecular mechanisms associated with a broad range of diseases, such as Alzheimer's or Parkinson's disease [8].

To prevent misfolding and decrease the toxic effects of aggregation on an organism, a specific class of proteins has emerged during evolution, referred to as molecular chaperones. Organized in chaperoning networks, they bind to unfolded, misfolded or even aggregated proteins and lead them towards their native (i.e. functional) state, prevent aggregation or initiate degradation of aggregates [9] (see Fig. 1.2). Their increased metabolism makes cancer cells 'addicted to chaperones' [10] and, hence, chaperones have also become a drug target for chemotherapy in cancer treatment [11].

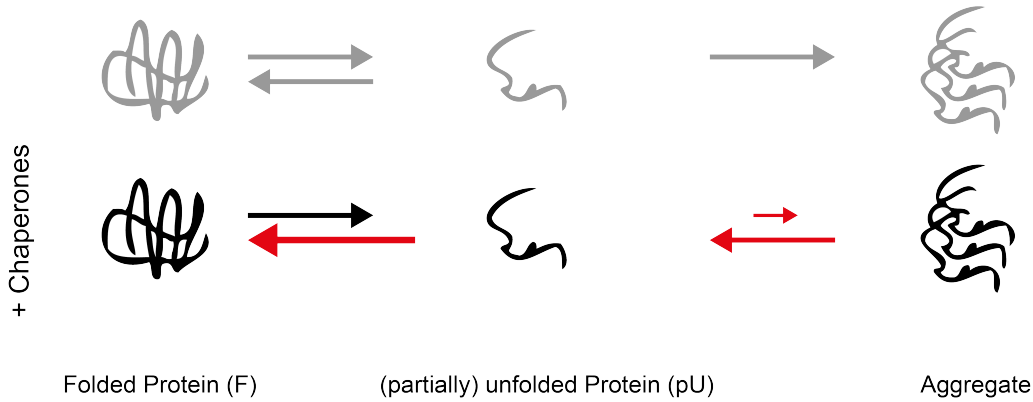

Figure 1.2: The diverse function of molecular chaperones. Proteins exist in an equilibrium of folded (F) and (partially) unfolded (pU) structures. The latter comprise the potential for aggregation, which means the formation of (insoluble) non-functional oligomers. Chaperones facilitate the refolding, the decomposition of aggregates or prevent the formation of the latter. Chaperones may also initiate degradation of aggregates, which is not shown here for clarity.

Nevertheless, the way they fulfill their molecular function remains enigmatic, most likely, because each chaperone interacts with hundreds of different proteins called 'clients'. Hence, chaperones have to fulfill a general function but must cope with the wide variety of its clients. One of the most important and complex cellular chaperone systems is the heat shock protein 90 (Hsp90) machine that is studied in this work. Its main characteristics are summarized in the following.

1.2 Heat Shock Protein 90: A key regulator of protein folding in the cell

Hsp90 is the most abundant protein within a single cell, constituting about 1-2 % of the cytoplasmic protein (i.e. $c_{cell} \approx 50\ \mu$M) [12–14]. It is highly conserved and found in all species with the exception of archaea and essential in eukaryotes. It is overexpressed under stress conditions, such as heat shock, and involved in the chaperoning of a broad range of cellular proteins.[1]

Hsp90 is often described as the hub of refolding, as it was found to be involved in most folding and activating mechanisms within a cell [15]. Within an eukaryotic cell, Hsp90 is located mainly in the cytosole, but homologue proteins also exist in the endoplasmic reticulum, mitochondria and chloroplast. In addition, cytosolic Hsp90 can translocate into the cell nucleus and is engaged in gene expression regulation [16]. Furthermore, Hsp90 is self-regulating its own expression level by the interaction with the ubiquitous transcription factor heat shock factor 1 (HSF-1) [17].

1.2.1 Structure of Hsp90

Hsp90 is a large multi-domain homodimer, with a molecular weight of about 90 kDa per protomer. Each protomer consists of three domains: The N-terminal domain (NTD) binds and hydrolyzes adenosine triphosphate (ATP). The middle domain (MD) is mainly attributed to the various interactions with unfolded or inactive client proteins. The C-terminal domain (CTD) accounts for a stable dimerization interface, with a dissociation constant K_d of 60 nM [18–20]. The NTD and MD are connected via a stretch of about 60 mainly negatively charged amino acids, referred to as charged linker (CL) that forms a transient secondary structure and interacts with the NTD [21]. The structure and domain organization of Hsp90 are shown in Fig. 1.3.

This structure represents the X-ray crystal structure of yeast Hsp90 obtained by protein crystallization in presence of the non-hydrolyzable ATP transition analogue adenylyl-imidodiphosphate (AMP-PNP). The protein is in a compact state with the two N-termini dimerized. One commonly refers to this state of Hsp90 as closed state [18]. This conformation, as well as the structure of the nucleotide binding domain with the Bergerat-fold [22] of the binding pocket, are features, which Hsp90 shares with a few other proteins that fulfill very different functions in a cell, making up the class of GHKL ATPases [23].

One can conclude from the diverse X-ray crystal structures of homologues, small angle X-ray scattering (SAXS) data and electron microscopy studies that Hsp90 is able to undergo large global conformational changes in terms of domain rearrangements [24–26]. The number of structurally different structures that have been published demonstrates the complexity of Hsp90. It suggests a very flat and broad energy landscape for Hsp90's

1 In e.g. yeast, two highly similar homologues exist, Hsc90 and Hsp90. While Hsc90 is constantly expressed at high levels, the expression level of Hsp90 are tenfold lower at physiological conditions, but reach similar levels upon heat shock [12].

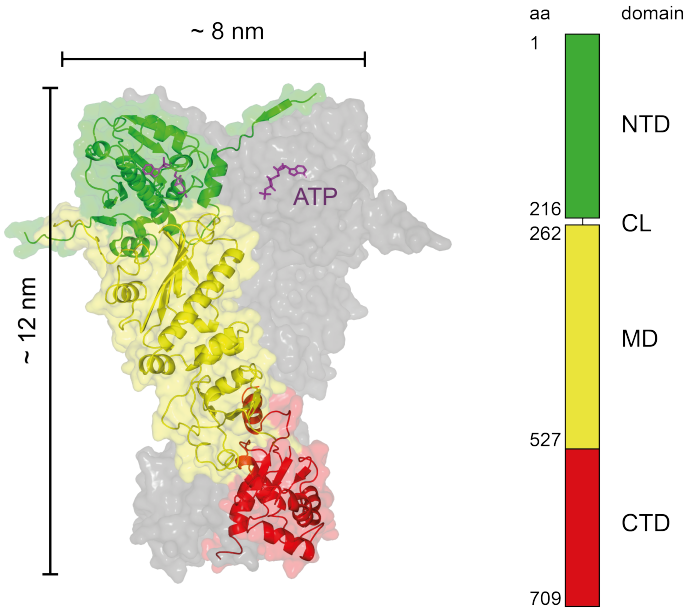

Figure 1.3: The crystal structure of full-length yeast Hsp90 dimer in its closed conformation with AMP-PNP bound (PDB 2cg9) and the domain lengths in amino acids (aa). Depicted are the N-terminal (N) in green, the middle (M) in yellow and the C-terminal (C) domain in red. The charged linker (CL) was partly substituted and is not resolved in this crystal structure.

structure, rather than a steep funnel. This energy landscape likely results in a wide conformational space the protein can adopt at (near-)physiological conditions. On the other hand, the variety of the data rises the question, if experimental artifacts impeded the general picture of Hsp90's dynamic structure. In this regard, the dynamics of the global conformation of Hsp90 are only weakly coupled to its ATPase activity [27]. Accordingly, two main conclusions about the origins of the flexibility of Hsp90 can be drawn from this variety of published structures: (1) The interface of the NTD and the MD is not rigid but flexible. It further allows a relative, and most likely rotary motion of the two domains. (2) The two protomers are able to move apart to a great extend and seem to occupy a large conformational space. Both features can be seen in a comparison of published structures to the closed state of Hsp90, shown in Fig. 1.4.

In all published structures so far, the domains of Hsp90 display symmetric arrangements. Although an intrinsic asymmetry of Hsp90 has been suggested [28, 29], the asymmetry arises from the deformation of local motifs that are poorly resolved in other crystal structures. Global asymmetry has only been shown for complexes with other proteins [26, 30–32].

Several local motifs in Hsp90 are involved in dynamic intra- and cross-protomer interaction and a correlation of their kinetics with the ATPase activity has been shown by quenching experiments [33]. Fig. 1.5 depicts three of those motifs. The extreme N-terminus of Hsp90 is known to have at least two binding sites, either extending the β-sheet of the NTD in *cis* or making a cross-monomer contact with the β-sheet in *trans* [34]. Hsp90's binding pocket can dynamically open and close its ATP-lid [18, 34], while the stably closed form has only been observed in the Hsp90 dimer so far. A stabilization of the closed ATP-lid conformation increases the apparent enzyme activity [35, 36]. Furthermore, the catalytic loop between

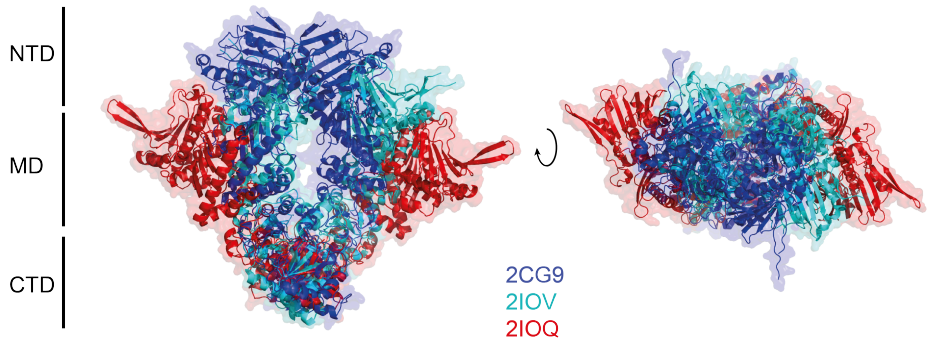

Figure 1.4: Comparison of the X-ray crystal structure of yeast Hsp90 in presence of AMP-PNP (PDB 2cg9, blue), the endoplasmic reticulum homologue Grp94 from *C. lupus* in presence of ADP (PDB 2iov, cyan) and the *E. coli* homologue HtpG (PDB 2ioq, red) in absence of nucleotide.

amino acids 370 and 387 including Arg_{380} binds to the γ-phosphate of AMP-PNP in the crystal structure. More dynamic motifs have been identified, for instance mutations at the CL impair Hsp90's ATPase rate [37]. However, it remains unclear how the local motifs affect the global conformation and vice versa.

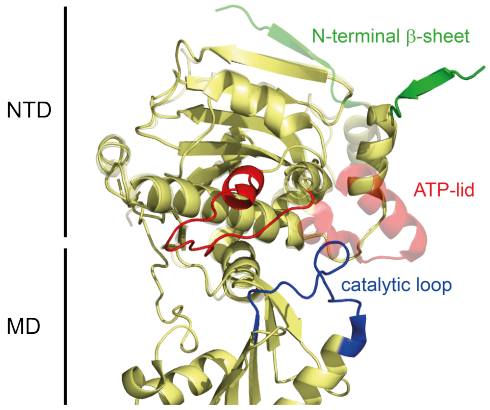

Figure 1.5: Local motifs in Hsp90 exhibit dynamics. Depicted are the N-terminal β-sheet (green), the ATP-lid (red) and the catalytic loop (blue), with alternative arrangements shown transparent (PDB 2cg9, 2wep and 2iov).

The general flexibility of Hsp90 comes in hand with its very low affinity for nucleotide binding and weak ATPase activity. ATP, as well as adenosine diphosphate (ADP) and AMP-PNP, are bound with a dissociation constant (K_d) above 1 μM, with the reported affinities varying by two orders of magnitude. A summary is given in Appendix B.1.2, page 114 [34, 38–42]. The affinities for nucleotides, as well as the ATPase rate of the different Hsp90 homologues, vary by at least one order of magnitude. The ATPase activity of Hsp90 is very slow at about 1 min^{-1} at 30 °C for the yeast homologue [41, 43]. This is even more surpising, considering that the characterized dynamics, such as global domain arrangements or the motion of lcoal motifs have been found to happen on a timescale of milli-second to microsecond [27, 33]. The numbers suggest only weak or no coupling

between the conformational changes and the ATPase activity of Hsp90.

The low affinity and the weak ATPase activity may constitute the basis for Hsp90 to react in many diverse ways to external stress stimuli, because weak interactions with regulators can already change the protein's dynamics.

1.2.2 The molecular relevance of Hsp90

As a chaperone, Hsp90 interacts with unfolded and misfolded proteins, called clients. It can prevent unfolded clients from aggregation and help unfolded proteins to regain their native structure [44–46]. Client proteins, such as the kinases Src [47] or Cdk4 [48], rely on Hsp90 for their functional activity.

The ATPase activity of Hsp90 is stimulated by clients, which hints towards a coupling between the ATPase function and chaperone activity [49, 50]. However, a recent study suggests the ATPase activity being not essential for yeast viability under physiological conditions [51]. Therefore, the role of ATP in Hsp90's function is not clear. Although the interaction of Hsp90 with several model client proteins has been subject to prior research, general conclusions could not be drawn until now [52–54].

1.2.3 Regulation of Hsp90 by co-chaperones

Hsp90 interacts additionally with proteins that have regulatory effects on its function, referred to as co-chaperones. More than 20 co-chaperones have been found for eukaryotic Hsp90 so far [15]. They entail different and partially adverse effects on Hsp90 and work together with Hsp90 in a complex and dynamic network to fulfill the task of folding and activating proteins [55]. Accordingly, the biologically relevant 'Hsp90' might rather be a complex protein machine than one single protein.

Co-chaperones bind either via a specific tetratricopeptide (TPR) repeat domain to Hsp90's C-terminal `MEEVD` amino acid motif or more diverse at the domain surfaces of Hsp90. The most prominent effect that is observed for many co-chaperones is the change in ATPase activity of Hsp90. The interactions of the co-chaperones with Hsp90 are transient and characterized by weak affinities, which complicates mechanistic studies.

The interactions of Hsp90 with the co-chaperones Aha1, Sba1 and Cdc37 present the focus of this thesis. A scheme of the domain organization of these proteins is shown in Fig. 1.6.

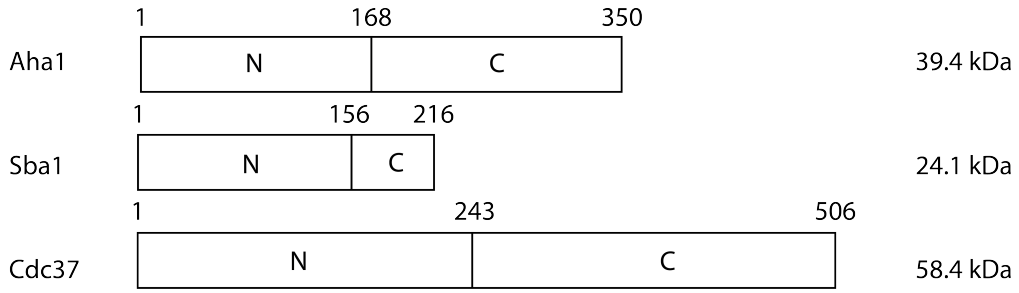

Figure 1.6: Domain representation and amino acids for the three Hsp90 co-chaperones Aha1, Sba1 and Cdc37, as well as the molecular weight (in yeast) [13, 56, 57].

Aha1

Activator of Hsp90 ATPase protein 1 (Aha1) is found at a cellular concentration of about 0.5 μM [13, 58, 59]. It stimulates the ATPase activity of Hsp90 in a salt dependent manner up to more than tenfold [51]. The interaction of Aha1 and Hsp90 was characterized by isothermal titration calorimetry (ITC), and a K_d of 0.2 μM and 5 μM was found in presence of AMP-PNP and ADP, respectively [60, 61].[2] A crystal structure of Aha1's NTD in complex with the MD of Hsp90 reveals an interaction of Aha1 with the catalytic loop of Hsp90 [62]. As shown in Fig. 1.7, it thereby interferes with the interaction of the catalytic residue Arg_{380} with the γ-phosphate of ATP. That is essential for hydrolysis in a functional homo dimer [63].

Aha1 seems to tighten the control of ATP-binding and successive molecular rearrangements. It accelerates structural rearrangements within the Hsp90 dimer even in the absence of nucleotide [64]. As a consequence, other local or even global rearrangements of the domains must be influenced additionally. Indeed, the interaction between Hsp90 and Aha1 involves both complete protein chains. The stimulation of Hsp90's ATPase with only the NTD of Aha1 is much weaker than with the full-length protein and the affinity of Aha1 to Hsp90's MD is lower than the affinity to the complete Hsp90 dimer [13, 60, 62]. Full-length Aha1 stabilizes Hsp90 in a closed conformation [51]. It can accelerate the ATPase activity of the Hsp90 dimer in *cis* and *trans*, hinting towards a complex stoichiometry of 1:1 (Aha1:$Hsp90_2$) [32]. Nuclear magnetic resonance (NMR) studies reveal a second interaction site of Aha1's NTD at Hsp90's NTD and a binding of Aha1's CTD at the groove between the two NTD of the closed Hsp90 dimer formed in presence of AMP-PNP [32]. Aha1 seems to affect the ATP-lid of Hsp90, since it can partly resemble the effect of the Hsp90 mutant A107N that stabilizes the closed lid conformation [60].

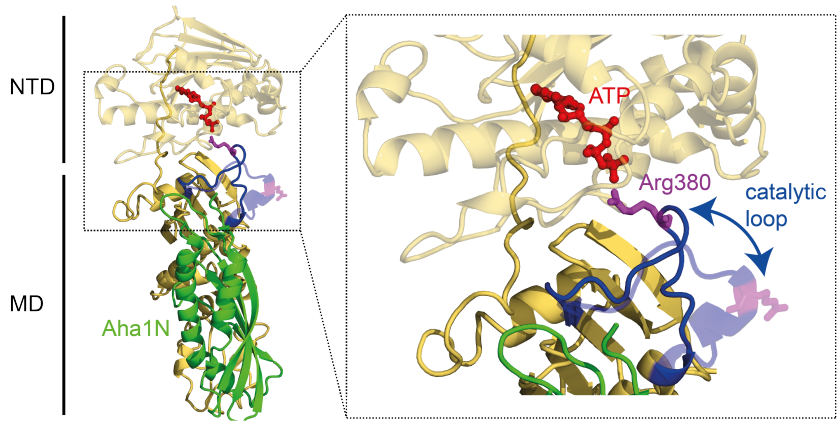

Figure 1.7: Aha1 affects the catalytic loop and therefore the orientation of Arg_{380} of Hsp90. Shown is a superposition of an Hsp90 protomer from the X-ray crystal structure of closed Hsp90 (PDB 2cg9) and the X-ray crystal structure of Hsp90 MD in yellow and Aha1 NTD in green (PDB 2iov). The catalytic loop (blue) is rearranged (transparent blue) in the crystal structure with Aha1 and hence the Arg_{380} cannot bind to the γ-phosphate of the nucleotide anymore.

2 This characterization has been done for the interaction between the yeast homologues.

Sba1

Sba1 is found in cells at a cellular concentration of about 1 μM [58, 59, 65]. It inhibits yeast Hsp90's steady state ATPase activity down to 50 % [60, 66], but has a negligible effect on its single-turnover ATPase rate [50, 67]. It binds with higher affinity to Hsp90 in presence of AMP-PNP than ADP or in absence of nucleotide with the dissociation constants K_D(AMP-PNP) = 1.5, K_D(ADP) = 10, K_D(Apo) = 17 μM[61, 66][3]. The affinity of AMP-PNP for human Hsp90 increases in presence of Sba1 by one order of magnitude [68]. Sba1 is suggested to stabilize a 'post-hydrolysis state' of Hsp90, which is not accessible with ADP and prevents the release of the hydrolysis products, ADP and P_i. The complex Sba1:$Hsp90_2$ coexists in both stoichiometries 1:1 and 2:1 with a presumed negative cooperativity for the binding of the second Sba1 [61, 66, 68]. Sba1's NTD was co-crystallized with Hsp90 and AMP-PNP [18]. This complex has the stoichiometry of 2:2:1 (Sba1:AMP-PNP:$Hsp90_2$) and reveals an interaction of the co-chaperone with the NTD of each Hsp90 monomer, keeping the ATP-lid in its closed conformation (shown in Fig. 1.8). The C-terminal 90 amino acids of Sba1 are not resolved in the crystal. In addition, the NTD of Hsp90 alone is insufficient for binding of Sba1 [41] and mutations in the MD of Hsp90 impair Sba1 binding [69]. Altogether, this suggests an additional interaction complex of the two proteins. Interestingly, Sba1 has a chaperoning function itself [70, 71], which is mainly mediated by the unstructured part at its C-terminus [72]. It has thus been proposed to couple Hsp90's ATPase activity with substrate release.

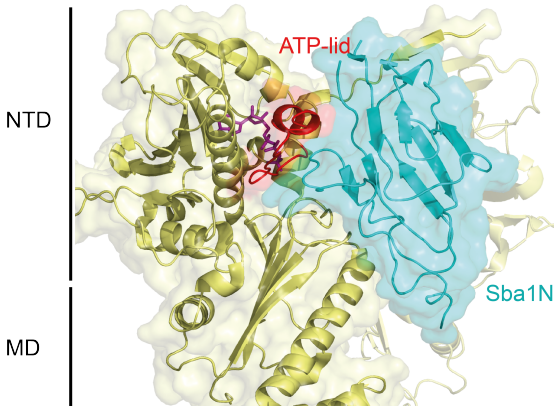

Figure 1.8: Sba1 (cyan) binds with its NTD to the NTD of the closed Hsp90 dimer (yellow) and keeps the ATP-lid (red) in the closed conformation (PDB 2cg9). The complex is symmetric: two Sba1 bind to the Hsp90 dimer.

Cdc37

Cell division cycle protein 37 (Cdc37) is found at a cellular concentration of about 0.3 μM [58, 59, 73]. It links the wide spectrum of protein kinases to Hsp90 and is required for their stable folding or activation [74–76]. Compared to other co-chaperones, the sequence of Cdc37 is much less conserved and the homologues differ by up to two orders of magnitude in their binding affinities towards Hsp90, with their K_d approximately determined in the range of 4-100 μM (yeast/human homologue) [77, 78]. Cdc37 inhibits the ATPase activity

3 This characterization has been done for the interaction between the human homologues and has been determined by ITC and surface plasmon resonance (SPR).

of Hsp90, which is likely mediated by its C-terminal domain binding to the opened ATP-lid of Hsp90, as concluded from the X-ray crystal structure shown in Fig. 1.9(A) [78, 79]. Earlier work reported weak effects on the binding and unbinding rates of labeled ATP [80]. The dynamic N-terminal domain of Cdc37 binds to kinases and is regulated by reversible phosphorylation of a highly conserved Ser_{14} [81–83].

The structure of the ternary complex $Hsp90_2$:Cdc37:Kinase has been investigated by two studies [30, 84]. Both find a stoichiometry of 1:1:1, and in both, Hsp90 adopts a closed conformation alike the structure found for Hsp90 crystallized in presence of AMP-PNP. However, the kinase and Cdc37 bind at completely different sites in each structure, demonstrating the dynamic nature of this complex [85].

Cdc37's CTD binds either to the NTD or the MD of Hsp90, while Cdc37's NTD constitutes a coiled-coil structure and binds at the interface of Hsp90's NTD and MD [30, 80, 86]. A comparison of the structures is shown in Fig. 1.9.

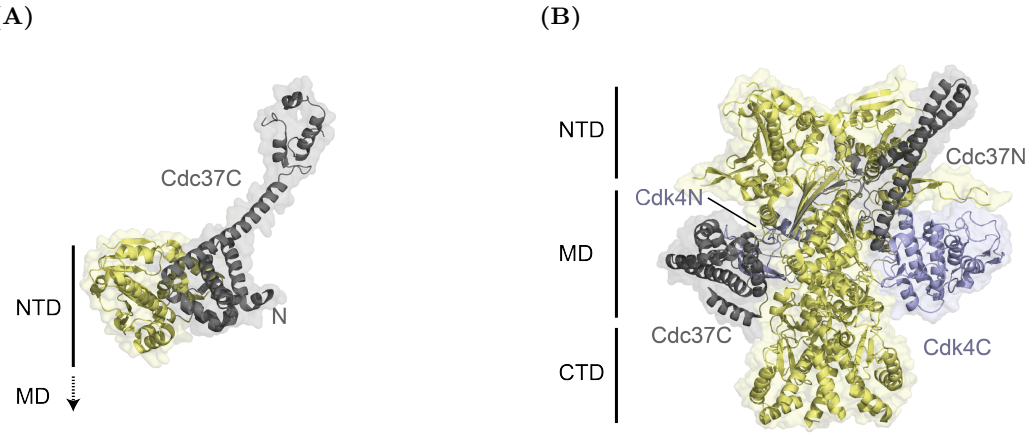

Figure 1.9: Cdc37 can interact with Hsp90's NTD and MD via its two own domains in two completely different orientations. (A), X-ray crystal structure of yHsp90's NTD with a C-terminal fragment of hCdc37 (PDB 1us7). (B), Cryo-EM reconstruction of a Hsp90:Cdc37:Cdk4 complex [30]. Hsp90 is colored in yellow, Cdc37 in grey and the kinase in blue.

A network of co-chaperones

All Hsp90 co-chaperones co-exist in a cell. They consequently interact with each other and preformed Hsp90 complexes. However, their overall cellular concentration is much lower than the concentration of Hsp90. Even though their interactions with Hsp90 are transient, it is thus unclear how the Hsp90 machinery's function depends on their interplay *in vivo*.

Whereas the interaction of Sba1 and Aha1 with Hsp90 has been suggested to be exclusive [87], their binding sites do not overlap and a modulation rather than a competition has been concluded from ATPase assays [32]. Aha1 and Cdc37 can coexist in a complex with the open conformation of Hsp90, found by UV/VIS spectroscopy [61]. Fluorescence ultra-centrifugation (UC) experiments show that Sba1 and Cdc37 compete for binding to the closed state of Hsp90 induced by AMP-PNP or ATP-γ-S [77].

The interaction of co-chaperones with Hsp90 is characterized by transient binding. Furthermore, the co-chaperones bind Hsp90 at multiple and distinct sites with different domains. The strength of each interaction depends on the conformational state of Hsp90 and in turn may change the conformational rearrangement of Hsp90 itself. For the interaction between co-chaperone and the Hsp90 dimer, stoichiometries of 1:1 and 2:1 are reported,

suggesting that even this depends on the conformational state of Hsp90. Only in the case of a strong positive cooperative binding the presence of two co-chaperones of the same type on Hsp90 is likely, due to the low cellular concentration of the proteins. Taken together, the different bindings sites for each co-chaperone suggest the complexes between co-chaperones and Hsp90 may switch between asymmetry and symmetry.

Co-chaperones feature flexibility themselves, which complicates structural studies. Only the correlated information on kinetic and structural features in complexes will therefore be able to complete the picture of the multiple protein interactions and can address the question, how each interaction contributes to the assigned function of the Hsp90 machinery as chaperone.

1.3 Single molecule experiments

The description of Hsp90 and its interaction network above nicely demonstrates the dynamics of the Hsp90 machine. In this context, Hsp90 represents a very good example for a dynamic biological system. Such biological systems must exhibit dynamics in order to maintain the steady-state within an organism. Dynamics imply that biological molecules (such as proteins) undergo structural changes. Studying these dynamics is complicated in absence of or at weak synchronization between the respective molecules, because the ensemble emits an averaged signal in biochemical assays otherwise. Most commonly, this problem is solved by synchronizing the molecules of interest, for instance in stopped-flow experiments studying the re-equilibration of the system. However, as soon as the system populates more than two states, these methods will not be able to resolve the single states and their kinetics.

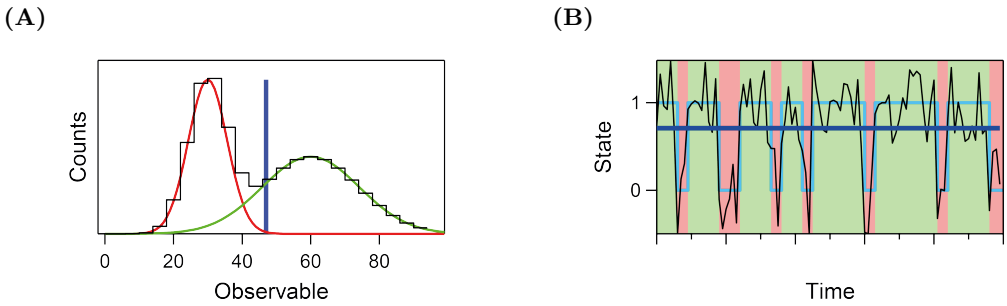

Figure 1.10: Additional information is accessible by single molecule experiments. (A), the average signal (depicted in blue) may hide the information on two microscopic states of a given system. These states (green, red) can be recovered from single molecule data (black). This is demonstrated on the exemplary equilibrium distribution derived from a single molecule experiment (binned histogram) on a two-state system. (B), exemplary kinetics observed in a single molecule experiment on a two-state system. The current state of the system is depicted by the colored background, the transition path by the cyan line.

Studying single molecules separately, instead of an ensemble of molecules, opens the possibility to avoid averaging artifacts, to resolve multiple different conformations or states and, at the same time, to study the system at equilibrium. Their ability to separate states is illustrated in Fig. 1.10(A). Moreover, single molecule experiments can resolve the kinetics of dynamics, such as fluctuations at thermal equilibrium or directionality under steady-state conditions. This is shown in Fig. 1.10(B). Thus, single molecule experiments are an ideal complimentary tool to study complex biological systems like the Hsp90 machine.

1.3.1 Single molecule fluorescence and FRET

Single molecule experiments can be applied to biological samples, and the most common readouts are force or fluorescence. This work uses single molecule Förster Resonance Energy Transfer (smFRET), based on the fluorescence of single molecules, to study molecular interactions, their dynamics and structural changes within the Hsp90 system.

Fluorescence refers to the phenomenon of spontaneous emission of light by a material shortly after absorbance of light (with $E_{em} \leq E_{abs}$) [88, p. 443]. The energy of a molecule can be described in terms of its electronic, vibrational and rotational state. When a molecule absorbs a photon (i.e., it takes up the energy of it), an electron is excited into a state of higher energy. The energy of the transition equals the energy of the photon. At wavelengths of 300-700 nm, this electron is usually the one in the highest occupied molecular orbit (HOMO), which then transits into the lowest unoccupied molecular orbit (LUMO). The electron is typically excited from the singlet state S_0 to the singlet state S_1, as demonstrated in a Jablonski diagram Fig. 1.11 [89, p. 9].

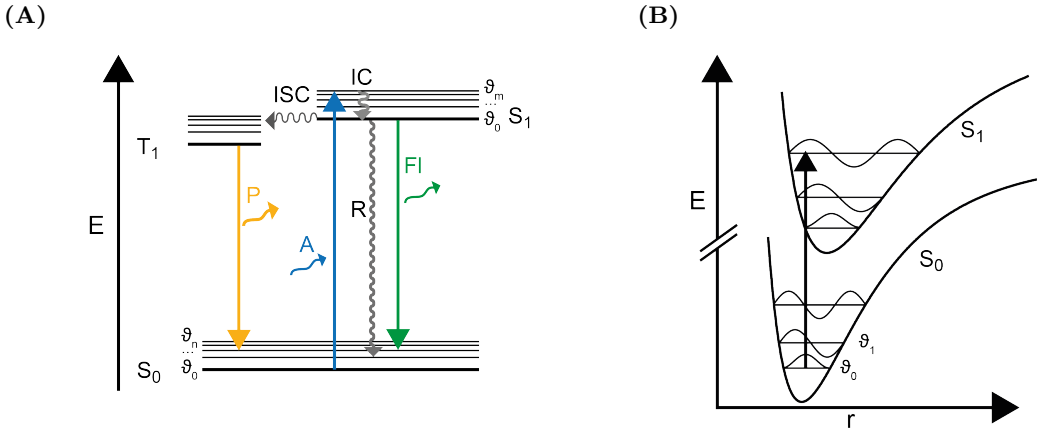

Figure 1.11: The mechanisms of absorption and fluorescence. (A), Jablonski diagram to illustrate the processes involved in fluorescence. S_0,S_1 are singlet states, T_1 the triplet state, ν indicates the vibrational states. Rotational states are not indicated for clarity. A, absorption; IC, internal conversion; ISC, inter-system crossing; P, phosphorescence; Fl, fluorescence; R, relaxation. (B), according to the Franck-Condon principle, electronic transitions (absorbance, shown exemplary as black arrow and fluorescence) are much faster than the nuclear movements and therefore happen vertical on the axis of inter-nuclei distance r.

The absorption of a photon occurs on a much faster timescale (10^{-15} s) than the movement of the nuclei within the molecule due to the smaller mass of electrons (Franck-Condon principle). Therefore, the nuclear momenta (as well as their kinetic energies) are preserved and the new vibrational level ν_j in the electronic excited state S_1 must be compatible with the nuclear positions and momenta of the vibrational level ν_i of the molecule before excitation. This corresponds to a vertical transition on the axis of inter-nuclei distance. The probability for each transition $S_0\nu_i \rightarrow S_1\nu_j$ can be calculated from the overlap of their wavefunctions [88, p. 443f].

After the excitation, the energy of the molecule rapidly decays to lower vibrational states in S_1 due to vibrational relaxation by collisions with surrounding molecules (dissipation) (10^{-12} s) and due to reorganization of the solvent (10^{-10} s). This decay is also known as internal conversion (IC). It happens generally directly after an excitation event,

therefore processes that follow are approximately independent of the excitation energy (Kasha's rule).

From the vibrational ground state in S_1, the molecule can return to the electronic ground state S_1 by the emission of a photon with a dwell time of around 10^{-9} s. This is referred to as fluorescence. For the transition during fluorescence the Franck-Condon principle applies again, which leads together with the vibrational relaxation in between absorption and fluorescence (i.e. the energy loss, referred to as Stokes shift) to fluorescence spectrum that mirrors the spectrum of absorption.

Fluorescence competes with other processes for the depopulation of the excited state S_1. By inter-system crossing (ISC), the spin of the excited electron is reversed, i.e. the electron enters the triplet state T_1. The transition $T_1 \rightarrow S_0$ (i.e. phosphorescence) involves changing two quantum numbers and is thus 'forbidden', i.e. slow (10^{-3} to 10^{0} s). In addition, the molecule can de-excite by further relaxation and thus dissipation without the emission of a photon. Therefore, the number N_e of photons emitted by a fluorescent dye after absorbing a certain number N_a of photons can be characterized as ratio of the different processes, the quantum yield Q_D (giving the efficiency of a fluorophore):

$$Q_D = N_e/N_a = \frac{k_{fl}}{k_{fl} + k_{isc} + k_{relax} + ...} = \frac{k_{fl}}{\sum_{i=0}^{i} k_i} \tag{1.1}$$

with k_i being all de-exciting processes and k_{fl} the rate of fluorescence. Among those, one can be FRET, which is introduced in the following.

FRET refers to the phenomenon of energy transfer between two fluorescent molecules by dipole-dipole coupling. It was first explained quantitatively by Theodor Förster [90]. One fluorphore (called donor, D) is excited by light as described above and can now additonally de-excite by an energy transfer to another appropriate fluorophore in its proximity (called acceptor, A), as shown in Fig. 1.12. At an inter-atomic distance $r \ll \lambda$, this energy transfer is radiation-less by a coupling of the transition dipoles of the two fluorophores [91, 92]. The process of FRET has been derived both in semi-classic physics and quantum mechanics, resulting in the same formulae [90, 93].

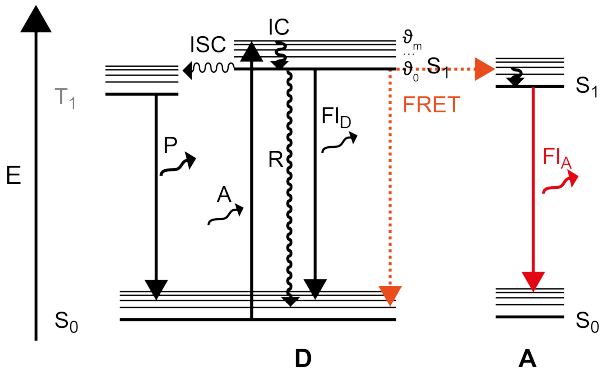

Figure 1.12: FRET in the Jablonski diagram shown in Fig. 1.11. After excitation of the donor dye, the absorbed energy can be transferred radiationless to the acceptor, which can subsequently emit a photon to relax to the electronic ground state. A/D refers to acceptor/donor.

The rate of the energy transfer for a donor and acceptor separated by the distance r can

be described by [89, p 445]:

$$k_T(r) = \frac{Q_D\,\kappa^2}{\tau_D\,r^6}\left(\frac{9000\,\ln 10}{128\Pi^5 N_A n^4}\right)J(\lambda) \tag{1.2}$$

$$J(\lambda) = \int_0^\infty F_D(\lambda)\varepsilon_A(\lambda)\lambda^4\,\mathrm{d}\lambda \tag{1.3}$$

where Q_D is the quantum yield of the FRET donor, τ_D is the lifetime of the excited donor in absence of the acceptor, N_A is Avogadro's number, n is the refractive index of the medium, κ^2 is the dipol orientation factor and $J(\lambda)$ is the overlap integral of donor fluorescence $F_D(\lambda)$ and acceptor extinction $\varepsilon(\lambda)$ spectra.

The overlap integral describes quantitatively the equivalence between the energy levels of donor and acceptor. It is exemplified in Fig. 1.13(A). It is calculated from the fluorescence spectrum of the donor normalized to unity and the extinction coefficient spectrum of the acceptor. The dipole orientation factor κ^2 (Fig. 1.13(B)) is given by:

$$\kappa^2 = (\cos\Theta_T - 3\cos\Theta_D\,\cos\Theta_A)^2 \tag{1.4}$$

$$= (\sin\Theta_D\,\sin\Theta_A\,\cos\phi - 2\cos\Theta_D\,\cos\Theta_A)^2 \tag{1.5}$$

with Θ_D/Θ_A being the angles between the dipoles and the vector joining donor and acceptor and ϕ, the angle between their planes. Depending on the relative orientation of the dipoles during transfer, κ^2 can vary from 0 to 4. It is usually assumed that within the timescale of the FRET transfer (which is the dwell time and not the transfer itself) the dipoles reorientate randomly, leading to a dynamic averaging and, therefore, $\kappa^2 = 2/3$.

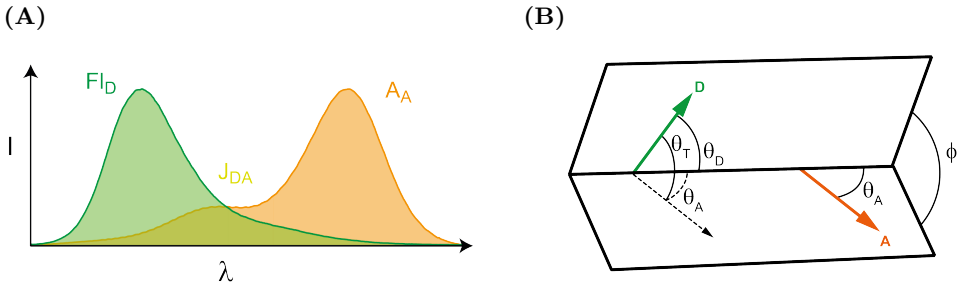

Figure 1.13: Properties that affect Förster distance. (A), fluorescence spectrum of the FRET donor and absorbance spectrum of the FRET acceptor.(B), orientations of the dipole moments that affect the radiationless energy transfer by FRET.

With all these predefined quantities ($J(\lambda)$, n and τ_D can be determined in independent experiments and freely rotation of dyes is assumed), the rate of FRET depends only on the distance between donor and acceptor to the power of -6. The characteristics of a FRET are usually specified by the Förster distance R_0 via:

$$k_T(r) = \frac{1}{\tau_D}\left(\frac{R_0}{r}\right)^6 \tag{1.6}$$

$$\Rightarrow R_0^6 = \frac{9000\,\ln 10\,\kappa^2\,Q_D}{128\Pi^5 N_A n^4}J(\lambda) \tag{1.7}$$

The energy transferred via FRET and thus the distance between two fluorophores in an experiment can be calculated from the fluorescence lifetime of the donor (D) in presence (τ_{DA}) and in absence (τ_D) of the acceptor (A) molecule or from the fluorescence intensity emitted by the two fluorophores after donor excitation (I_A and I_D), when all other parameters have been determined before:

$$E = \frac{k_T(r)}{\tau_D^{-1} + k_T(r)} = 1 - \frac{\tau_{DA}}{\tau_D} = \frac{I_A}{I_D + I_A} \tag{1.8}$$

$$= \frac{1}{1 + \left(\frac{r}{R_0}\right)^6} \tag{1.9}$$

The Förster distance R_0 for two appropriate fluorophores lies typically in the range of 45-65 Å. This is usually the lengthscale of biological molecules, such as proteins or nucleic acids, as well as of their rearrangements. Due to its high distance dependency close to R_0, the FRET efficiency can be used as a time-resolved probe for interactions between and rearrangements of those molecules. Therefore, smFRET is often referred to as 'spectroscopic ruler' [89, 94].

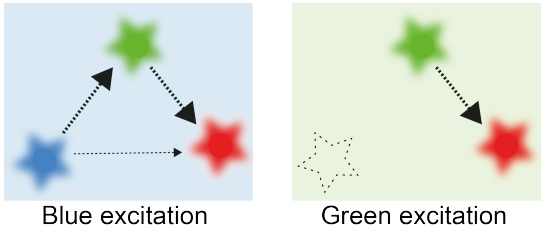

Figure 1.14: Multi-color FRET. In a system of more than two fluorophores (three shown here), the energy transfers by FRET to the different acceptors compete. Alternating excitation of all fluorophores that can function as FRET donor results in full information about the three-dimensional arrangement of the dyes. Figure published in [2].

A FRET experiment is not restricted to a single pair of fluorophores. It is also possible to combine three or four appropriate dyes with consecutive excitation wavelengths in a multi-color FRET approach [95–100]. These dyes constitute a network with inter-dye energy transfer by FRET, where the single energy transfers from one dye to all others compete with each other and, in addition, with all other processes involved in depopulating the excited singlet state S_1 of each dye. Therefore, it is difficult to extract exact distance information from this data, because dyes transfer their energy to multiple acceptors. However, by the excitation of each possible donor dye separately it is possible to resolve the spatial arrangement of all dyes and thus of the labeled specimen, e.g. proteins or DNA (shown in Fig. 1.14). This can be used to separate and identify multiple states of the studied system. A benefit from such an approach is the directly correlated information on all labeled components that are studied. This information is only accessible by indirect conclusions from separated experiments otherwise.

In this work, I combine two- and multi-color FRET with single molecule microscopy and spectroscopy to study Hsp90 and its various interactions with other molecules by smFRET.

1.3.2 Detection of smFRET

An appropriate method to perform smFRET experiments must ensure that only one single molecule is observed at the time. Furthermore, it must reduce the background fluorescence in order to gain a reasonable signal to noise (S/N) ratio. This thesis utilizes two approaches to study biological molecules by smFRET: confocal spectroscopy and total internal reflection fluorescence (TIRF).

Confocal spectroscopy reduces the illuminated volume by focusing the excitation beam into the medium, as shown in Fig. 1.15. It makes use of a pinhole in the detection pathway in order to define the detection volume. To ensure only single molecule observations, the sample is studied at picomolar concentrations [101].

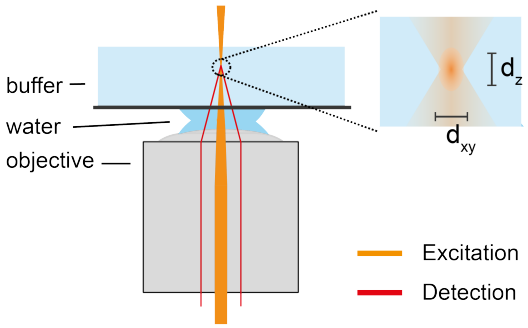

Figure 1.15: Scheme of confocal illumination. Excitation of diffusing molecules and detection of fluorescence are restricted to the confocal volume. The shape of the detection path is given by the outer limits.

In TIRF microscopy, the sample is immobilized at the surface at a low density such that single molecules are still separated by light microscopy ($\Delta d \gg \lambda_{ex}$). The excited volume is reduced by the utilization of an evanescent field. A light beam that comes from medium 1 at angle α into medium 2 is usually refracted to angle β according to Snellius' law, i.e.:

$$sin\alpha = \frac{n_2}{n_1} sin\beta \tag{1.10}$$

At $n_2 > n_1$ and the critical angle α_{crit}, the light is completely reflected, such that:

$$\alpha_{crit} = sin^{-1}(\frac{n_2}{n_1}) \tag{1.11}$$

However, the intensity penetrates a short distance z into the optically less dense medium as an evanescent field that decays exponentially:

$$I(z) = I(0)\, exp(-z/d) \tag{1.12}$$

with $I(0)$ being the intensity at the interface and d being the decay constant. The decay constant gives the distance from the interface at which the intensity is 1/e of $I(0)$, i.e. 37 %. It is given by [89, p. 759]:

$$d = \frac{\lambda_0}{4\Pi\sqrt{n_1^2\, sin\alpha - n_2^2}} \tag{1.13}$$

At $n_1 = 1.46$ (quartz), $n_2 = 1.33$ (water), $\lambda = 532$ nm and $\alpha = 65°$, this gives a penetration depth of about 128 nm. This is by far a penetration deep enough for the excitation of fluorescent molecules close to the surface (with a typical size < 10 nm), but limits the illumination of the surrounding and thereby reduces the background fluorescence.

Two experimental realizations of total internal reflection (TIR) illumination exist, objective-type and prism-type TIR. In the former, the excitation beam is focused with a lens and passed through a prism onto the quartz-water interface between prism and measurement chamber (Fig. 1.16(A)). The latter relies on the use of an oil objective with high numerical aperture (NA). The beam is focused on the back-focal plane of the objective and translated from the optical axis, which results in an evanescent field at the glass-water interface (Fig. 1.16(B)).

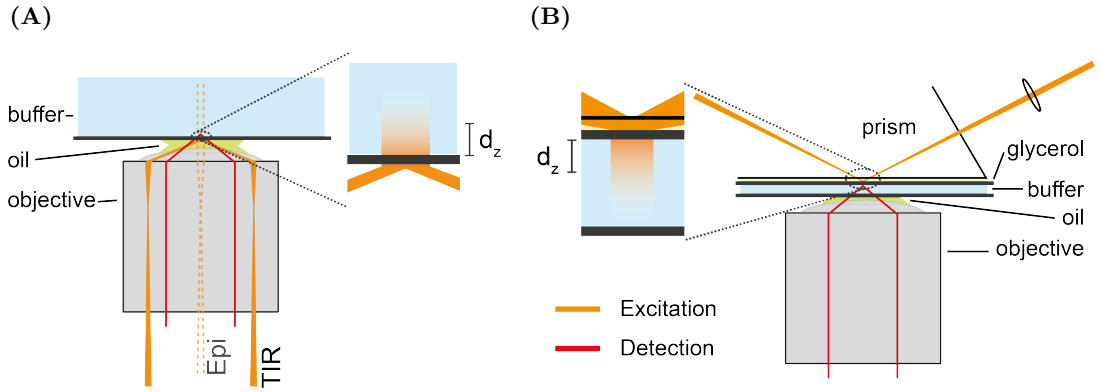

Figure 1.16: Setups for TIR illumination. (A), objective-type TIR.(B), prism-type TIR.

In a TIRF microscope, the fluorescence is typically detected with an electron multiplied charge coupled device (EMCCD) camera and recorded under continuous illumination, allowing for the detection of several single molecules at the time with a time resolution of the recorded movie down to 10 ms.

1.4 Objective

Although extensive research has been conducted on the chaperone machine Hsp90, its function is still not completely understood. As detailed before, some published results are even contradicting. For example, the function of the ATPase activity of Hsp90 has not been determined yet, or the motifs that co-chaperones or clients bind to vary, depending on the applied method and used model system.

Single molecule methods have already proven to give further insight into the function of Hsp90, mainly smFRET [21, 27, 99, 102]. To study the dynamics of Hsp90 by smFRET, one attaches two fluorophores at appropriate positions in the Hsp90 dimer. The FRET efficiency measured on single molecules then provides information about the distance between the two fluorophores. This is expanded by the time-dependent information, i.e. the protein dynamics that lead to changes in the distance between the dyes and therefore the FRET efficiency.

Based on this idea, smFRET has revealed that Hsp90 exists in four kinetically different states [27], of which two are open and two are closed states. Nucleotides can bind to both, open and closed Hsp90 [99]. Nevertheless, the knowledge of *what* exactly Hsp90's functions

are and *how* it fulfills them still remains limited.

1.5 Outline

This work aims to solve questions regarding Hsp90's function by the development and application of novel single molecule FRET methods:

- Chapter 2, Methods and developments, on page 19 introduces the methods and developments that this work is based on.
- In Chapter 3, Results and discussion, on page 47, the results from three different projects that I worked on within this thesis are presented and discussed separately:
  - In Section 1 on page 49, the ability of smFRET as a tool in structural ability is advanced in order to resolve the dynamic structure of yeast Hsp90.
  - In Section 2 on page 67, we develop multi-color smFRET further to gain correlated information on the transient interplay of different components comprising the Hsp90 machine.
  - In Section 3 on page 85, the restriction of smFRET to the investigation of high-affine interactions is eased by the development of a novel molecular tether, and the low-affine interaction between Hsp90 and the co-chaperone Cdc37, including the native Hsp90 client protein Ste11, is studied.
- The Conclusion on page 99 discusses the results on the dynamics of and the interactions in the Hsp90 machine in the context of the chaperone function and mechanisms in homologue protein systems.
- In the Outlook: Studying the complete Hsp90 machine on page 103, I present a possible solution to overcome the limitation of smFRET experiments to *in vitro* experiments.

Altogether, this work significantly increases the knowledge of how Hsp90 interacts with nucleotides, co-chaperones and clients and how these partners influence Hsp90 (and vice versa) in order to fulfill the function of the chaperone system.

CHAPTER 2

Methods and developments

In this chapter the methods I used within my work and further developments are introduced.

I built two TIRF setups and used them, as well as a confocal setup, for smFRET experiments on the Hsp90 system to gain novel insights into Hsp90's complex function. The setups are custom-built to achieve maximal photon sensitivity while maintaining flexibility to adapt to different experiments. Their construction, and the experimental setup for confocal smFRET studies and the experimental procedure are described on Pages 20 to 27. The implemented methods for smFRET data evaluation are introduced on Pages 28 to 37.

Experimental methods to measure the properties of proteins or dyes in bulk are presented in Section 2.6. The molecular biology and protein biochemistry to obtain the samples are introduced on Pages 40 to 44 and the prediction procedure for SAXS profiles on page 45. The molecular dynamic simulations conducted by the group of Martin Zacharias (TU München, Munich) in our collaborative work on Hsp90's dynamics are briefly described in the Appendix on page 110.

All chemicals (i.e. solvent, buffer agents and similar) used within this work are purchased from Sigma-Aldrich (St. Louis, USA) if not stated otherwise.

2.1 Optical Setups

2.1.1 Four-color prism type TIRF

Common smFRET experiments are based on the FRET between two dyes. Thus, they can provide binary information about the system studied. In contrast, many biological machines such as the Hsp90 system consist of several interaction partners, fulfilling their function within a cell by transient and/or sequential interaction. Their dynamic interplay can only be understood by information on their correlations. This can be achieved by multi-color excitation and detection. In the following, I describe the setup Markus Götz and I constructed and used for four-color smFRET experiments.

The setup is designed as a prism-type TIRF, as shown in Fig. 2.1. All components are mounted on a vibration damped optical table (RS2000, Newport Corporation, Irvine, USA). The beams of four lasers at the wavelengths 473 nm (Cobolt Blues 50 mW, Cobolt AB, Solna, Sweden), 532 nm (Compass 215M 75 mW, Coherent, Santa Monica, USA), 594 nm (Cobolt Mambo 100 mW, Cobolt, Solna, Sweden) and 637 nm (LPM635-25C 25 mW, Newport Corporation, Irvine, USA) are expanded and collimated individually by Keplerian telescopes and subsequently overlaid using dichroic mirrors. An iris selects the central part of the beam to obtain homogeneous illumination. An acousto-optical tunable filter (AOTF) (AOTFnC-Vis, AAOptics, Orsay, France) is used to control the excitation power and allows fast switching of the different excitation colors. Additional mechanical shutters (SH1, Thorlabs, Newton, USA) in each beam ensure that the excitation is blocked completely for measurements on a slower time scale (> 20 ms). The combined excitation beam is circularly polarized by a $\lambda/4$ plate (AQWP05M-600, Thorlabs) and focused on the sample by an achromatic lens via a quartz prism. This allows for an excitation in TIR illumination. The emitted fluorescence is collected by a high NA oil immersion objective with 100x magnification (CFI Apo TIRF 100x, Nikon, Tokyo, Japan) and a lens positioned as close as possible to the objective. An adjustable optical slit (Owis GmbH, Staufen i. Br., Germany) is placed in the intermediate image plane to adjust the field of view and to remove off-axis beams. The light is collimated again and spectral regions are separated into the different detection channels with dichroic mirrors. Each channel is focused with a separate lens onto the chip of the respective EMCCD camera (iXon Ultra 897, Andor Technology Ltd., Belfast, United Kingdom). The final magnification with the setup is 101 ± 1x for all four channels. Bandpass filters decrease the leakage of fluorescence from other dyes. Mechanical shutters in the blue and orange detection channels (Uniblitz VS35, Vincent Associates, Rochester, USA) can block excitation light from the corresponding excitation laser. One camera is used per two detection channels that are imaged side by side. The orientation of the camera was chosen in a way that channels do not overlap during readout. In the detection paths achromatic aspheric lenses with 50.8 mm diameter and 200 mm focal length (Qioptiq, St. Asaph, United Kingdom) are used in order to collect as much light as possible and to prevent aberrations, e.g. distortions in off-center regions of the image. Shutters, AOTF and cameras are synchronized by TTL signals from a digital I/O card (PCIe-6535, National Instruments, Austin, USA) that is controlled by PC software developed with Labview (National Instruments).

The setup is optimized for the fluorescent dyes Atto488, Atto550, Atto594 and Atto647N (AttoTec, Siegen, Germany). Their spectra and detected spectra are shown in Fig. 2.2. The theoretical detection efficiency achievable with an ideal detector at this configuration would be 50%, 27%, 42% and 36% of emitted photons collected by the objective, respectively.

(A)

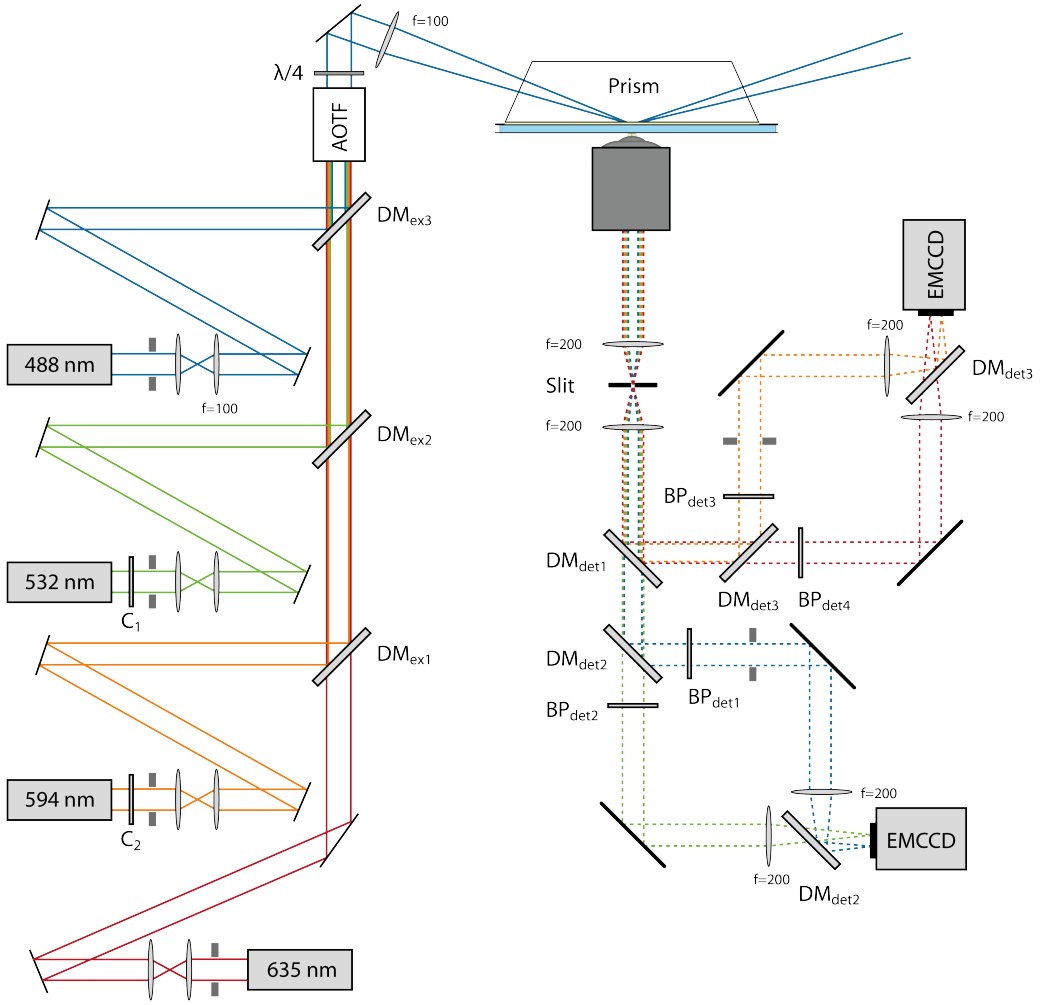

(B)

Identifier	Part
C_1	ZET532/10
C_2	ZET 594/10
DM_{ex1}	ZQ594RDC
DM_{ex2}	570DCXR
DM_{ex3}	ZT491RDC

(C)

Identifier	Part
DM_{det1}	T 600 LPXR
DM_{det2}	H 560 LPXR
DM_{det3}	HC BS R635
BP_{det1}	525/40 BrightLine HC
BP_{det2}	586/20 BrightLine HC
BP_{det3}	631/36 BrightLine HC
BP_{det4}	700/75 ET Bandpass

Figure 2.1: A four-color prism type TIRF setup for smFRET experiments. (A), scheme of the setup. The detailed description is given in the main text. (B) and (C), optical parts in the setup. C, clean-up filter; DM, dichroic mirror; BP, bandpass filter. All filters are purchased from AHF Analysentechnik (Tübingen, Germany). The focal length f of all lenses is given in millimeter.

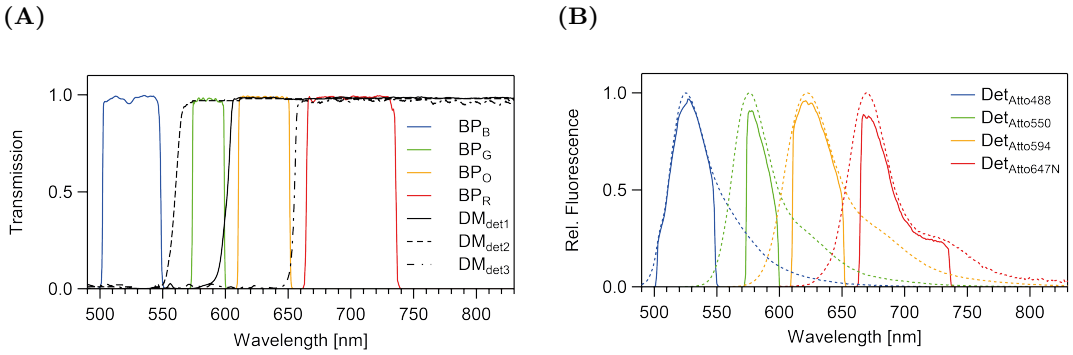

Figure 2.2: Relevant spectra for the fluorescence detection in the four-color smFRET setup. (A), spectra of the filter and dichroic mirrors in the detection pathways. (B), fluorophore spectra and their fluorescence detected in the setup.

The sample is studied in a custom-built flow-chamber described on page 25.

2.1.2 Two-color HILO

The evanescent field in TIRF setups is limited to an excitation of fluorophores in the close proximity (up to 400 nm) of the surface. Single fluorophores within a living cell spanning several μm in height are not observable. A highly inclined laminar optical sheet (HILO) can overcome this limitation of a TIRF and obtains a similar S/N ratio [103]. Based on an objective-type TIRF, the angle of the incident beam is adjusted to a high refraction angle instead of a total internal reflection at the glass/water interface.

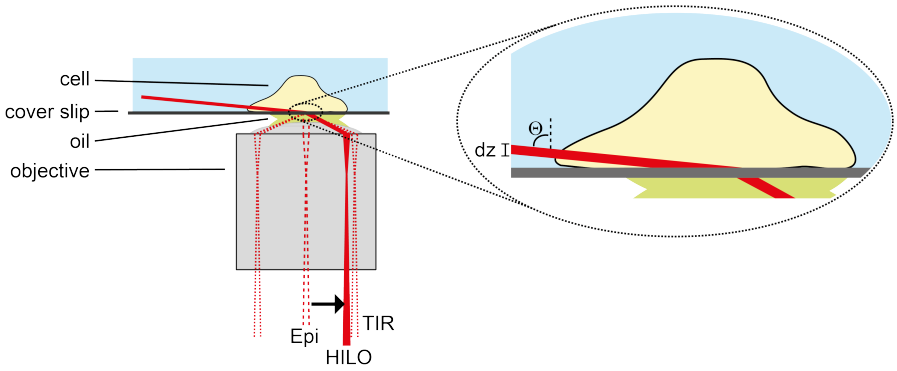

Figure 2.3: The concept of HILO illumination. The excitation beam is displaces from the optical axis (Epi illumination) towards the displacement necessary for TIRF. It is then adjusted such that the excitation beam penetrates the specimen to about dz = 5-10 μm (compared to about 200 nm in TIRF). Sketch adopted from [103].

I constructed a two-color smFRET setup with excitation in the red/near-IR range by an HILO. The setup construction is described and characterized in the following. Experiments will be presented in Chapter 5 on page 103.

The setup is designed as an objective type TIRF with three excitation wavelengths. It is shown schematically in Fig. 2.3. All components are mounted on a shock damped optical table (Newport). As excitation sources three continuous wave diode lasers at 728 nm (Obis 730LX, Coherent) for near infra-red (NIR) excitation, 637 nm (Obis 637LX, Coherent) for

(A)

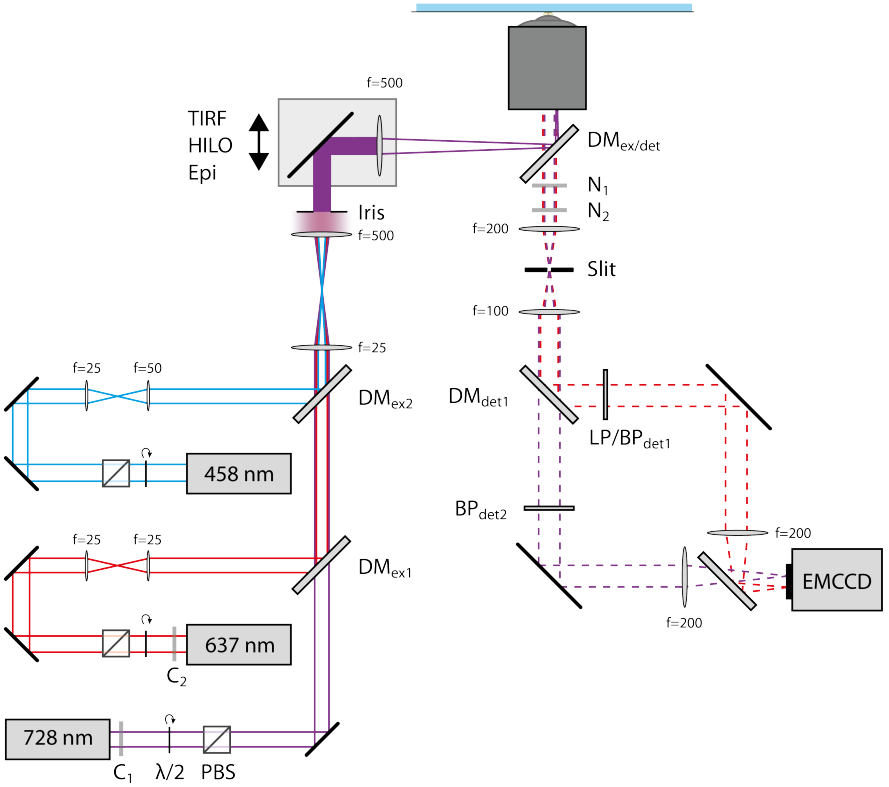

(B)

Identifier	Part
C_1	F49-634
C_2	F39-722
DM_{ex1}	F48-677SG
DM_{ex2}	F48-473SG
$DM_{ex/em}$	F73-732

(C)

Identifier	Part
DM_{det1}	F43-725
N_1	F40-635
N_2	F40-730
BP_{det1}	F47-675
BP_{det2}	F49-778
LP	FEL0500 (Thorlabs)

Figure 2.4: The two-color objective type TIRF setup for smFRET experiments in the R/NIR range. (A), scheme of the setup described in detail in the main text. PBS, polarization beam splitter; $\lambda/2$, rotatable lambda half plate; DM, dichroic mirror; C, clean-up filter; N, notch filter; LP, long-pass filter. For all lenses the focal length f is given. Apart from the telescopes that expand and collimate the red and blue lasers, only achromat lenses are used. (B) and (C), filters used in the setup. Filters are purchased from AHF Analysentechnik if not stated otherwise.

red excitation and 458 nm (Obis 458LX, Coherent) for blue excitation are used. Noise emissions from each laser are removed by clean-up filters and the beams are aligned. The beam is expanded, cut with an iris and focused onto the back focal plane of a high NA apochromat 100x magnification objective (CFI Apo TIRF 100x, Nikon). Red and blue lasers are collimated separately before with Keplerian telescopes as the three lasers diverge differently. With the last mirror together with the lens focusing on the back focal plane

mounted on a translation stage (Thorlabs) the excitation mode can be switched from epi- to HILO to TIRF illumination by moving the excitation beam from the optical axis of the objective.

The fluorescence light is separated from excitation light with a dichroic mirror and residual reflected excitation light is blocked by notch filters. A Keplerian telescope with an adjustable slit (Owis GmbH) allows to remove off-axis beams and extends the setup magnification by factor two. All lenses in the detection path are achromatic aspheric lenses with 50.8 mm diameter (Qioptiq). In the red detection channel, a rotatable filter wheel (Thorlabs) enables to switch from a band-pass filter to select red fluorescence to a long-pass filter to select green fluorescence. The two detection paths are adjusted with a slight parallel offset and side by side on one EMCCD camera (iXon Ultra 897 EX2 dual AR coated with fringe suppression, Andor Technology Ltd.), which is again inserted with an orientation preventing overlap of the channels during readout. The final setup has a magnification of 204±1x in both channels. Lasers and camera are synchronized by TTL signals from a digital I/O card (PCIe-6535, National Instruments) that is controlled by PC software developed with Labview (National Instruments).

The setup is optimized for the dyes Atto647N (AttoTec GmbH) and Cy7 (Lumiprobe GmbH, Hannover, Germany) as FRET donor and acceptor fluorophores, as shown in Fig. 2.5. The Theoretical Förster distance R_0 for FRET between the dyes is 73 Å. The spectra of the chosen set of dichroic mirrors and filters including the fluorescence spectra of Atto647N and Cy7 is shown in Fig. 2.4. A third excitation color at 458 nm is included for the excitation of the green fluorescent protein (GFP) and its derivatives.

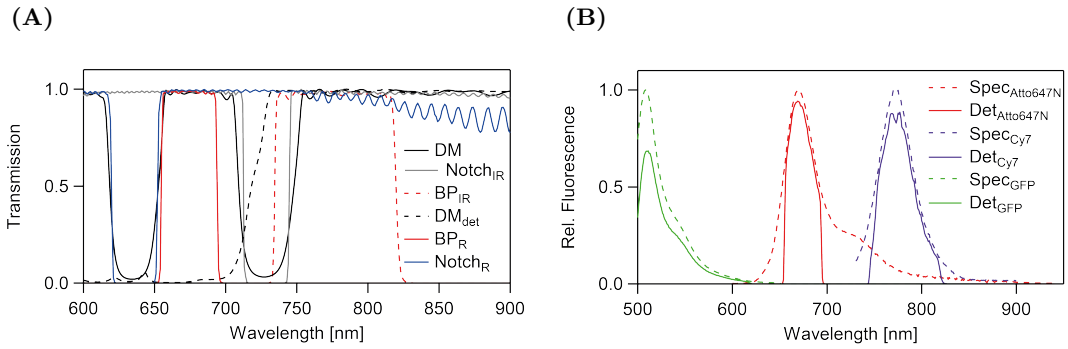

Figure 2.5: Detection in the setup for R/NIR smFRET experiments enabling the simultaneous detection of GFP fluorescence. (A), spectra of the optical parts in the detection of the setup. (B), fluorescence spectra and detected fluorescence of GFP and the dyes Atto647N and Cy7 with the setup.

As the spectral properties of the dye LD750 (Lumidyne Technologies, New York, USA) are highly similar to Cy7, it is an optional substitution for Cy7 as FRET acceptor.

A chamber with integrated temperature, humidity and CO_2 control (Okolab, Naples, Italy) can optionally be used on the microscope stage in order to grow and observe cells on the setup. Cells are grown on an enclosable μ-slide 8 well with glass bottom (Ibidi GmbH, Munich) in Opti-MEM I reduced serum medium (Thermo Fisher Scientific, Waltham, USA), which produces negligible background compared to standard media.

2.1.3 Two-color PIE-FRET

Data for structural studies on Hsp90 by smFRET are recorded on a homebuilt confocal microscope similar to others published [104–106] and described in detail in [3]. The setup is shown schematically in Fig. 2.6. Time-resolved fluorescence intensities from diffusing molecules at a concentration of approximately 100 pM are recorded with picosecond time resolution with single photon avalanche photodiodes (PDM-50 μm and τ-SPAD, PicoQuant, Berlin, Germany) for color- and polarization-sensitive detection and processed with a commercial data acquisition system (HydraHarp 400, PicoQuant). The data is stored

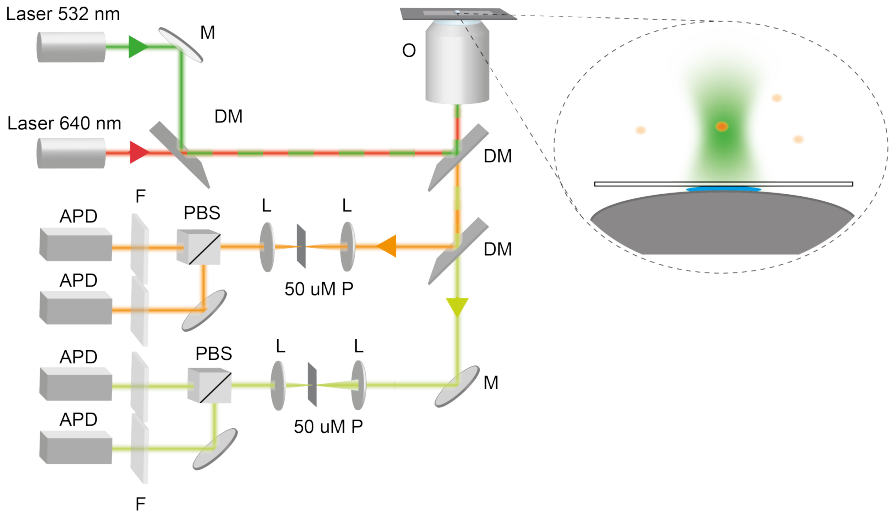

Figure 2.6: Schematic view on the confocal setup used to measure PIE-FRET. Proportions are changed for demonstration. A detailed description of the setup components is given in the text. M, mirror; DM, dichroic mirror; O, objective; L, lens; P, pinhole; PBS, polarization beam splitter, F, fluorescence filter; APD, avalanche photodiode. The zoom shows the confocal volume illuminated and the diffusing fluorescent specimen, which are only excited and able to fluoresce when within the volume.

in the ht3 format, i.e. the micro-time data with 16 ps resolution (for the determination of lifetimes and time-resolved sub-ensemble anisotropies) and macro-time data with 200 ns resolution (for the determination of FRET efficiencies and stoichiometries) using the Symphotime acquisition software (PicoQuant). Two alternating, pulsed diode lasers (532 nm LDH-P-FA-530 and 640 nm LDH-D-C-640, PicoQuant) are used as excitation sources and an Apo 60x water immersion objective (Nikon) for focusing excitation and detection. Laser scanning and moderate laser intensities (50 μW) reduce blinking and bleaching of the dyes.

2.1.4 Measurement chambers

Every reduction of background fluorescence is beneficial for the outcome from smFRET experiments. This is achieved on the one hand by the reduction of the excited and observed volume in the optical setups (as described above), on the other hand by a reduction of unspecific binding of labeled molecules or impurities to the surface of the measurement chamber, in which the sample is studied.

While in PIE-FRET experiments on a confocal setup, the adsorption of molecules to the

surface is generally impeding the signal, in TIRF setups the molecule of interest has to bind specifically at a low density to the surface, while all other specimen should not. In the following I describe the procedures to ensure both.

Surface functionalization

Glass surface are first cleaned and activated, and then functionalized. For the pTIRF, quartz slides (Suprasil2000, G. Finkenbeiner, Inc., Waltham, USA) are cleaned and functionalized, for the oTIRF and PIE experiments cover slips (170 $\pm 5\mu$m, Paul Marienfeld GmbH & Co. KG, Lauda Königshofen , Germany). The protocol used for cleaning and activation of the glass surface is described in the following:

1. Sonificatation of slides/cover slips in 2 % Hellmanex (Hellma Analytics, Müllheim, Germany) solution, 3 x
2. Incubation of slides/cover slips for 2 h in Piranha solution (3:1 vol% H_2SO_4 : H_2O_2) at 60 °C
3. Repetition of step (1)
4. Incubation of slides/cover slips for 2 h in RCA (5:1:1 H_2O : H_2O_2 : NH_4OH) at 60 °C.
5. Rinsing the slides/cover slips 5 x with ultra-pure water

Subsequently, the cleaned and activates glass surface is functionalized (which is done directly after the cleaning). For the confocal setup, the surface is passivated by using polyethyleneglycole (PEG), while for the TIRF setups, the surface is functionalized with a mixture of PEG and biotinylated PEG. The sparsely and homogenous distribution of biotin molecules present afterwards allows the targeting of a molecule of interest by Biotin-Streptavidin interaction, as described in Section 2.1.4. The protocol for functionalization is described in the following:

1. Drying of the slides/cover slips with a stream of N_2 and incubation in acetone for 15 minutes
2. Incubation of slides/cover slips in a 1:200 dilution of Vectabond (Vector Laboratories, Burlingame, USA) in acetone for 5 min.
3. Rinsing of the slides/cover slips 5 x with ultrapure water
4. PEG[4] is dissolved in 600 μl 100 mM $NaHCO_3$
5. A droplet of 50 μl PEG solution is put on each slide, a clean cover slip is placed on top, and reaction is incubated overnight at 8 °C in humid atmosphere
6. Slides/Cover slips are rinsed 5 x with ultrapure water and subsequently dried in a stream of N_2, then stored in a dry and light-protected place

4 80 mg α-methoxy-ω-NHS-ester of size 5 kDa (mPEG) and in case of slide/cover slip preparation for TIRF experiments 3 mg Biotin-CONH-PEG-O-C3H6-CONHS (3 kDa), both from Rapp Polymere GmbH, Tübingen, Germany.

Chambers for pTIRF and oTIRF

The functionalized slides/cover slips are used to build measurement chambers for the single molecule experiments.

For the oTIRF, a custom block made of Teflon with drilled holes is cleaned an fused to the functionalized surface by a sandwich with Nescofilm with laser cut holes is heated to 60 °C for five minutes. The holes can subsequently used for separate experiments (see Fig. 2.7, right). The same procedure applies for the PIE-FRET chambers.

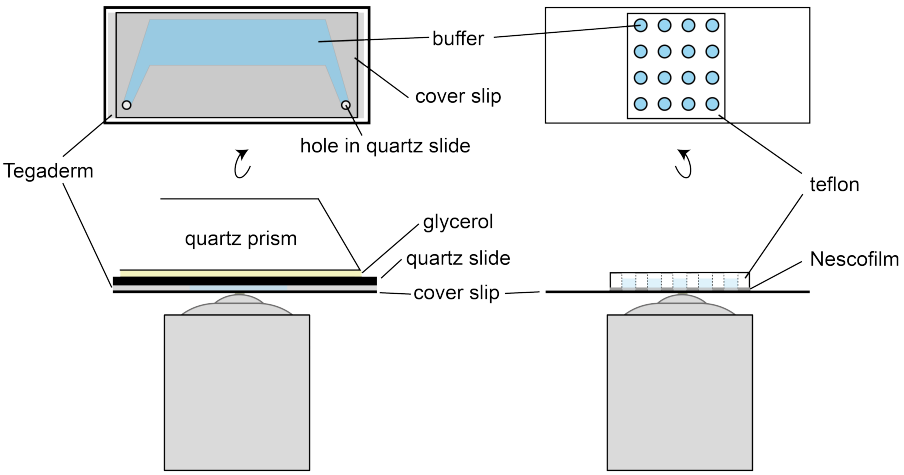

Figure 2.7: The chambers used in measurements on the pTIRF (left) and oTIRF (right).

For the pTIRF, a flow chamber is built. This flow chamber consists of a sandwich between a clean cover slip, Tegaderm film (3M, St. Paul, USA) that is cleaved in the middle as shown in Fig. 2.7 (top left) and sprayed with an adhesive (Photomount, 3M) and the functionalized quartz slide with two holes drilled inside. This sandwich is heated to 70 °C for five minutes. Subsequently, it is fixed to the quartz prism frame made from aluminum by screws. Between prism and quartz slide Glycerol is placed. Because it has approximately the same refraction index as quartz, it prevents refraction at the interfaces. Two teflon tubings (Bola GmbH, Grünsfeld, Germany) are connected to the holes in the quartz slide and on one side a syringe pump (PHD22/2000, Harvard Apparatus, Holliston, USA) such that can then be used to flush solutions into the measurement chamber.

2.2 Experimental procedure for smFRET experiments on immobilized Hsp90

In the following, the general procedure before starting the experiments on the pTIRF is described. Procedure on the oTIRF is similar, except solutions are pipetted instead of using a syringe pump.

1. A 0.25 mg/ml solution of Neutravidin (Thermo Fisher Scientific) is flushed into the chamber and incubated five minutes.
2. Unbound Neutravidin is flushed out with buffer and, in case of multi-color experiments, the remaining surface functionalization defects are blocked by flushing a 0.5 mg/mL bovine serum albumine (BSA) solution.
3. The biotinylated, labeled, and (in case of Hsp90) exchanged sample is flushed into the chamber at rising concentrations until a sufficient surface density is reached, which is

usually the case at a concentration of 1–10 pM.

4. Unbound sample is flushed out with buffer.
5. Interacting molecules, whose inpact is studied (e.g. proteins, nucleotides) are flushed into the chamber; this is repeated a second time 5 min later.

All experiments are conducted in 40 mM Hepes, 150 mM KCl, 10 mM $MgCl_2$, pH 7.5 at room temperature, if not stated otherwise.

The resulting setup is sketched in Fig. 2.8.

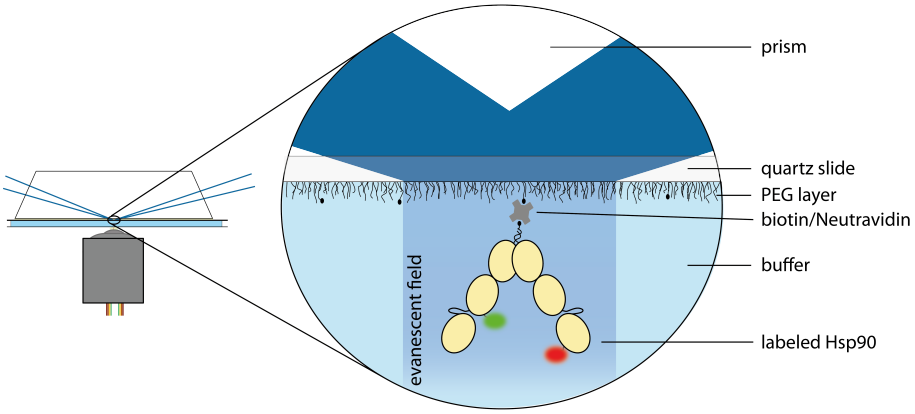

Figure 2.8: Sketch of the measurement chamber on the pTIRF in action. Labeled Hsp90 in bound by Biotin/Neutravidin interaction specifically to the otherwise passivated (by mPEG) quartz slide surface. Labels are excited by an evanescent field from the top, fluorescence is detected by the objective through the cover slip on the other side of the chamber. This figure has already appeared in [2].

2.3 Data evaluation of smFRET data

In this section, I describe the general procedure to process the raw movie data recorded in two- and multi-color smFRET experiments on TIRF setups (as in [2]) and further evaluation methods I applied onto the data within this work. Data recording and evaluation procedures of smFRET experiments conducted on a PIE-FRET setup differ and have been described in [107]. Nevertheless, the general procedure for the selection of the FRET popuation from alternating laser excitation applies also for PIE experiments, even though the frequency of the laser pulses is much faster (20 MHz). On the TIRFs, all smFRET experiments with alternating laser excitation (ALEX) are conducted at 5 Hz (with 70 ms excitation and 30 ms read-out time per excitation), if not stated otherwise.

2.3.1 Data processing

The raw data from the EMCCDs (i.e., frames of 512x512 pixels of the fluorescence intensities in 16-bit gray scale) are stored as TIFF stacks. Analysis is done with scripts written in Igor Pro (Wavemetrics, Lake Oswego, USA). The movies are automatically split into the respective detection channels when loaded according to predefined settings.

Image registration

Image registration is achieved by recording calibration images with fluorescent beads (Fluospheres amine-modified, 0.2 μm, yellow-green fluorescent, Thermo Fischer Scientific) that show fluorescence emission in the spectral range of all detection channels of the

respective setup upon excitation with the laser of the lowest wavelength. After each measurement, a 1:1000 dilution of the beads in ddH_2O is flushed into the chamber and a movie is recorded while driving stepwise through the chamber.

Bead positions are detected in the calibration movie by searching for the brightest spots. The central position is determined from a Gaussian fit to the intensity profile of each spot. Bead positions in the different channels are linked to their closest proximity. A distance cut-off is applied to exclude incorrectly assigned beads. The coordinates of beads that are found in all detection channels are saved, and the mapping offset in x- and y-direction is each fitted with a 2D polynomial of degree three.

Data selection

Individual molecules are identified in each movie by searching for the brightest spots in the sum of five consecutive frames of a certain channel. The central position of the spot is calculated for all channels using the image registration. For each channel the intensity traces are obtained by a software binning of the pixels around the central coordinates in each frame. The bin size depends on the used setup: For the four-color setup, a 3x3 binning is determined empirically to give the best S/N ratio, while a 5x5 binning is found to give the best S/N ratio in the two-color HILO.

The intensity traces are corrected for an offset originating from the dark current of the EMCCD and background fluorescence. This is done by automatically subtracting a background time trace that is the mean intensity of the 200 darkest pixels in each channel. For each molecule, a joint raw intensity trace is calculated as the sum of all traces with the same excitation color. Traces are selected according to the following criteria: The joint raw intensity trace should have a roughly flat plateau, a single bleaching step, and the appropriate channel intensities have to show anti-correlated behavior. About 200 to 400 spots in each detection channel of a movie are tested for single molecule behavior.

Data correction

The measured fluorescence intensities depend not only on the energy transfer but also on fluorophore and setup properties. To obtain the true energy transfer efficiency between two fluorophores, the measured intensities are corrected for systematic deviations to yield the corrected intensities ${}^{corr}I_{em}^{ex}$.

In two-color smFRET experiments, the donor and acceptor intensities have in general to be corrected for the following three different aspects:

1. Leakage, l: A fraction of the photons emitted by the donor dye are detected in the channel for acceptor fluorescence.
2. The gamma factor, γ: The fluorescent dyes have different quantum yields and the detection of photons from different dyes depends on the detection efficiency of the setup in each detection channel.
3. Direct excitation, d: Upon donor excitation a small fraction of photons excite the acceptor dye directly. This is commonly referred to as direct excitation.

With carefully determined correction factors one yields the corrected intensities:

$$ {}^{corr}I_b^a = I_b^a - lI_b^b - dI_b^b \tag{2.1} $$

$$ {}^{corr}I_a^a = \gamma I_a^a \tag{2.2} $$

The correction factors are determined from 2D plots, calculated from the data obtained by ALEX of the sample [104, 108, 109]. Both FRET donor and acceptor are excited alternatingly, and the fluorescence intensities I_a^a, I_b^a and I_b^b are recorded. As the result of ALEX experiments additionally depends on the ratio of excitation efficiency in all excitation channels (which in turn depends on absorbance cross section and excitation power), a fourth correction factor β is introduced that corrects for excitation efficiency. From the experimentally determined intensities, the stoichiometry S and FRET efficiency E are calculated by:

$$E = I_b^a/(I_b^a + \gamma I_a^a) \tag{2.3}$$

$$S = (I_b^a + I_a^a)/(I_b^a + I_a^a + I_b^b) \tag{2.4}$$

S is then plotted against E, as shown in Fig. 2.9. By this plot, specimen within the sample

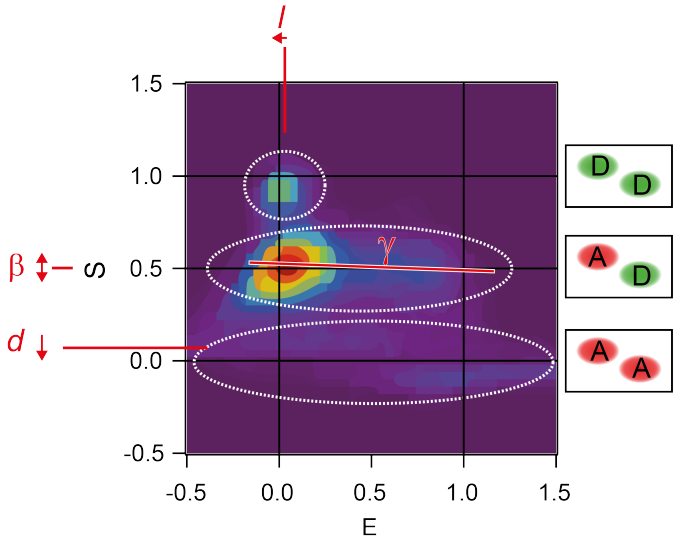

Figure 2.9: Stoichiometry (S) vs FRET efficiency (E) plot for an two-color ALEX experiment. The plot allows discrimination of donor-only, acceptor-only and FRET-populations and therefore the correction for leakage (l), direct excitation (d), γ-factor, as detailed in the text and in [104, 108, 109]. The β-factor corrects for the intensity ratio of the overall emission intensity after donor and acceptor excitation.

containing only donor or only acceptor fluorophore are separated from those carrying one donor and one acceptor fluorophore. The correction factors (as defined in [104]) are iteratively refined, until the donor-only peak is located at a FRET efficiency of 0, the acceptor-only peak is located at S of 0, and all FRET populations are located at S of 0.5. A deviation of the corrected data from the latter condition hints towards different γ-factors for the FRET pair in different FRET populations, but was not observed in the studied systems with the used rhodamine and carborhodamine derivatives as labels.

Because fitting the parameters in each experiment was found to be less accurate due to the impact of varying background fluorescence, the correction factors for l and d are determined in a clean sample without any additive and kept constant in all compared experiments.

Two-color smFRET experiments on the multi-color TIRF setup with both labels on Hsp90 are generally corrected with $d = 0.055$, $l = 0.062$ and $\gamma = 1 \pm 0.1$. Experiments with one label on Cdc37 and one on Hsp90 are generally corrected with $d = 0.055$, $l = 0.062$ and $\gamma = 1.15 \pm 0.05$. The β-factor is adjusted to the single experiments, since the excitation intensities vary significantly among the experiments. Generally, excitation intensities are adjusted to obtain $\beta \approx 1$. A 2D illumination intensity profile is used to correct for the variation of excitation intensities within the field of view (FOV). The FRET histograms are cut between $0.3 < S < 0.7$ to select only fluorescence data from molecules harboring one donor and one acceptor dye.

The correction procedure described above is not generally suited for multi-color smFRET experiments, because the full ALEX information might not be accessible anymore. This is the case, when the last acceptor is present at concentrations higher than 10 nM. Then its direct excitation would lead to saturation of the EMCCD chip. Nevertheless, correcting the raw intensities facilitates the discrimination of different populations and the comparison of multi-color smFRET with two-color smFRET experiments. Thus, a more rudimentary correction procedure is applied on the multi-color smFRET data. A short description of this procedure is given in the following.

Correction factors for apparent leakage (lk) and apparent gamma (ag) are calculated from single-molecule traces that show an acceptor bleaching event. The correction factors are determined independently with a high-FRET double stranded deoxyribonucleic acid (DNA) sample for each dye in combination with the acceptor having the longest excitation wavelength (in this case Atto488–Atto647N, Atto550–Atto647N, Atto594–Atto647N). Properties of the used Atto dyes do not change significantly between DNA and protein conjugates. The calibration sample is measured in TNM buffer (5 mM Tris pH 7.5, 5 mM NaCl, 20 mM $MgCl_2$) and 2 mM trolox. The sequence of the respective DNA strands is shown in Table 2.1.

Table 2.1: Sequences of the DNA strands used for the determination of the correction factors for multi-color smFRET. **X** = dT-C6-Dye, with dye = Atto488/Atto550/Atto594 as donor fluorphore. **Y** = dT-C2-Atto647N NHS as acceptor fluorophore.

DNA strand	Sequence
Donor	5'-GAG CTG AAA GTG TCG AGT TTG TXT GAG TGT TTG TCT GG-3'
Acceptor	Biotin-5'-CCA GAC AAA CAC TCA AAC AAA CTC GAC ACT YTC AGC TC-3'

ALEX is used to exclude photophysical artifacts such as acceptor blinking. The obtained intensity traces are corrected manually for offset. The leakage of the donor dye into every possible acceptor channel is calculated from all data points in the recorded FRET traces where the acceptor dye bleached but the donor is still fluorescent (marked by a dagger):

$$lk_b^a = {}^{\dagger}I_b^a / {}^{\dagger}I_a^a \tag{2.5}$$

The median of the leakage histogram is used as the apparent leakage factor. After correction for leakage, the apparent gamma factor is determined from the same set of traces. It is calculated by dividing the change of fluorescence in the acceptor channel by the change of

fluorescence in the donor channel upon bleaching of the acceptor dye:

$$ag_a = \frac{\Delta I_c^a}{\Delta I_a^a} \tag{2.6}$$

$$= \frac{I_c^a - {}^{\dagger}I_c^a}{{}^{\dagger}I_a^a - I_a^a} \tag{2.7}$$

with c being the detection channel for Atto647N. The median of the apparent gamma factor distribution is used as an apparent correction factor. The apparent gamma factor for any FRET pair combination is then approximated by the ratio between the two apparent gamma factors of the dyes measured in combination with Atto647N. The determined apparent correction factors lk and ag include a small contribution from the direct excitation and are therefore dependent on the FRET efficiency. As a result, the corrected FRET efficiency is less accurate than the S vs E correction for two-color experiments. However, the deviation has negligible influence on the subsequent analysis, because the multi-color smFRET experiments do not aim to provide exact distance information. The corrected fluorescence intensity in each channel is then calculated by:

$${}^{corr}I_b^a = (I_b^a - \sum_{i=a}^{b-1} lk_i^a \cdot I_i^a) \cdot ag_b \tag{2.8}$$

As a measure of transfer efficiency within the multi-color FRET system, the partial fluorescence (PF) is defined for each color by:

$$PF_b^a = \frac{{}^{corr}I_b^a}{\sum_{i=a}^{c} {}^{corr}I_i^a} \tag{2.9}$$

Multi-color smFRET experiments are corrected with the correction factors summed up in Table 2.2.

Table 2.2: Experimentally determined correction factors used for the correction of raw data from multi-color smFRET experiments.

Name	Ex	Det	Correction factor
γ	b	r	0.6767
γ	g	r	1.155
γ	o	r	2.182
lk	b	g	0.123
lk	b	o	0.034
lk	b	r	0.009998
lk	g	o	0.2597
lk	g	r	0.0814
lk	o	r	0.4646

2.3.2 State separation in multi-color smFRET data

The three-color smFRET experiments with ALEX result in three partial fluorescence traces, namely PF^{blue}_{green}, PF^{blue}_{red} and PF^{green}_{red}, making up 3D information on each time point of the measured traces. An exemplary 3D scatter plot of a set of data points is shown in Fig. 2.10. States are discriminated by using the different 2D projections. Each population is selected beforehand by drawing a free-hand polygon. The relative populations are kept constant and the 3D scattered data is fitted with five 3D Gaussian with each Gaussian's width and position free (by the Lebvenberg-Marquart algorithm). Each Gaussian is defined by:

$$p(x,y,z) = \frac{1}{\sqrt{2^3 \Pi^3}\sigma_x\sigma_y\sigma_z} \exp(-\frac{(x-\mu_x)^2}{2\sigma_x}\frac{(y-\mu_y)^2}{2\sigma_y}\frac{(z-\mu_z)^2}{2\sigma_z}) \tag{2.10}$$

with x,y,z being the respective partial fluorescence, σ the standard deviation and μ the position in each dimension.

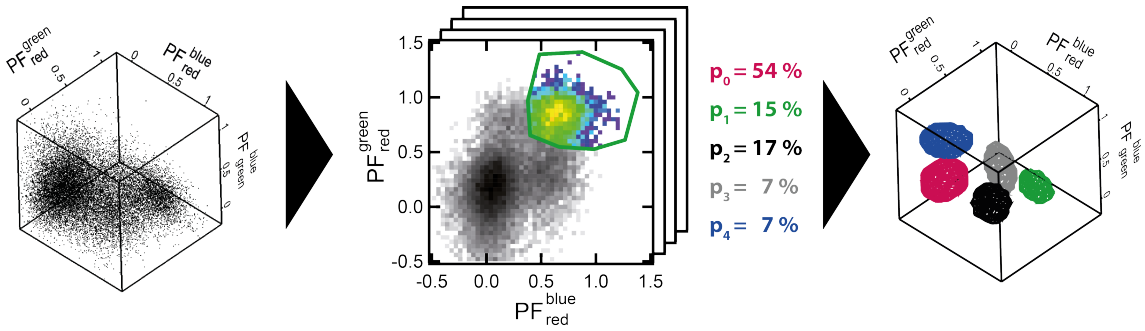

Figure 2.10: State separation in three-color smFRET experiments. Left, the three PFs span a 3D scatter plot. Center, free-hand polygons are used to select each state's relative population beforehand. Right, five independent 3D Gaussian, with free widths and positions but constant populations are fitted to the data. This figure has already appeared in [2].

This procedure is repeated three times to account for erroneous selection. The best fit is selected by the lowest χ^2.

2.3.3 Kinetic analysis with Hidden Markov Models

State allocation and rate extraction from FRET trajectories is achieved by the application of hidden Markov model (HMM). HMM have been successfully applied on smFRET data [110], and can overcome common issues impeding smFRET data evaluation, which are the low S/N ratio, the broad FRET efficiency distributions [111, 112] and possible kinetic heterogeneity [113].

A Markov process is a memoryless stochastic process of a system with different states or values, where the next value of the Markov process depends on the current value, yet being conditionally independent of the previous values of the stochastic process. An HMM models this system assuming the succession of states is not directly observable (i.e., hidden). Each state has a probability distribution over the observable signal range (e.g., the fluorescence intensity, FRET efficiency or partial fluorescence).

A time-discrete HMM is described by a vector of start probabilities with elements Π_i per state i, the transition matrix A containing the transition probabilities a_{ij} between all hidden states, and state-specific emission probabilities b_i that link the hidden states to the

observables, as exemplary shown in Fig. 2.11.

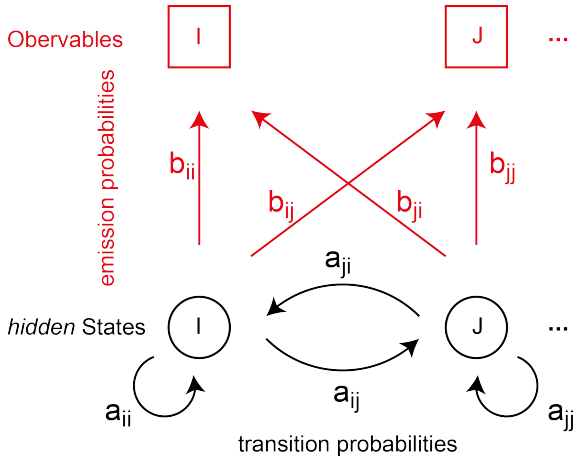

Figure 2.11: A simple example for an HMM. A system passes memoryless through its states that cannot be observed directly. The state sequence depends only on the transition probabilities between the states. Each state has a certain probability for the emission of the different observations, which results in a sequence of observation (e.g. $IJJIIIJ$...).

Two-color smFRET data is evaluated using the program SMACKS [113].[5] SMACKS applies the HMM on the 2D information from the fluorescence intensity traces of donor and acceptor after donor excitation without discretization, describing each b_i by continuous Gaussian probability density functions. It works in a semi-ensemble approach, optimizing each b_i separately on each trace before the model is optimized on the ensemble of all data. The model $\lambda(p,A,B)$ is then iteratively rated by the forward-backward algorithm and optimized by the Baum-Welch algorithm until the maximum likelihood estimator (MLE) is derived. The Viterbi algorithm is used to compute the most probable sequence of hidden states [114, 115]. Models are rated by the bayesian information criterion (BIC) [116].

The idea of SMACKS is extended to the data from multi-color smFRET experiments. This work has been done by Markus Götz [2]. Because fluorescence intensities in three-color smFRET exhibit significantly worse S/N than the data from two-color experiments, calculated PF traces are used for model optimization. Furthermore, data points with $PF > 2$ or $PF < -1$ are assigned the minimal emission probabilities for all states to prevent artificial transitions. Traces with more than 10 % of the respective data points are excluded from further analysis.

One ensemble HMM is optimized over the full data set with the b_i's fixed to the parameters from the Gaussian 3D fit described, and the same for all traces. The resulting transition matrix and Viterbi path are subsequently analyzed. As a quality control, the Viterbi path is displayed with the PF traces and checked by eye for plausibility regarding state allocation and transitions for all molecules of the data set. The HMM optimization is run on each data set with the three different b_i's from the different Gaussian fits. Results differ only slightly in their production probability and produced an overall similar transition

5 https://www.singlemolecule.uni-freiburg.de/smacks [March 2017].

matrix.

The uncertainty of extracted transition probabilities is calculated as the 95% confidence interval (CI) for each transition [117, 118]. The likelihood profile of the parameter space around the MLE is calculated for each transition probability. Each parameter is separately varied with all other parameters being fixed to the MLE, yielding the test model λ'. A likelihood ratio (LR) test of the likelihood $L(\lambda|O)$ given the data set O is performed according to

$$LR = 2 \cdot (lnL(\lambda MLE|O) - lnL(\lambda'|O)) \tag{2.11}$$

The confidence bound for the parameter is reached when LR exceeds 3.841, the 95% quantile of a χ^2-distribution with one degree of freedom. The CI can be compared to the deviation of the three independent fits done for each data set. The deviation of the fits is typically smaller than the CI, thus the CI is used a error estimate on the transition probabilities.

2.3.4 Average dwell time and time to absorption

The dissociation behavior of labeled nucleotide bound to Hsp90 is estimated by two complementary approaches.

First, we simply integrate over all HMM-assigned dwells n, where nucleotide is bound, τ^b. This gives the average dwell time, <dwell time>. We thereby ignore possible conformational changes in between where the nucleotide is not affected. Thus, the system is treated as a simple two-state system with the states bound and unbound. The average dwell time of boud nucleotide is then calculated by:

$$< dwell\,time >= \frac{1}{n} \sum_{i=0}^{n} \tau_i^b \tag{2.12}$$

Incomplete dwells (i.e. dwells without a beginning or an ending) are included. This makes the procedure much more robust, because the studied system is dominated by dwells being incomplete on the timescale of our measurements. However, due to this procedure the quantity represents the upper bound for the dwell time of labeled nucleotide on Hsp90.

Correspondingly, the dissociation behavior is calculated from the transition probabilities as calculated by the HMM. Therefore the whole system is treated as an absorbing Markov chain. All states with nucleotide bound are treated as transient states, and all others as absorbing (i.e. the probability to leave this state is set to 0).

For all absorbing states in the chain the i,j-th entry of the fundamental matrix N gives the expected number of times the chain is in transient state j starting from state i:

$$N = (I - Q)^{-1} \tag{2.13}$$

with I being the identity matrix and Q being the transition density matrix for all transient states [119, Chapter 11].

Weighting by the starting probabilities in the i-th state, the time to absorption (tta), which gives the expected time until the labeled nucleotide dissociates, is calculated:

$$tta = B\,N \tag{2.14}$$

with B being the relative starting probabilities in the state i.

Generally, for large data sets we find the <dwell time> and the tta correlated. Due to the non-symmetric confidence intervals for each transition contributing to the tta, statistical tests for significant differences between data sets are conducted on the average dwell time. Hence this value is shown in most figures. However, in case of significant discrepancy between the two values, differences between data sets are not interpreted as significant.

The dwell time distributions follow one or multiple exponential functions. The mean of random samples from a dwell time distribution is approximately normal distributed for a large number of samples due to the central limit theorem. Therefore, we can estimate the error of the average dwell time by the jackknife-1 method, as described in the following Section 2.4. However, the calculated error does not take into account possible errors from the state allocation and model imperfection. Thus, the error estimate's accuracy increases with goodness of the 3D fit, the HMM and the number of data points. Hence, we test dwell time distributions by the Wilcoxon-Mann-Whitney two sample rank test on the distributions themselves and not on the average dwell time to ensure their difference is significant.

2.4 Statistical methods

Data sets are compared by testing the statistical significance to reject the H_0 hypothesis that two data sets are derived from the same distribution. Non-normal distributed data is tested pair-wise with the Wilcoxon-Mann-Whitney two sample rank test. Normal distributed data is tested pair-wise by the student t-test. In all cases unpaired data is assumed.

2.4.1 Tests on normality

Data sets are tested size-dependent on their normality. Small data sets with $n < 50$ data points are checked with the Shapiro-Wilk test, which analyzes the variance of the data comparing the statistics of W to a normal distribution [120]. Large data sets or data, which can be resampled automatically via bootstrapping (see below), are checked by the Kolmogorow-Smirnow test comparing the cumulative distribution function with the one of a normal distribution [121]. In all cases, the confidence limit used in the test statistics for accepting H_0 (data follows normal distribution) is set to $\alpha = 95\%$.

2.4.2 Precision estimation

The distribution of an observed quantity that follows the normal distribution is approximated by resampling data with random subsets. In case of Jackknife-1, where systematically one observation (i.e. one of n FRET traces) is excluded from analysis, the estimates of the bias $\widehat{B}$ and the variance $\widehat{s^2}$ of a normal distributed variable x are given by [122, 123]:

$$\overline{x} = \frac{1}{n}\sum_{i}^{n} x_i \tag{2.15}$$

$$\widehat{B} = (n-1)(\frac{1}{n}\sum_{i}^{n} x_i - \overline{x}) \tag{2.16}$$

$$\widehat{s^2}_{jack-1} = \frac{n-1}{n}\sum_{i}^{n}(x_i - \overline{x})^2 \tag{2.17}$$

where x_i is the estimator in the i-th jackknife sample and $\overline{x}$ is the mean calculated from the complete data set.

In two-color FRET experiments with two FRET populations, subsets of (n-1) size are generated n times and fitted by a linear combination of two Gaussian distributions to estimate the population size variance.

In three-color smFRET experiments the standard deviation of the average dwell time is also estimated by jackknife-1. This is possible, because we sample a large number of dwells, which follow single or multiple exponential distributions. This is turn allows to apply the central limit theorem, thus the error of the average dwell time can be estimated by this method.

Nonparametric bootstrapping, which is resampling the data by drawing b random samples of size n with replacement, also results in an estimate of the sample variance by [124]:

$$\widehat{s^2}_{boot} = \frac{1}{b}\sum_{i}^{b}(x_i - \frac{1}{b}\sum_{i}^{b}x_i)^2 \tag{2.18}$$

The bias is estimated by the difference between the data mean $\overline{x}$ and the mean over all bootstrapped samples. Bootstrap samples were generated with n > 1000, but the resulting distribution generally overestimates the variance due to computational variance and is only used as control to the variance estimated by the jackknife.

2.5 Determination of dye and FRET pair properties

For a quantitative evaluation of smFRET experiments, the accessible volume (AV) of each dye and the Förster distance R_0 for each studied FRET pair has to be known.

2.5.1 Correct Förster distances

In order to determine the correct Förster distance for distance determination from sm-FRET experiments, each point mutation labeled with either donor or acceptor, the donor fluorescence $F_D(\lambda)$ and acceptor extinction spectra $\varepsilon_A(\lambda)$ are measured. For the latter, the extinction coefficient at the maximum of the spectrum is assumed not to change and used for renormalization of the experimentally determined absorbance spectrum.

The donor quantum yield is determined from the lifetime of the donor only population observed in the stoichiometry vs FRET efficiency histogram by:

$$Q_D = Q_{Dye} \cdot \frac{\tau_D}{\tau_{Dye}} \tag{2.19}$$

with the lifetime τ_{Dye} of free dye in water determined independently and the quantum yield of it in water Q_{Dye} given by the manufacturer. The refractive index is estimated $\eta = 1.339$[6] and the dye dipoles are assumed to average over all orientation on the timescale of FRET transfer, thus for the dipole orientation factor κ is assumed to be $\kappa^2 = 2/3$. Then,

6 http://www.chemicalbook.com/chemicalproductproperty_en_cb5408557.htm [March 2017].

R_0 is calculated by [89]:

$$R_0[\text{Å}] = 0.2108 \cdot \left(\frac{\kappa^2 Q_D}{n^4} \cdot \int_0^\infty F_D(\lambda)\varepsilon_a(\lambda)\lambda^4 \mathrm{d}\lambda \right)^{1/6} \tag{2.20}$$

2.5.2 Test on isotropic dipole orientation during FRET transfer

The assumption of $\kappa^2 = 2/3$ is only valid in case of sufficient dynamic averaging of the dipole orientations of FRET donor and acceptor dye. The time-resolved anisotropy decay $r(t)$ of fluorescent dyes recorded within confocal FRET-PIE measurements provides information on the timescales of different dye motions with the relaxation of the dynamic dye anisotropy due to rotation (r_1, τ_1) and diffusion (r_2, τ_2) and the residual static anisotropy r_∞:

$$r(t) = r_1^{-\frac{t}{\tau_1}} + r_2^{-\frac{t}{\tau_2}} + r_\infty \tag{2.21}$$

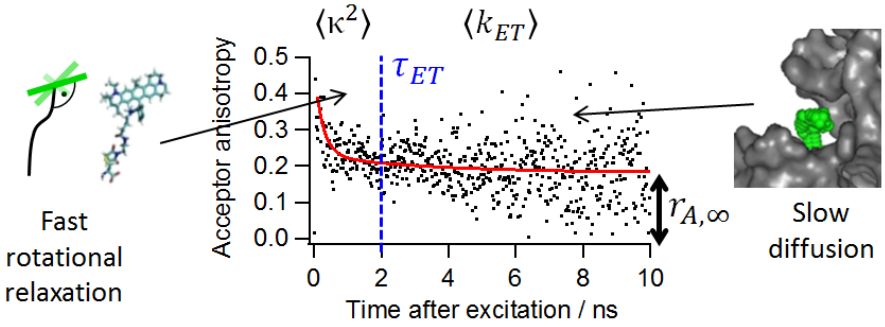

Figure 2.12: The time-resolved anisotropy of a fluorescent dye bound to a large protein is usually the sum of a fast decay due to rotational relaxation of the dipole axis and a slow decay from dye diffusion along the protein surface. The combined residual anisotropies r_∞ of both dyes of each FRET pair are used for the selection criterion, as shown in Eq. (2.22). Figure taken from [3].

A representative anisotropy decay is shown in Fig. 2.12. To guarantee sufficient dynamic averaging within the timescale of FRET, relatively small dyes with dipoles orientated perpendicular to their linker that exhibit fast rotational relaxation times and long fluorescence lifetimes are used (in this work Atto550 and Atto647N). Thus, the anisotropy affecting the average dipole orientation within the energy transfer is the residual anisotropy r_∞. Because the isotropy of a dye can compensate the anisotropy of its FRET partner to a large extend, the geometric mean of the time-resolved anisotropies of FRET donor and acceptor, i.e. the combined anisotropy r_c is determined:

$$r_c = \sqrt{r_{D,\infty}} \cdot \sqrt{r_{A,\infty}} \tag{2.22}$$

2.5.3 Accessible volume estimation

The estimated AV of each dye is calculated using the fluorescence positioning system (FPS) tool from the Seidel lab [125] and available structures from the protein data base (PDB)[7]

7 http://www.rcsb.org/ [March 2017].

[126]. Dye attachment site was set to the C_β-atom of the respective point mutated amino acid. Linker properties were set to a length of 12 Å, a width of 4.5 Å and a dye radius of 3.5 Å. In case this setting could not result in an appropriate AV, it was approximated by 12/6/6 Å.

2.6 Ensemble experiments

All ensemble experiments are conducted in the standard buffer, which is 40 mM Hepes, 150 mM KCl, 10 mM $MgCl_2$, pH 7.5, is not stated otherwise.

2.6.1 Spectroscopy

Absorbance spectra and timetraces are recorded on a Lambda25 UV/VIS spectrometer (PerkinElmer, Waltham, USA) with a temperature control unit (±0.1 °C) in a 60 μl quartz cuvette (Hellma Analytics, Müllheim, Germany). Protein concentration and degree of labeling are determined by measuring the absorbance spectra on a Nanodrop (Thermo Fischer Scientific) Spectrometer.

Fluorescence spectra and timetraces are recorded on a Fluoromax-4 (Horiba, Kyoto, Japan) with a temperature control unit (±0.1 °C)(Quantum Northwest, USA) in a 80 μl quartz cuvette (Hellma Analytics). In fluorescence anisotropy experiments the anisotropy r is determined by:

$$r = \frac{I_{vv} - G \cdot I_{vh}}{I_{vv} + 2 \cdot G \cdot I_{vh}} \tag{2.23}$$

with I_{ed} being the intensity measured with the polarizers in the excitation and the detection channel (e/d) in horizontal/vertical (h/v) orientation and the G-factor for correction of the detection efficiencies in the different channels. The G-factor is determined ahead of titration experiments or the free sample and kept constant during titration. It is calculated by:

$$G = \frac{I_{hv}}{I_{hh}} \tag{2.24}$$

The following settings are used for the fluorescence experiments with the different dyes:

Table 2.3: Spectrometer setting in ensemble fluorescence measurements.

Label	Slit width (ex/em) [nm]	λ_{ex} [nm]	λ_{em} [nm]
Atto647N	2/2	630	660
Atto550	2/2	530	560
Atto532	2/2	520	550

2.6.2 K_d calculation from titration experiments

The dissociation constant K_d is derived from titration experiments of a ligand L present in the experiment at a concentration L_0 with a protein of concentration P by fitting the following function:

$$\frac{L_P(P)}{L_0} = A \cdot \frac{\frac{P+L_0+K_D}{2} - \sqrt{(P+L_0+K_D)^2 - 4PL_0}}{2L_0} + z \tag{2.25}$$

with $L_P(P)$ being the protein bound ligand (dependent on the protein concentration), A being the amplitude and z being offset as adjustment parameters to the experimental data. It is assumed that the measured signal gives the ratio of protein-ligand complex to the overall ligand concentration.

This function is derived from the definition of the dissociation constant K_d and the law of conservation of mass, shown in the following.

$$K_D = \frac{P \cdot L}{L_P} = \frac{(L_0 - L_P)(P_0 - L_P)}{L_P} \tag{2.26}$$

$$L_P K_D = (L_0 - L_P)(P_0 - L_P) = L_0 P_0 - L_P L_0 - L_P P_0 + L_P^2 \tag{2.27}$$

$$L_P = \frac{(L_0 + P_0 + K_D) - \sqrt{(L_0 + P_0 + K_D)^2 - 4L_0 P_0}}{2} \tag{2.28}$$

2.6.3 ATPase assay

The biological activity of Hsp90 mutants and constructs is checked by measuring their ATPase. It is determined with a regenerating ATPase assay to prevent product inhibition by ADP. ATP is regenerated by the consumption of Phosphoenolpyruvate (PEP), catalyzed by Pyruvatekinase (PK). PEP is then converted to lactate by the oxidation of NADH to NAD^+, catalyzed by Lactate-Dehydrogenase (LDH). All reactions have a stoichiometry of 1:1, thus each hydrolyzed ATP results in one oxidized NADH. The oxidation of NADH can be monitored via absorbance spectroscopy by a decrease of the absorbance at 343 nm, $A_{343\ nm}$, because NAD^+ displays negligible absorbance at this wavelength, while NADH has an extinction coefficient of $\varepsilon_{343\ nm} = 7500\ \mathrm{M^{-1}cm^{-1}}$. Reagents and enzymes are used at concentration of 2 U/ml PK, 1 U/ml LDH, 0.2 mM NaDH and 2 mM PEP. ATPase rates are measured for 5 min at an interval of 1 s. The ATPase background is detected by specific inhibition of Hsp90 with an excess of the competitive inhibitor radicicol. Both data are fitted with a linear regression model and correction is substracted. Rates are calculated following Lambert-Beer's law:

$$\frac{\Delta c}{\Delta t} = \frac{\Delta A}{\Delta t} \cdot \frac{\varepsilon_{343\,nm}}{l} \tag{2.29}$$

with A being the absorbance, c being the concentration, l being the distance.

2.7 Molecular biology and protein biochemistry

2.7.1 Protein constructs and sequences

Hsp90

Hsp90 is studied as the heat inducible isoform of the yeast *S.cerevisiae* Hsp90 (Uniprot ID P02829 [127]). It was engineered into different constructs, which resulted in the proteins described and named in Fig. 2.13. The term zipper refers to a short amino acid sequence derived from the kinesin heavy chain of *Drosophila melanogaster*, dmKHC, which forms homodimers with very low K_D and a slow dissociation rate, preserving the dimeric nature of the protein even at the dilutions necessary for single molecule experiments [27, 128]. Sumo refers to a part of the sequence of the ubiquitin-like protein yeast Smt3 (Uniprot ID Q12306 [127]) that is recognized by the protease Senp and cleaved C-terminally. It is used to cleave the N-terminal His_6-tag after protein purification, resulting in the native-like protein [129]. The AviTag (Avidity LLC, Aurora, USA) is used for *in vivo* biotinylation of

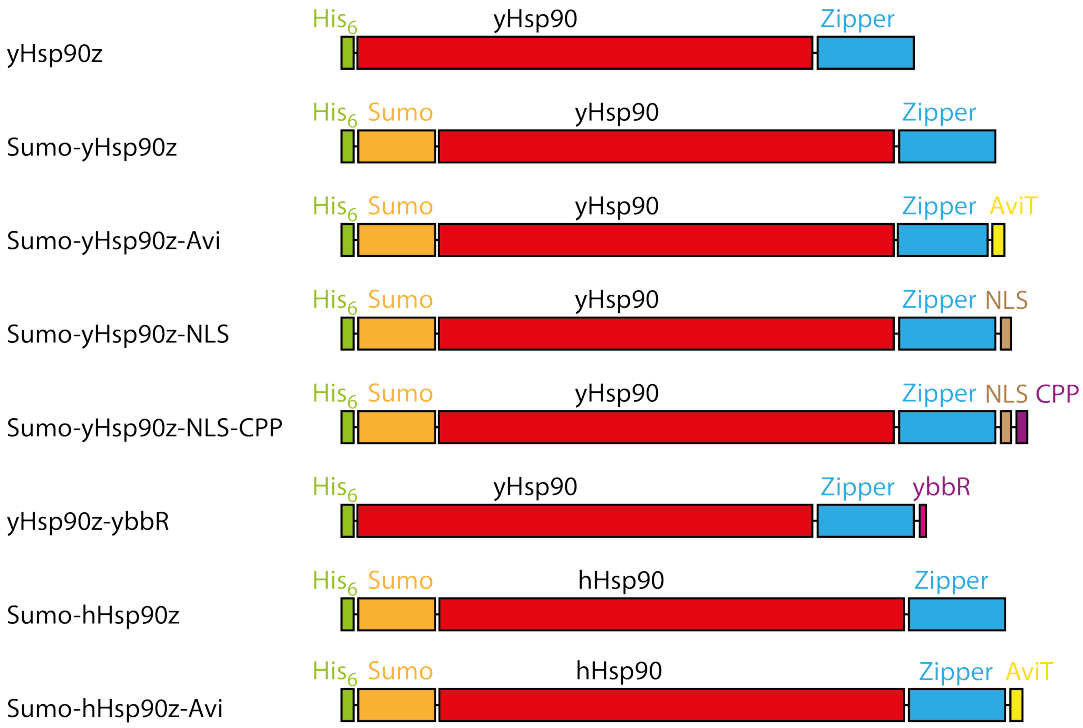

Figure 2.13: The Hsp90 constructs used in this work. The length of each pictogram is representative for the protein chain length.

the protein [130].

For the experiments on protein transfection into HeLa cells, two constructs of yeast Hsp90 harboring either a nuclear localization sequence (NLS) or an NLS and a cell penetrating peptide (CPP) sequence with Glycine-Serine linkers in between are used. The NLS is a short peptide sequence from the SV40 large T antigen that leads to rapid translocation of protein from the cytoplasm into the nucleus [131, 132]. The CPP is a short peptide sequence derived from human immunodeficiency virus (HIV) Tat protein, which has been shown to rapidly translocate through the plasma membrane [133, 134].

The constructs are derived by Phusion PCR insertion following the manufacturer's protocol (Thermo Fisher Scientific). The sequences of the peptides including the used linker amino acids are shown in Table 2.4.

For experiments on co-localization by DNA-anchors, Hsp90 is tagged at its C-terminus with the ybbR sequence `DSLEFIASKLA` by Phusion polymerase chain reaction (PCR) (Thermo Fisher Scientific). The gene of human Hsp90 investigated in order to explore its usability as sample for *in vivo* studies is synthesized (GenScript, Piscataway, USA) with an N-terminal His_6-Sumo-tag and a C-terminal zipper as described in Table 2.4. All native cysteines in the heat-inducible human Hsp90β isoform (Uniprot ID P08238 [127]) are substituted by an appropriate amino acid (residues from homologues, alanine or serine) in order to enable site-specific labeling of artificially introduced cysteines later on. The substitutions are C366F, C412T, C512A, C564L, C89A, C590A.

Table 2.4: Sequences of the peptides introduced into the different yeast Hsp90 constructs. Ineffectual or linker amino acids are colored red.

Peptide	Sequence
His_6	MGSSHHHHHHSSGLVPRGS
Sumo	ASMSDSEVNQEAKPEVKPEV KPETHINLKVSDGSSEIFFK IKKTTPLRRLMEAFAKRQGK EMDSLRFLYDGIRIQADQTP EDLDMEDNDIIEAHREQIGG
Zipper	PGEQKAEEWKRRYEKEKEKN ARLKGKVEKLEIELARWRPG SAWSHPQFEK
AviTag	SLGGGLNDIFEAQKIEWHE
NLS	GGSGGSGPKKKRKVED
CPP	GGSGGSYGRKKRRQRRR

Cdc37

Cdc37 of the yeast *S.cerevisiae* (Uniprot ID P06101 [127]) is studied as an N-terminally His_6-tagged fusion protein with C-terminal yHsp90z and an AviTag, linked by a designed peptide of the sequence $P(GGS)_{15}P(EAAAK)_5P(GGS)_{15}P$. This construct is synthesized at GenScript. A construct of yeast Cdc37 with N-terminal His_6-tag followed by a ybbR-tag with the sequence SLEFIASKLA is created by Phusion PCR (Thermo Fisher Scientific) on the wild-type sequence [135]. The constructs are shown schematically in Fig. 2.14.

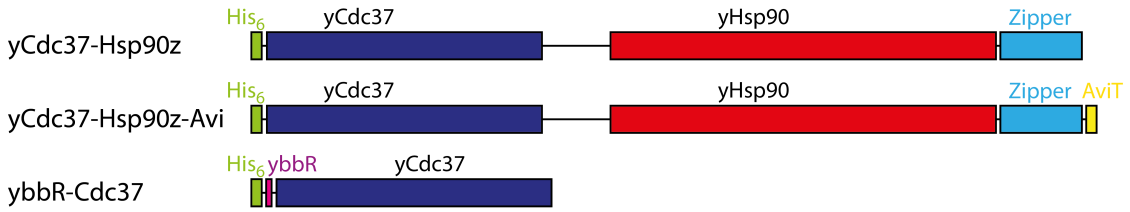

Figure 2.14: The Cdc37 constructs used in this work. The length of each pictogram is representative for the protein chain length.

Aha1 and Sba1

Aha1 and Sba1 from *S. cerevisiae* (Uniprot ID Q12449 and P28707 [127]) are used as N-terminal His_6-Sumo-tagged wild-type protein constructs contained in pET28a.

2.7.2 Point mutations

Point mutations are introduced to obtain functional mutants or single cystein variants for site-specific labeling with maleiimide derivatives of fluorophores. They are obtained using the Quik Change Lightning Kit (Agilent Technologies, Santa Clara, USA), following the manufacturer's protocol and verified by sequencing. A list of all mutants is shown in Table 2.5.

Table 2.5: Point mutants in the constructs studied in this work. Numbers refer to the position of the amino acid in the native protein (given as index in fusion proteins). Type refers to the aim of the mutation.

Point mutant	Construct(s)	Type
Q9C	yHsp90z	Label
S51C	yHsp90z	Label
D61C	yHsp90z, Sumo-yHsp90z, yHsp90z-ybbR	Label
A142C	yHsp90z	Label
A152C	yHsp90z	Label
216C	yHsp90z	Label
T285C	yHsp90z	Label
N298C	yHsp90z, Sumo-yHsp90zNLS, Sumo-yHsp90zNLS	Label
A327C	yHsp90z	Label
Q385C	yHsp90z, Sumo-yHsp90zAvi	Label
A409C	yHsp90z	Label
E431C	yHsp90z	Label
D452C	yHsp90z	Label
466C	yHsp90z	Label
517C	yHsp90z	Label
560C	yHsp90z	Label
637C	yHsp90z	Label
E33A	yHsp90z D452C	Function
D79N	yHsp90z	Function
D79N	yHsp90z D452C	Function
E70C	Sumo-hHsp90z	Label
Q405C	Sumo-hHsp90z	Label
G129$_{Cdc37}$C	yCdc37-Hsp90z, ybbR-yCdc37	Label
K396$_{Cdc37}$C	yCdc37-Hsp90z	Label
D61$_{Hsp90}$C	yCdc37-Hsp90z	Label
Q385$_{Hsp90}$C	yCdc37-Hsp90z-Avi	Label

2.7.3 Expression and purification

All proteins are expressed from the vector pET28a. The vector is transformed chemically into BL21 star DE3 *E. coli* (Thermo Fischer Scientific). In case of *in vivo* biotinylation,

biotin ligase (BirA) is coexpressed from pBirAcm (Avidity LLC, Aurora, USA) following the manufacturer's instructions. Bacteria are grown in TB-medium using appropriate antibiotics (Kanamycin at 50 μg for pET28a) at 37 °C to OD_{600} of 0.7, then expression is induced with 1 mM isopropyl-β-D-thiogalactoside (IPTG) for 3-4 hours. Bacteria are harvested by centrifugation, washed with phosphate buffered saline (PBS), and pelleted again. Cell pellets are stored at -20 °C until purification.

For purification, the cells are resuspended in 30 mL PBS and lysed with a cell disrupter (Constant Systems, Daventry, UK) at 1.6 kbar. Cell debris is pelleted by centrifugation at 25,000 g at 4 °C for 30 min (Avanti JXN-26, Beckman Coulter, Brea, USA). After filtration (Filtropur S 0.45, Sarstedt, Nümbrecht, Germany) the solution is applied to a 5 mL HisTrap HP (GE Healthcare, Freiburg i. Br., Germany) and eluted by a linear gradient from 0 to 500 mM imidazole in 100 mM sodium phosphate, 300 mM NaCl pH 8.0 at 8 °C. Protein containing fractions are pooled and dialyzed into the imidazole-free buffer overnight. As an alternative, the solution is applied on a Strep-Tactin column (IBA GmbH, Göttingen, Germany) to purify the protein by affinity for the strep-tag and dialyzed into low salt buffer (50 mM NaCl, 40 mM Hepes, pH 7.5). If the proteins contains an N-terminal His_6-Sumo tag, it is meanwhile incubated with 1/100 mol Senp protease, which cuts off the N-terminal His-SUMO sequence, leaving the native, tag-free protein [129], which is again applied to the HisTrap column and the flow-through is collected and diluted 1:3 with ddH_2O to decrease the ionic strength. With all Hsp90 and Cdc37 construct, as well as Sba1 the purification is proceeded by applying the solution to a HiTrapQ 5 mL (GE Healthcare), and the respective protein is eluted with a linear gradient rom 50 mM to 1 M NaCl in 40 mM Hepes pH 7.5. Hsp90 fractions are pooled and concentrated using centrifugal filters with a 50 kDa molecular weight cut-off (Amicon Ultra, Merck Millipore, Darmstadt, Germany). In case of Aha1, the solution is applied on a HiTrapSP (GE Healthcare) cation exchange column in 40 mM MES, pH 6, 40 mM NaCl and eluted with a linear gradient to 1 M NaCl. Subsequently, 1 mM DTT is added to prevent oxidation. Finally, each solution is applied to a HiLoad 16/600 Superdex200 (GE Healthcare) and the protein is eluted with 40 mM Hepes, 200 mM KCl pH 7.5. Peak fractions are again pooled and concentrated to 50–100 μM protein concentration. Protein concentration is measured by its absorbance at 280 nm using the theoretical extinction coefficient as calculated from the amino acid sequence by the online tool ProtParam [136]. Aliquots are snap-frozen in liquid nitrogen and stored at -80∘C until further usage. Expression and purification is monitored by SDS-PAGE.

2.7.4 Labeling and monomer exchange

Cysteine point mutations in proteins are labeled as follows. 100 μl 50 μM protein is incubated with 5 mM tris(2-carboxyethyl)phosphine (TCEP) for 30 minutes at room temperature to reduce possibly oxidized cysteines. Using a centrifugal filter in a cooled centrifuge, the protein is washed repeatedly (> 5 times) with ice-cold 1x PBS pH 6.7, and the final concentration of the protein is adjusted to about 50 μM. A two- to threefold excess of maleiimide-dye (dissolved in DMSO at millimolar concentration) is added and the reaction is incubated at room temperature in the dark for 1 h. The dye is removed either with gel filtration spin columns (PD-10, GE Healthcare), again by repeated centrifugation in centrigual filter, or by dialysis in microdialyzers over night at 4 °C.

In order to create heterodimers of Hsp90, a mixture of one donor labeled protein and one acceptor labeled protein with a total protein concentration below 10 μM is incubated

at 47 °C for 20 min. This destabilizes the C-terminal zipper and enables exchange of the monomers [27]. Aggregates are removed by centrifugation at 14,000 g at 4 °C for 30 min. When one variant is biotinylated and the sample is studied on a TIRF setup later on, the non-biotinylated variant is given in a tenfold excess to the reaction, resulting in the observation of mainly heterodimers in the final experiment.

Fluorophores employed in this study are Atto488, Atto550, Atto594, Atto647N, Atto725, Atto740 (AttoTec GmbH), Cy7 (Lumiprobe GmbH), LD750 (Lumidyne Technologies), Alexa647 and Alexa750 (Thermo Fisher Scientific).

2.8 Prediction of scattering profiles and the distance distribution function

Prediction of SAXS data from protein structure files is based on the programs CRYSOL and GNOM from the EMBL [137, 138].[8]

SAXS experiments typically result in an intensity profile giving the scattered intensity I in dependence of the displacement vector S ($[S] = \mathrm{nm}^{-1}$), $I(S)$. The program CRYSOL is used to calculate an expected scattering profile from PDB structures at high resolution (50 harmonics, 18th order of the Fibonacci grid, 1.0 $\mathrm{Å}^{-1}$ maximum scattering vector, 256 points). Solvent density and hydration shell are set to default.

The indirect Fourier transform (FT) of the intensity profile results in the distance distribution function $p(r)$. This function is calculated using the program GNOM with default settings.

8 European molecular biology laboratory, Hamburg, https://www.embl-hamburg.de/biosaxs/ [March 2017].

CHAPTER 3

Results and discussion

In this chapter I present and discuss the results of my studies on the Hsp90 chaperoning system. A brief summary and discussion is given at the end of each section.

- In 3.1, The dynamic structure of Hsp90, I present the results from structural studies with confocal smFRET on Hsp90's closed and open conformation and their time-resolved three-dimensional structures in solution. Our results finally make smFRET a valuable tool in structural biology.
- In 3.2, Cooperativity in Hsp90, we extend the studied system of Hsp90 to its interaction with nucleotides. The correlation between conformational dynamics of Hsp90 and the binding and unbinding of nucleotides, as well as the effect of co-chaperones on it, are investigated with three-color smFRET. Based on this system, we suggest microscopic causes for cooperativity in Hsp90 and the regulation by co-chaperones.
- In 3.3, The mechanism of the Hsp90 regulation by Cdc37, I present the results on the interaction of the co-chaperone Cdc37 with Hsp90, which together are responsible for the chaperoning of most cellular kinases. A protein construct is developed that allows single molecule studies on this very weak interaction. The effects of nucleotides, the co-chaperones Sba1 and the native client protein Ste11 are characterized. The results constitute the basis for detailed studies on the client/chaperone interaction.

3.1 The dynamic structure of Hsp90

As remarked in Section 1.2 on page 3, Hsp90 is an highly abundant and one of the most important molecules in eukaryotic cells, which makes it important as a possible drug target in cancer treatment. However, none of the developed drugs has reached the commercial launch yet, although research started more than 20 years ago. It seems reasonable that the limited knowledge of Hsp90's structure with the published structural data being not overall consistent, as well as the limited knowledge of its functionality prevents an effective rational drug design.

In the following, I describe how I accessed and resolved the dynamic structure of Hsp90 in a work together with Björn Hellenkamp by developing a new method in structural biology based on confocal smFRET. This approach enables us to assess the dynamics and the structure of multi-domain proteins like Hsp90 simultaneously and reveals the nature of the interaction between Hsp90 and a model client protein. While I took main responsibilities concerning the biochemical methods and protein chemistry, Björn Hellenkamp conducted most confocal single molecule FRET experiments and wrote the script for structural docking.

Most of the presented data on the dynamics structure of Hsp90 has been published in:

Hellenkamp, Björn, Philipp Wortmann, et al.: 'Determination of structural ensembles and correlated dynamics of a multi-domain protein'. *Protocol Exchange* (2017), vol. DOI:: 10.1038/ protex.2016.078

Hellenkamp, Björn, Philipp Wortmann, et al.: 'Multidomain structure and correlated dynamics determined by self-consistent FRET networks'. *Nature methods* (2017), vol. 14(2): pp. 174–180

Hellenkamp, Björn: 'Dynamic Structure Of A Multi-Domain Protein: Uncovered Using Self-Consistent Fret Networks And Time-Correlated Distance Distributions'. PhD Thesis. Munich: Technische Universität München, 2016

3.1.1 Self-consistent networks increase the accuracy of smFRET

To gain information on the three-dimensional structure of Hsp90, we span a FRET network across Hsp90's structure. This is achieved by the combination of several single site-specific labeled protomers, as shown in Fig. 3.1. The labels (i.e. dyes) are attached by coupling a dye-maleiimide to cysteines introduced by site-specific mutagenesis.[9] An inter-combination of the different point mutations is achieved by using a zipped Hsp90 dimer, where the two protomers are connected via a coiled-coil motif that melts upon heating but remains stable at physiological conditions [27].

Each combination results in a single FRET efficiency for each conformation. The different combinations constitute the FRET efficiency network (shown in Fig. 3.1(C)) that contains information about the inter-dye distances and therefore the three-dimensional position of each dye. Due to the distance dependency of FRET, the network of efficiencies can be used to back-calculate a network of distances and therefore as a tool in structural biology.

Our assumption is that in most cases secondary structure elements such as α-helices or β-sheets and even most domains remain stable during protein rearrangements. Therefore, it is sufficient to sample a certain number of distances distributed along a protein structure to obtain enough information for resolving the three-dimensional domain arrangement and hence the complete structure of a specific protein conformation. Only the information on the arrangement of small motifs or single amino acid side chains remains limited and might necessitate refinement, e.g. by molecular dynamic (MD) simulations.

Notably, the assumption of intrinsic domain stability is of use as well in X-ray crystallography. Many structures of multi-domain proteins at atomic resolution are solved by the method of molecular replacement, where the structure of the full-length construct can be solved based on the known structures of constructs comprising e.g. single domains [139, 140].

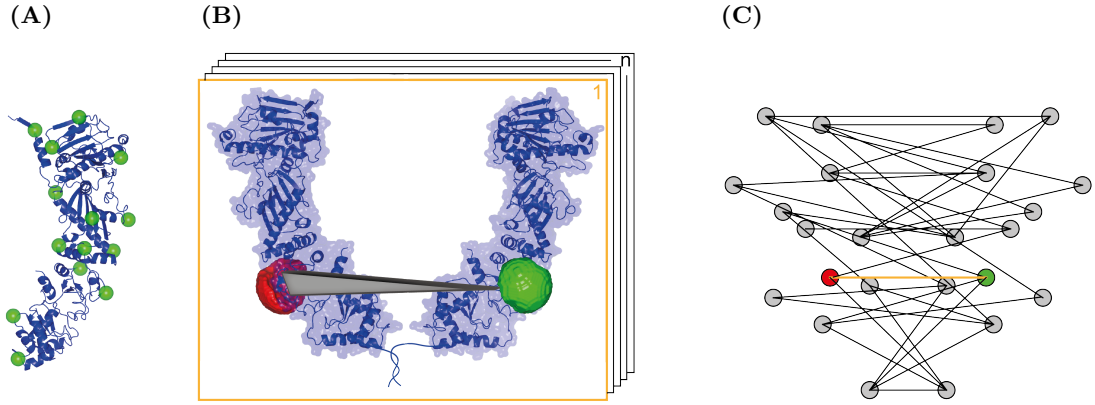

Figure 3.1: Accessing the three-dimensional structure of Hsp90 by smFRET. (A), dye attachments positions are distributed along the structure of Hsp90 (PDB 2cg9). (B), FRET efficiency for several different FRET pairs are determined. Dyes are indicated by their AVs [125]. (C), the sum of all pairs constitute a FRET efficiency network that can be reverted in a distance network.

The location of each cysteine and thus label is selected such that no highly conserved amino acid is substituted (which would otherwise likely lead to a loss of biological function

9 Yeast Hsp90 wild-type does not contain any cysteines, making this method is site-specific.

by altering the protein structure), and such that the label attachment site is located at small hinges or loops with an expected great solvent accessibility. Each single cysteine point mutant is labeled with the either Atto550 as donor or Atto647N as acceptor dye. Preserved biological activity is tested by the ATPase assay to ensure only functional Hsp90 variants are further studied (c.f. Appendix A.1 on page 107).

Single molecule FRET within exchanged dimers is measured in solution on a confocal setup by pulsed interleaved excitation (PIE) FRET, as described in Section 2.1.4, page 25. FRET donor and acceptor are excited alternatingly, their fluorescence is separated by dichroic mirrors and detected polarization sensitive by avalanche photodiodes (APDs). From the resulting two-dimensional stoichiometry (S) vs FRET efficiency (E) histogram Hsp90 dimers carrying one donor and one acceptor fluorophore (i.e. the FRET pair) are specifically selected.

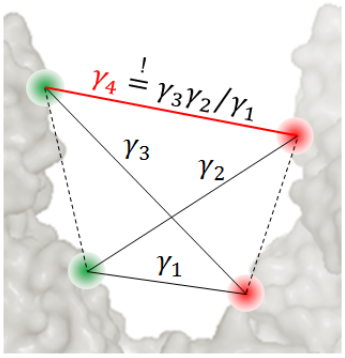

Figure 3.2: Correction factors such as the gamma factor γ can be checked within a large network of FRET pairs, because of their redundant determination [3].

A network of FRET pairs between several positions comes along with the advantage of self-consistency. Errors arising from wrong distances due to erroneous determination of a quantity, such as correction factors, or due to local rearrangements within the network, can easily be detected (Fig. 3.2). E.g. the γ-factor for a FRET pair consisting of a donor D_1 and an acceptor A_1 can be calculated by a set of the γ-factors of the respective dyes in FRET pairs with the donor D_2 and acceptor A_2:

$$\gamma_{D_1A_1} = \gamma_{D_1A_2} \cdot \gamma_{D_2A_1}/\gamma_{D_2A_2} \tag{3.1}$$

Hence, the accuracy of smFRET derived structure information can be increased dramatically by the intrinsic quality control of a joint distance network. This makes the network a major improvement to previous studies on protein complex structures [125, 141]. In addition, it can enable the detection of correlations between local rearrangements and changes in the global conformation of a multi-domain protein such as Hsp90, because in that case properties of single FRET pairs change according to the global arrangement of protein.

3.1.2 The crystal structure of Hsp90 is reproduced by smFRET

As first step, we aim to reproduce the known crystal structure of Hsp90 in its closed, AMP-PNP bound state by our smFRET network [18]. In presence of AMP-PNP, Hsp90 is trapped in this closed state and the FRET efficiency histogram displays only one population, which simplifies subsequent analysis [27, 113].

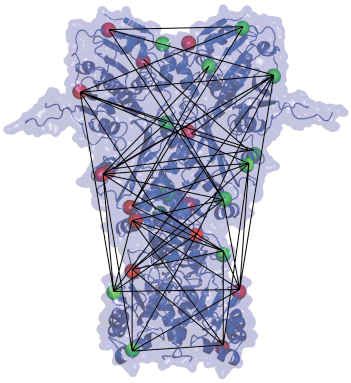

Figure 3.3: Reproducing the crystal structure of AMP-PNP bound yeast Hsp90 [18] by a self-consistent FRET network. A representation of the network of FRET pairs spanned over the Hsp90 dimer by measuring FRET of inter-combined donor and acceptor labeled monomers is shown. Based on this network, the evaluation of smFRET data is improved.

160 different intra- and intermolecular FRET pairs are measured, as depicted in Fig. 3.3. The Förster distance for each pair is calculated individually. Absorption and fluorescence spectra are measured on spectrometers and the fluorescence quantum yield is determined from the single molecule data using the donor-only population (at $S \approx 0$ and $E \approx 0$ in the S vs E histogram).[10] The dipole orientation factor is assumed $\kappa^2 = 2/3$.

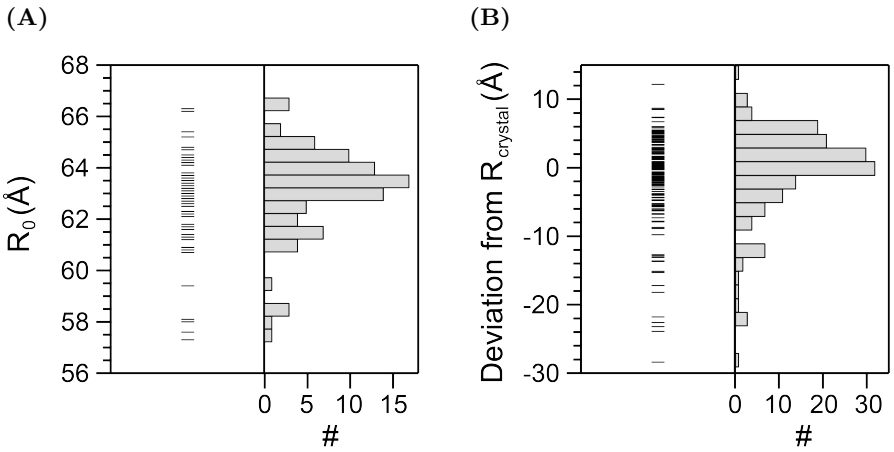

Figure 3.4: Comparison of the determined Förster radii and distances in the AMP-PNP induced, closed structure for the studied FRET pairs.(A), distribution of Förster radii for all distances. Left panel, each FRET pair is represented by a line. Right panel, histogram of the determined radii. The Förster radius for the used dyes Atto550 and Atto647N in water is 65 Å. (B), distribution of the deviations of FRET distances within closed Hsp90 from the crystal structure [18]. Left panel, each distance deviation is represented by a line. Right panel, histogram of the deviations.

10 See Section 2.5 on page 37 for a detailed description of the procedure. The determined quantities have been published [3, 107] and can be found at `http://www.nature.com/nmeth/journal/v14/n2/extref/nmeth.4081-S2.xlsx` [March 2017].

Notably, the dyes vary in their Förster distance by up to 9 %. The radii are overall significantly smaller than the radius expected from the spectra of the uncoupled donor and acceptor fluorophores (c.f. Fig. 3.4(A)). This demonstrates the necessity of a correction for shifted absorbance and fluorescence spectra. The corrected pair-wise distances are compared to the expected distances[11] to be measured in the crystal structure of closed, AMP-PNP bound yeast Hsp90 in Fig. 3.4(A). Strong deviations occur for distinct FRET distances, but no direct correlation with the calculated R_0 values is found. The complete set of N distances is compared to the distances in the crystal structure by the root mean square deviation (RMSD) based on the difference δ_i of the i-th distance pair:

$$RMSD = \sqrt{\frac{1}{N}\sum_{i=0}^{N}\delta_i^2} \tag{3.2}$$

The calculation reveals an overall deviation of the determined smFRET distances from the distances expected from the crystal structure by an RMSD of 4.8 Å. The RMSD is impaired and probably biased by the distinct distances between dyes deviating to a much larger extend than the mean. These strong deviations arise from the (in their case) wrong assumption of an averaged relative dipole orientation, i.e. an isotropic dye/dye orientation within the time of FRET transfer (which is the fluorescence lifetime of the donor, < 4 ns in our experiment). This leads to a different Förster distance and in consequence to an erroneous calculation of the inter-dye distance.

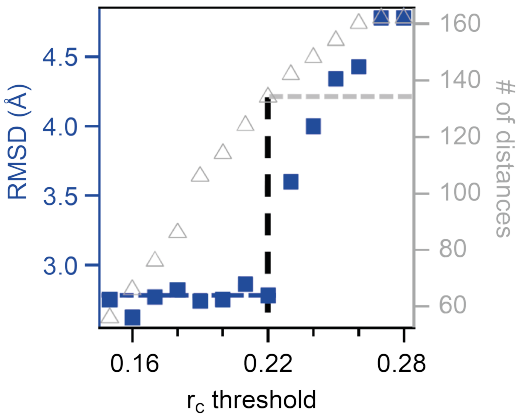

Figure 3.5: The deviation of smFRET derived distances from the crystal structure depends on the combined anisotropy r_c of the respective FRET pair. A threshold on r_c is varied and the RMSD of the remaining smFRET distances is calculated. A steep drop in the RMSD to 2.8 Å is observed at a threshold of $r_c = 0.22$ that included 132 from 160 distances. Further decreasing the threshold does not affect the resulting RMSD.

The time-resolved anisotropy decay $r(t)$ of fluorescent dyes recorded within the measurements provides information on the timescales of different dye motions and thus the dipole motions. Evaluating the data in terms of the combined anisotropy r_c (that represents the

11 The expected distance deviates from the atomic distances (e.g. C_α-C_α) due to the sterical hindrances that direct the average dye position. Expected distances are thus calculated using the FPS software package as described in Section 2.5.3 on page 38.

transfer anisotropy, c.f. Section 2.5.2, page 38) reveals the dependency of the RMSD of the remaining distances upon the application of an r_c threshold on the data, as shown in Fig. 3.5.

A clear cut-off at $r_c = 0.22$ is visible, at which the RMSD of the remaining 132 measured distances decreases to 2.8 Å. The application of a lower threshold does not result in any further improvement of the distance deviations from the crystal structure. No correlation between the anisotropy values of the remaining FRET pairs and their respective distance deviations from the crystal structure can be found. The remaining RMSD is within the overall resolution of the crystal structure, which is 3.1 Å [18]. Structural differences between the structure in solution that is studied in this experiment and the structure within the crystal might contribute to the observed RMSD. The crystal structure of Hsp90 has been obtained with a construct that had a charged linker substitution and a single point mutation incorporated [18]. Single smFRET distances are checked for this construct, and do not exhibit any difference to the distances measured in wild-type Hsp90.

Thus, we verified and tuned our novel method on the multi-domain protein Hsp90, reproducing the X-ray crystal structure of the closed conformation.

3.1.3 The open conformation of Hsp90 is highly dynamic

Being able to resolve the three-dimensional structure of Hsp90 in its closed conformation, we use our set of FRET pairs to access yeast Hsp90's open conformation, whose structure has not been resolved so far. This is much more challenging, as Hsp90 cannot be trapped by the addition of a nucleotide in the open state [27]. However, assuming two states of Hsp90 that exhibit Gaussian distributed distances fits the data very well and allows us to separate and analyze the open state.

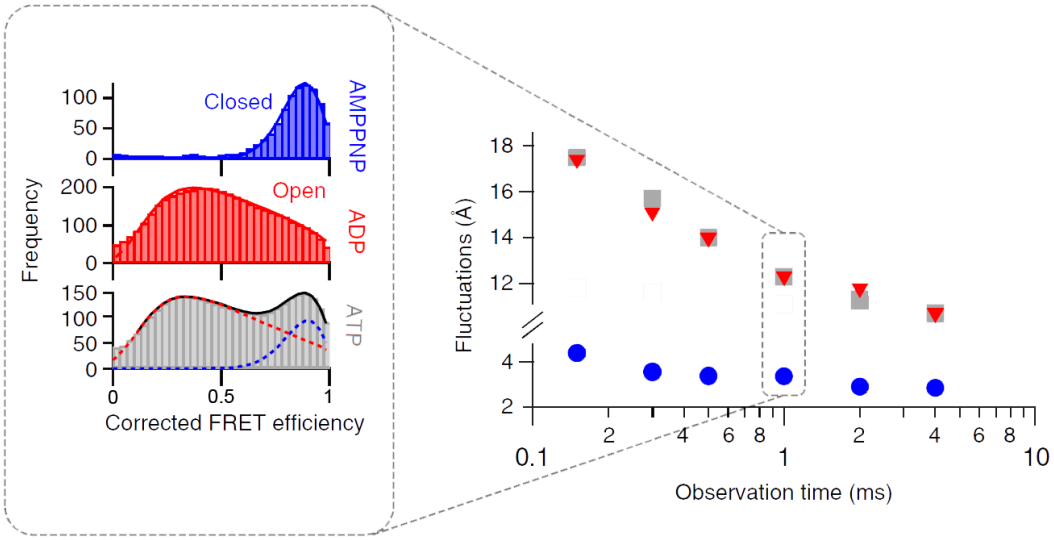

Figure 3.6: Hsp90 fluctuates nucleotide dependent on the micro- to millisecond timescale, with AMP-PNP suppressing them. The fluctuation amplitude depends on the observation time, as revealed by variation of the binning time on smFRET distances measured in presence of 2 mM AMP-PNP, ATP or ADP. The inset shows the FRET efficiency histograms at a binning time of 1 ms. The dotted lines indicate the equilibrium of closed and open conformation and the attributed populations of Hsp90 in presence of ATP. Figure has been published in [3].

Hsp90's open conformation results in much broader FRET peaks than the closed, which had resulted in peak widths close to the shot noise limit. This is likely due to dynamic fluctuations of Hsp90 in the open state. A variation of the binning time of the smFRET data changes the width of the FRET peaks and thus reveals protein dynamics on the timescale of 0.1 to 10 ms, as shown in Fig. 3.6. Complementary to the binning time variation, the inter-domain dynamics are accessed by fluorescence lifetime analysis (c.f. Fig. 3.7(B)) [142, 143], resolving faster fluctuations occurring between 10 ns and 1 ms.

The dynamics of Hsp90 are found to be similar in presence of ADP and ATP, and in both cases much larger than the fluctuations in presence of AMP-PNP. Assuming the separate domains of Hsp90 to remain stable, our large data set allows to discriminate the relative motions of them with respect to each other (shown in Fig. 3.7). Large fluctuations occur between the MD of the two protomers, but minor fluctuations occur also between the NTD and MD within one protomer. Fluctuations between the protomers increase the further the label positions are located towards the NTD of Hsp90. The CTDs of both Hsp90 do not fluctuate to a large extend at the studied timescales.

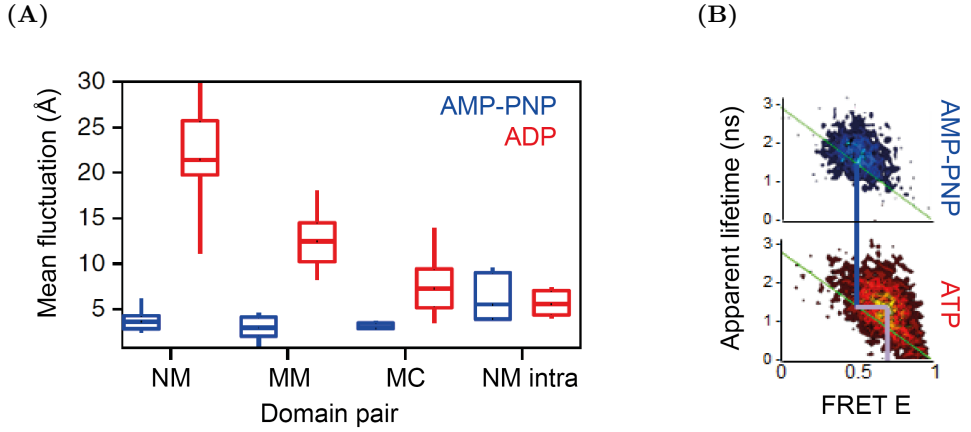

Figure 3.7: The domains of Hsp90 contribute different to the fluctuation. (A), box-whisker plot of the fluctuation amplitude observed at 1 ms binning time in presence of 2 mM AMP-PNP or ATP for the distances between the different domains of the two protomers (N-M, M-M, C-M) and between the domains of one protomer (N-M intra). (B), the fast inter-domain fluctuation between the NTD and the MD in a single protomer is revealed by fluorescence lifetime analysis. Figures have appeared in [3].

3.1.4 Open Hsp90 is an ensemble of conformations

The distance network gained from the assignment of the closed state is further used to solve the three-dimensional structure of yeast Hsp90 in its open state. Because the open conformation is usually assigned to the 'ADP-state' of Hsp90, we subsequently apply our structure analysis on data measured in presence of 2 mM ADP.

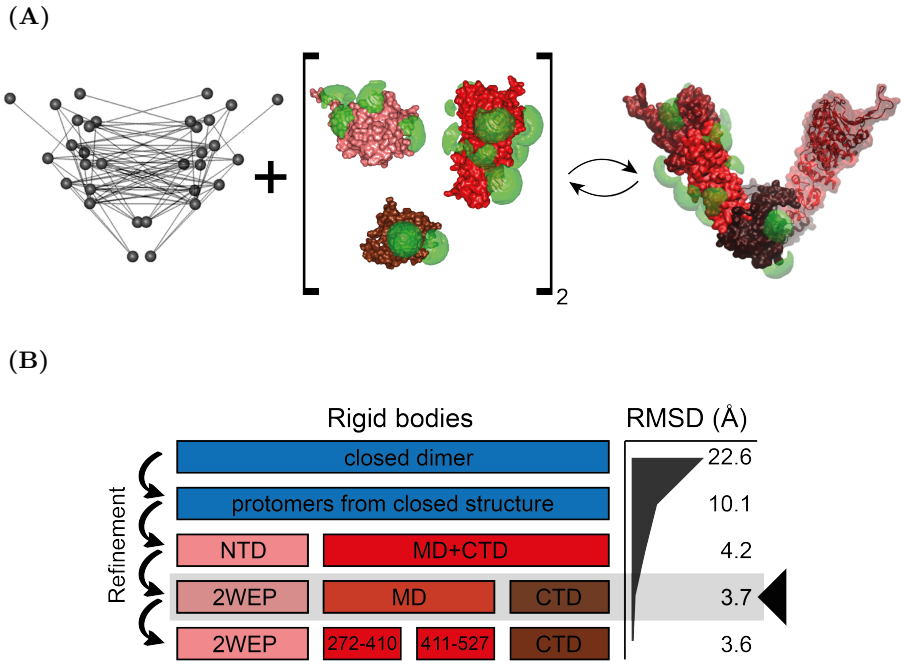

Figure 3.8: Resolving the structure of open yeast Hsp90 with smFRET derived distances. (A), the Hsp90 structure is arranged by a global distance distribution analysis to fulfill the distance set and iteratively refined by division into separate domains as rigid bodies. (B), starting from the crystal structure of closed Hsp90, the rigid bodies are step-wise divided into separate domains the arrangement is refined. A substitution of the NTD by the crystal structure of this domain in presence of ADP (PDB 2wep [34]) significantly decreases the refined RMSD, while a division of the MD into its sub-domains has negligible influence. Thus, the arrangement dividing Hsp90 into CTD, MD and NTD (the latter in the crystal structure 2wep) is considered as optimal representation of Hsp90's structure within the error of the method.

An ensemble of model structures for Hsp90's open state is generated based on a global distance distribution analysis developed[12] by creating average domain arrangements. The structure of Hsp90 is subsequently divided into rigid bodies that are arranged to fulfill the experimental distances (c.f. Fig. 3.8(A)). Fig. 3.8(B) demonstrates that the division of the structure into the single domains (NTD, MD, CTD) as resolved in the crystal structure of closed Hsp90 results in a significantly improved RMSD of the refined arrangement. Further improvement is achieved by substitution of the NTD by the crystal structure of the isolated NTD of Hsp90 in presence of ADP, where the nucleotide lid is opened and neighboring motifs rearranged correspondingly [34]. Analog to our data evaluation procedure on the closed conformation of Hsp90, we apply a threshold for the combined anisotropy r_c on the data to exclude artifacts from anisotropic dipole-dipole coupling (c.f. Appendix A.2, page 110).

MD simulations are applied subsequently on the final arrangement for structural refinement of local motifs and amino acid side chains. We follow this general procedure, because on the one hand the large fluctuations of Hsp90's domains are not sampled on the

12 The developed software is available online at `https://www.singlemolecule.uni-freiburg.de/software/structure` [March 2017] and a detailed description of the underlying algorithm is given in [3].

timescale of currently accessible simulation times, while on the other hand our method is not capable of resolving single amino acids side chain orientations or the orientation of e.g. loops not included directly in our data by a respective label position.

Five model structures are generated by the global distance distribution analysis and refined by MD simulations. One structure equals the average symmetric structure, and the other four correspond to the left and right intervals of the single Gaussian distance distribution of the open Hsp90. Hence, the analysis results in model structures representing the mean, the $\pm\sigma$ and $\pm 2\sigma$ of the distance distribution at an observation time of 1 ms.

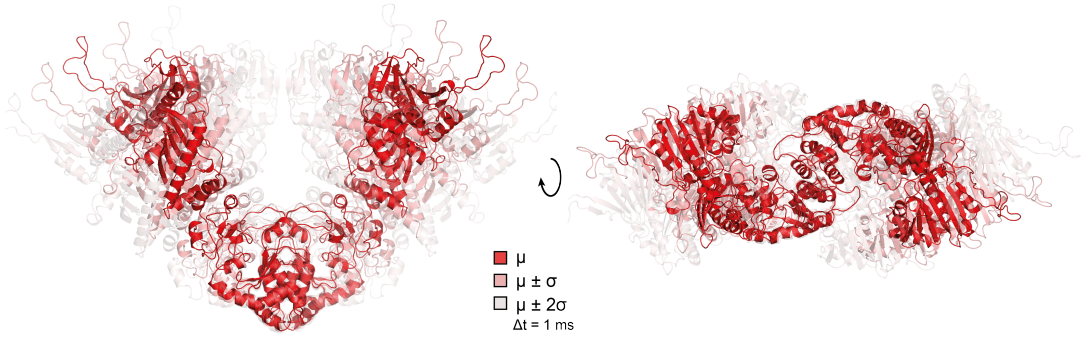

Figure 3.9: The structural ensemble that represents the most likely trajectory of the Gaussian fluctuations of Hsp90 at a time resolution of 1 ms. Shown are the mean μ and its right and left intervals σ and 2σ, with a transparency gradient emphasizing the population probability.

The generated structures are shown in Fig. 3.9. The average structure and the $\pm\sigma$-structures all match the experimental distances with an RMSD of about 4 Å. The structural ensemble represents the most likely average trajectory on which Hsp90 dynamically fluctuates in the open state.

A comparison of the average open structure with the X-ray crystal structure of closed yeast Hsp90 is shown in Fig. 3.10. It emphasizes an opening of the Hsp90 dimer at its N-terminus perpendicular to the N-terminal dimerization interface. The domain interfaces NTD/MD and MD/CTD are flexible hinges that allow Hsp90 large fluctuations. While the NTD rotates by approximately 90° with respect to the MD, a partial shift is observed for the MD/CTD interface.

The combination of the findings on the different domain dynamics and the ensemble structure of open Hsp90 leads to the model shown in Fig. 3.10(D). In the open state, the MD/CTD interface fluctuates on the millisecond timescale and hence enables large, but defined inter-monomer fluctuations. The NTD/MD interface fluctuates faster (sub-millisecond) and allows a transient rotational motion of the N-terminal domain. Local motifs are likely to fluctuate additionally, possibly on even faster timescales. The large dwell time of the global open state in the timescales of seconds [27, 113] is probably caused by the low conditional probability that the N-terminal domains are in close proximity and both in the correct orientation for the state transition simultaneously.

MD simulations provide a first insight into the mechanisms that underlie this complex behavior. Unrestrained MD simulations in explicit solvent starting from the experimentally arranged average closed structure and average open structure reached a plateau regime of 6–8 Å, indicating a stable open structure. The root mean square fluctuation (RMSF) are shown color-coded in Fig. 3.11(A).

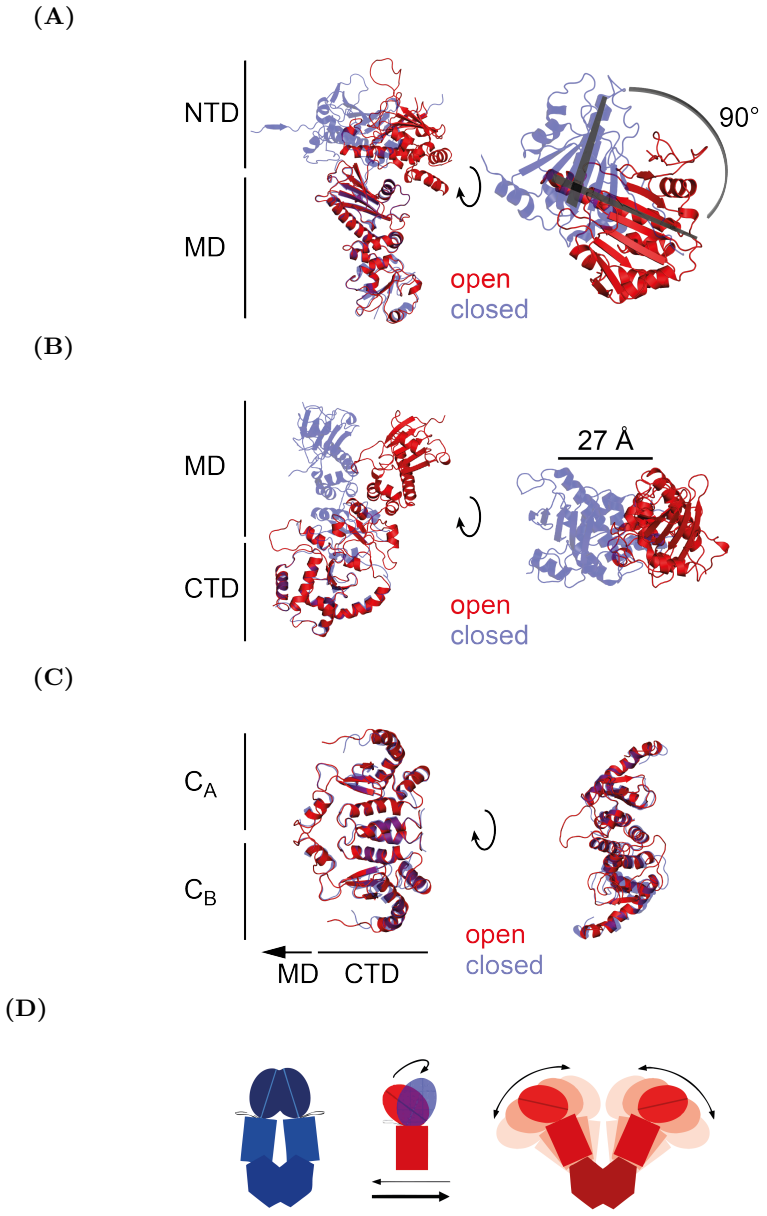

Figure 3.10: Structural rearrangements of Hsp90 in the transition between open and closed state. (A), The NTD can rotate with respect to the MD by about 90° and Hsp90 prefers the different rotations either in the open or in the closed state. This is demonstrated by an alignment of the MD in each structure. (B), the MD/CTD interface functions as a hinge (CTDs aligned). (C), The CTDs of the two protomers do not exhibit a significant rearrangement, but the dimer interface stays rigid. (D), model of Hsp90's fluctuations on different timescales and their effect on the global transition between the open and the closed state of Hsp90. Only with both NTDs being in close proximity (MD/CTD fluctuation) in their right orientation (NTD/MD fluctuation), Hsp90 is able to enter the closed state. This very likely causes the slow transitions observed in TIRF experiments [27, 113].

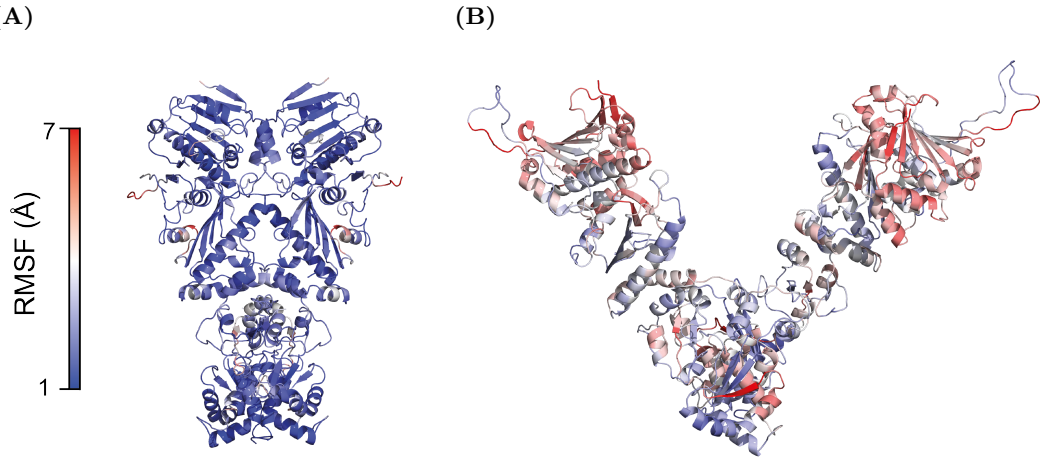

Figure 3.11: RMSF of Hsp90 in the open and the closed state from unrestrained MD simulations, mapped onto the structure of (A), closed and (B), the open state of Hsp90. While the closed state is overall very rigid, the open conformations of Hsp90 exhibits strong flexibility in several local motifs.

The closed conformation results in an overall rigidness with fluctuations in almost all regions of only 3 Å. In contrast, the open structure reveals several flexible elements (c.f. Fig. 3.11). The ATP-lid at the interface of the NTD and MD remains in the α-helical conformation (as in PDB 2wep) while contacting the MD. The loop conformation of the ATP-lid as in the AMPPNP-bound X-ray structure is sterically not accessible. An interference of the ATP-lid with the NTD/MD arrangement has been suggested before [25].

The interface contacts at the interface between MD and CTD are shifted in the open structure compared to their configuration in the closed. The α-helix 10, the loop at amino acid (aa) 568–575 and the loop at aa 524–533 contribute to the interface, which is consistent with hydrogen exchange experiments [67]. The interface seems to be stabilized by salt bridges between charged residues that are not present in the closed state. In the simulations, most of these charged residues exhibit (anti-)correlated switching, supporting the flexibility of this interface.

While only one X-ray crystal structure of full-length yeast Hsp90 exists, several other structures from homologue proteins have been published. Notably, structures of the endoplasmic reticulum homologue Grp94 from *C. lupus* [24] and the *E. coli* homologue HtpG [25] are contained within the conformational ensemble (c.f. Fig. 3.12). The NTD/MD arrangement of the average open structure resembles the one seen for Grp94 with an RMSD of 3 Å, and the full-length structure is resembled by the -2σ with an RMSD of 4.5 Å. The structure of HtpG found is highly similar to the +σ structure from the ensemble. The crystal structures are probably snapshots from the conformational ensemble we solved. Because protein crystallization traps proteins in a structure of its energy minimum, the flat energy landscape of the open Hsp90 allows it to crystallize in different sub-conformations, already influenced by very weak differences in the crystallizing conditions.

Hsp90's structure and the effects of nucleotides have been studied by others using SAXS [53, 144]. SAXS experiments give information on the inter-atomic distance distribution of proteins in solution $p(r)$ by elastic scattering of photons by macromolecules. It thus

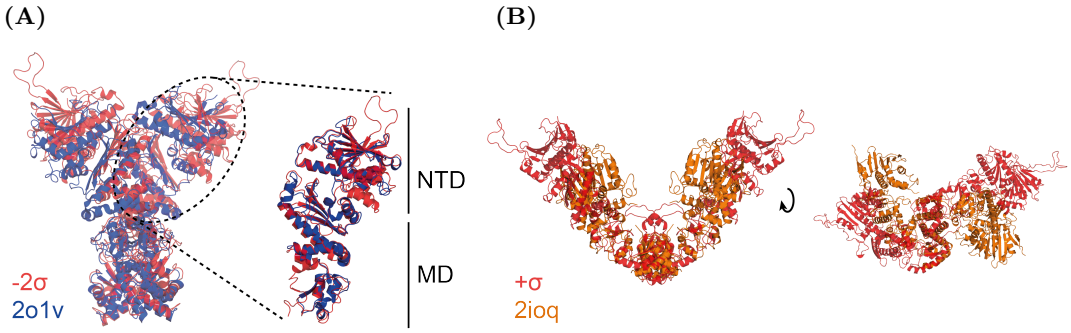

Figure 3.12: Comparison of crystal structures from Hsp90 homologues to the structural ensemble of yeast Hsp90 in the open state. (A), The crystal structure of Grp94 in presence of ADP (PDB 2o1v, blue) resembles the dimer structure of the -2σ structure by 4.5 Åand the arrangement of the NTD/MD by 3 Å. (B), the crystal structure of open HtpG (PDB 2ioq, yellow) is similar to the +σ structure from the ensemble.

allows conclusions about a protein's global shape and changes of this shape upon modified conditions [145]. From structures at atomic resolution, the expected scattering pattern and distance distribution function can be estimated [137, 138].[13]

Comparing the theoretical scattering pattern of the structures within the structural ensemble to the experimental SAXS data, we can nicely explain the broad distribution observed for Hsp90 in absence of nucleotides (c.f. Fig. 3.13). Two deviations occur: First, at very small inter-atomic distances, second at very large inter-atomic distances.

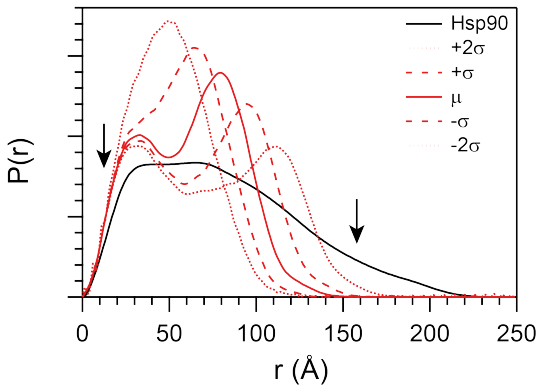

Figure 3.13: Experimental distance distribution function of Hsp90 in absence of nucleotide (Hsp90) and the theoretical functions of the structures from the structural ensemble of open Hsp90, as calculated with CRYSOL/GNOM (relative probabilities). With arrows the distance ranges that cannot be explained are indicated. Experimental data was kindly provided by Dr. Tobias Madl, TU Munich, Munich.

The first is easily explained by an under-estimation of the hydration layer of the molecule in solution. The second deviation is also not expected from any of the other published

13 See Section 2.8 on page 45 for detailed description of the procedure.

crystal structures. These distances vanish when the experiment is repeated in presence of ATP [53]. It is likely representing an partially unfolded or a low affinity oligomeric state of Hsp90 being populated in absence of nucleotides, which is thus not accessed by smFRET experiments at picomolar concentrations.

As already mentioned, the structural ensemble that is resolved here represents the most likely trajectory on which Hsp90 fluctuates, with the different domains fluctuating on different timescales mostly independent. A comparison between the open and closed Hsp90 in terms of their respective energy landscape is given in Fig. 3.14. While the closed state of Hsp90 is a well-defined and rigid structure, the open state exhibits a broadened energy minimum enabling the large fluctuations on fast timescales. The motions of the different motifs and domain that we found are probably the explanation of a much larger overall dwell time of the open state found in earlier smFRET studies [27, 113], which lies on the timescale of seconds. The different domains must all be in their right orientation for the transition into the closed state of Hsp90 to enable Hsp90 the state transition. This joint conditional probability – as a product of all single probabilities – is very low and results in the observed long dwell times.

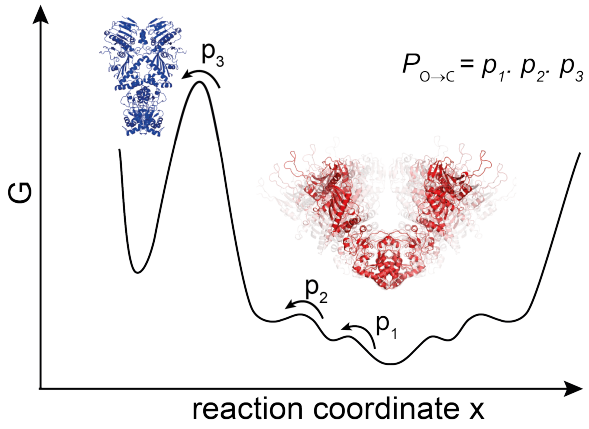

Figure 3.14: The simplified energy landscape of Hsp90. Slow transitions between a rigid and confined closed state (blue, left), which is weakly populated in absence, but nearly completely populated in presence of AMP-PNP and a highly dynamic and flexible open state (red, right), which exhibits fluctuations on the (sub-)millisecond timescale between different substrates within its rough energy landscape. The transitions are slow due to the low conditional probability $P_{O\to C}$ as the product of the probabilities of all single motifs and domains being in their right configuration.

It should be noted that within our study of the data, we found an additional aspect and an advantage of investigations on proteins' structure by smFRET. The combined anisotropy r_c is found to represent a very sensitive sensor to local rearrangements correlating with global conformational changes. This rearrangements could be either changes in the AV of the dye or in the polarity of the surrounding protein surface, as described in detail in [3].

3.1.5 Opening of Hsp90 exposes amino acids involved in client binding

Hsp90 is a chaperone and hence interacts with (partially) unfolded proteins. A fragment from *Staphylococcus* nuclease, Δ131Δ remains in solution in an unfolded but not aggregation-prone state [146]. It has been used in other studies as a model client protein to Hsp90 [147,

148].

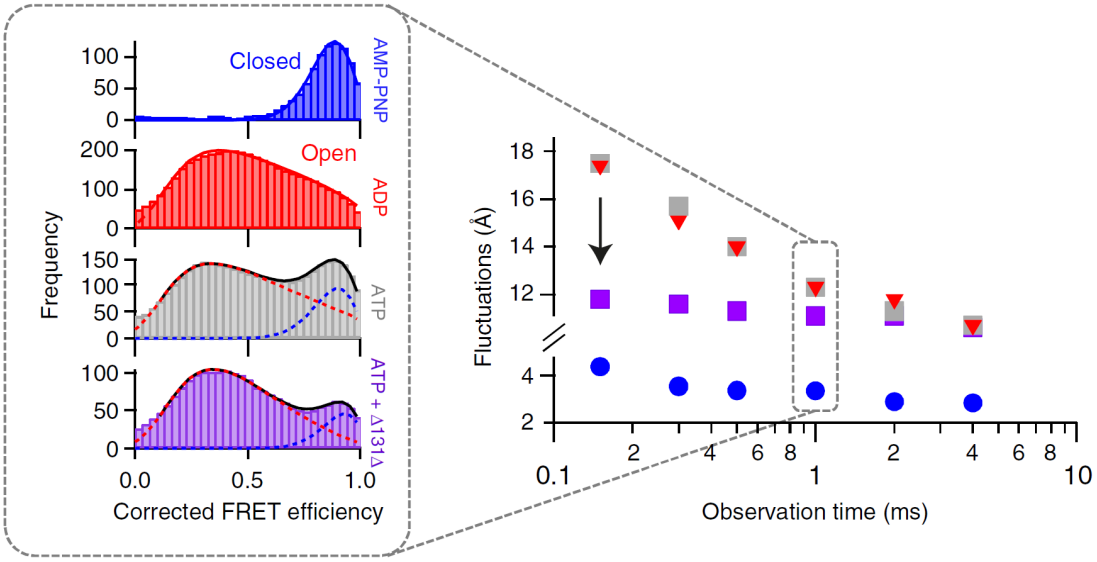

Figure 3.15: The effect of Δ131Δ(20 μM) in combination with ATP (2 mM) on the fluctuations of Hsp90 in the open conformation. Sub-ms fluctuations of Hsp90's open state are dampened by the client protein (as indicated by the arrow). The amplitude of the fluctuation at 100 μs is decreased by 6 Å. This hints towards a previously unknown kind of interaction between Hsp90 and client protein.

The addition of Δ131Δ[14], affects the dynamics of the structural ensemble representing the open state of Hsp90. Interestingly, it suppresses the fast, sub-millisecond inter-monomer fluctuations. Co-chaperones modify the Hsp90 kinetics on a slower timescale, observed by population shifts between the FRET peaks [107]. This allows Hsp90 two interaction modes that are separated by their timescales and can act independently on Hsp90. It furthermore emphasizes that the binding and dissociation of client proteins to/from Hsp90 is independent of the ATPase activity (as it is the finding for the conformational transitions of Hsp90 between the open and the closed state [27]), because the timescales of the interactions with the client protein and the ATPase differ by five orders of magnitude. Nevertheless, it remains unclear from these experiments, *where* on the Hsp90 surface the interaction takes place, *how* the interaction dampens Hsp90's fluctuations and *how* the interaction affects the client protein itself.

Δ131Δ has been reported to bind to the inner dimer interface of Hsp90 [147]. The open state of Hsp90, as resolved by smFRET, leads to the exposure of several amino acids and motifs to the solvent, which are in consequence accessible to client proteins. Namely, a loop within the C-terminus, which was not resolved in the X-ray crystal structure of closed Hsp90 (aa 595-610 in yeast Hsp90). From the crystal structures of homologues, it seems that this structure is able to undergo transitions between a random-coil and an α-helix, and it could possibly interact with the protomer in *cis* or in *trans*. It could adopt to different interaction partners as well, exposing different kind of amino acids (e.g. charged

14 The construct of Δ131Δ was kindly provided by the group of David A. Agard, UCSF, San Francisco, USA (`http://www.msg.ucsf.edu/agard/` [March 2017]) and expressed and purified by Markus Götz.

or hydrophobic ones) for each interaction. This would enable Hsp90 to interact with the very broad range of client proteins and in return enable client proteins to stabilize Hsp90's conformations, explaining the dampening of Hsp90's fluctuations in its open state. This loop might represent one binding motif for the model client and a promising target for further studies.

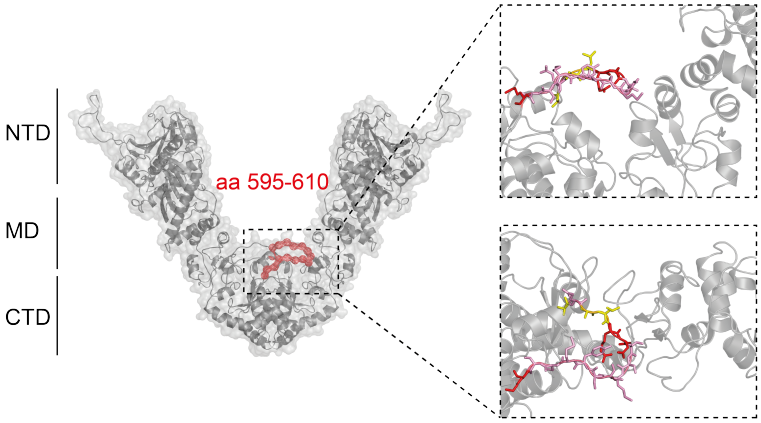

Figure 3.16: A C-terminal loop is exposed in the open structure of Hsp90. It can make contact with the Hsp90 protomers in *cis* or *trans*, but would also be accessible to client proteins binding to Hsp90. In the zoom on the right, charged amino acids are shown in red, hydrophobic in yellow, hydrophilic in pink.

Our findings suggest that the ATPase activity of Hsp90 is not essential for the structural dynamics of Hsp90. If ATP hydrolysis was affecting one of the observed, fast transitions, most of the energy from hydrolysis would dissipate, rendering it useless. Thus, our findings imply that the ATPase function is not relevant for the global structural rearrangement of Hsp90 at all. Additionally, it may not be essential for the binding of client proteins and also not for chaperoning of those clients, because we find the interaction with $\Delta 131\Delta$ affecting much faster timescales as well.

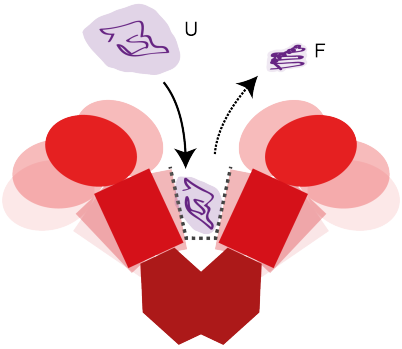

Figure 3.17: The possible function of Hsp90 (red) as a chaperone, which confines the volume accessible to weakly bound unfolded clients (purple, U: unfolded), facilitating and accelerating the correct folding (F: folded) of the protein similar to a function attributed to the 'cage' GroEL/ES constitute.

A recent study on the chaperone system of GroEL/ES proposed the combined effects of steric confinement and charged cavity wall functioning cooperatively on the correct folding

of substrates [149], with the latter linked to ATPase and thus active refolding activity. No evidence for active refolding mechanisms by isolated Hsp90 is found in this study, but the idea of steric confinement would also apply on this system. The way Hsp90 could achieve this steric confinement with respect to the client protein is just not as straight-forward as it is for a structural 'cage' as it is constituted by GroEL/ES. The large and fast fluctuations of Hsp90 essentially have a similar effect, reducing the average space accessible to a bound client protein and thereby facilitating (re-)folding (c.f. Fig. 3.17). One main advantage of Hsp90's function in this context was ability to chaperone client proteins of all sizes, while this function of GroEL/ES is restricted by its cage size.

3.1.6 Summary

Our method reproduces the X-ray crystal structure of closed, AMP-PNP bound Hsp90 with an RMSD 2.8 Å. The large number of FRET pairs (and hence distances), as well as the separate determination of the Förster radii R_0 increases the accuracy of our method compared to previous studies significantly.

The determination of the individual FRET efficiency correction factors and their validation within the network additionally increases the accuracy of our method. The dependency of the RMSD between our data and the crystal structure on the time-resolved anisotropies of the respective FRET pair is used to derive the criterion based on the combined anisotropy r_c, which represents the anisotropy during energy transfer. It rectifies the assumption of average random dipole orientation for each FRET pair separately and therefore allows to detect and remove wrong distances from the data. The deviation of our smFRET derived distances from the distances in the crystal structure lies within the structure's uncertainty itself and could possibly hint towards slight reorientation of the protein structure in a crystal. Thus, smFRET has finally become an appropriate and reliable tool to resolve the three-dimensional structure of multi-domain proteins in solution.

Open Hsp90 fluctuates with a very large amplitude of up to 12 Å at the timescale of milliseconds. The amplitude of the inter-protomer fluctuations increases from the C- to the N-terminus of the protein and fluctuations shift to faster timescales. The CTDs function as anchors of the two protomers and do not change their interface significantly. Fluctuations within one protomer are mainly observed between the NTD and MD of Hsp90.

Unlike the rigid structure of closed Hsp90, open Hsp90 exists as an ensemble of conformations. This ensemble is resolved by our smFRET network. The structures represent the most likely trajectory on which Hsp90 fluctuates.

The motions of the different motifs and domains are probably the explanation of a much larger overall dwell time of the open state found in earlier smFRET studies [27, 113], because the joint probability for all domains and motifs being in the right orientation for a state transition is very low. Our data enables us to explain the variety of different crystal structures published for Hsp90 homologues – these structures lie within the trajectory of the fluctuations and are thus most likely snapshots of the conformational ensemble.

Our findings provide the basis for an understanding of the diverse interactions of Hsp90 with its client proteins and co-chaperones and their interplay, on a structural level. Although these interactions have extensively been studied [30, 31, 53, 54], the knowledge of the structure of Hsp90 and hence the state-dependent localization of recognition patterns enables a much better understanding of the function of the Hsp90 machine. E.g. the introduced network of label positions on Hsp90s structure allows for structural investigation

of the transient interaction complexes between Hsp90 and co-chaperones like Sba1 or Aha1 in the future, from which only fragments are known [18, 62].

We could not find any direct link between structural rearrangements of Hsp90 and its ATPase activity, similar to the results from earlier studies [27, 99]. On the contrary, Hsp90's ATP independent dynamics occur on even faster timescales. This suggests that the ATPase activity is not essential for the global structural rearrangement of Hsp90, and it may not be essential for the interaction with client proteins. Hsp90 might therefore fulfill its role as a chaperone in a mainly ATP-independent way and in a manner that is similar to one assumed for the GroEL/ES chaperone system.

3.2 Cooperativity in Hsp90

As an ATP binding and hydrolyzing homodimer, Hsp90 is in principle capable of binding two nucleotides at the same time. As pointed out in the introduction, no cooperativity between the two protomers of Hsp90 concerning ATP binding and/or hydrolysis has been detected in ensemble experiments [40, 150].

However, the weak affinities of Hsp90 to nucleotides and its very slow ATPase activity complicate biochemical studies on the inter-dimer communication. Hence, weak effects are likely to stay hidden in ensemble data such as the previously published. Single molecule experiments can give a more detailed view onto the mechanisms of Hsp90, thus it is a reasonable idea to probe the nucleotide binding properties of Hsp90 by smFRET.

In this chapter I present the results from my work together with Markus Götz on the nucleotide binding properties of Hsp90. We develop a method that resolves the structure and the nucleotide binding state of Hsp90 simultaneously. The effect of unlabeled nucleotides, co-chaperones and the type of nucleotide is presented.

Most of this work has been published in:

Götz, Markus, Philipp. Wortmann, et al.: 'A Multicolor Single-Molecule FRET Approach to Study Protein Dynamics and Interactions Simultaneously'. *Methods in enzymology* (2016), vol. 581: pp. 487–516

Wortmann, Philipp, Markus Götz, and Thorsten Hugel: 'Cooperative nucleotide binding in Hsp90 and the underlying mechanisms'. *bioRxiv* (2017), vol. DOI:10.1101/113191

3.2.1 A fluorescent nucleotide analogue binding specific to Hsp90

In order to study the nucleotide binding on Hsp90 directly, one has to be able to report on the absence or presence of nucleotide. Nucleotide analogs labeled with a fluorescent dye open up the opportunity to study the binding and dissociation of nucleotide.

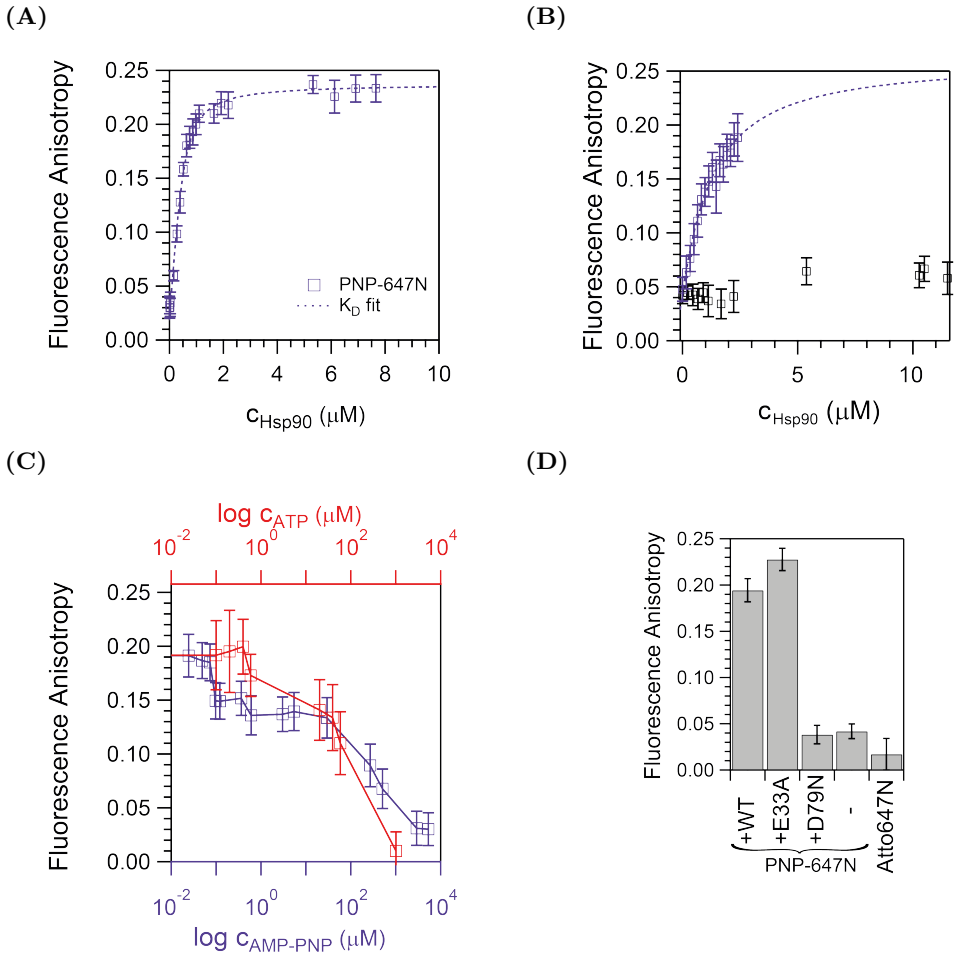

Figure 3.18: The fluorescent nucleotide analog AMP-PNP-647N binds specifically with high affinity to Hsp90. (A), titration of Hsp90 to 500 nM AMP-PNP647N, monitored by fluorescence anisotropy. (B), no binding of labeled nucleotide to Hsp90 D79N (black) is detected in comparison to the binding of wild-type (blue). (C), competition of 500 nM labeled nucleotide bound to 1 μM Hsp90 by unlabeled AMP-PNP or ATP . (D), the fluorescence anisotropy of bound/free labeled nucleotide compared with the anisotropy of the dye. The point mutant Hsp90 E33A binds AMP-PNP647N similar to wild-type (WT), Hsp90 D79N does not bind to the nucleotide.

Several nucleotide analogs are characterized (detailed in Appendix B.1.1) in terms of their binding properties. Binding to Hsp90 is monitored by measuring the fluorescence anisotropy of the respective dye covalently coupled to the nucleotide in bulk. The anisotropy measured in a fluorescence spectrometer mainly reports on the timescale of rotational motions of the fluorescent molecule. The small labeled nucleotide alone results in a very small fluorescence anisotropy of $r_\infty = 0.05 \pm 0.01$, slightly larger than the one measured of fluorescent dyes alone. Binding to the 180 kDa Hsp90 dimer results in a large increase of

fluorescence anisotropy, as the overall molecule exhibits much slower motions.

The nucleotide AMP-PNP labeled at the γ-Phosphate with the dye Atto647N, AMP-γ-(6-Aminohexyl)-PNP-Atto647N (PNP*) is chosen for further investigations. It is derived from the transition analog of ATP, AMP-PNP, which is not hydrolyzed by Hsp90 (demonstrated in Appendix B.3, p. 118). Thus, we can exclude effects from hydrolysis on all subsequently measured data. It binds with high affinity to Hsp90, as shown in the titration experiment with Hsp90 (see Fig. 3.18(A)) - which results in a dissociation constant estimate of K_d=119±15 nM (assuming two nucleotides binding to one Hsp90 dimer). It binds specifically into the nucleotide binding pocket of Hsp90 with contacts to the same amino acid side chains as the native nucleotide. The single point mutation D79N does not exhibit binding of AMP-PNP-647N in the studied concentration regime, thus its K_d is significantly (by at least two magnitudes) increased, while the point mutation E33A marginally affects binding (c.f. Figs. 3.18(B) and 3.18(D)). These experiments with the fluorescent labeled nucleotide resemble experimental data on the native substrate [20, 29, 151]. The specific binding is further supported by our finding that the addition of native ATP or unlabeled AMP-PNP displaces it from Hsp90, with a kinetic faster than the time resolution of the titration experiment, which is about 5-10 seconds. The on-rate of another fluorescent nucleotide analog has been found to be in the range of a second [36, 152]. The binding of PNP* to Hsp90 is characterized by a much higher affinity than the affinity of Hsp90 for native nucleotide. As shown in the competition experiment in Fig. 3.18(C), the affinity of Hsp90 for the labeled AMP-PNP is about two orders of magnitude higher than the one for native nucleotide. Although the literature on the K_d between Hsp90 and nucleotides is ambiguous with a reported K_d for e.g. AMP-PNP in the range of 60 μM (c.f. Table B.1 on page 114), a K_d of about 10 μM would fit the finding in our competition experiment.

We chose the γ-phosphate labeled nucleotide for further experiments due to the advantageous high affinity. A nucleotide that binds Hsp90 with great affinity is much more suitable for single molecule experiments, because lower concentrations of labeled species can be used, which reduces the fluorescent background distorting the data and complicating evaluation otherwise (if possible at all).

3.2.2 Multi-color smFRET resolves Hsp90's conformation and binding state simultaneously

The binding and dissociation kinetics of nucleotide to and from Hsp90 depend on the conformation of Hsp90 [99]. Therefore, we study the interaction of Hsp90 with nucleotide by a three-color smFRET approach that enables us to track the nucleotide binding state and discriminate the conformations of Hsp90 at the same time.

Three-color smFRET measurements with Hsp90 immobilized on the surface of a flow chamber are performed on a prism-type TIRF, as described in Section 2.1.1, page 20. The binding and dissociation of labeled nucleotide is monitored by the fluorescence of the reporter nucleotide AMP-PNP-Atto647N characterized above (further on abbreviated as PNP*). We use 25 nM PNP*, which is about one order of magnitude below the previously found K_d. Thus, only the binding and dissociation of exactly one PNP* is accessed in all subsequent experiments.

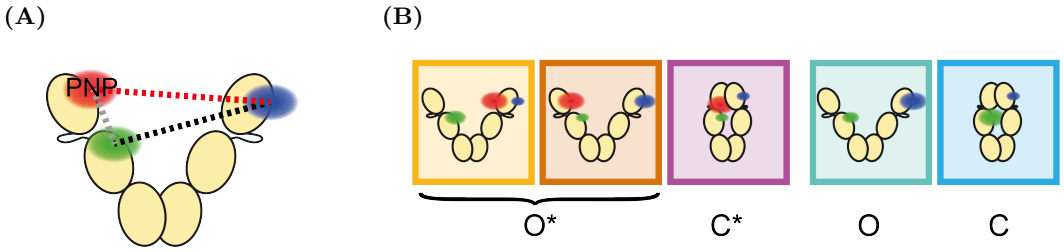

Figure 3.19: Pictogram of the studied system. (A), Hsp90 is labeled at its protomers with two different dyes, Atto488 (blue) at aa 61 and Atto550 at aa 385; AMP-PNP-647N is present in solution at 25 nM. (B), the different states the system can populate: Open and closed Hsp90 in absence of nucleotide (O, C) and open and closed Hsp90 with one nucleotide bound (O^*, C^*). The functional state O^* can appear in two different orientations of the labels.

Simultaneously, we track the global conformation of Hsp90 by FRET between Atto488 attached to the NTD of one protomer at amino acid position 61 and Atto550 attached to the MD of the other, at amino acid position 385. These two positions have been used in several other studies to track the conformational change of Hsp90 [27, 64, 99, 113] and do not exhibit strong effects of the label and attachment site on the ATPase activity of Hsp90.[15] Absence and presence of the reporter nucleotide is detected by red fluorescence after energy transfer from one of the dyes attached to Hsp90. Because Hsp90 labeled at the depicted positions populates two FRET peaks (i.e. one low-FRET and one high-FRET peak, referred to as 'open' and 'closed' state) and could bind a nucleotide in both states, we expect five different arrangements of protein and nucleotide. These can be separated by their different fluorescence intensity ratios due to the Förster energy transfer in between, i.e. the partial fluorescence. The partial fluorescence represents the ratio of fluorescent light detected after excitation at one wavelength, with PF_{em}^{ex} [16]. It is the multi-dimensional equivalent to the FRET efficiency and thus a proxy for the inter-dye distance in a multi-dye system. The different states are depicted in Fig. 3.19.

We use alternating laser excitation of the blue and green dye in order to completely determine the system, which would not be the case at single excitation of the blue fluorophore. An additional excitation of the red fluorophore is not possible, because the fluorescence after direct excitation at the used dye concentration saturates the detection camera chip and thus does result in additional information. Nevertheless, the red fluorophore we use has been found to be the most photostable dye within the experiment and therefore effects from its bleaching on the data are neglected. We can then calculate three different fluorescence intensity ratios per frame, i.e. the partial fluorescences PF_g^b, PF_r^b and PF_r^g from our data. An exemplary fluorescence trace and the resulting PFs are shown in Fig. 3.20.

The complete data set results in a three dimensional space of partial fluorescence, which we use to separate the different states. State populations are assigned by hand on 2D-projections, as described in Section 2.3.2 (p. 33). The complete three-dimensional data is then fitted by the sum of five Gaussians keeping the relative populations (i.e., the Gaussian's volumes) fixed. The fit is further used as basis for the allocation of the states in each traces by an ensemble HMM (shown in Fig. 3.21). This data evaluation allows

15 This is demonstrated in Appendix B.3 on page 118.
16 see Section 2.3.1 on page 28 for details on the calculation.

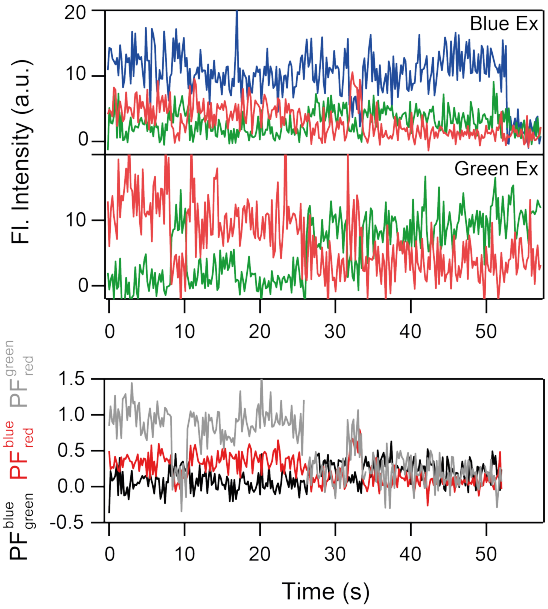

Figure 3.20: Fluorescence traces from one exemplary single particle measured by three-color smFRET. The immobilized particle is excited alternating with blue and green lasers and fluorescence is recorded. From the fluorescence traces, the three PFs are calculated for the range, where neither the blue nor the green dye is bleached. In this case, the blue dye bleaches after 52 s.

(A) **(B)**

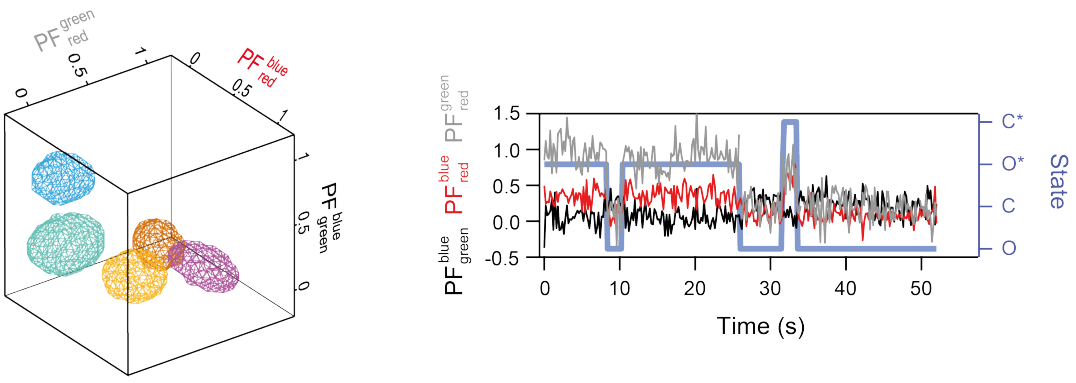

Figure 3.21: State assignment and allocation. (A), using the partial fluorescence data, the state populations are assigned by hand, as described in Section 2.3.2, p. 33, and fitted by 3D Gaussians (full-width at halft maximum representation). Color code is the same as in Fig. 3.19. (B), all partial fluorescence traces are allocated by an HMM with the emission parameters derived from the Gaussian fits. It is here shown exemplary on the fluorescence trace presented in Fig. 3.20.

us to separate the different conformational states of Hsp90 in absence and presence of bound nucleotide. Although increasing the resolution by the correlated information on the conformational and nucleotide binding state of Hsp90, we lose the ability to resolve the states of Hsp90, which are hidden behind the FRET between the two positions in Hsp90. Hsp90 is known to populate four states, from which two states can only be recovered by their kinetics [113].

3.2.3 Cooperativity between the nucleotide binding sites of Hsp90

Being able to resolve the five different states representing four functionally different states, we use our assay to address the question, whether the presence of a second, unlabeled and native nucleotide (ATP or AMP-PNP) in the experiment has effects on the interaction between the labeled reporter nucleotide PNP* and Hsp90 (i.e., the corresponding kinetics). Thus, the three-color smFRET experiment described above is repeated in the presence of 250 μM unlabeled, native nucleotide.

Because we simplify the data evaluation by only selecting for traces, which exhibit at least one binding event of the reporter nucleotide (i.e. red fluorescence after blue or green excitation), the results are not completely representative for the studied system. The populations of nucleotide free Hsp90 (O and C), as well as their off-rates are likely biased by the data selection process. To circumvent this problem, we concentrate on the evaluation of the processes, where PNP* is involved: the ratio between the nucleotide bound Hsp90 in the open and the closed conformation (O^*/C^*), and the transitions between C^* and O^*, as well as the dissociation of PNP* from O^* or C^*.

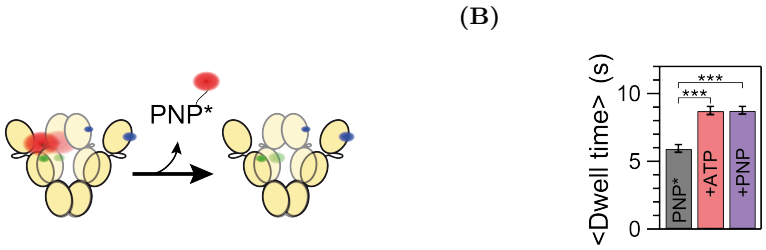

Figure 3.22: The presence of ATP or AMP-PNP increases the dwell time of PNP* on Hsp90. (A), the dwells of PNP* on Hsp90 are summed, ignoring the distinct conformations Hsp90 populates. (B), the average dwell time of PNP* in absence and in presence 250 μM ATP or AMP-PNP. Error bars represent s.d. calculated by jackknife-1. (*** : $p < 0.001$ by Wilcoxon sum rank test (detailed results shown in Appendix B.5.4, p. 122)).

A first proxy for general effects is the overall average dwell time of PNP* on Hsp90 (c.f. Fig. 3.22(A)). If the two nucleotide binding pockets were independent of each other (as it was concluded in prior research from ensemble titration experiments monitoring the change of intrinsic fluorescence in Hp90 [40]) the addition of native nucleotide would only affect the association of PNP* with Hsp90 by competition, but not the dissociation. We simplify the states allocated by the HMM to a two state system, i.e. the states PNP*-bound and PNP*-free for the evaluation. Surprisingly, we find the average dwell time of PNP* on Hsp90 (5.9±0.3 s) increased by more than 50 % to 8.8±0.3 s when ATP is present (Fig. 3.22(B)). This effect is resembled also in presence of AMP-PNP instead of ATP, underlying that it is due to binding of the second nucleotide and not due to its hydrolysis. This effect is not introduced into the data by different lengths of the smFRET traces due to different bleaching times (c.f. Table B.3, page 121 for a comparison of bleaching times). Hence, the

only property that is changed between the experiments is the probability of the second binding pockets being occupied (from a probability of zero to aproximately one). The experiment demonstrates that the presence of a second nucleotide on the Hsp90 dimer decreases the apparent overall dissociation probability of the reporter nucleotide PNP*. Thus, the two nucleotide binding pockets are not independent of each other, but they act cooperative in nucleotide binding.

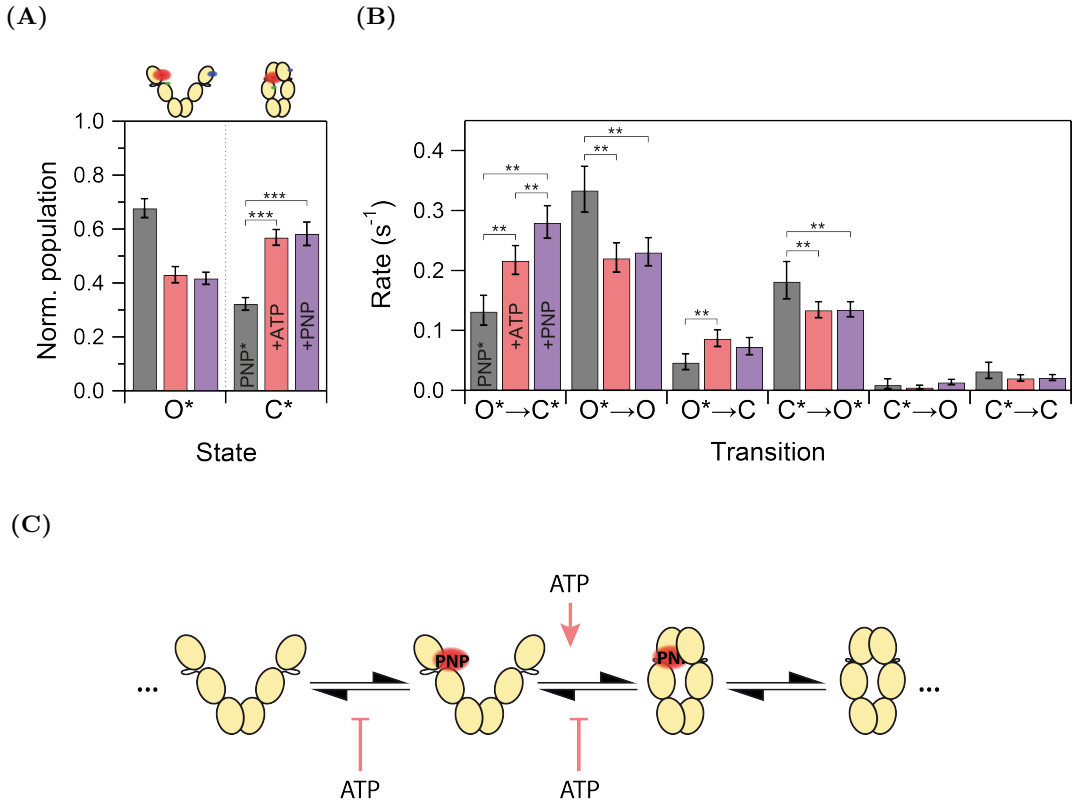

Figure 3.23: Effects of ATP and AMP-PNP on the conformational equilibrium of Hsp90/PNP* and on the rates of state transitions. (A), the equilibrium between O^* and C^* is affected by additional nucleotide. Error bars represent the s.d. calculated from ten random subsets comprising 75 % of all data points. (*** : $p < 0.001$, by t-test (results are summarized in Appendix B.5.6, p. 125)). (B), rates for the respective state transition. Error bars represent the 99 % CI. (** : $p < 0.01$). (C), a minimal model for the state transitions of Hsp90 in presence of PNP* and the effects of ATP on it (which are resembled by AMP-PNP). Only the most likely, step-wise transitions are shown. ATP increases the closing rate of Hsp90 with PNP* bound, and decelerates the reverse reaction, as well as the dissociation of AMP-PNP*.

The evaluation of the population ratio between the PNP* bound Hsp90 conformations gives further insight into the complex interaction. In Fig. 3.23(A) it is shown that the ratio of Hsp90 with PNP* bound in the open and the closed state (O^*/C^*) is shifted towards the closed state in the presence of additional nucleotide. Again, AMP-PNP resembles the effect of ATP, as already observed for their effect on the dwell time. However, the mechanism(s) underlying these effects remain unclear at this stage. The increase in the population of C^* could be due to an increase in the rates leading to this state or due to a decrease in the rates depopulating this state. Accordingly, the increase in the average dwell time of bound PNP* may be caused by the shift from O^* to C^* (which has a slower off-rate for PNP* and

thus could explain the observed effect) or by a decrease in the dissociation rate from O^* - or by a combination of both. Only a complete kinetic description can provide information about the actual mechanism mediating cooperativity in Hsp90. For a multi-state system consisting of the dynamic Hsp90 and the nucleotide PNP*, this is to date only possible by a single molecule approach that takes advantage of the full kinetic resolution achievable by HMM analysis.

The microscopic rates for the studied system consisting of Hsp90 and PNP* are resolved as described in Section 2.3.3, page 33. Fig. 3.23(B) shows that additional nucleotide affects the nucleotide dissociation and the conformational transitions differently. On the one hand, additional nucleotide decreases the rates for PNP* dissociation from both conformational states of Hsp90 ($O^* \rightarrow O$ and, slightly $C^* \rightarrow C$). On the other hand, the equilibrium between O^* and C^* is shifted by both, increasing the rate for closing ($O^* \rightarrow C^*$) and decreasing the rate for opening ($C^* \rightarrow O^*$). The effects of a second nucleotide on the most frequent single state transitions are summarized in Fig. 3.23(C).

Our methods allows us to show for the first time a direct, weak cooperativity between the two nucleotide binding pockets in Hsp90. Remarkebly, this cooperativity is not caused by one nucleotide affecting one single rate, but by the combined effects of the single nucleotide on several rates in the studied system.

Common biochemical approaches to investigate the cooperativity of a ligand binding to a macromolecule (e.g. DNA or protein) study the saturation of binding sites on the macromolecule in a ligand-concentration dependent manner (log-log plot, also known as Hill plot). Especially for dynamic systems, such an approach will only reveal strong cooperativity with a ratio c of the K_d^n/K_d^1 for binding the 1st and n-th ligand above ten, as demonstrated in Appendix B.6 one page 126. This explains the interpretation of previous experiments that studied the interaction of Hsp90 with nucleotides [40], where a cooperativity of a factor of two (as found here) was easily missed.

The observed cooperativity between the nucleotide binding sites explains the effects of point mutations in one of the nucleotide binding pockets of Hsp90 heterodimers on the protein's kinetics. The point mutations D79N and E33A impair nucleotide binding and nucleotide hydrolysis, respectively [151]. In heterodimers, the ATPase activity of Hsp90 varies significantly from the wild-type homodimer [20, 29, 51]. The Michaelis-Menten kinetics of both heterodimers have been characterized in literature [20, 29]. While E33A/WT exhibits a decreased Michaelis-Menten constant $K_M = 140\pm20$ μM, D79N/WT exhibits an increased $K_M = 1000\pm100$ μM, compared to a $K_M(\mathrm{WT}) = 370\pm30$ μM. The K_M value is a measure of the apparent substrate affinity.[17] Thus, the ability to bind nucleotide in one protomer without hydrolysis increases the apparent substrate affinity of the dimer. Vice versa, the inability to bind nucleotide in one protomer decreases the apparent substrate affinity of the dimer.

Our observation of cooperativity among the two nucleotide binding pockets explains this observation nicely. If one binding pocket is occupied by a non-hydrolyzable nucleotide, additional ATP and thus the occupation of the second binding pocket results in a prolonged binding of this nucleotide. This in turn results in an increased population of the closed state by nucleotide-bound Hsp90. The closed state is the conformational prerequisite for

17 The K_M value represents an apparent substrate affinity in case of Hsp90, because Hsp90 populates more than two states and binds nucleotide in at least two of them [99].

hydrolysis, since a correlation between population of the closed conformation of Hsp90 and ATPase rate has been reported [51, 153].

Interestingly, cooperativity among the two nucleotide binding sites has already been suggested for another member of the GHKL class, the DNA gyrase [154]. Therefore, the effects identified here for Hsp90 might play a role in the diverse molecular mechanism GHKL proteins are involved in, e.g. DNA supercoiling or mismatch repair.

3.2.4 The co-chaperone Aha1 modulates the cooperativity

Hsp90's function *in vivo* is regulated by co-chaperones. Among those, Aha1 (detailed in Section 1.2.3, p. 7) exhibits the strongest positive effect in ensemble experiments, increasing the ATPase activity of Hsp90 by more than tenfold [60]. ATP binding is the prerequisite for its hydrolysis, and in the previous section we could demonstrate that this step involves cooperativity. Thus, by investigating the effects of Aha1 on the cooperativity, we aim to address the question for a possible coupling between nucleotide binding and hydrolysis. We repeat the three-color smFRET assay with 10 μM Aha1, and 10 μM Aha1 + 250 μM ATP to study the effects of the co-chaperone on the dwell time of PNP* on Hsp90 and the population ratio of nucleotide bound Hsp90 (O^*/C^*).

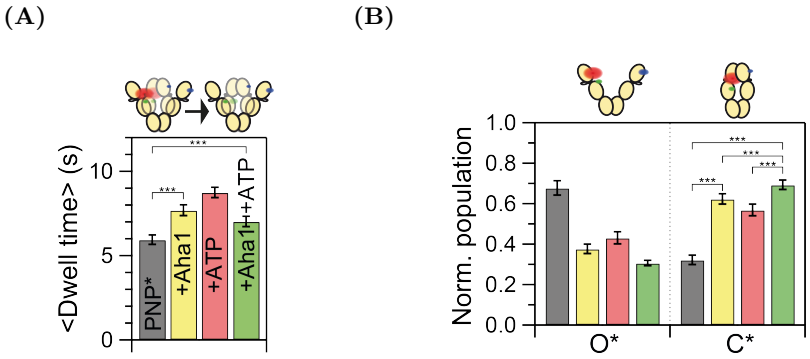

Figure 3.24: Aha1 affects the average dwell time of PNP* on Hsp90 and the equilibrium between open and closed, PNP*-bound Hsp90. However, the effects of ATP and Aha1 do not accumulate. (A), the average dwell time of PNP* on Hsp90 in absence and in presence of Aha1 and/or ATP. (B), the equilibrium between open and closed Hsp90 with PNP* bound (O^* and C^*) at the same conditions, the color code is the same as in (A). (*** : $p < 0.001$).

In absence of additional ATP, Aha1 alone already increases the mean dwell time of the reporter nucleotide bound Hsp90 from 5.9±0.3 s to 7.7±0.3 s (Fig. 3.24(A)). This would suggest that both Aha1 and the nucleotide cooperativity work in conjunction towards an increased dwell time and therefore ATPase rate. On the contrary, we find the combination of Aha1 and ATP increasing the dwell time of PNP* (7.0±0.3 s) to a lesser degree than either Aha1 or ATP do. Thus, the effects of ATP and Aha1 are not simply additive.

Another interesting fact in this context is our finding from the ensemble experiment on the effect of Aha1 on the interaction of PNP* with Hsp90 studied by fluorescence anisotropy monitored titration (Appendix B.1.5, p. 117). In this assay the overall affinity of Hsp90 for the nucleotide is decreased, thus the on-rate of Hsp90 must decrease in presence of Aha1 even further than the off-rate increases in absence of ATP.

(A)

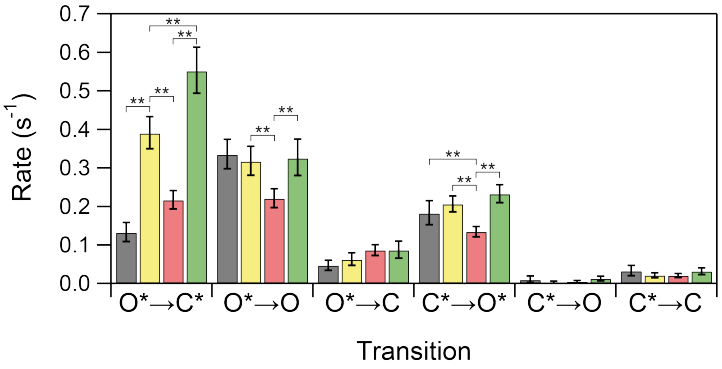

(B)

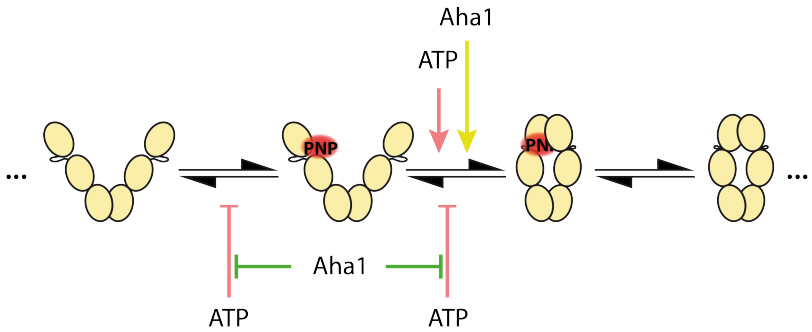

Figure 3.25: Effects of Aha1 and Aha1+ATP on the transition rates. (A), rates for the respective state transition of Hsp90/PNP* in presence of ATP, Aha1 and both together. Error bars represent the 99 % CI. (** : $p < 0.01$) (B), a minimal model for the state transitions of Hsp90 in presence of PNP* and the effects of ATP, Aha1 and the combination of both on it. Only the most likely, step-wise transitions are shown. Aha1 increases the closing rate of Hsp90 with PNP* bound by affecting an ATP-independent process, therefore both co-chaperone and ATP work synergistic on this transition. The other effects of ATP on Hsp90/PNP* are inhibited by Aha1, thus the affected processes interfere.

The complexity of the system consisting of Hsp90, PNP*, ATP and Aha1 is further demonstrated by our findings on the state populations. We find the O^*/C^* ratio of nucleotide bound Hsp90 shifted towards the C^* state by the addition of Aha1 (c.f. Fig. 3.24(B)). In contrast to our findings for the dwell times, the combination of ATP and Aha1 leads to a more pronounced effect on the O^*/C^* ratio than each of them separately – although their effects do not add up linearly. In conclusion, this first data evaluation demonstrates that Aha1 and ATP affect independent processes of Hsp90, which interfere with each other.

Again, we apply an HMM analysis on the three-color smFRET data in order to gain detailed information on the microscopic mechanisms causing our observations. We find Aha1 accelerating the closing transition of PNP* bound Hsp90 ($O^* \rightarrow C^*$) stronger than ATP. In the combination with ATP, this effect from both adds up. In the experiment combining ATP and Aha1, the opening transition of PNP* bound Hsp90 ($C^* \rightarrow O^*$) and the dissociation of PNP* from open Hsp90 ($O^* \rightarrow O$) exhibit rates similar to those found in absence of both. Hence, Aha1 attenuates the decelerating effects ATP has on these transitions. The picture that emerges from our detailed HMM analysis on the complex interaction between Hsp90, PNP* and ATP/Aha1 is shown schematically in Fig. 3.25(B).

ATP and Aha1 work both separately and together on the closing transition of PNP* bound Hsp90 ($O^* \rightarrow C^*$), while Aha1 prevents ATP from its rate-decelerating effects on the transitions $C^* \rightarrow O^*$ and $O^* \rightarrow O$.

Because the concentration of Aha1 in our experiments is above the reported K_d for the interaction with Hsp90 [60, 61], we conclude that it exerts its full potential already in absence of ATP - therefore ATP and Aha1 must act independently on different motifs in Hsp90.

We have identified the effects of nucleotides and Aha1 on the microscopic state transitions, but the actual molecular mechanisms that cause these effects remain hidden. However, some structural data and mutational analysis offer explanations, *how* nucleotide and co-chaperone achieve their effects. The motifs we find most likely to be affected are shown in Fig. 3.26.

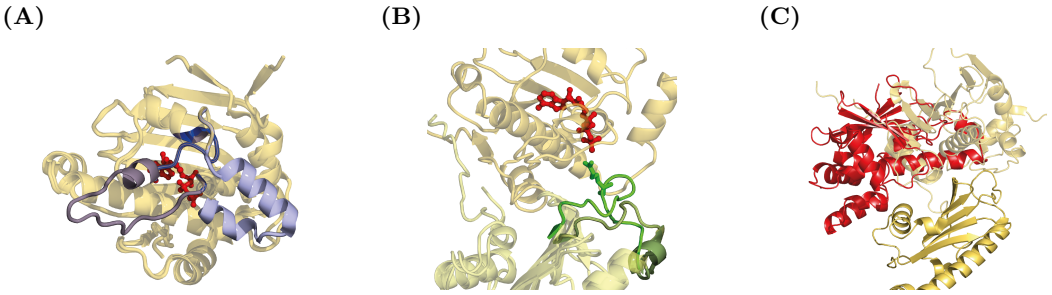

Figure 3.26: Local motifs that are likely affected by nucleotides and co-chaperones. (A), The ATP-lid (blue) can switch between an open and closed conformation (superposition of PDB 2cg9 and 2wep [18, 34]). (B), Aha1 affects the catalytic loop (green), which can form a bond via Arg_{380} with the γ-phosphate of AMP-PNP (superposition of PDB 2cg9 and 1osv [62]). (C), the arrangement between Hsp90's NTD and MD changes between its open (red) and closed state.

Nucleotide binding will first of all affect the ATP-lid of Hsp90. Effects on the fluctuations have been found by dynamic quenching experiments [33]. A mainly open lid is found in the isolated N-domain, as well as in presence of ATP or ADP, while only in the closed, AMP-PNP bound X-ray crystal structure the lid is closed [18, 34]. A higher propensity of each Hsp90 protomer having a closed ATP-lid might facilitate the correct arrangement of the NTD and MD and thus accelerate the closing and decelerate the opening. Because the Hsp90 protomers can have steric contacts in the open state (c.f. Section 3.1, page 49) that could also contribute to the decreased dissociation of labeled nucleotide from the open state.

Aha1 has been found to bind Hsp90 preferentially in an asymmetric complex, interacting with both, the NTD and the MD of Hsp90 [32]. Dimer exchange experiments have found an accelerated closing of Hsp90 [51], where Aha1 shifts Hsp90 towards the closed state in analytical UC experiments [155]. The X-ray crystal structure of the MD of Hsp90 and the NTD of Aha1 suggests that Aha1 affects the orientation of the catalytic loop (ca. aa 375-385) of Hsp90 [62] and thereby accelerates the transition. This was then the independent motif, which Aha1 affects working together with the nucleotide's effect on the ATP-lid. Aha1 accelerates the ATP-lid opening in constructs comprising the NTD and MD of Hsp90 [33]. Thus, in the mostly isolated NTD/MD of the open Hsp90 state, it could prevent the effect of ATP on the *trans* nucleotide binding site that we observe. Nevertheless, Aha1 can also affect the NTD/MD arrangement of Hsp90, which promotes

accelerated closing (c.f. Section 3.1, page 49). In addition, Aha1 could also impair the contact of the nucleotide's γ-phosphate with Arg_{380} within the catalytic loop (in closed Hsp90 [18]) that stabilizes closed Hsp90 [156] together with ATP/AMP-PNP.

Our data also gives an insight into the meaning of Aha1 to Hsp90. Aha1 seems not to work in the fashion of a typical enzyme (defined as biological catalyst) on Hsp90 and PNP*, because it affects only one rate. A catalyst would decrease the energy of the transition state, increasing forward and backward rate with the same factor. Instead, Aha1 increases only the rate $C^* \rightarrow O^*$, but not $O^* \rightarrow C^*$ and thus shifts the equilibrium. Interestingly, such a deviation from enzyme characteristics has already been reported for the co-chaperone Sba1 as well [100].

3.2.5 The co-chaperone Sba1 diminishes the cooperativity

To test, whether the effects we characterized for Aha1 on the cooperativity are a general effect of co-chaperones on this system, we investigate the effects of the co-chaperone Sba1 in our single molecule assay in a next step. Contrary to Aha1, the co-chaperone Sba1 is known to inhibit the ATPase activity of Hsp90 [60] (as detailed in Section 1.2.3, p. 6). We conduct two three-color smFRET experiments. We study labeled Hsp90 and 25 nM PNP* in presence of 10 μM Sba1, and in presence of 10 μM Sba1 + 2.5 mM ATP. The data is analyzed as described above. Because of the smaller number of traces and dwell times, I focus in the following on the effects visible in the dwell times and equilibrium between states.

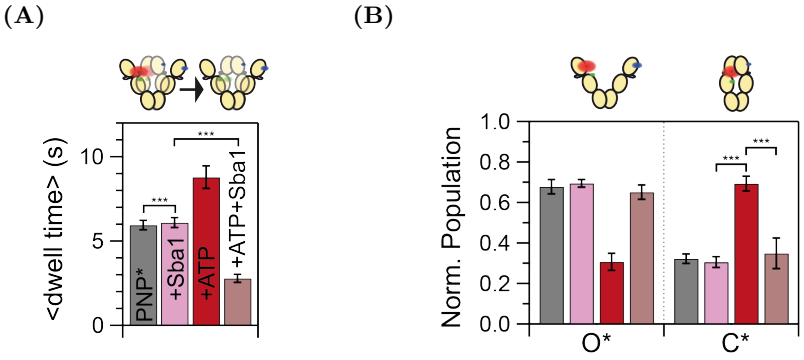

Figure 3.27: Sba1 weakly affect the average dwell time of PNP* on Hsp90, but reverts the cooperativity upon addition of native ATP. (A), the average dwell time of the indicated labeled nucleotide on Hsp90 in absence and in presence of 10 μM Sba1 and 2.5 mM ATP. (B), the equilibrium between open and closed Hsp90 with the nucleotide bound (O^* and C^*) at the same conditions, the color code is the same as in (A). (*** : $p < 0.001$).

The presence of Sba1 alone does not affect the ratio between the states O^* and C^* (Fig. 3.27(B)). The average dwell time of PNP* on Hsp90 (5.9±0.3 s) is only weakly affected (6.1±0.3 s), although the dwell time distributions differ significantly with $p < 0.001$ (Fig. 3.27(A)). This finding goes in hand with the results from a fluorescence anisotropy monitored titration, where no effect of Sba1 on the equilibrium binding (and hence the K_d summed over all weighted conformations) is observed (c.f. Appendix B.1.5, p. 117). The addition of 2.5 mM ATP alone increases the average dwell time of PNP* on Hsp90 to 8.8±0.7 s, similar to the dwell time in presence of 250 μM ATP – it seems the cooperative effect is only slightly increased by full saturation. But this effect is strongly reversed in presence of Sba1, to an average dwell time of 2.8±0.2 s. Nevertheless, the O^*/C^* ratio in presence of Sba1 is

not changed by the addition of ATP.

Our finding that Sba1 does not exhibit a strong effect on the interaction of Hsp90 with one AMP-PNP contradicts ITC experiments, which found a decreased K_d between AMP-PNP and hHsp90 in presence of the human Sba1 homologue p23 [40, 68]. However, these titration experiments were conducted in presence of the reducing agent dithiothreitol (DTT), whose hydrolysis impedes ITC data and likely renders the result useless due to baseline drift.

The effect of Sba1 in absence of nucleotide already differs from the effect found with Aha1, which increases the average dwell time strongly. However, the addition of ATP decreases the overall dwell time of PNP-647N on Hsp90 to a large extend in presence of Sba1. Additionally, the ratio between the two nucleotide bound states, O^* and C^* is not shifted in this case. Thus, the presence of Sba1 and ATP together decreases the affinity of Hsp90 for AMP-PNP - the previously positive cooperativity between PNP* and ATP becomes negative. This is not a competitive effect, because the studied quantity is the dwell time on Hsp90 and competition would affect the on- and not the off-rate.

The effect of Sba1 on the binding and dissociation of labeled ATP, ATP-γ-(6-Aminohexyl)-Atto647N (ATPγO*), has been studied before by multi-color smFRET [99, 100]. Sba1 did not affect the interaction between Hsp90 and nucleotide in the open state, but it increased the mean dwell time on the closed (estimated by a single exponential fit on the cumulative dwell time histogram) from 3.6 s to 9.8 s, which is a factor of 2.7. The average dwell time we find here is a weighted average over the conformations of Hsp90. However, about 30 % of PNP*-bound Hsp90 is in the closed state (C^*), thus if this effect was present within our data to a similar extend, it should be visible by an increase of the average dwell time:

$$< dwell\,time >_{exp} = 30\,\% \cdot 2.7 \cdot 5.9\,s \;+\; 70\,\% \cdot 5.9\,s \;=\; 8.9\,s \tag{3.3}$$

This number is far beyond the error of the characterized average dwell time. Different experimental procedures might contribute to the deviation between our and the published data. Nevertheless, the difference suggests that ATP and AMP-PNP - as well as their labeled analogs - are interacting different with Hsp90. That would also explain the effect of native ATP on the interaction of Hsp90, PNP* and Sba1. In the presence of Sba1, Hsp90 seems to prefer ATP over AMP-PNP. Additionally, the binding of one ATP decreases the dwell time of PNP* on Hsp90. Therefore, Sba1 must recognize Hsp90 bound to one ATP and prevent molecular rearrangements that would increase the binding stability of AMP-PNP once it binds to the second nucleotide binding site. This could be an effect on e.g. the catalytic loop, preventing the Arg_{380} to bind to the γ-phosphate. Additional structural data will be necessary to identify the motifs that mediate this effect of Sba1.

In ITC experiments, Sba1 bound to Hsp90 with increasing affinity to nucleotide-free Hsp90, AMP-PNP bound Hsp90 and ATP-bound closed Hsp90 [66, 68]. Thus, the structural arrangement of Sba1/Hsp90 as in the X-ray crystal structure of AMP-PNP bound closed Hsp90 [18] is not the only conformation of the two proteins' complex. Moreover, these experiments fit to our observation of Hsp90 preferring ATP over AMP-PNP in presence of Sba1. Sba1 exhibits different effects that cannot be explained by a function of just keeping the nucleotide bound ATP-lid closed. Our data suggests that it moreover accelerates the closing and affects the nucleotide binding in *trans*.

ATP single turnover experiments found that Sba1 is a 'late co-chaperone' [62] stabilizing

the post-hydrolysis state [67]. The prolonged presence of ATP post hydrolysis by Sba1 might play a part in the inter-nucleotide binding pocket communication that leads to the decreased dwell-time of AMP-PNP on the *trans* binding site.

3.2.6 Asymmetric binding of nucleotides to Hsp90

The diverse effects of two studied co-chaperones on the cooperativity in Hsp90, as well as the deviation of our findings for the effect of Sba1 from published data, suggest an asymmetry in nucleotide binding between the two nucleotide binding pockets. This asymmetry is further accessed by a combination of ensemble and single molecule experiments, as presented in the following. Three-color single molecule experiment with the same setup as in the experiments presented above, but with ATP instead of AMP-PNP as labeled reporter nucleotide, ATP-γ-(6-Aminohexyl)-imido-Atto647N (ATP*), are conducted.[18] The system is studied in absence of any additive and in presence of 2.5 mM native ATP. Because the number of traces and therefore dwells we find in the data is rather small, the rates have a high uncertainty. Thus, I discuss again only the equilibrium and dwell time effects.

In absence of additional nucleotide, the labeled AMP-PNP has a longer average dwell time on Hsp90 than labeled ATP (4.4±0.4 s), hence AMP-PNP binds longer than ATP (c.f. Fig. 3.28(A)). The population ratio between opened and closed, reporter nucleotide bound Hsp90 (O^* and C^*) is highly similar between the experiments with ATP* and PNP*. While the addition of ATP to PNP* reveals the cooperativity between the two nucleotide

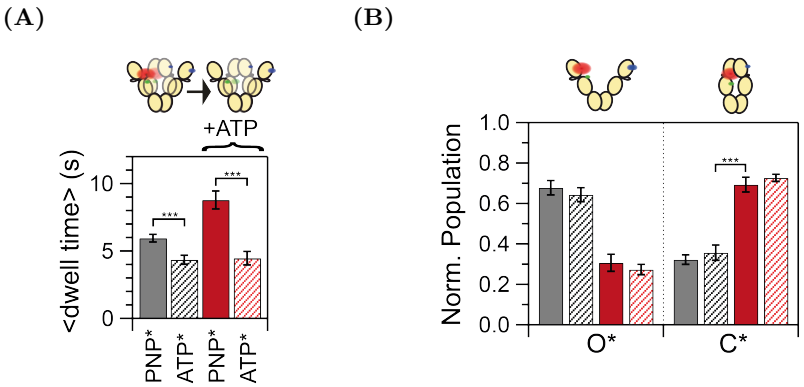

Figure 3.28: ATP and AMP-PNP bind differently to Hsp90 and are differently affected by the addition of ATP. 25 nM ATP-Atto647N (ATP*) or AMP-PNP-647N(PNP*) are measured in the three-color smFRET setup as described before. (A), the average dwell time of the indicated labeled nucleotide in absence and in presence of 2.5 mM (unlabled) ATP. (B), the equilibrium between open and closed Hsp90 with the nucleotide bound (O^* and C^*), the color code is the same as in (A).(*** : $p < 0.001$).

binding pockets by increasing the dwell time of the labeled nucleotide, the situation is different with ATP* as reporter nucleotide, as visible in Fig. 3.28(B). The average dwell time of ATP* is not significantly affected by additional ATP (4.5±0.5 s), but the ratio between O^* and C^* is shifted in the same manner as observed with PNP*. Hence, the direct cooperativity observed with PNP* is not seen with ATP. However, an effect on the equilibrium between the reporter nucleotide bound populations is still detected.

18 Both reporter nucleotides are neither hydrolyzed by Hsp90 (demonstrated in Appendix B.1.3 on page 114).

Thus, the presence of triphosphate nucleotides (AMP-PNP *or* ATP) in both binding pockets increases the closing rate and shifts the equilibrium of Hsp90 towards the closed state. But only the dwell time of AMP-PNP is affected by ATP (or AMP-PNP). Because the cooperativity – in terms of an increased average dwell time of labeled nucleotide – remains hidden with the combination ATP*/ATP, it seems that the AMP-PNP, which resembles the transition state of ATP during hydrolysis, is the origin of this effect. Most likely, the cooperativity is therefore affecting that nucleotide, which is in this transition state. The labeled ATP is not able to enter that state, as it would be hydrolyzed otherwise.

The direct interaction as well as the intramolecular communication are different for ATP and AMP-PNP. The only difference, which can cause these effects is the bridging atom between the β- and the γ-phosphates of the nucleotide, which is a nitrogen in AMP-PNP and an oxygen in ATP. The asymmetry in the HOMO of nitrogen (that has only one electron pair, while oxygen has two) must cause this effect. Because the difference in bond angle and inter-phosphate distance is very small [157], it is most likely the changed charge distribution, which presumably makes a different orientation of the residues within the binding pocket more favorable. This in turn shifts the conformational equilibrium of Hsp90.

The single molecule experiments demonstrate that the two nucleotide bindings pockets are not equal, when ATP and AMP-PNP are bound (which would be an intrinsic asymmetry from their different chemistry), as well as in the case, where two ATP are bound. Nevertheless, is remains unclear, if the binding of two AMP-PNP leads Hsp90 towards a completely symmetric structure. In order to probe this effect, Hsp90 is incubated for 30 minutes at room temperature with an excess of nucleotide (either AMP-PNP or ADP) at 2 mM. As shown earlier in this work (Section 3.1, p. 49), the incubation with AMP-PNP leads to a complete closing of Hsp90 in the conformation found in the X-ray crystal structure (PDB 2cg9). The protein is then step-wise titrated to 500 nM labeled AMP-PNP, and binding of labeled nucleotide to the protein is monitored by fluorescence anisotropy on a spectrometer (shown in Fig. 3.29).

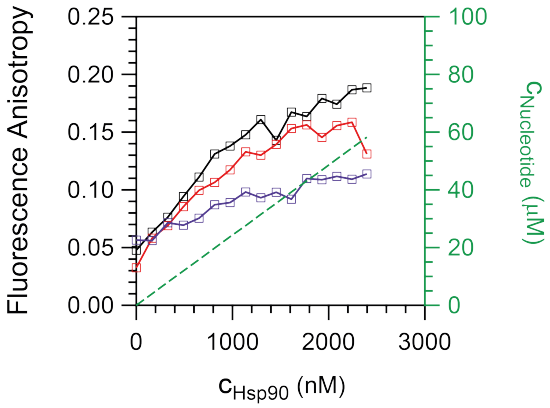

Figure 3.29: Binding of AMP-PNP-647N to preincubated Hsp90. Hsp90 is preincubated with 2 mM AMP-PNP (blue) or 2 mM ADP (red) or buffer (black) and subsequently titrated to 500 nM AMP-PNP-647N. Binding of the labeled nucleotide to Hsp90 is monitored by fluorescence anisotropy. The concentration of residual unlabeled nucleotide is indicated in green. A K_d fit results in an estimated decrease of the affinity between control and AMP-PNP incubation to 50 %.

The labeled nucleotide binds to Hsp90 instantly within the dead-time of the experi-

ment (5 to 10 s). This demonstrates that neither ADP nor AMP-PNP are able to kinetically trap Hsp90 in a state, where both binding pockets are able to prevent the exchange of the bound nucleotides. Nevertheless, the apparent affinity of Hsp90 to the labeled AMP-PNP is decreased. This decrease is much larger than the effect expected for a simple competition between the nucleotides, which can be estimated from the chase experiments.[19] A pure competitive behavior seems to be the case for a preincubation with ADP. The apparent K_d estimated from the titration curve with AMP-PNP preincubated Hsp90 is increased by a factor of about two. Thus, AMP-PNP traps Hsp90 in a closed state similar to the X-ray crystal structure, but only one nucleotide binding pocket is not accessible and traps an AMP-PNP, while the other nucleotide can easily exchange with the solvent. In conclusion, the AMP-PNP induced, closed Hsp90 conformation is asymmetric, too.

Another evidence of AMP-PNP not acting as a classical competitor to ATP for binding to Hsp90 is the comparison of its effects on Hsp90's ATPase activity to the well known and characterized competitor radicicol, which binds with nanomolar affinity to Hsp90 [34]. We measure the ATPase activity of Hsp90 at saturating ATP concentration. Increasing amounts of AMP-PNP and radicicol are added and the resulting ATPase activity is tracked (c.f. Fig. 3.30).

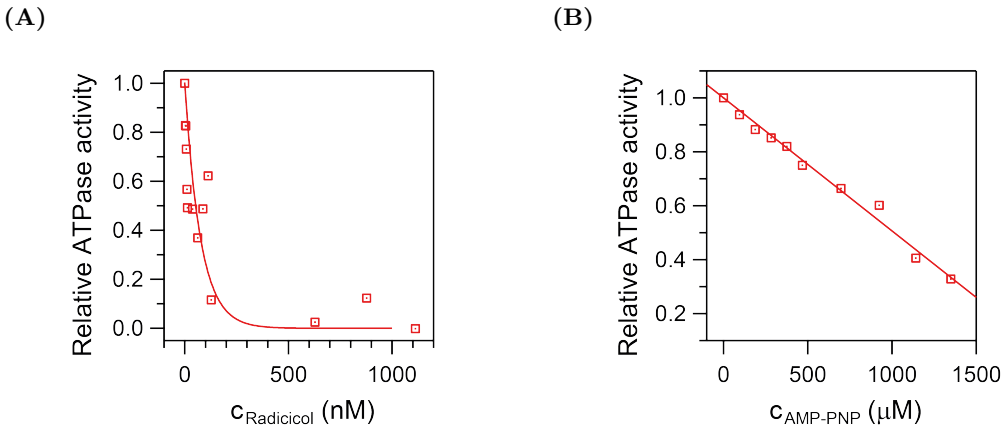

Figure 3.30: Unlike radicicol, the transition analogue AMP-PNP is a non-competitive inhibitor. The steady-state ATPase activity of 1 μM Hsp90z is measured at 37 °C, with 10 mM ATP (a fivefold substrate saturation). (A), the concentration dependent effect of radiciol on the ATPase activity of Hsp90. The red line indicates an exponential fit. (B), the concentration dependent effect of AMP-PNP on the ATPase activity of Hsp90, with a linear fit.

As can be seen in the comparison in Fig. 3.30, radicicol and AMP-PNP have different effects on the steady-state ATPase activity of Hsp90. While radiciol exhibits the typical effect of an competitive inhibitor, leading to a concentration-dependent exponential decay of the ATPase activity of Hsp90, AMP-PNP induces a linear decay usually observed in enzyme inactivation. Interestingly, AMP-PNP induces a loss of 50 % activity already at less than 10 % of the ATP concentration in the assay. The most likely explanation for this observation is that AMP-PNP induces an Hsp90 conformation (namely the closed state), which favors the binding of a second AMP-PNP over ATP. Such a difference in the affinity of Hsp90 for AMP-PNP and ATP has not been reported so far and is also not observed in

19 Shown in Fig. 3.18 on page 68.

the titration experiments conducted with the fluorescent nucleotide analogs.

3.2.7 Summary

Our novel reporter assay based on three-color smFRET and γ-labeled fluorescent nucleotide analogues enables us to study the correlated effects of a single nucleotide binding to a protein on its dynamics and its interaction with further ligands. This is extremely useful, because it allow to access the intramolecular communication underlying allosteric effects such as cooperativity. Allostery and cooperativity are highly important in the fine-tuning of biological systems and their non-linear responses to stimuli [158, 159].

With our assay, we observe cooperativity between the two nucleotide binding sites in Hsp90. The presence of ATP or AMP-PNP in one protomer results in a prolonged binding of AMP-PNP to the other protomer. This effect may be relevant for other members of the GHKL protein class. Additionally, we observe the presence of two ATP (with one not being hydrolyzable) not or only weakly affecting the average dwell time, but the conformational equilibrium to a similar degree as AMP-PNP.

Moreover, co-chaperones Aha1 and Sba1 regulate the cooperativity between the two binding pockets. While Aha1 alone affects both the conformational equilibrium of Hsp90 by shifting it to the closed state and increases the average dwell of AMP-PNP on Hsp90, Sba1 modulates the coupling between the two nucleotide binding pockets, likely on both the level of global (domains), as well as the level of local (motifs) conformational arrangements. It decreases the average dwell time of AMP-PNP on Hsp90 in presence of of another nucleotide, inverting positive towards negative cooperativity.

On the microscopic level of single state transitions, we can discriminate the effects of ATP, Aha1 and their combination on the system consisting of Hsp90 and (labeled) AMP-PNP. Both affect the dissociation rates of AMP-PNP, and both affect the open/closed equilibrium of AMP-PNP bound Hsp90. However, the combined effect of Aha1 and ATP is not a linear combination of their isolated effects. Hence, co-chaperones and nucleotides act independently on Hsp90, but the affected motifs themselves interfere with each other. This once more demonstrates the high complexity of the Hsp90 machine. The cooperativity and its regulation by co-chaperone can be seen as an additional aspect of Hsp90's cross-monomer coordination, which happens before the actual hydrolysis of nucleotide [150]. Our findings demonstrate that it is necessary to study the system on the microscopic scale (i.e. states and their transitions) in order to understand its function completely. Therefore, our method provides the basis for further detailed investigations on the interplay between Hsp90, nucleotides and different co-chaperones.

As Aha1 affects the equilibrium of states both in absence and presence of a possible energy source, our data also demonstrates once more that co-chaperones do not act as classical enzymes on Hsp90. Our observation matches with a similar finding on the microscopic effect of Sba1 [100].

A summary of the findings is given in Fig. 3.31. The presence of two triphosphate nucleotides (ATP or AMP-PNP) shifts the equilibrium towards the closed state of Hsp90, as soon as one nucleotide is not hydrolyzable (which is the case for AMP-PNP and labeled ATP). When Hsp90 enters the closed state with two nucleotides bound, it constitutes a structure with an asymmetric affinity towards nucleotides: One pocket binds kinetically stable AMP-PNP (hence one nucleotide is trapped in the transition state), while the other nucleotide is weakly bound and easily exchanges with the solvent. Nevertheless, this second

(A)

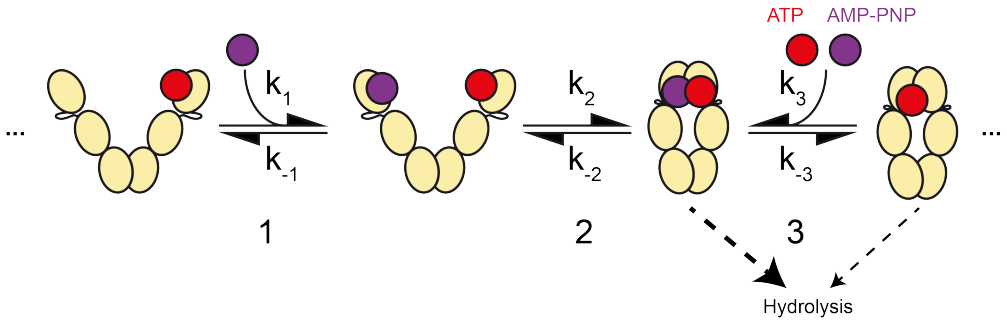

(B)

rate	ATP	Aha1	ATP+Aha1	ATP+Sba1
k_{-1}	$\downarrow$	$\circ$	$\circ$	$(\uparrow^{*})$
k_2	$\uparrow$	$\uparrow$	$\uparrow\uparrow$	$\frac{k_2}{k_{-2}}$ $\circ$
k_{-2}	$\downarrow$	$\circ$	$\circ$	
k_3	$\circ$	$\circ$	$\circ$	$(\uparrow^{**})$

Figure 3.31: Relative effects of nucleotide and co-chaperones on the interaction of a second nucleotide with Hsp90 and on Hsp90's conformation (compared to the absence of additional nucleotide or co-chaperones). (A), minimal model for the interaction. (B), observed changes in rates compared to absence of further interactors. */** Effects of Sba1 on single rates are not resolved; however Sba1 leads to a shift of the equilibrium between open and closed, AMP-PNP bound Hsp90 in presence of ATP and a decrease of the dwell time of the reporter nucleotide on Hsp90. Hence, the off-rates are likely affected, most likely k_{-1}, because most Hsp90 is in the open conformation.

nucleotide binding pocket still exhibits an higher affinity to AMP-PNP than to ATP.

The closed state of Hsp90 is the ATPase active conformation [51, 153], but does the actual hydrolysis occur more likely in the state, where one nucleotide is bound or in the state, where two nucleotides are bound? Published results from ensemble experiments might help to tackle this question. The maximal catalytic activity of Hsp90 as heterodimer D79N/WT increases, while it is not changed in E33A/WT [29]. Hence, the presence of a second nucleotide decelerates the hydrolysis.

Overall, the most likely model for Hsp90 and its interaction with ATP is therefore that it takes two nucleotides for it to enter the hydrolysis competent state, but the actual hydrolysis itself happens asymmetric with only one nucleotide bound. However, the coupling between the effects is not deterministic, i.e. Hsp90 may also follow different state transitions, which are just less likely. Further studies will be necessary to test both hypotheses on the affected motifs in the future, e.g. experiments on point mutants affecting nucleotide binding/hydrolysis (E33A/D79N) or γ-phosphate arrangement (R380A).

3.3 The mechanism of the Hsp90 regulation by Cdc37

Most interactions of Hsp90 with kinases are mediated by the co-chaperone Cdc37. As outlined in Section 1.2.3 on page 6, at least two possible binding sites for Cdc37 have been identified by the determination of the respective structure of the complex. The biological relevance of these two complexes and their effect on the Hsp90 machinery's cycle remains unclear. Artifacts from the respective method or from the combination of homologue proteins in the studies cannot be excluded with the very heterogeneous protein family of Cdc37, whose amino acid sequence is little conserved and differs largely in its length (e.g. human and yeast homologues by more than 20 % at $I = 23.64$ %) [160].

In the following, I present a novel biochemical approach to assess the low affinity interaction between Hsp90 and Cdc37. The two proteins are covalently tethered by a peptide linker, ensuring high local concentration. Thereby, the effects of Cdc37 on Hsp90's kinetics and equilibrium are studied at the single molecule level, as well as the nucleotide dependent binding of Cdc37 to Hsp90. This allows a much more detailed view onto their interactions and regulatory switch points within the transient complexes consisting of Hsp90, co-chaperones and clients.

3.3.1 Tethering Cdc37 to Hsp90

The reason why the interaction of Cdc37 with Hsp90 has not been accessed by single molecule experiments so far is the low affinity of their complex, with a dissociation constant K_d in the range of 100 to 200 μM between the two yeast homologues [78]. Although single molecule experiments with an unlabeled protein at this concentration are technically possible, molecular crowding may impact and impede the results. Crowding has already been shown to affect Hsp90 by destabilizing its open conformation [153]. Direct monitoring of the interaction would additionally necessitate both interacting proteins to be labeled and thus require concentrations below 100 nM for a reasonable S/N ratio, making the observation of interactions impossible.

The chosen alternative is to study the proteins' interaction via a fusion protein mimicking a very high apparent concentration of the co-chaperone with respect to Hsp90. A protein construct harboring Cdc37 and Hsp90 is designed (shown in Fig. 3.32). Based on the crystal structure of Cdc37's CTD binding to Hsp90's NTD [79], the two proteins are linked between Cdc37's C-terminus and Hsp90's N-terminus with a linker peptide of the sequence P-(GGS)$_{15}$-P-(EAAAK)$_5$-P-(GGS)$_{15}$-P.

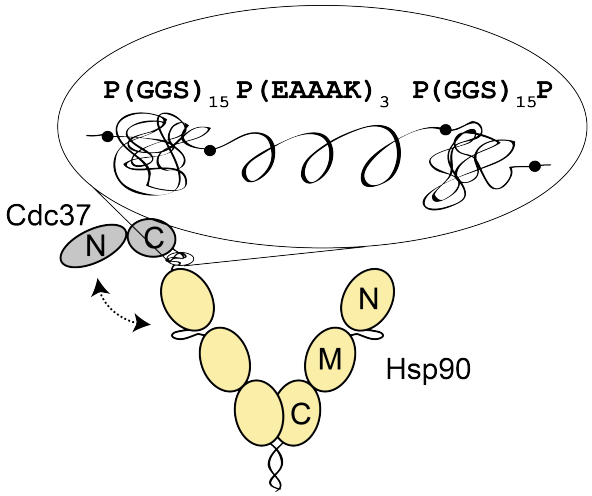

Figure 3.32: Schematic view on the fusion protein construct to study the low affinity interaction of the yeast proteins Cdc37 and Hsp90 and the effect of this interaction on Hsp90's mechano-chemical cycle at single molecule conditions.

While GGS-repeats are known to constitute random-coil (RC) peptides, EAAAK-repeats form α-helical peptides, constituting stiff rods (SR) [161, 162]. Prolines in between are expected to break the secondary structure beside the RCs [163]. Thus, the linker is expected to build up a structure of the form RC-SR-RC. The local concentration of Cdc37 can be estimated (c.f. Appendix C.1 for details), and a local concentration above the K_d is expected, allowing to study the interaction between the two proteins at low concentrations.

To estimate the local concentration of Cdc37 experimentally, its effects on Hsp90's ATPase and closing are compared to reported effects of Cdc37 in solution. The steady-state ATPase activity of the fusion protein at 37 °C with saturating substrate concentration is decreased down to 45 % of the wild-type Hsp90 (see Fig. 3.33(A)), an effect that is quantitatively reproduced by the addition of wild-type yeast Cdc37. The inhibition of Hsp90's ATPase activity by human Cdc37 has been described previously, with a reported

reduction of 50 % at a Cdc37 concentration close to the K_d of the interaction [78].

The conformational equilibrium distribution of the fusion protein is studied in an smFRET experiment with the dyes attached to the opposing amino acids 61_{90} and 385_{90} of yHsp90, as done in earlier smFRET studies of Hsp90 [27, 113]. The fraction of closed Hsp90 is significantly decreased compared to the wild-type protein at AMP-PNP saturating conditions. This resembles the observation of T. Zhang et al. [164] in chromatography experiments.

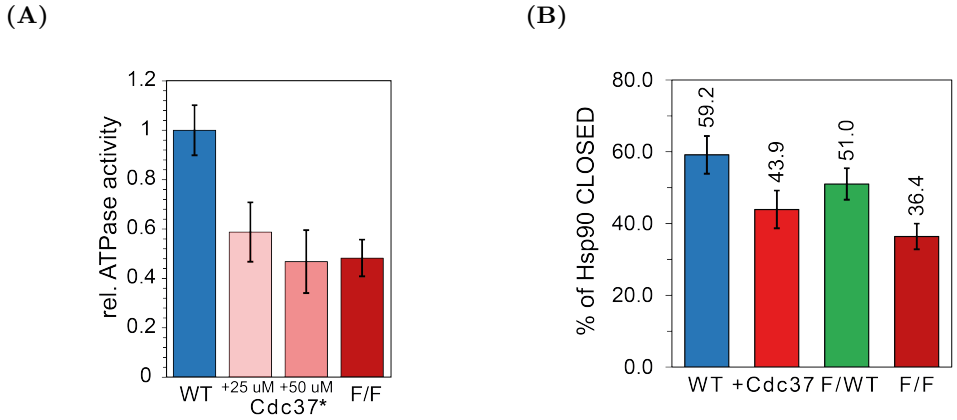

Figure 3.33: The fusion protein mimics the effects of Cdc37 on Hps90 in solution. (A), rel ATPase activity of wild-type Hsp90zip (WT) in absence and presence of yCdc37, and of the fusion protein yCdc37-yHsp90zip dimer (F/F), measured at 37°C, 1 μM protein and 3 mM ATP. Error bars represent the standard deviation from three independent experiments. *The yCdc37 protein sample exhibits non-Hsp90 background, although no impurities are found on an SDS-gel. (B), the AMP-PNP induced closing of the Hsp90 dimer is attenuated by Cdc37, both with separate proteins in solution (+Cdc37, 100 μM) and in the fusion protein construct with one (F/WT) and two Cdc37 (F/F) present.

The equilibria between the open and closed state of the different constructs Fig. 3.33(B) gives another experimental estimate of the apparent local concentration of Cdc37 in the fusion protein. The local concentration of Cdc37 in the F/F construct must be greater than the K_d of the interaction and lower in the F/WT construct. Thus, the concentration is estimated experimentally as $c_{Cdc37} \approx 50 - 100$ μM, which is roughly two orders of magnitude lower than the theoretical estimate, likely due to steric hindrances (Appendix C.1).

These results demonstrate that the fusion protein mimics the effects of Cdc37 on Hsp90 in solution without the necessity for a highly concentrated protein sample. Artifacts from molecular crowding or aggregation are avoided. In the following, I study the effects of Cdc37 on Hsp90's equilibrium and kinetics as well as the interaction of Cdc37 with Hsp90 based on experiments with the fusion protein and finally extend the system towards studying the interplay between Hsp90, co-chaperones and a native substrate.

3.3.2 Cdc37 can partly compensate the effect of ATP on Hsp90

The effect of Cdc37 on Hsp90's conformations is characterized by studying the FRET pair 61_{90}-Atto550/385_{90}-Atto647N under saturating nucleotide concentrations of ADP, ATP and the transition state analogue AMP-PNP. smFRET experiments are conducted under ALEX on the prism-type TIRF setup. Data statistics can be found in Appendix C.5.1 on

page 132.

The nucleotides ADP and ATP have only a weak effect on the conformational equilibrium of Hsp90 in presence of one Cdc37, as observed by the FRET efficiency histograms (Fig. 3.34(A)). While ADP slightly depopulates the high-FRET peak (from 5 % to 3 % Hsp90 closed), ATP has an equally weak, but adverse effect (10 % closed), estimated by Gaussian fits. As already shown in Fig. 3.33(B), AMP-PNP increases the high-FRET population. These effects resemble qualitatively the effect of the nucleotides on wild-type Hsp90, as characterized before [27, 113]. The presence of Cdc37 in the fusion protein shifts the low- and high-FRET peaks slightly further apart. Fig. 3.34(B) demonstrates that this very weak effect is increased with a homo dimer of the fusion protein. It is unlikely caused by photo-physical effects, as the apparent γ-factors remain similar. An effect of Cdc37 binding on the accessible volume of the dyes cannot be excluded, but seems unlikely from the crystal structures of Cdc37 in complex with Hsp90 suggesting large accessible volumes for the dyes.

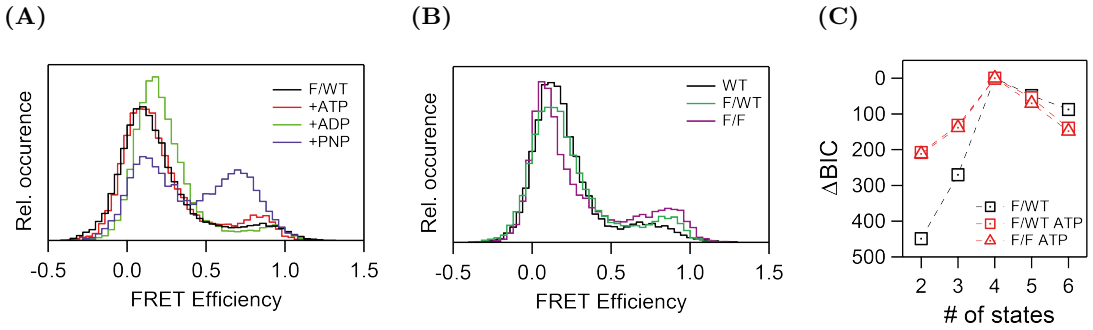

Figure 3.34: The smFRET efficiency of Hsp90 as wild-type and fusion protein. (A), native nucleotides (2 mM each) have only weak effects on the equilibrium distribution. (B), in presence of 2 mM ATP, the FRET peaks in the fusion proteins shift apart. (C), all data sets can be described best by a 4-state model, as confirmed by they relative BIC.

The conformational kinetics of Hsp90 are analyzed with a semi-ensemble HMM by the program SMACKS [113]. SMACKS has been developed to analyze the kinetics of wild-type Hsp90 under various nucleotide conditions. It allows to recover hidden states that share the same FRET efficiency. This study has found that Hsp90 is described best with a cyclic 4-state model under all investigated conditions. Two high- and two low-FRET states, respectively, are only distinguishable by their kinetics. In presence of ATP transitions between the assigned long lived low- and high-FRET states (assigned as 0 and 3) have been observed that did not occur otherwise. However, no energy flux has been detected under any condition.

Both fusion protein constructs are best described with a 4-state model, as it is the case for wild-type Hsp90. However, the cyclic transitions 3→0 and 3←0 are found both in absence and presence of ATP (Fig. 3.35). In contrast to the measurement with wild-type Hsp90,[20] the transition rates are slightly increased upon addition of ATP. However, no directionality can be observed in any of the data sets. The conformational transitions, which occur on the reaction coordinate studied with the used FRET-pair, do not exhibit

20 Data evaluation shown in Appendix C.2, page 131.

any energy flux.

The combined effect of the co-chaperone Cdc37 and nucleotide is further characterized by a comparison of Hsp90's kinetics in presence of the non-hydrolyzable ATP analog AMP-PNP. In presence of AMP-PNP, Hsp90 has been found to populate mainly the state 3, which accumulates because of its slow off-rate to state 2 [113]. A reproduction of this experiment results in a similar picture. However, the presence of Cdc37 results in the observation of a conformational cycle, similar to the experiment with ATP.

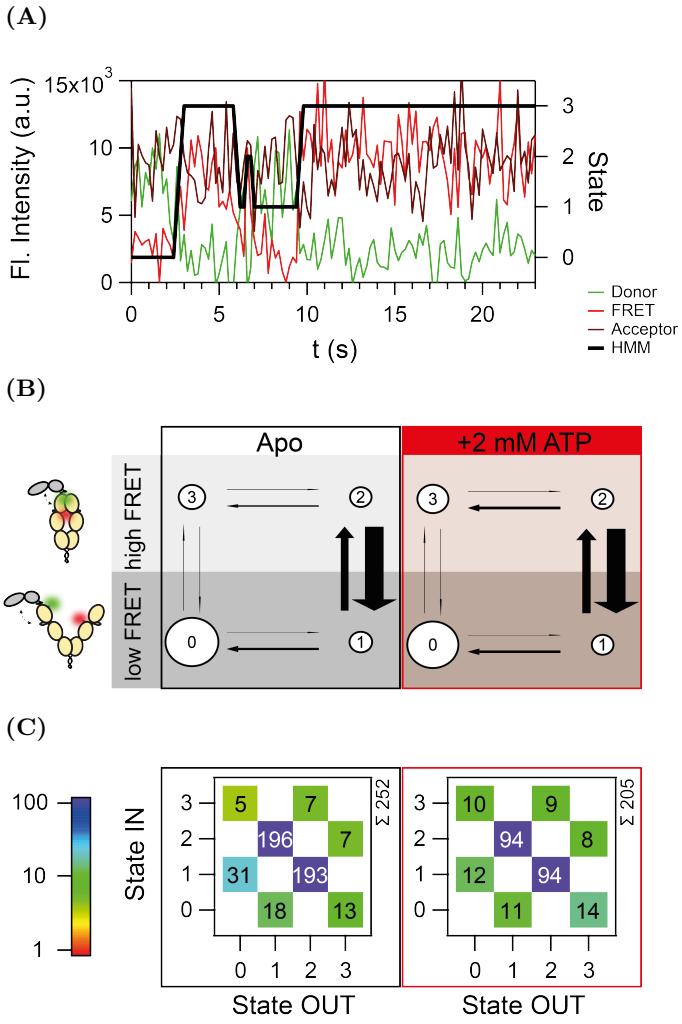

Figure 3.35: The effect of Cdc37 on the kinetics of Hsp90. The F/WT construct consisting of an Hsp90 dimer with one Cdc37 is studied in absence (Apo, black) and presence of 2 mM ATP (red). (A), exemplary fluorescence trace measured at apo condition. Donor, donor fluorescence after donor excitation; FRET, acceptor fluorescence after donor excitation; Acceptor, acceptor fluorescence after acceptor excitation; HMM, viterbi path of the optimized model. (B), in presence of Cdc37, Hsp90 exhibits a kinetic cycle including the state transitions between states 3 and 0 independent of ATP presence. (C), number of transitions occurring in each data set. The wild-type kinetics are characterized in Appendix C.2.

Compared to Hsp90 in absence of Cdc37 (c.f. Appendix C.2), both rates for the transition between the states 2 and 3 are decreased, whereas mainly the transition 3→2 is strongly affected by Cdc37 in absence of ATP and in presence of AMP-PNP. This effect of Cdc37 is

stronger at saturating AMP-PNP than at saturating ATP conditions. The state transitions 3→0 occur at a similar frequency and thus reduce the accumulation of state 3, explaining the effect of Cdc37 on the FRET histogram, as determined in Fig. 3.33(B). Both effects are resembled by the addition of 100 μM Cdc37 to wild-type Hsp90 (c.f. Appendix C.3 on page 131). Hence, in presence of Cdc37, the effects of the nucleotides ATP and AMP-PNP on Hsp90's kinetics become similar, and the transition 3⇌0 does not differ in its velocity from all other state transitions anymore.

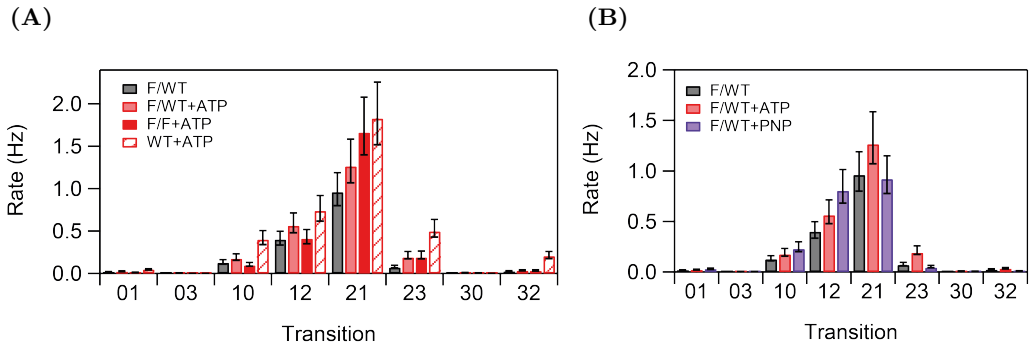

Figure 3.36: The effects of Cdc37 on the transition rates of Hsp90. (A), transition rates in presence of Cdc37 and ATP. (B), the effect of nucleotides on the transition rates of Hsp90 in F/WT construct (PNP, AMP-PNP; rates are assigned as initial state→final state). Error bars represent the confidence interval for the transition rates.

The equilibrium and the kinetics of Hsp90, as monitored by the FRET-pair of $61_{90}/385_{90}$ are both affected by Cdc37. Most of its effects are weak, which seems to be a general feature of the Hsp90 machinery components [27, 113]. Cdc37 shifts the low- and high-FRET populations of Hsp90 slightly apart. This is probably achieved by changing NTD-MD interface of the Hsp90 domains – either by shifting the charged linker equilibrium towards a more stretched state or by shifting the equilibrium between the two rotations of the NTD with respect to the adjacent MD.

Cdc37 does not affect the number of observed states, which Hsp90 adopts in presence of different nucleotides. It decreases the number of hidden state transitions and the correspondent rates, thereby decelerating Hsp90. Hsp90 responds differently to the addition of ATP in presence of Cdc37, with generally accelerated rates. This hints towards a more tightly regulated Hsp90 machinery *in vivo* than found with the reconstituted Hsp90 *in vitro*.

The overall strongest effect is observed on the state transitions between Hsp90's states 3 and 0. Cdc37 alone enables Hsp90 to undergo this transition, similar as it has been observed with ATP [113]. As no energy flux can be determined within the kinetic cycle, the dynamic transitions and thus the monitored cycle are most likely thermal fluctuations on a flat energy landscape. ATP seems to act as a co-factor stabilizing the transition state $(3\text{-}0)^{\ddagger}$ and thereby enabling the corresponding transitions (shown in Fig. 3.37). The co-chaperone Cdc37 substitutes ATP for this effect and therefore enables the otherwise inaccessible state transitions already under non-ATP conditions. Interestingly, conflicting findings on the ATPase activity of Hsp90 have been published. While for a long time the potential of Hsp90 to hydrolyze ATP was considered to be essential for cell viability [29, 43], recent

data suggests only the ability to bind ATP is essential, while a mutation impairing the ATP hydrolysis is not lethal [51]. This is consistent with the experiments presented here, which show that the function of ATP for Hsp90 is rather to provide structural flexibility (in terms of enabling state transitions) than to serve as an energy source.

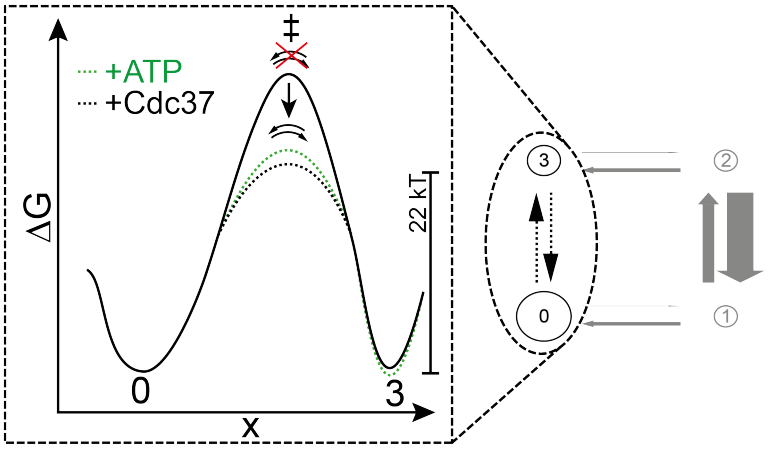

Figure 3.37: The function of Cdc37 and ATP as catalysts. Both are found to stabilize the transition state between states 3 and 0 of Hsp90 and thus permit the conformational transition between both states, which is inaccessible otherwise. No energy is consumed and no hydrolysis occurs within this step. The energy barrier is estimated by the calculated rate by $\Delta G^{\ddagger} = k_b T ln(\frac{k_{30}}{k})$ and $k_{30} \approx 0.0336\, s^{-1}$ with an estimated attempt frequency k of $10^8\ s^{-1}$.

3.3.3 Cdc37 forms at least three distinct complexes with Hsp90

Two completely different structures of the complex between human Cdc37 and yeast Hsp90 have been published at atomic resolution [30, 84]. This fact highlights the importance of different Cdc37:Hsp90 conformations for the function of the Hsp90 machinery *in vivo*. The fusion protein construct with one label on Cdc37 and the other on Hsp90 enables studies on the interaction of Cdc37 on Hsp90 at the single molecule level. Single molecule studies have the advantage that they can resolve and discriminate the different states of the dynamic interaction between the two proteins, while bulk experiments are limited to indirect conclusions from data that intrinsically is averaged. The two domains of Cdc37 carry out very different functions according to literature, but Cdc37N does not bind exclusively to kinases and Cdc37C not only to Hsp90's NTD as shown by the solved cryo-EM structure of an Hsp90:Cdc37:Cdk4 complex [30]. Thus, to understand the protein's interaction necessitates screening of the interaction between Hsp90 and the N- and C-domain of Cdc37 separately.

The interaction of Cdc37N and Cdc37C with Hsp90 is monitored measuring the FRET efficiency between the amino acids 129_{37} – 61_{90}, and 396_{37} – 61_{90}, respectively (Fig. 3.38). The homologue label positions in human Cdc37 are found by sequence alignment with yeast Cdc37. From the two known complex structures, the one published first (referred to as state 2 in Fig. 3.39) consists only of the CTD of Cdc37 and NTD of Hsp90. Due to steric clashes, this arrangement is not compatible with any known crystal structure of full-length Hsp90, and also not with any snapshot of the dynamic open structure presented in Section 3.1. Hence its physiological relevance remains unclear. The complex structure published latest (referred to as state 1) does also not allow for rotation of Hsp90's NTD

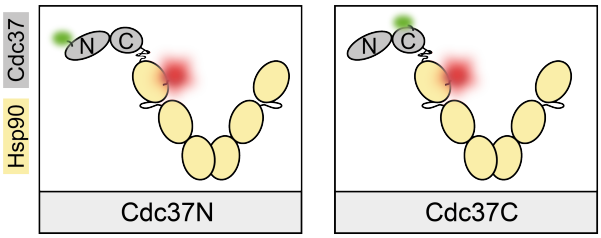

Figure 3.38: The two constructs used to study the dynamic interaction between Cdc37 and Hsp90. Cdc37N, Cdc37 is labeled at amino acid 129; Cdc37C, Cdc37 is labeled at amino acid 396. In both constructs its position relative to amino acid 61 of Hsp90 is probed by smFRET.

with respect to the MD. It is assumed that both arrangements can be mirrored within the asymmetric construct. With the FPS software package, the accessible volumes and expected FRET efficiencies per structure are calculated [125]. Two and three FRET efficiencies that differ from zero are expected for the monitored distances from the molecular arrangement in the structures. The FRET efficiencies are summarized in table 3.39(C). In the following FRET histograms, the expected efficiencies representing state 1/2 are indicated by a blue/brown bar. Because molecular arrangements are possible that would be observed at $E = 0$, and because the system populates more than two states, off-rates cannot be assigned directly. Therefore, a kinetic analysis is omitted.

(A) **(B)**

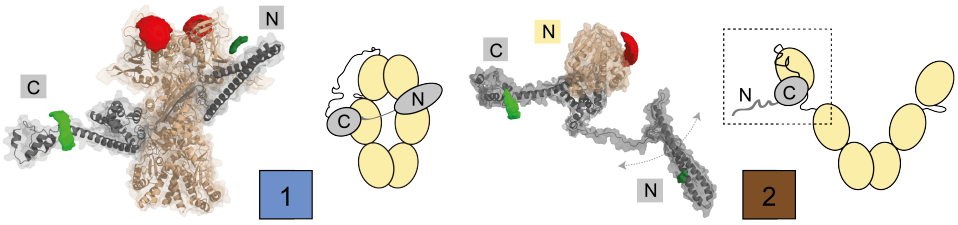

(C)

State	FRET E(Cdc37N:Hsp90N)	FRET E(Cdc37C:Hsp90N)
1	0.84; 0.26	0.17
2	0.12	0.14

Figure 3.39: The two published structures of the Cdc37:Hsp90 complex at atomic resolution and as schemes. (A), the structure assigned as state 1 [30]. (B), the structure assigned as state 2 [84]. In red/green the accessible volumes of the dyes attached to Hsp90 (amino acid 61) and Cdc37N or Cdc37C (amino acid 129 or 396, green) are incorporated. (C), expected FRET efficiencies (> 0.05) for the interaction of Cdc37N and Cdc37C with Hsp90, calculated by the FPS. The first FRET efficiency is expected for the binding of Cdc37 on the same protein chain in *cis*, the second (if stated) for the binding of Cdc37 on the opposing Hsp90 protomer in *trans*. As in structure 1 Cdc37C and in structure 2 Cdc37N is not completely resolved, the position of the missing amino acids is estimated from structural alignment.

The binding of the two Cdc37 domains to Hsp90 is studied by smFRET measured on

the prism-type TIRF setup. Their binding is found to be strongly nucleotide dependent. The two domains behave different upon the addition of a certain type of nucleotide. Both domains exhibit the strongest binding in presence of ATP.

The high FRET peak in Fig. 3.40(A) represents the binding of Cdc37N to Hsp90 as seen in state 1. 44 % of Cdc37N are bound to the Hsp90 protomer in *cis* in this structure (estimated by Gaussian fits). Binding in *trans* cannot be quantified, but is likely to be less probable due to the entropic penalty for stretching the peptide linker. However, more than 50 % of the Cdc37N is bound in this state. The interaction of Cdc37N with Hsp90 is reduced dramatically in presence of AMP-PNP. In presence of ADP, a FRET efficiency between Cdc37N and Hsp90 is measured that cannot be assigned to any of the structural arrangements known from published data at atomic resolution. This unassigned peak is populated by 50 % at a FRET efficiency $E \approx 0.6$ (Fig. 3.40(A)).

The FRET efficiency histograms measured for the interaction between Cdc37C and Hsp90 are more broadened than the one of Cdc37N and complicate assignment of specific efficiencies to conformations. However, in presence of ATP or AMP-PNP a FRET peak at $E \approx 0.9$ is populated. Similar to the observation of the binding of Cdc37N to Hsp90 in presence of ADP, this efficiency does not fit to any of the known structures of the Cdc37/Hsp90 complex. The population vanishes in presence of ADP, which in turn leads to a broadening of the lower FRET efficiency peak.

Both Cdc37 domains are able to bind to Hsp90 in structures as expected from published data. The binding of Cdc37N to Hsp90 seems stronger between the yeast homologues used here, than for mixed complexes or homologues of other species characterized by fluorescence ultra-centrifugation [80]. The structure of the complex between Cdc37 and Hsp90 as found in state 1 with Hsp90 closed is weakly populated in presence of AMP-PNP, although the closing of Hsp90 is induced by the nucleotide. It is likely that this structure is rather a transition state trapped under the experimental conditions that had been used to stabilize the complex for cryo-EM (e.g. the addition of molybdate). It is thus unstable under the near-native conditions in the experiments conducted here. For both domains three populations are identified. Two can be assigned to published structures, while a

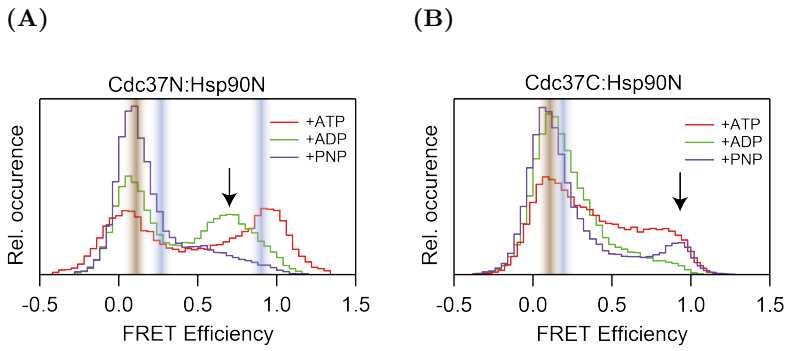

Figure 3.40: The nucleotide dependent binding of Cdc37 to Hsp90. (A), Cdc37N and (B), Cdc37C binding to Hsp90N at nucleotide concentrations of 2 mM. The expected FRET efficiencies calculated by the FPS for the two structures shown in Fig. 3.39 are sketched as colored bars. The populations that probably indicate novel complex arrangements are indicated by arrows.

third likely represents a novel coordination of the complex. These populations might have been hidden within the averaged data from ensemble experiments. Because the novel complex coordination is found for Cdc37N in presence of ADP, but for Cdc37C in presence of ATP/AMP-PNP, they probably represent two different structures.

The tight binding of Cdc37N at ATP and ADP conditions and the tight binding of Cdc37C at ATP and AMP-PNP conditions could be interpreted in terms of Hsp90's ATPase activity as directionality in the proteins' interaction. Cdc37N and Cdc37C bind tightly to Hsp90 loaded with ATP, Cdc37C is released upon hydrolysis, while Cdc37N is then still associated, but reorientated on the surface of Hsp90.

3.3.4 Hsp90 and Cdc37 preferentially form an asymmetric complex

The stoichiometry of the complex between Cdc37 and Hsp90 is still under discussion [78, 79, 84]. Some structural data suggests binding of two Cdc37 molecules per Hsp90 dimer, while some does not [30, 84]. The fusion protein construct permits the investigation of the complex stoichiometry. The presence of a second, unlabeled Cdc37 molecule is mimicked in a measurement with two tethered Cdc37 within the construct, where only one Cdc37 is labeled.

The binding of Cdc37N is found to be significantly reduced, with only 26 % of all Cdc37N bound in state 1 in *cis* (estimated from Gaussian fits). As the decrease by 18 % must be caused by the second, unlabeled Cdc37 binding to the opposing Hsp90 protomer, the population of Cdc37N in the conformation of state 1 at the previously studied 1:2 stoichiometry lies above 60 %. The binding of Cdc37C is slightly reduced, but this loss cannot be assigned to a specific conformation.

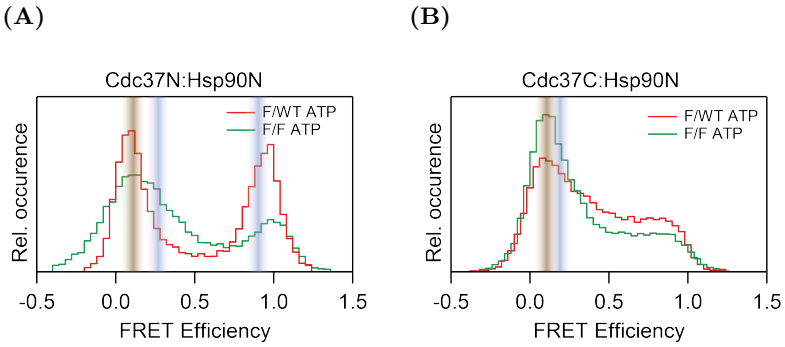

Figure 3.41: Cdc37 binds Hsp90 in a stoichiometry of 1:2. The binding of (A), Cdc37N and (B), Cdc37C to Hsp90 was measured in the constructs F/WT and F/F in presence of 2 mM ATP. The two constructs differ in the Cdc37:Hsp90 stoichiometry.

The results do not show any cooperative binding between the two Cdc37, as it had been proposed before [84], because this should lead to an increase of the populations different from zero. Instead, the results suggest the interaction in state 1 to happen exclusively in a 1:2 stoichiometry of Cdc37:Hsp90, because the presence of a second Cdc37 competes with the labeled Cdc37 for binding to Hsp90. The other FRET efficiencies are only slightly affected by the presence of a second Cdc37. Thus, these complex arrangements can exist with 1:1 stoichiometry, probably because they do not involve binding to the interface of separate Hsp90 protomers. Nevertheless, also for them no cooperative effects are observed.

The interaction in an asymmetric manner (in terms of a stoichiometry of one Cdc37 per Hsp90 dimer) is thus concluded to be the physiologically relevant complex, because in absence of cooperativity, the binding of two Cdc37 to Hsp90 at the same time is very unlikely at the cellular protein concentration of Cdc37, which is below 1 μM [73].

3.3.5 Sba1 facilitates substrate release by competing with Cdc37 for binding to Hsp90

The interaction of Cdc37 with Hsp90 *in vivo* does not happen in isolation but is part of the dynamic network of the several co-chaperones and substrates constituting the Hsp90 machine. Cdc37 is the link of most kinases to Hsp90, necessary for their successful folding and maturation [74–76]. Thus, the ternary interaction of kinase, Cdc37 and Hsp90 is a very useful model system to understand the interaction of Hsp90 with a native substrate. Vice versa, the co-chaperone Sba1 is thought to interact with Hsp90/substrate complexes, inducing the substrate release. A competition and thus subsequent binding of Cdc37 and Sba1 during the interaction of Hsp90 with its client proteins has been concluded from analytical UC and circular dichroism (CD) data [61, 77]. The exact structural origin of the interference between the two proteins is unclear, but from the known crystal structures a competitive binding to Hsp90's NTD is likely [18, 30].

The competition between the co-chaperones Sba1 and Cdc37 is investigated first. The influence of Sba1 on the binding of Cdc37 to Hsp90 is probed in presence of ATP. Sba1 is found to exhibit a stronger negative effect on the binding of Cdc37N to Hsp90 than additional Cdc37 (as described in Section 3.3.4). Binding of Cdc37N to Hsp90 in *cis* in state 1 is decreased to 13 %. The binding of Cdc37C to Hsp90 is weakly affected by Sba1 and, notably, the high-FRET peak is not affected at all. In presence of a second Cdc37 (as mimicked by the F/F construct), the effect of Sba1 on the interaction between Cdc37C and Hsp90 is changed, with an increased population of the high-FRET peak (c.f. Appendix C.4). The binding of Cdc37N to Hsp90 is then not affected by Sba1 anymore.

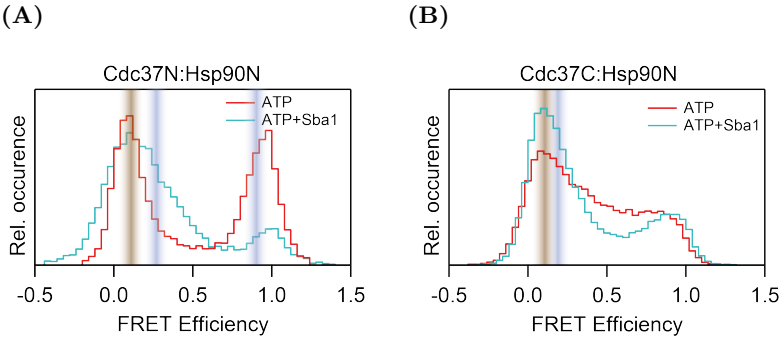

Figure 3.42: The effect of Sba1 on the binding of Cdc37 to Hsp90. The binding of (A), Cdc37N and (B), Cdc37C to Hsp90 was measured in presence of 2 mM ATP and 20 μM Sba1.

Second, the complex of Hsp90, Cdc37 and a kinase is studied. The proteins resemble the ones present in the ternary complex that had been resolved at atomic resolution and assigned here as state 1 [30]. Instead of a combination of homologues, only yeast proteins are used here. Therefore, the studied complex resembles the native interaction to an even greater extent. The C-terminal fragment of the yeast mitogen activated (MAP3) kinase Ste11 (Ste11C) is used instead of the human cyclin dependent kinase Cdk4 from

the cryo electron microscopy (cryo-EM) study. The alignment of both kinases (shown in Fig. 3.43(A)) demonstrates their high homology with an identity of 28.24 %.

The addition of Ste11C to the Cdc37:Hsp90 complex in presence of ATP has different effects on the binding of the two Cdc37 domains to Hsp90. Ste11C does not affect the binding of Cdc37N, but its presence leads to reduced binding of Cdc37C.

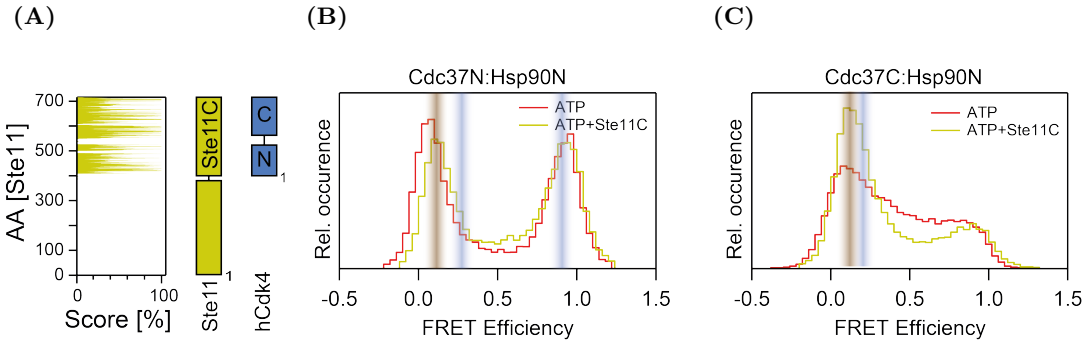

Figure 3.43: The effect of the kinase Ste11 on the binding of Cdc37 to Hsp90. (A), sequence alignment of Ste11 and hCdk4. (B), the effect of 10 μM Ste11C on the binding of Cdc37N to Hsp90 at 2 mM ATP. (C), the effect of 10 μM Ste11C on the binding of Cdc37N to Hsp90 at 2 mM ATP.

The 'late' co-chaperone Sba1 competes mainly with Cdc37N and weakly with Cdc37C for binding to Hsp90 in presence of ATP. As the competition of Sba1 with Cdc37N is not observed in the F/F construct, the mechanism must happen in a stepwise manner. Sba1 first binds to the unoccupied Hsp90 protomer in a Cdc37:Hsp90 complex of stoichiometry 1:2 and then is able to compete with Cdc37N, probably enabled by its increased local concentration. Afterwards, it displaces Cdc37 from the complex structure as found in state 1, where Cdc37 is thought to stabilize the complex consisting of Hsp90 and kinase. This fits well to the characterization of Sba1 as a co-chaperone facilitating the release of folded client proteins [49]. Sba1 does not affect the binding of Cdc37C to Hsp90 in the conformation characterized by a high-FRET peak. This allows to form a ternary complex as possible intermediate, in which Cdc37 and Sba1 may both bind to Hsp90.

Surprisingly, the addition of Ste11 to Cdc37, Hsp90 and ATP does not impede the interaction between Cdc37N and Hsp90. The N-terminus of Cdc37 is usually assigned the major role in the direct interaction with kinases rather than the interaction with Hsp90. Therefore, a competitive binding of kinase and Hsp90 to it was expected [81]. In complex with Hsp90, the direct interaction between Cdc37 and the kinase seems attenuated, while Cdc37 serves more as a regulator of the Hsp90/kinase interaction. Again the complete conformation found in state 1 represents rather a transition state of the complex Hsp90/Cdc37/Ste11 than a stable and long lived structure. The binding of Cdc37C to Hsp90's MD in this transition state, constituting a 'molecular clamp' [30] on an Hsp90/kinase complex, is dynamic. Cdc37C's transient binding to Hsp90's MD likely increases the closing time of Hsp90. This would enable Hsp90 to increase the time it separates the kinase domains for isolated folding.

It is noteworthy that the distinct effect of Ste11C on Cdc37C's binding to Hsp90 monitored by smFRET resembles the effect observed upon the addition of Sba1 (with

highly similar means and medians of their FRET efficiency distributions), while their effect on Cdc37N differs dramatically.

The transient association of its CTD might allow Cdc37 to increase the closing time of Hsp90, as the off-rate from the kinetically more stable closed state of Hsp90 is decreased by Cdc37. With the kinase bound in between the Hsp90 dimer (as observed in [30]) that would increase the time span, in which the two kinase domains are separated (c.f. Fig. 3.44). This permits them to fold independently.

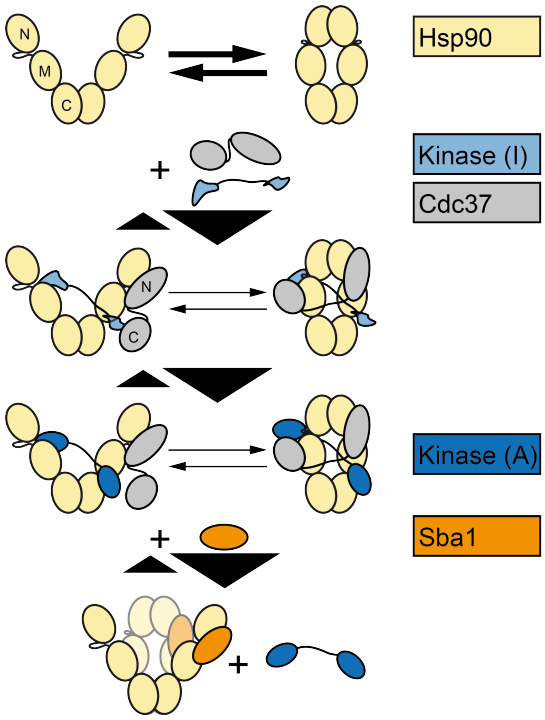

Figure 3.44: A model on the interaction of Hsp90 with Cdc37 and kinase. Cdc37 increases the dwell times of the open and closed conformation of Hsp90, which could lead to from an inactive (I) to an active (A) kinase. A subsequent addition of Sba1 would then displace Cdc37 from Hsp90 and lead to release of the kinase. ATP hydrolysis might play a role by giving directionality in the dynamic assembly and disassembly of the co-chaperones and their domains.

While the association, reorientation and dissociation of Hsp90, co-chaperones and clients occurs dynamically at thermal equilibrium, a directionality in terms of a consecutive association/dissociation of the different co-chaperones would ensure the efficient separation of different client segments necessary for folding of the latter into a functional structure. This directionality could be given by the ATP hydrolysis of Hsp90.

3.3.6 Summary

In order to allow single molecule studies on the weak interaction between Cdc37 and Hsp90, a fusion protein construct tethering the proteins together was successfully created. It mimics the effects of Cdc37 in solution. This construct was first used to characterize the influence of Cdc37 on the nucleotide-dependent conformational equilibrium and the kinetics of Hsp90. Subsequently, the nucleotide dependent binding of Cdc37 to Hsp90 and the effect of another co-chaperone as well as a client protein onto the Cdc37/Hsp90 complex were characterized.

Cdc37 decelerates Hsp90's ATPase activity and its conformational transitions. It does not couple the ATP hydrolysis to the conformational transitions monitored. Instead, a cyclic transition between two states of Hsp90 is enabled by Cdc37 in absence of nucleotide, which has been observed previously only in presence of ATP [113]. This is another evidence that the large conformational changes of Hsp90 are ATP independent and thus driven by thermal fluctuations [99]. Within this cycle, ATP stabilizes a transition state of Hsp90 and thereby enables a complete conformational cycle. Therefore, it fulfills the role of a co-factor on this reaction coordinate. Cdc37 can compensate for this stabilizing effect. The results concur with recent findings that only the ability to bind ATP is essential for Hsp90 functionality and thus cell viability, rather than the ability to hydrolyze it [51].

The interaction of Cdc37 with Hsp90 is nucleotide dependent and involves more than two different structures of the Cdc37/Hsp90 complex. The interaction between the two proteins happens at a stoichiometry of one Cdc37 per Hsp90 dimer. The two domains of Cdc37 can bind independently and respond differently to the type of nucleotide bound by Hsp90. Due to the flexible association of Cdc37 and Hsp90, the previously described competition between Cdc37 and the co-chaperone Sba1 for binding to Hsp90 is not exclusive, but allows intermediate, ternary complexes consisting of Hsp90, Cdc37 and Sba1.

In contrast to expectations from literature, the client protein kinase Ste11 diminishes the binding of Cdc37's C-terminal domain to Hsp90, but not the association of Cdc37's N-terminal domain. The co-chaperone Sba1 similarly affects the binding of Cdc37 to Hsp90.

The large conformational changes of Hsp90 appear independent of ATP hydrolysis, but the results also suggest that ATP hydrolysis could enable a directionality in the transient association and dissociation of the client, co-chaperones and Hsp90 and therefore provide a possible reason for Hsp90's ATPase activity. Another evidence for the link between transient association and hydrolysis might be the finding of a possible function of Cdc37 as nucleotide exchange factor (NEF) (c.f. Appendix C.6 on page 134).

CHAPTER 4

Conclusion

This work gives several novel insights into the mechanisms underlying Hsp90 function by the application of different smFRET techniques on the Hsp90 machine. The results of each of my three projects have already been discussed in detail separately. In the following, I will try to integrate these results into a joint picture of Hsp90, its functions and underlying mechanisms.

The Hsp90 dimer switches between two global conformations on the timescale of seconds (c.f. Fig. 4.1). One conformation is N-terminally closed, stable and rigid and one is N-terminally open, highly flexible and dynamic, with a large fluctuation amplitude of 12 Å. The open conformation is populated by more than 90 % in presence of ATP, ADP or in their absence.

Its flexibility and hence its broad and flat energy landscape facilitates regulation of the protein function in general, because only weak interactions are necessary for a perceivable effect. This is underlined by the effect of crowding agents, that effectively shift the conformational equilibrium of Hsp90 [153]. On the other hand, the flexibility also requires weak interactions, because a single, strong interaction could dominate the regulation otherwise, rendering all other regulatory interactions useless. This is likely the explanation for the relative weak binding (characterized by high K_d values) of the interaction between co-chaperones, clients or nucleotides and Hsp90. Hsp90's different local motifs (like the ATP-lid, loops in the domains, inter-domain arrangements, to name a few) offer a large number of interaction sites for them. Its dimeric nature additionally improves the efficiency of regulation, because it allows a non-linear response to stimuli by allosteric or by cooperative effects. The latter was characterized within this work for the interaction between nucleotides and Hsp90.

Since the rigid closed conformation is heavily populated only in presence of the ATP transition analog AMP-PNP, it represents a transition state of the protein. In this context, the observed rigidity of the transition state is highly useful, because it decreases fluctuations on reaction coordinates being orthogonal to the ATP hydrolysis. Thus, it decreases the loss of energy from ATP hydrolysis due to dissipation. However, no significant effect of hydrolysis in terms of an induced directionality is observable on the scale of global conformational changes, not even in presence of co-chaperones.

Similar to co-chaperones, nucleotides regulate the flexibility and transitions of Hsp90 and decrease the fluctuations. In accordance to the finding of the viability of cells expressing an Hsp90 variant that lacks ATPase activity [51], the main effect of ATP on the dynamics of Hsp90 is of structural kind. This structural impact is essential for Hsp90's function [29, 51, 151]. Moreover, the function of co-chaperones and nucleotides overlap, i.e. they can substitute for certain effects on the dynamics of Hsp90. The multiple processes affected

by both can be additive or competitive. Hence, co-chaperones and nucleotides together constitute a complex interaction network of Hsp90, which balances the dynamics and function of the protein. The orientation of the domain interfaces seems to represent the main regulatory switch point, which is affected by e.g. the ATP-lid or the catalytic loop including the residue Arg_{380}.

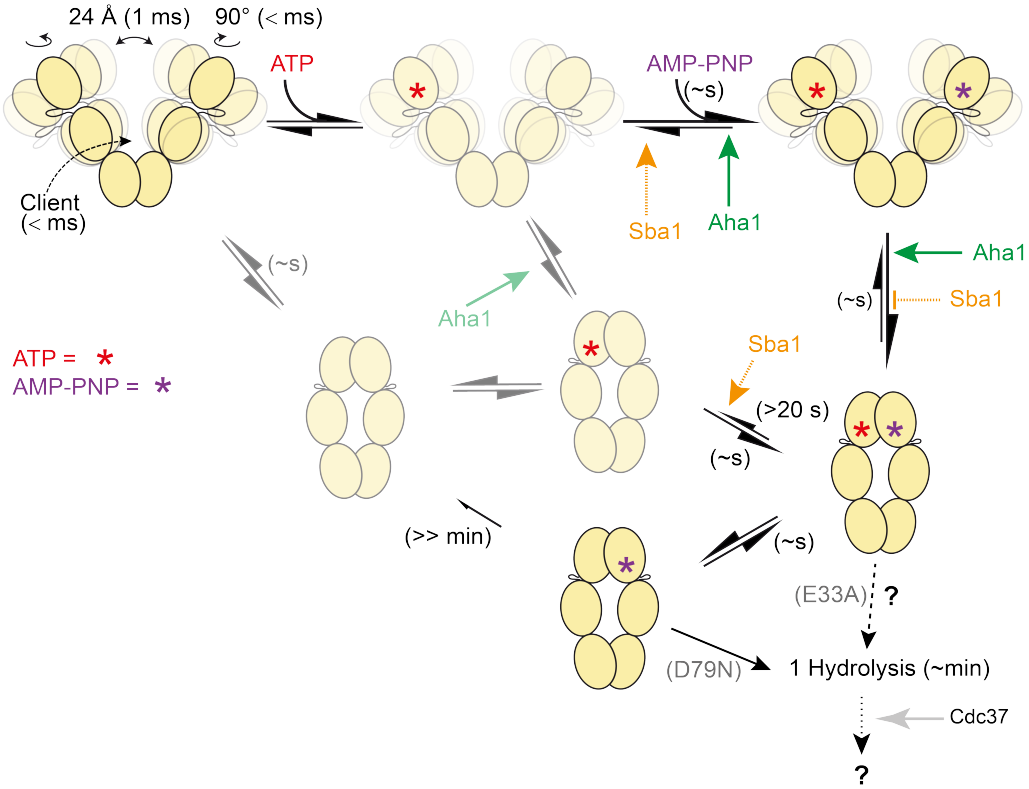

Figure 4.1: The dynamics of and regulations within the Hsp90 machine that have been characterized. States and transitions that were not in focus of this work are shown transparent. Hsp90's NTD rotates and its MD fluctuates at fast timescales with large amplitudes. The interaction with client proteins occurs mainly in this dynamic open state at similar timescales and reduces the amplitude of fast fluctuations. We found multiple effects of nucleotides and co-chaperones on state transitions as indicated. The timescales of transitions are given in brackets. The effects of ATP were studied by using labeled AMP-PNP (i.e. one ATP at the transitions state) as reporter. Within the closed conformation of Hsp90, AMP-PNP is assumed to function as transition analogue, thus to represent ATP close to hydrolysis. Published research on heterodimer mutants comprising point mutations (indicated in grey) [29] suggests that Hsp90 can hydrolyze ATP in the closed state with one ATP bound, possibly (but unlikely) also with two.

Client proteins bind to Hsp90's open conformation. Their interaction affects Hsp90 at faster timescales than the interaction with co-chaperones or nucleotides. This hints towards fast on- and off-rates for the interaction. The fast dissociation rate might be the explanation for Hsp90/client complexes being difficult to characterize with ensemble methods. It furthermore demonstrates, that the interaction itself does not depend on the ATPase activity, because again the hydrolysis rate is by far slower. The nature of the interaction between client and Hsp90 suggests an entropic chaperone, which affects the

structure of client proteins by decreasing the conformational space and thereby allows them 'to fold graciously'.

In summary, our results demonstrate the necessity for a description of the Hsp90 system as a network, because models implying that the addition of each component affects only one single state transition simplify too much. Those models therefore fail to correctly predict the behavior of Hsp90 e.g. upon the addition of inhibitors and thus impair a rational drug development.

As a member of the GHKL family, Hsp90 shares several characteristics beyond the Bergerat-fold of the ATP binding domain with other members (like the DNA supercoiling gyrase or the DNA mismatch repair protein MutL), e.g. their oligomeric nature. Most importantly, their inherent low ATPase activity is in all cases stimulated by the target molecule (i.e. DNA/client proteins) [50, 165–168] and might lead to target release [49]. Interestingly, a stepwise hydrolysis occurs in the DNA gyrase, where vanadate can inhibit the second hydrolysis [169] and DNA transport occurs after the first hydrolysis [170, 171]. Together with our findings on the cooperative binding of nucleotides to Hsp90 with implicit asymmetry between the binding pockets, this also suggests a stepwise hydrolysis in Hsp90. However, it remains unclear, if the second ATP is (or has to be) bound during the first hydrolysis event and what happens afterwards. Ensemble experiments suggest that hydrolysis occurs preferentially in absence of a second nucleotide, because the absence of nucleotide in one binding pocket (induced by the point mutation D79N) results in an increased v_{max} [29]. This hints towards an auto-regulatory mechanism of the GHKL proteins. Nevertheless, this question has to be addressed in further experiments.

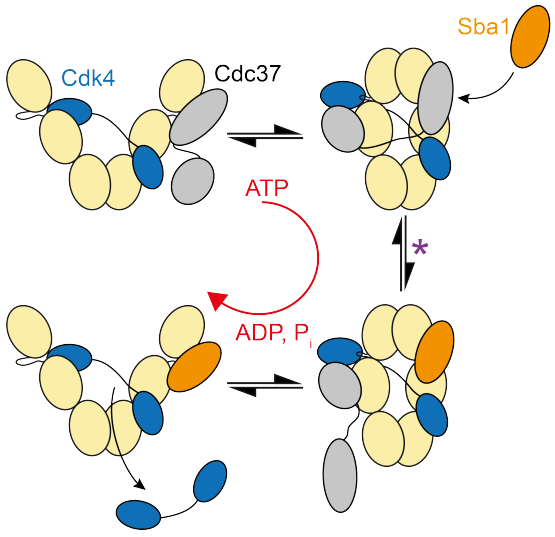

Figure 4.2: A possible function of ATP hydrolysis by Hsp90. The ATPase activity introduces directionality into the dynamic interaction of Hsp90, co-chaperones (like Sba1 and Cdc37) and client proteins (Cdk4). The purple star indicates the most likely step, where ATP hydrolysis occurs, because Sba1 preferentially binds to a post-hydrolysis state, while Cdc37 decreases the ATPase activity by decreasing Hsp90's affinity for the hydrolysis transition state represented by AMP-PNP.

None of the results directly revealed the function of the ATPase activity of Hsp90. However, there must be a function of this activity, because the potential for hydrolysis is

conserved among homologues [172]. If it was not related to Hsp90's function, this activity would have vanished within evolution, because it would mean a loss of ATP and thereby energy to a cell, decreasing the cell's fitness.

A function of the ATP hydrolysis could be the induction of directionality in the Hsp90 machine and not Hsp90 itself. The interaction of all co-chaperones with Hsp90 is affected by nucleotides. Hydrolysis could lead their transient assembly towards a non-random, step-wise manner, as the results on the interaction between Ste11, Cdc37, Sba1 and Hsp90 suggest (depicted in Fig. 4.2). However, this seems not to be essential to Hsp90's basic function in the context of the viability experiments either. But, the Hsp90 chaperone machine is also interacting with the other main chaperoning system in a cell, Hsp70 [54, 173]. Since this chaperone is an ATPase as well [174], Hsp70's ATPase activity could therefore indirectly induce directionality in the Hsp90 machine. This energy might be sufficient under physiological conditions to maintain (weak) directionality.

Chaperones are often described in the context of their function as 'holders' and 'folders'. While the holding activity is usually independent of ATP hydrolysis, the folding activity requires ATP hydrolysis [175]. Hsp90 can interact with client proteins and function as a holding chaperone without ATP hydrolysis [176, 177]. This seems to be the main function of it in a cell, and it would also explain the finding of the viability of cells expressing only Hsp90 lacking ATPase activity [51]. In some cases, however, Hsp90 consumes ATP. It seems to be an additional function of Hsp90, to actively refold client proteins, probably assisted by the set of co-chaperones, which are present at concentration in the cell by far lower than the concentration of Hsp90 itself (c.f. Section 1.2.3). Thus, it could represent a rescue mechanism for client proteins that would aggregate otherwise, a tendency that is not necessarily given with each misfolded conformation. Instead of aggregating, the client enters a stable complex with Hsp90 that is dissolved by unfolding of the client with the consumption of the energy from ATP hydrolysis by Hsp90. As the holder function of Hsp90 would always be predominant, this could also be the reason why no directionality is detectable within Hsp90's dynamics. In this context, it is interesting that for the Hsp70 chaperone a holding and a folding activity are both presumed likewise [178]. Hence, such a combination of two mechanisms could represent a more general function of large chaperone machines in the cell.

However, only integrative approaches that includes a large part of the Hsp90 machine might be able to reveal directionality and its impact on the function of Hsp90 in the future.

CHAPTER 5

Outlook: Studying the complete Hsp90 machine

Within my work, it became clear that the pair-wise interactions between Hsp90, nucleotides, co-chaperones and clients do not occur independently, but interfere with each other's effects by more than just competitive binding. Hence, the complexity of the machine is much higher than usually assumed in interpretations that aimed to describe the complete machine in a model – and the prediction quality of those models is therefore very limited.

It is therefore necessary to cope with the complete system of the Hsp90 chaperone machine in order to predict effects of e.g. inhibitors or mutations *in vivo*. The reconstitution of the machine *in vitro* from the bottom-up is still challenging, because the numer and exact stoichiometries of the single parts (i.e. co-chaperones, clients) *in vivo* always depend on the dynamic interplay between a cell and its environment.

A complementary, top-down approach is able to access the complete machine as it is, where it is – in the cell. This is the logical next step towards a more thorough understanding of Hsp90. The challenges and preliminary results of my efforts solving them are briefly presented in the following.

5.1 Challenges for smFRET in living cells

I identified the following challenges to investigations on the dynamics of a protein by smFRET in living cells:

- The imaging of the cell to determine the localization of the studied single molecule.
- The background fluorescence, which impedes the S/N ratio due to the auto-fluorescence of metabolites in a cell that are present at nano- to micromolar concentration and not necessarily isotropically distributed (e.g. NAD(P)H or flavines [179, 180]).
- The signal intensity depending on the employed fluorophores. Intrinsic labeling by fluorescent protein labels come with the disadvantage of decreased photo-stability and lower quantum yield, when compared to organic dyes, impeding the S/N ratio.
- Only a very low number of labeled proteins ($c \approx$ pM) must be present to ensure separation of single molecules.
- Site-specific labeling with one donor and one acceptor dye must be ensured.
- The diffusion of the protein must be hindered in order to access the dynamics of single proteins on the second to minute timescale.

My work on the issues presented above and and the results are briefly summarized. This work is a collaborative work together with Fernando Aprile-Garcia.[21]

21 Laboratory of Ritwick Sawarkar at the Max Planck Institute for epigenetics, Freiburg, Germany.

5.2 Towards smFRET in living cells

To decrease the background fluorescence, I construct a microscope with highly inclined laminar optical sheet (HILO) illumination in the red and near-infrared (NIR) spectrum.[22] Auto-fluorescence is mainly observed at wavelengths between 400 and 600 nm [180], thus we use lasers of the wavelengths 635 nm and 728 nm for the excitation of fluorescent dyes. In HILO illumination, only a section of a few μm within the cell is illuminated, which additionally reduces background fluorescence.

The fluorescent background in the two channels (R/NIR) differs, with a significant lower background in the NIR channel. The cell nucleus seems in general much better suited for future smFRET studies *in vivo*, because the background fluorescence is much weaker and homogenous (c.f. Appendix D.3, p. 140).

The injection of recombinantly expressed, purified and labeled protein circumvents further problems as detailed in the following. The S/N ratio is increased by employing organic fluorophores. The number of fluorescent molecules is controlled by the respective injection method. Site-specific labeling at two distinct positions can be achieved by the creation of hetero-dimers via monomer-exchange of zipped Hsp90 prior to the insertion into the cell.

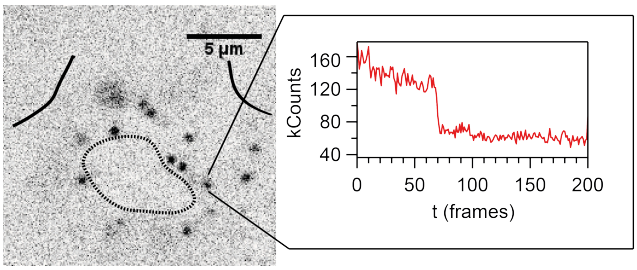

Figure 5.1: dsDNA labeled with one Cy7 fluorophore is successfully transfected into a HeLa cell and resolved as single molecule. The cellular and nuclear membrane are indicated in black. The inset shows the time dependent fluorescence at 10 Hz at the indicated spot in the cytosole. One single bleaching step indicates that this is indeed a single molecule. A control experiment in absence of transfection agent did not results in such fluorescent spots in the NIR channel. Further single molecule traces are shown in Fig. D.8 on page 142.

The organic dyes Atto647N and Cy7 as FRET donor and acceptor fluorophores have been employed in earlier smFRET studies to their relative high photo-stability, high quantum yield and high extinction coefficients [181, 182]. While Atto647N has been characterized in the previous smFRET studies, I find the NIR dyes Cy7 and Alexa750 being functional as FRET acceptors on DNA and yeast Hsp90 *in vitro* (c.f. Appendix D.1 and Appendix D.2 on page 137 ff.). However, the dyes remain photo-stable only in presence of an oxygen scavenger system. The redox potential in a cell implies a much lower oxygen concentration than in buffer solutions and should at least partly substitute for an artificial scavenger system, but scavenger systems for fluorescence experiments in cell is also available [183]. The previously characterized kinetic 4-state model of Hsp90 is successfully reproduced with the FRET pair Atto647N and Alexa750 on different positions of yeast Hsp90 Appendix D.2, proving functionality of the labeled Hsp90.

Furthermore, labeled DNA is successfully transfected into HeLa cells and traces from

22 Detailed in Section 2.1.2 on page 22.

single molecules can be observed (see Fig. 5.1).

A third excitation color at 458 nm is included in the setup, which is used to excite the green fluorescent protein (GFP) and derivatives. GFP-fusion protein (e.g. GFP-actin) can be constantly expressed within the cell of interest and thereby enable imaging of the whole cell by fluorescence. GFP does not fluoresce at R/NIR wavelengths and thus does not produce crosstalk into the detection channels for smFRET. A stable HeLA cell line expressing GFP-actin fusion protein could be imaged in the GFP detection channel (c.f. Appendix D.4, p. 141). Thus, imaging GFP fluorescence works as sensitive substitute for bright-field imaging.

So far, the remaining challenges are the incorporation of labeled protein into cells, because transfection with the DNA transfection kit produces too much background of protein stuck to the cell membrane and the localization of the protein. While the first can be solved by testing of alternative transfection methods (see also Appendix D.5, p. 141), we tackle the latter by biochemical tags for Hsp90. We created an Hsp90 tagged C-terminally with a nucleus localization sequences (NLS) that should direct Hsp90 into the nucleus. Further localization would be possible by introducing e.g. a DNA binding tag. However, we found already single molecule traces from transfected short double stranded DNA that did not feature a localization tag. This suggests that at least a fraction of inserted molecules might exhibit hindered diffusion and a localization tag is rather optional.

These first results demonstrate that our approach essentially works and thereby opens the route towards the first smFRET study on Hsp90 *in vivo*.

A Supplementary data on the dynamic structure of Hsp90

A.1 ATPase activity of Hsp90 point mutants

A detailed characterization is done for the studied protein variants depicted in Fig. A.1. This makes clear that rather the labeled protein determines the ATPase activity of each studied Hsp90 variant than the unlabeled cysteine mutant.

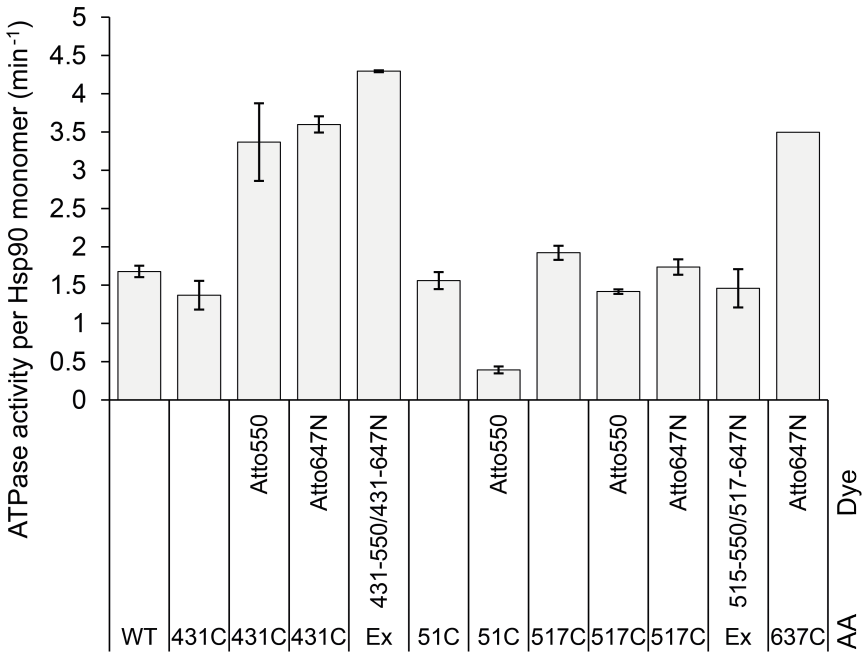

Figure A.1: The ATPase activity of the depicted constructs compared to the wild-type (WT) activity. The point mutation 51C exhibits a similar activity, but loses more than 70% of activity upon dye attachment (Atto550). The position 431C gains activity due to labeling. The ATPase activity of 517C does not significantly change upon the addition of dyes (Atto550 or Atto647N). The exchange (a 1:1 mix, which is heated 30 minutes at 47 °C) does not significantly affect the ATPase activity of the depicted variants. ATPase activity is measured with a regenerating assay with 1 μM protein under saturating ATP concentration (2 mM) at 37 °C. The error bars represent the standard deviations from three replicates.

A broad variation of activities was observed (summarized in Table A.1), but as in this project we study the structure of Hsp90 and not the kinetics of conformational transitions (which are suspected to be linked somehow to the ATPase activity, even though not directly coupled), we only excluded Hsp90 variants from our analysis that do not exhibit ATPase activity at all (which is e.g. the labeled S51C mutant). Other mutants that do not exhibit ATPase activity at all are labeled at the amino acid positions 141, 109, 179, 466.

Interestingly, we find a correlation of complete loss of ATPase activity and incomplete

closing after addition of AMP-PNP (as monitored by smFRET). Thus, this is checked for all constructs as well.

Table A.1: The ATPase activities of Hsp90 point mutants. The following single cysteine point mutations labeled with the maleiimide derivative of the depicted label are tested at 30 °C, 2 mM ATP and 1 μM protein. Two numbers indicate double cysteine mutants, ex refers to exchanged samples that are mixed in a 1:1 ratio and incubated for 30 minutes at 47 °C.

Cysteine mutation	Label	ATPase activity (monomer^{-1}min^{-1})
9	-	1.06
9	Atto550	1.90
9	Atto647N	0.71
61	Atto550	0.60
61	Atto647N	0.31
152	Atto550	1.32
159	Atto550	1.20
159	Atto647N	1.50
216	-	1.75
216	Atto550	1.54
216	Atto647N	1.60
285	Atto550	0.84
285	Atto647N	1.55
298	Atto550	0.60
298	Atto647N	0.98
327	Atto550	2.45
327	Atto647N	2.86
385	Atto550	0.87
385	Atto647N	0.96
409	Atto550	1.12
409	Atto647N	1.33
431	Atto550	1.92
431	Atto647N	1.74
452	Atto550	2.47
452	Atto647N	2.20
503	Atto550	1.87
503	Atto647N	1.95
517	Atto532	0.68
517	Atto550	0.69
517	Atto647N	0.71
61/452	Atto550/Atto647N	0.19
61/431	Atto550/Atto647N	1.12
152/452	Atto550/Atto647N	2.02
Ex 61 & 431	Atto550 & Atto647N	0.76
Ex 61/452 & WT	Atto550/Atto647N & -	0.37

A.2 Combined anisotropy threshold for open Hsp90

The RMSD between the optimal structure arrangement for the open conformation of Hsp90 and the smFRET derived distances depends on the combined anisotropy r_c, similar to what we find for the closed state of yHsp90. We apply a threshold on r_c at 0.21, because lower thresholds do not result in an improved RMSD. The remaining 81 distances have an RMSD of about 4 Å.

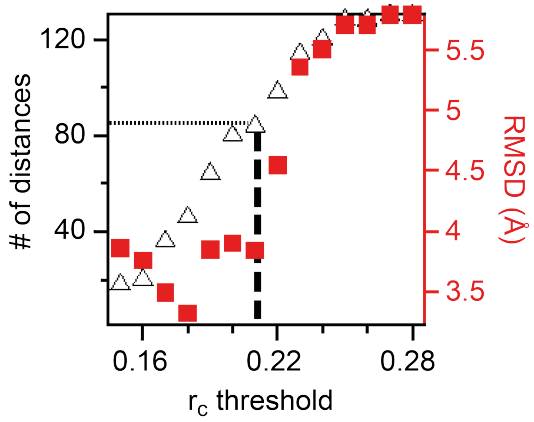

Figure A.2: RMSD between optimal structure arrangement for the open state of Hsp90 and the r_c threshold applied on the set of distances.

A.3 Molecular dynamics simulations

Molecular dynamic (MD) simulations on the structure of Hsp90 are conducted by Florian Kandzia and Martin Zacharias, TU München, Munich. Their methods and implementation are described in the following. The text is retrieved from the joint publication on the dynamic structure of open Hsp90 [3].

Restrained MD simulations

MD simulations and energy minimization to generate Hsp90 structural models are performed using the Sander module of the Amber14 molecular simulation package [184]. During structural modeling the core structures of the single domains are restrained to experimental reference structures by adding distance restraints between C_α atoms within 15 Å(force constant 3 kcal $mol^{-1}Å^{-2}$). This allows translational and rotational mobility but limits internal flexibility in each domain. Additionally, the core structure of the C-domains is kept close to the geometry of the X-ray structure owing to the corresponding experimental distances being equal in the presence of ADP and AMP-PNP. For the structure generation steps, an implicit solvent model with a distance dependent dielectric constant ($\varepsilon = 4r$) is employed.

As start structure the -2σ domain arrangement is used. The connection between the NTD and MD is modeled by a short Gly_{10} linker inserted between residues 216 and 261. For inclusion of the FRET-derived distance data, pseudoatoms with a van-der-Waals radius of 6.5 Å, representing approximately the size of the dyes, are connected to the C_β atoms of the dye-labeled residues using a pseudobond (linker) of 11 Å. The distance between each donor–acceptor pseudoatom pair is allowed to vary within an interval given

by the experimentally determined FRET-derived distance range. Beyond the allowed distance interval, further variation is penalized with a force constant of 3 kcal $mol^{-1}Å^{-2}$. In addition, the optimal spatial NTD/MD-arrangement in the dimer serves as additional positional restraints (on heavy atoms, with a force constant 1 kcal $mol^{-1}Å^{-2}$) during MD based structure generation. To keep the structure symmetric with respect to the spatial arrangement of each monomer, the option to penalize the difference between two distances implemented in the sander module of the Amber14 package is employed. The option is applied to a subset of equivalent backbone distances within each monomer and between monomers. MD simulations are performed for 0.5 ns at 450 K followed by 0.5 ns at 300 K using a time step of 0.001 ps. Structures are energy minimized within 7,500 steps of conjugate gradient minimization. Structural models of the open Hsp90 structure are re-evaluated by the FPS to check compatibility with the FRET data. The final mean structure yield an average deviation from the FRET distance data of $\chi^2 < 0.3$.

Unrestrained MD simulations

In addition to restrained MD simulations in implicit solvent for structure generation, unrestrained simulations starting from the mean open ADP-bound Hsp90 structure are performed in the presence of explicit solvent and surrounding ions. The structure is solvated in a truncated octahedral box with explicit TIP3P water molecules [185] and neutralized with sodium and chloride ions by means of the leap module and employing the parm14SB force field [186]. Long-range electrostatic interactions are calculated with the particle mesh Ewald (PME) method and a real space cutoff radius of 9 Å[187]. During 0.5 ns equilibration the system is heated up to 300 K while heavy atoms of the protein are harmonically restrained (25 kcal $mol^{-1}Å^{-2}$) to positions in the starting structure. Positional restraints are gradually removed during another 0.15 ns. Then the structures are equilibrated for 0.2 ns in an unrestrained simulation. The simulation is extended to 100 ns at 300 K and a pressure of 1 bar. For comparison, explicit solvent MD simulations are started from the closed crystal structure of Hsp90 (PDB 2CG9) after removing the co-chaperone Sba1 and supplementing with the same Gly_{10} linker between N- and M-domain as used for modeling the open Hsp90 structures. Equilibration follows the same protocol, and simulations are extended to 100 ns. Several thousand structures in the form of simulation snapshots are evaluated by the FPS, resulting in an average χ^2 of 1.5. The generated trajectories are evaluated using the cpptraj module of the Amber14 package. Calculations of the RMSD of the backbone and RMSF are performed using the cpptraj module. The RMSF is calculated as the mean over all heavy atoms of each residue. For a subset of 200 snapshots of the open and closed simulations, the buried surface area (BSA) of the CTD/MD interface are calculated. Therefore, the solvent-accessible surface area of the CTD, MD and both domains is calculated atom-wise using the SHRAKE algorithm [188]. This is done for both monomers of the Hsp90 dimer, and the arithmetic mean is used in the following. For each residue the normalized total contribution as well as the number of contributions to the BSA is determined. The same procedure is repeated for the NM interface.

B Supplementary data on the cooperativity in Hsp90

B.1 Characterization of fluorescent nucleotide analogues

In the following, the characterization of different fluorescent nucleotide analogs and the results are described briefly.

B.1.1 Binding of labeled nucleotides to Hsp90

Binding of different fluorescent analogs to Hsp90 is tested by measuring fluorescence anisotropy on a fluorescence spectrometer. All nucleotides exhibit very low anisotropies in buffer. The binding to a macromolecule such as Hsp90 is expected to result in an increase of the anisotropy. Thus, Hsp90z is titrated stepwise to a solution of 500 nM nucleotide up to 10 μM protein concentration. Experiments are conducted at 25 °C. At these conditions, only analogs labeled with the fluorophore at the γ-position exhibit binding to Hsp90 Section 3.2.1 (p. 68). The type of linker that tethers the dye to the γ-phosphate of the nucleotide, as well as the type of nucleotide (ATP or AMP-PNP) affects the binding affinity, but the K_d values remain within the same magnitude.

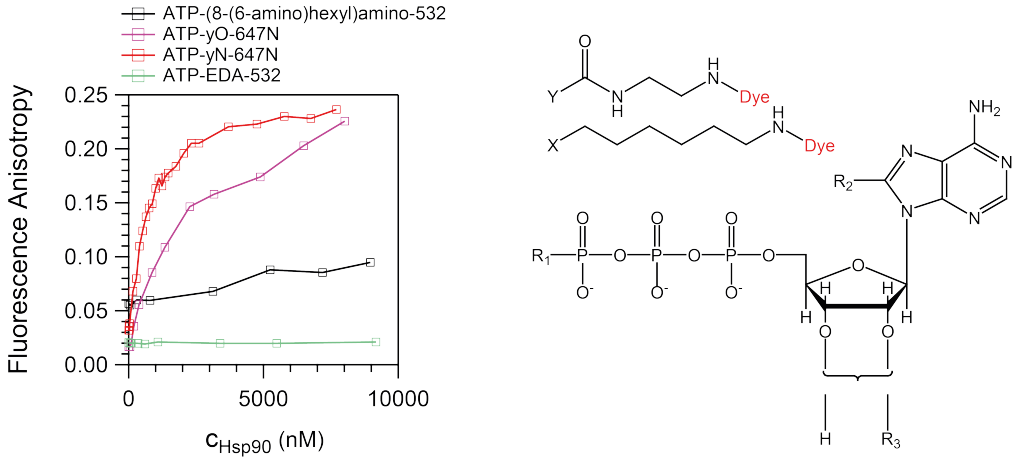

(A) **(B)**

Figure B.1: Binding of different fluorescent ATP analogs to Hsp90. (A), titration of labeled nucleotide with Hsp90z. Binding is monitored by fluorescence anisotropy of the respective dye. (B), structures of the different analogs. ATP-(8-(6-amino)hexyl)amino-Atto532: R_1=OH, R_2=H, R_3=-NH-X. ATP-yO-Atto647N: R_1=-O-X, R_2=H, R_3=H. ATP-yN-Atto647N: R_1=-NH-X, R_2=H, R_3=H. ATP-EDA-Atto532: R_1=OH, R_2=Y, R_3=H.

B.1.2 Binding of AMP-PNP to Hsp90 in literature

In Table B.1 the published experimental data on the affinity of Hsp90 for AMP-PNP that should not be affected by artifacts like spontaneous hydrolysis of reducing agents is presented. For the same reason, ATP titrations in ITC are also not considered. The overall average K_d for binding of AMP-PNP to Hsp90 is 62±41 μM, which means the affinity of Hsp90 for AMP-PNP is only known within an uncertainty of one order of magnitude.

Table B.1: Published experimental data on the affinity of Hsp90 for AMP-PNP. ITC, isothermal titration calorimetry; CD, circular dichroism titration. ITC data recorded in presence of DTT is not shown, because spontaneous hydrolysis renders the respective experiments useless.

Methods	Temperature	Homologue	K_d (μM)	Literature
ITC	25°C	human Trap1	109	[42]
ITC	30°C	yeast Hsp90	111	[34]
CD	n.a.	yeast Hsp90	33	[41]
ITC	25°C	yeast Hsp90	30	[189]
ITC	25°C	human Hsp90a N-domain	8	[38]
ITC	30°C	human Hsp90b	85	[190]

B.1.3 ATPase activity of Hsp90 with labeled nucleotides

Possible hydrolysis of the nucleotide analogues labeled with fluorescent dyes is tested by the regenerating ATPase assay. 20 μM labeled nucleotide is incubated at 37 °C with 1 μM Hsp90z and the hydrolysis of ATP is monitored by a decrease in absorbance by NADH. For unlabeled ATP, an ATPase rate of 0.1 ±0.05 $mol^{-1}min^{-1}$ is found. A similar rate is found for the nucleotide analogue EDA-ATP-Atto532. An exemplary trace is shown in Fig. B.2. For all other nucleotides no hydrolysis can be observed. Higher nucleotide concentrations are not accessible due to the limited amount of sample.

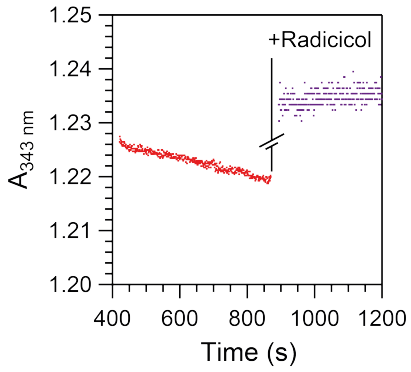

Figure B.2: EDA-ATP-Atto532 is hydrolyzed by Hsp90. Hydrolysis is monitored by a decrease in absorbance of NADH at 343 nm. The oxidation of NADH is coupled to the ATP hydrolysis in a 1:1 stoichiometry. Reaction is stopped by the addition of 100 mM radiciol (purple data points). Due to absorbance of radiciol, the y-axis is shifted but not rescaled.

To further assess the possible hydrolysis of the high affine γ-labeled nucleotides, these

analogs are incubated at 1 μM after the addition of 1 μM Hsp90 at 30 °C (and, in case of ATP in presence of 20 μM Aha1). Hydrolysis would lead to cleavage of the bond between β- and γ-phosphate and thus set the label free. This would in turn result in a decrease in fluorescence anisotropy. This does not happen. Hence, no hydrolysis of AMP-PNP or ATP occurs when the nucleotide is linked to a fluorescent dye by a C_4-linker, neither for an N-, nor for an O-linker.

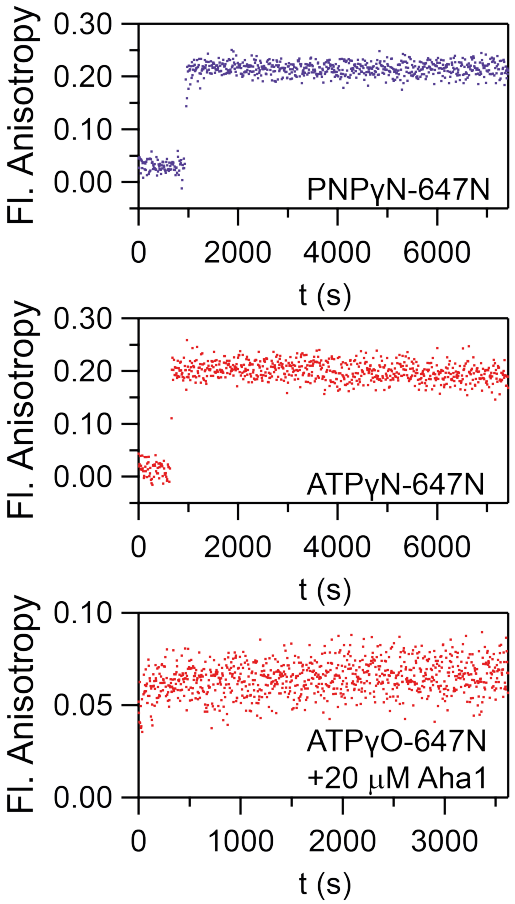

Figure B.3: γ-phosphate labeled fluorescent nucleotide analogues are not hydrolyzed by Hsp90, as measured by fluorescence anisotropy. A hydrolysis would lead to a decrease of the fluorescence anisotropy of the label. The studied reporter nucleotide is indicated. The step in the first two graphs indicates the addition of Hsp90.

Thus, the only fluorescent nucleotide analogue that allows the observation of binding to and hydrolysis by Hsp90 would be EDA-ATP variant. Unfortunately, this nucleotide does not bind with high affinity to Hsp90 (another property it shares with the native substrate). It therefore would allow single molecule studies only in an experimental setups with extremely small observation volume, such as a setup that uses zero mode waveguide excitation.

B.1.4 Effects of molybdate and temperature on binding of AMP-PNP-647N

The high affinity of Hsp90 for AMP-PNP-647N is used for further characterization of the interaction between Hsp90 and AMP-PNP. Molybdate is a non-competitive inhibitor of Hsp90's ATPase activity and modifies the structure of Hsp90 [30, 191]. It strengthens the binding of labeled AMP-PNP to Hsp90 (c.f. Fig. B.4(A)).

The AMP-PNP binding to Hsp90 is also temperature dependent, as shown in Fig. B.4(B). Fitting with the K_d model, the affinity drops by factor of two, when the temperature is increased from 20 to 30 °C. This contradicts the general finding of increased ATPase activity with increased temperature on the first sight, however, the binding/dissociation of nucleotide is not rate-limiting for the hydrolysis. The increased temperature increases the contribution of entropy ΔS to the Gibbs free enthalpy ΔG for the binding according to:

$$\Delta G = \Delta H - T \cdot \Delta S \tag{B.1}$$

with ΔH being the change in entropy upon complex formation. Thus, a decreased binding equilibrium at increased temperature hints towards an enthalpy-driven binding. Further studies will be necessary for validation of this first finding.

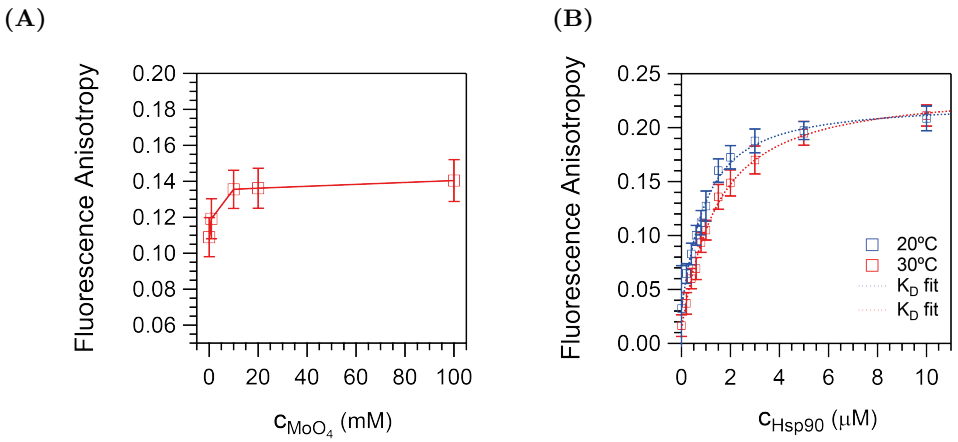

Figure B.4: Effects of MoO_4 and temperature on the affinity of Hsp90 for AMP-PNP-647N. (A), 500 nM labeled nucleotide and 1 μM Hsp90z are titrated with increasing amounts of MoO_4 at 25 °C. (B), titration of 500 nM labeled nucleotide with Hsp90 at 20 and 30 °C.

B.1.5 The ensemble effects of co-chaperones Aha1 and Sba1 on binding of AMP-PNP-647N

The effect of the co-chaperones Sba1 and Aha1 on the equilibrium binding of AMP-PNP-647N to Hsp90 is measured by fluorescence anisotropy. 500 nM Nucleotide are titrated with Hsp90z wild-type at 25 °C in presence of either 5 μM Sba1 or 10 μM Aha1. Only for Aha1 a slight effect is found, as shown in Fig. B.5. The apparent K_d increases in that case by factor of two.

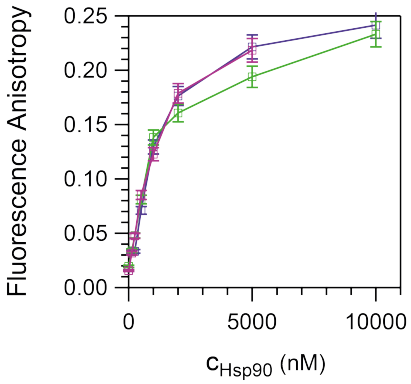

Figure B.5: The effect of the co-chaperones Sba1 and Aha1 on the affinity of Hsp90 for AMP-PNP-647N. Compared to the experiment in absence of co-chaperones (purple), no effect is observed for Sba1 (violet), Aha1 (green) slightly increases the K_d for the Hsp90/AMP-PNP interaction.

B.2 The effect of AMP-PNP on the ATPase activity of Hsp90

Due to the observed cooperativity between the two nucleotide binding pockets, AMP-PNP should also effect the ATPase activity of Hsp90, as soon as binding of two ATP becomes unlikely. This is only the case at low ATP concentration. Because of the Michaelis-Menten like enzymatic activity of Hsp90 the ATPase activity of Hsp90 drops non-linearly with decreased substrate concentrations. This complicates studies at low ATP concentrations, as the S/N ratio decreases.

To test the effect of AMP-PNP on the ATPase activity of Hsp90, 500 nM Hsp90z are incubated with 400 nM ATP in the regenerating ATPase assay at 37 °C. After 1 hour of pre-incubation and equilibration, the ATPase activity is measured for 10 minutes. Then, the same volume of either buffer or solutions of different concentration of AMP-PNP or AMP-PNP-647N is added, the reaction is equilibrated for another hour and subsequently ATPase activity measured for 10 minutes. Each experiment is replicated three times (all experiments from the same stock reaction), and the ratio of ATPase activity after/before addition is calculated per experiment. Standard deviation is calculated from the replica. The results are shown in Fig. B.6. A slightly accelerating effect of AMP-PNP in comparison to buffer is observed at micro-molar AMP-PNP concentration (as well as a stronger for the addition of labeled nucleotide). At higher AMP-PNP concentrations, the effect is diminished.

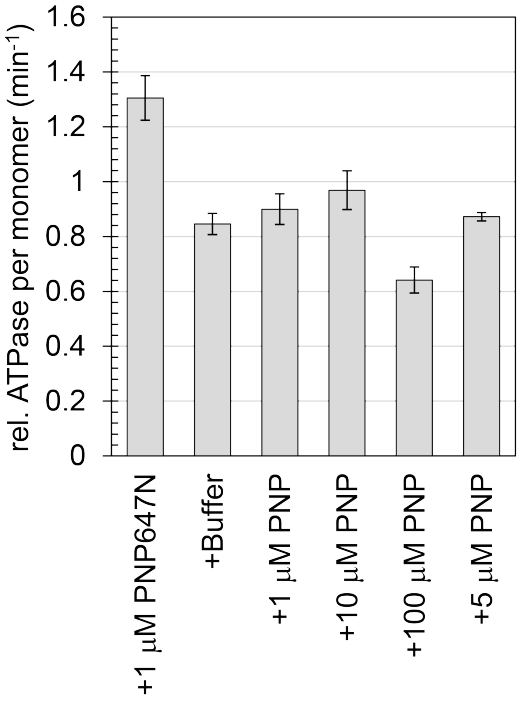

Figure B.6: Steady-state ATPase activity of Hsp90 and the effects of AMP-PNP on it. Low amounts of AMP-PNP can slightly accelerate the ATPase activity of Hsp90. Error bars represent standard deviation from three replicates.

B.3 ATPase activities of the Hsp90 variants

The ATPase activities of Hsp90z D61C-Atto488Mal and Hsp90z Q385C-Atto550Mal Biotin are measured at a protein concentration of 1 μM, 37 °C and saturating ATP (2 mM). Both variants exhibit an ATPase activity similar to wild-type Hsp90z.

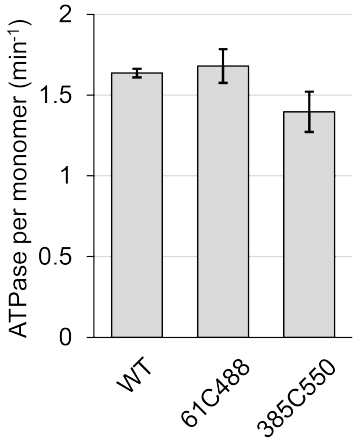

Figure B.7: Steady-state ATPase activity of the labeled Hsp90 mutants used throughout the experiments. Error bars represent standard deviation from three replicates.

B.4 Data variation

The evaluated data sets are the combined data from multiple experiments, because we find rather strong variations among different experiments conducted at the same conditions. The number of experiments that are evaluated for each conditions is given in Table B.2.

Table B.2: Number of experiments that are evaluated in a merged data set.

Reporter	Additive	No. of experiments
PNP*	-/-	3
PNP*	250 μM AMP-PNP	3
PNP*	250 μM ATP	3
PNP*	2.5 mM ATP	1
PNP*	10 μM Aha1	3
PNP*	10 μM Aha1 + 250 μM ATP	2
PNP*	10 μM Sba1	3
PNP*	10 μM Sba1 + 2.5 mM ATP	1
ATP*	-/-	1
ATP*	2.5 mM ATP	1

The variation among data sets affects the dwell time, the relative population and the HMM derived transition rates. We test this for data sets of Hsp90+PNP* in absence of nucleotide and in presence of 250 μM ATP. As can be seen in Fig. B.8, we find the average dwell time and the relative population to be more robust than the transition rates (Fig. B.9). Therefore, data sets consisting of one or two experiments are analyzed on their level and the transition rates are not considered for further analysis. The data set of Aha1+ATP is an exception because of the large number of traces included, which should compensate the problem to a certain degree.

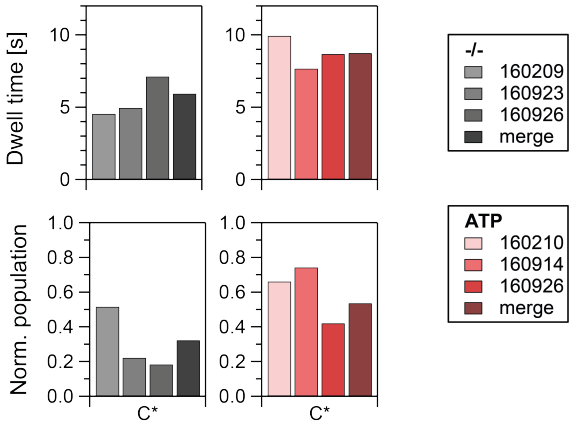

Figure B.8: Data set variation (1). Three experiments of Hsp90 with PNP* in absence (-/-) and presence of 250 μM ATP (ATP), depicted by the date of recording, are evaluated separately and together (merge). The variation of the evaluated average dwell time (top) and normalized, PNP* bound populations (bottom) is shown.

Technically, mainly the association rates involving labeled nucleotide should differ, because the concentration 25 nM labeled nucleotide will vary a lot between the experiments.

Labeled species tend to adsorb at surfaces and the PEG-ylation of the measurement chamber (to prevent adsorption) is not perfect – therefore the amount of adsorbed labeled nucleotide will vary. However, we find all populations and rates affected. As there is no reason to exclude single experiments from the result and all experiments should in principle represent the same studied system, we decided to analyze the merged data. In principle, this leads to a (non-linearly) weighted averaging of the different analyzed quantities. We assume, that the joint data samples represent the system's properties to a much larger extend than the single data sets and therefore believe that the error estimation from the merged data is more accurate than simple averaging of the analysis results on the single data sets.

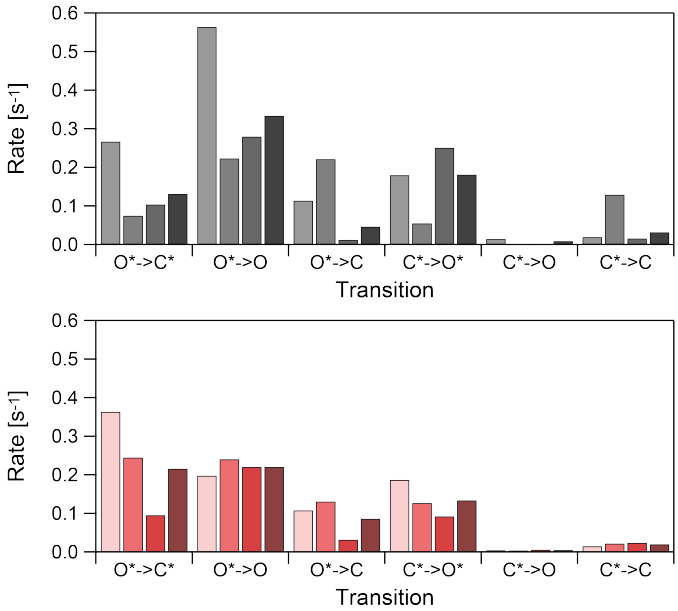

Figure B.9: Data set variation (2). Three experiments of Hsp90 with PNP* in absence (-/-) and presence of 250 μM ATP (ATP), depicted by the date of recording, are evaluated separately and together (merge). The variation of the HMM derived state transition rates is shown.

The data varies also regarding the position of the different populations. However, this is most likely due to the experimental setup (illumination and chamber change between the experiments) and is solved by fitting 3D Gaussians with the x,y,z position free. We do not observe a correlation between the populations' positions and certain conditions.

B.5 Data statistics

B.5.1 Data sets

In Table B.3, the statistics of all data sets used to evaluate the nucleotide binding properties of Hsp90 and its modulation. Dwells are allocated by the HMM analysis as described. The mean trace length is derived from a single exponential fit to a cumulative histogram over all trace lengths.

Table B.3: Statistics of the evaluated data sets. Shown are the number of traces, the allocated open dwells of the labeled nucleotide on Hsp90 and the mean trace length (τ_b).

Reporter	Additive	n (dwells)	n (traces)	τ_b (s)
PNP*	-/-	879	485	25.25
PNP*	250 μM AMP-PNP	1598	972	25.26
PNP*	250 μM ATP	1400	871	22.0
PNP*	2.5 mM ATP	329	180	24.1
PNP*	10 μM Aha1	939	666	23.2
PNP*	10 μM Aha1 + 250 μM ATP	829	647	19.5
PNP*	10 μM Sba1	746	443	17.6
PNP*	10 μM Sba1 + 2.5 mM ATP	251	129	20.6
ATP*	-/-	258	189	16.1
ATP*	2.5 mM ATP	74	78	12.5

B.5.2 Populations, average dwell times and tta

In Table B.4, the results from the data evaluation are shown, for the normalized populations of the states C^* and O^*, and the average dwell time (all open dwells included) and the time to absorbtion (tta). This data is the basis for the figures 3.22, 3.23, 3.24, 3.27 and 3.28.

Table B.4: Normalized populations, average dwell time and time to absorption found in the shown experiments. <d. t.>, average dwell time. Expriments were conducted at a resolution of 200m̃s/frame.

Reporter	Additive	Norm. pop C^*	Norm. pop O^*	<d. t.> (frames)	tta (frames)
PNP*	-/-	0.68±0.04	0.32±0.02	29.7±0.3	36.9
PNP*	250 μM AMP-PNP	0.42±0.02	0.58±0.04	43.9±0.3	61.8
PNP*	250 μM ATP	0.43±0.03	0.57±0.03	43.8±0.3	62.6
PNP*	2.5 mM ATP	0.31±0.04	0.69±0.04	43.9±0.7	63.5
PNP*	Aha1	0.38±0.02	0.62±0.03	38.5±0.3	54.9
PNP*	Aha1+250 μM ATP	0.69±0.02	0.69±0.02	35.1±0.3	48.3
PNP*	Sba1	0.31±0.01	0.31±0.03	30.4±0.3	41.0
PNP*	Sba1+2.5 mM ATP	0.65±0.04	0.35±0.08	13.9±0.2	18.8
ATP*	-/-	0.64±0.03	0.36±0.04	29.7±0.3	36.9
ATP*	250 μM ATP	0.27±0.03	0.73±0.02	22.3±0.5	34.4

B.5.3 Rates

In Table B.5, the results from the HMM analysis of the data sets with labeled AMP-PNP (PNP*) as reporter nucleotide are shown. These numbers are the basis for Fig. 3.23 and Fig. 3.25.

Table B.5: Transition rates in the depicted data sets with PNP* as reporter nucleotide as results of the HMM analysis (given in s^{-1}).

Additive	$O^* \rightarrow C^*$	$O^* \rightarrow O$	$O^* \rightarrow C$	$C^* \rightarrow O^*$	$C^* \rightarrow O$	$C^* \rightarrow C$
-/-	0.13	0.33	0.047	0.18	$9.1{\cdot}10^{-3}$	0.032
ATP	0.22	0.22	0.086	0.13	$4.8{\cdot}10^{-3}$	0.020
AMP-PNP	0.28	0.23	0.073	0.13	0.014	0.021
Aha1	0.39	0.32	0.062	0.21	$2.6{\cdot}10^{-3}$	0.021
Aha1+ATP	0.55	0.32	0.086	0.23	0.013	0.031

B.5.4 Wilcoxon-Mann-Whitney two-sample rank test results

The Wilcoxon-Mann-Whitney two-sample rank test compares the sums of all possible pairs x_i/y_j between two data sets X and Y by the median of the sum distribution. Therefore, it is not sensitive for certain differences between data sets: as soon as distributions exhibit multiple exponentials (as it is the case for dwell times as soon as more than a two state system is studied), changes in the two exponentials may lead to a different weighting in the sum rank and therefore render the test insensitive to actual differences. We believe this is the case for the data sets, where the average dwell times vary a lot (far beyond the error estimated by jackknife-1), but the test result is positive (i.e., the H_0 hypothesis of both data sets originating from the same distribution must be accepted within the 95 % CI). As an example, the integrated dwell time distributions of the experiment with Hsp90/PNP* in presence of ATP, Aha1 or ATP+Aha1 are shown in Fig. B.10, where the test is denying significant differences (shown in Table B.6).

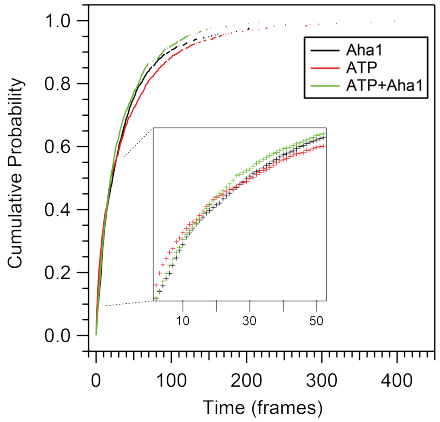

Figure B.10: The integrated dwell time histograms of the data sets Hsp90/PNP* +ATP, +Aha1 and +ATP/Aha1. The dwell time distributions cross. This is caused by different changes of the multiple exponentials underlying this distribution and causes the sum rank test to neglect significant differences.

Table B.6: p-values of unpaired Wilcoxon-Mann-Whitney two-sample rank test.

Data 1	-/-	-/-	ATP	Aha1	Aha1	Aha1	Aha1 +ATP	Aha1 +ATP	Aha1 +ATP	Aha1 +ATP
Data 2	ATP	PNP	PNP	PNP	ATP	-/-	ATP	-/-	PNP	Aha1
p	$1.97{\cdot}10^{-09}$	$6.38{\cdot}10^{-12}$	0.485	0.37	0.15	$2{\cdot}10^{-14}$	0.9815	$9.73{\cdot}10^{-10}$	0.526	0.139
Data 1	Sba1	Sba1	Sba1	Sba1	Sba1 +2.5 mM ATP	Sba1 +2.5 mM ATP	Sba1 +2.5 mM ATP	Sba1 +2.5 mM ATP	Sba1 +2.5 mM ATP	Sba1 +2.5 mM ATP
Data 2	Sba1 +2.5 mM ATP	250 μMATP	-/-	Aha1	2.5 mM ATP	Aha1	-/-	2.5 mM ATP	Aha1	-/-
p	$1.97{\cdot}10^{-09}$	$6.38{\cdot}10^{-12}$	0.485	0.37	0.15	$2{\cdot}10^{-14}$	0.9815	$9.73{\cdot}10^{-10}$	0.526	0.139

B.5.5 Shapiro-Wilk test results

The open, PNP* bound populations are tested separately. Tests on the joint O* populations in each subset result in even better probabilities.

Table B.7: The p-values and test statistics of the Shapiro-Wilk test on the different populations.

Population	Reporter	Additive	p-value	SW statistic
C^*	PNP*	-/-	0.769	0.958
C^*	PNP*	250 μM ATP	0.558	0.940
C^*	PNP*	250 μM AMP-PNP	0.936	0.975
C^*	PNP*	Aha1	0.025	0.819
C^*	PNP*	Aha1+250 μM ATP	0.156	0.887
C^*	PNP*	Sba1	0.818	0.963
C^*	PNP*	Sba1+2.5 mM ATP	0.030	0.827
C^*	ATP*	-/-	0.23	0.902
C^*	ATP*	2.5 mM ATP	0.973	0.982
O_1^*	PNP*	-/-	0.805	0.962
O_1^*	PNP*	250 μM ATP	0.545	0.939
O_1^*	PNP*	250 μM AMP-PNP	0.533	0.938
O_1^*	PNP*	Aha1	0.352	0.919
O_1^*	PNP*	Aha1+250 μM ATP	0.144	0.884
O_1^*	PNP*	Sba1	0.416	0.927
O_1^*	PNP*	Sba1+2.5 mM ATP	0.117	0.876
O_1^*	ATP*	-/-	0.754	0.957
O_1^*	ATP*	2.5 mM ATP	0.0599	0.851
O_2^*	PNP*	-/-	0.794	0.961
O_2^*	PNP*	250 μM ATP	0.420	0.927
O_2^*	PNP*	250 μM AMP-PNP	0.411	0.926
O_2^*	PNP*	Aha1	0.412	0.926
O_2^*	PNP*	Aha1+250 μM ATP	0.686	0.951
O_2^*	PNP*	Sba1	0.973	0.982
O_2^*	PNP*	Sba1+2.5 mM ATP	0.594	0.944
O_2^*	ATP*	-/-	0.125	0.878
O_2^*	ATP*	2.5 mM ATP	0.618	0.946

B.5.6 t-test results on the closed, AMP-PNP-647N bound population C^*

Table B.8: The p-values of unpaired pair-wise t-tests on the C^* population. [1], $c_{nuc} = 250\,\mu$M; [2], $c_{nuc} = 2.5\,m$M. All data sets are measured with PNP* as reporter besides the data set is indicted with ATP*.

Data set	-/-	ATP[1]	AMP-PNP[1]	Aha1	Aha1+ATP[1]	ATP[2]	Sba1
ATPP[1]	$1.8{\cdot}10^{-14}$						
AMP-PNPP[1]	$2.3{\cdot}10^{-11}$	0.40					
Aha1	$4.7{\cdot}10^{-12}$	$6.0{\cdot}10^{-4}$	0.0094				
Aha1+ATPP[1]	$5.0{\cdot}10^{-19}$	$1.0{\cdot}10^{-12}$	$1.8{\cdot}10^{-9}$	$1.1{\cdot}10^{-7}$			
ATP[2]	$1.3{\cdot}10^{-13}$	$1.9{\cdot}10^{-11}$					
Sba1	$2.7{\cdot}10^{-6}$	$8.5{\cdot}10^{-15}$			$9.2{\cdot}10^{-15}$		
Sba1+ATP[2]	$7.9{\cdot}10^{-4}$	$2.5{\cdot}10^{-16}$				$8.9{\cdot}10^{-18}$	$1.5{\cdot}10^{-7}$
ATP*	0.67	$5.0{\cdot}10^{-16}$				$4.0{\cdot}10^{-15}$	

B.6 Limitations of the Hill plot in the detection of weak cooperativity

Among the available methods describing the concentration dependent equilibrium between protein an ligand, the Monod-Wyman-Changeux model [192], based on the idea of conformational selection, describes Hsp90 the best. That is, a protein that can populate different states, from which at least two states are able to bind nucleotide [99].

According to Stefan et al. [193], the saturation of a protein with two conformations and n binding sites for a ligand X that it can bind in both conformations is calculated by:

$$\Theta = \frac{(1+\alpha)^{n-1} + L \cdot c \cdot \alpha(1+c\cdot\alpha)^{n-1}}{(1+\alpha)^n + L\cdot(1+c\cdot\alpha)^n} \tag{B.2}$$

$$L = \frac{[T_0]}{[R_0]} \qquad c = \frac{K_d^R}{K_d^T} \qquad \alpha = \frac{X}{K_d^R} \tag{B.3}$$

with L being the allosteric isomerisation constant describing the equilibrium between the two states, K_d^i being the dissociation constant of state i and α being the fractional occupancy.

The expected Hill plots displaying the log of fractional saturation versus log of the ligand concentration are calculated for $n = 2$, $L = 20$ and $K_d^1 = 50\mu$M, varying K_d^2. The assumed values are in the range of published data and our observations regarding the open/close equilibrium of Hsp90 and the affinity for binding nucleotide. The resulting Hill plots are shown in Fig. B.11.

It is concluded that Hill plots and equilibrium measurements on such a system are struggling from the detection of a cooperativity with $c = K_d^2/K_d^1 \leq 10$. At $c = 10$, the maximum slope within the plot is 1.25, and by applying a linear fit to the complete data from an experiment a much smaller slope would be found. Thus, experiments with an fitting error of ± 0.1 [40] would not be able to detect such a cooperativity. Varying L and K_d^1 has a negligible effect on this result. However, Hsp90 populated at least four different states; thus the system is even more complex and a the model might not fully apply. Nevertheless, this should not facilitate the detection of cooperativity from equilibrium experiments.

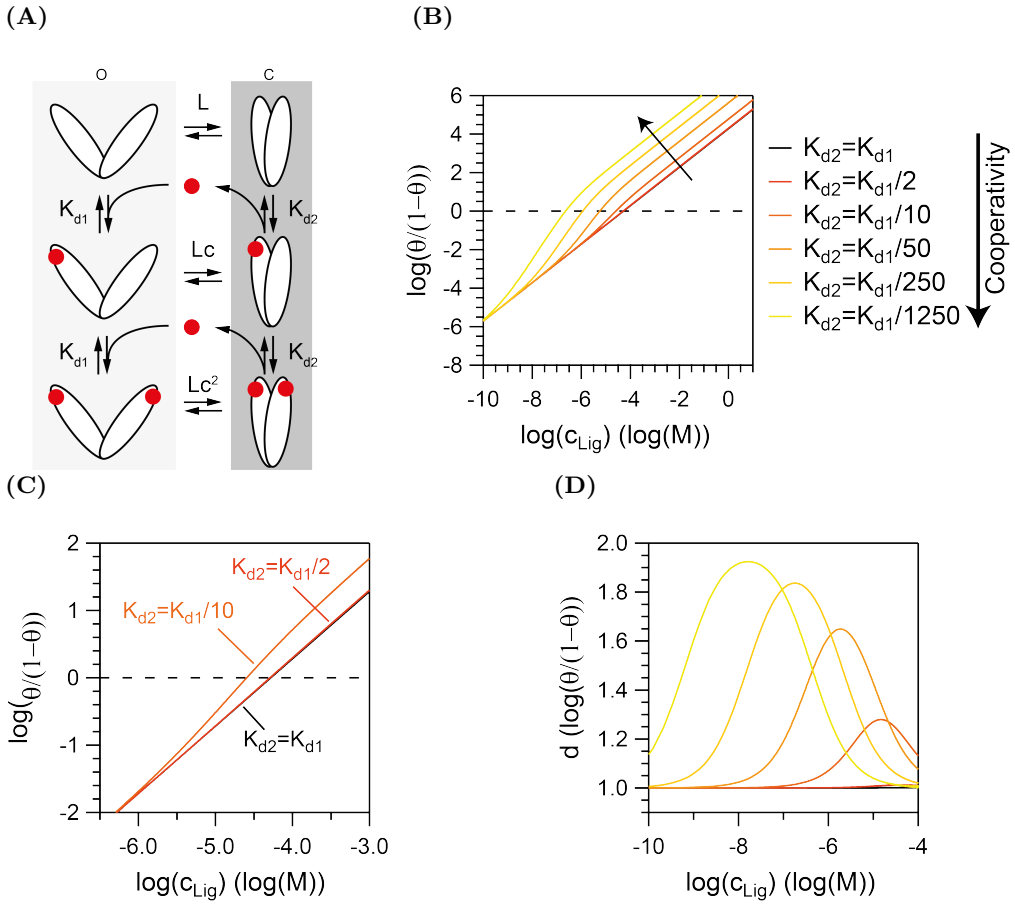

Figure B.11: Hill plots cannot detect weak cooperativity. (A), the MWC model applied on Hsp90. O, open, C, closed conformation. (B), Hill plots from the two-state system presented in (A) with differing c-values. (C), zoom in (B). (D), slopes of the different graphs in (A).

C Supplementary data on the Cdc37-Hsp90 fusion protein

C.1 Concentration estimate for the tethered proteins

The tether between the two proteins is treated as a linear combination of two worm-like chains (WLCs) connected by a SR. Prolines are included within the RCs and the contour length per amino acid within is estimated 0.38 nm [161, 194]. Each of the two RCs consists of 47 amino acids. The length of an α-helix is estimated as 0.15 nm per amino acid [195]. The average 1-dimensional mean square end-to-end distance in each RC (considered as freely jointed chains) and the SR are calculated by Eq. (C.1) and Eq. (C.2).

$$\sqrt{\overline{d_{RC}^2}} = \sqrt{N_{aa} \cdot a^2} = \sqrt{47} \cdot 0.38\, nm = 2.61\, nm \tag{C.1}$$

$$d_{sr,x} = N_{aa} \cdot 0.15\, \frac{nm}{aa} = 15 \cdot 0.15\, \frac{nm}{aa} = 2.25\, nm \tag{C.2}$$

Assuming the three components to add up independently and neglecting the asymmetrical distance distribution in freely jointed chains, the average end-to-end distance is estimated:

$$\overline{d_x} = \sqrt{\overline{d_x^2}} = \sqrt{2 \cdot d_{rc,x}^2 + \cdot d_{sr,x}^2} = 4.32\, nm \tag{C.3}$$

The three dimensions of the linker are independent, thus:

$$\overline{d_{3D}^2} = \overline{d_x^2} + \overline{d_y^2} + \overline{d_z^2} = 3 \cdot \overline{d_x^2} \tag{C.4}$$

$$\overline{d_{3D}} \approx \sqrt{3} \cdot \overline{d_x} = \sqrt{3} \cdot 4.32\, nm = 7.5\, nm \tag{C.5}$$

The two tethered molecules occupy a mean volume of a sphere with radius $\overline{d_{3D}}/2$. The local concentration of one molecule with respect to the other within this sphere can be estimated as:

$$c_{local} = \frac{N}{V \cdot N_A} = \frac{1}{\frac{4}{3}\Pi(\overline{d_{3D}}/2)^3 \cdot N_A} \tag{C.6}$$

$$c_{local} = \frac{1}{\frac{4}{3}\Pi(\sqrt{3} \cdot 4.32 \cdot 10^{-8}\, dm/2)^3 \cdot 6.022 \cdot 10^{-23}\, mol^{-1}} = 7.6\, mM \tag{C.7}$$

This estimate neglects the non-symmetrical distance distribution of random coils, as well as effects from sterical hindrance and the volume excluded by the tether or (more important) the two large proteins, because the (concentration dependent) on-rate depends on the right orientation of both proteins towards each other. Both lead to a larger mean end-to-end distance. The apparent concentration scales linearly with the apparent binding equilibrium and the latter scales linearly with the association rate k_{on} in a simple binary association reaction, $K_D = k_{off}/k_{on}$. Moreover, k_{on} scales linearly with the attempt frequency, which can vary by several orders of magnitudes. The estimate is therefore only

a rough upper estimate and the actual apparent concentration in the construct is most likely one to two magnitudes lower.

C.2 The kinetics of yHsp90 wild-type

In a two-color smFRET experiment yeast Hsp90 wild-type is studied. The kinetics are evaluated the same way as kinetics from the fusion protein constructs. A four state model resulted in the best BIC. The rates are included in Fig. 3.35, p 89. Surprisingly, and in contrast to findings from [113], no transitions between the states 0 and 3 are found within the data. However, this additionally highlights the findings on the fusion protein, where these transitions occurred both in absence and presence of ATP.

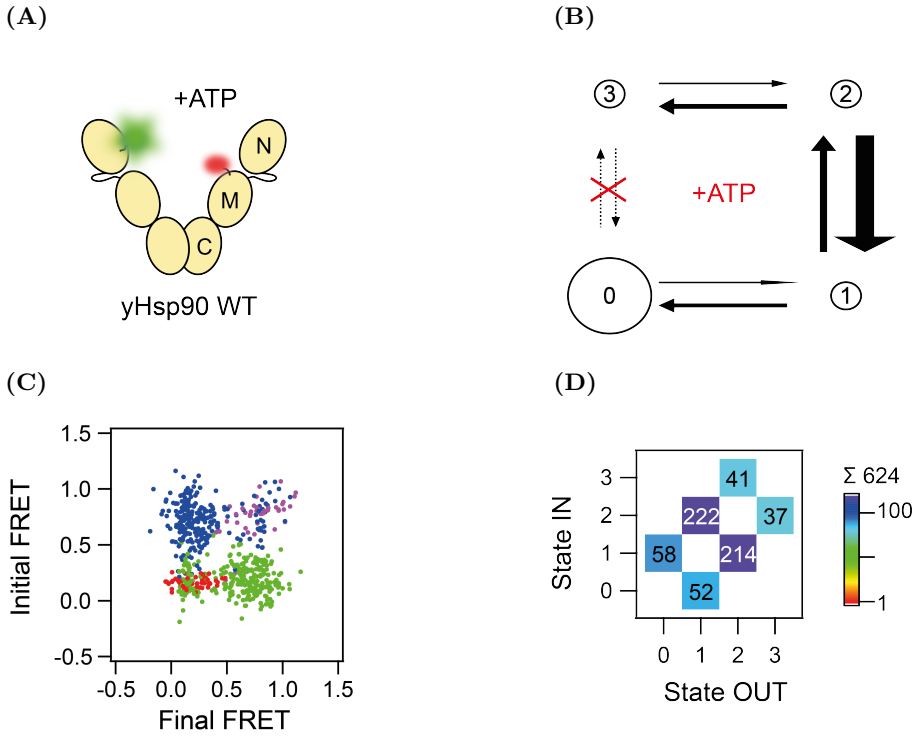

Figure C.1: The kinetics of Hsp90 in presence of 2 mM ATP evaluated by SMACKS. (A), the studied system. (B), in presence of 2 mM ATP, Hsp90 is found to populate four states, but the state transitions between states 3 and 0 does not occur. (C), the transition density plot for the data. (D), transition occureance in the data. No transitions between state 0 and state 3 occurred within the allocated 624 transitions.

C.3 The combined effect of AMP-PNP and Cdc37 on the kinetics of Hsp90

The combined effect of Cdc37 and AMP-PNP on the kinetics of Hsp90 as measured by smFRET between the amino acids 61 and 385 is shown in Fig. C.2. On wild-type Hsp90, AMP-PNP has the effect of overall increased rate transitions [113]. Cdc37 introduces the cyclic transitions $0 \rightleftharpoons 3$ and attenuates this effect.

A comparison of the experiment on wild-type Hsp90 with 100 μM Cdc37 in solution and the F/WT construct revealed highly similar effects. The only difference found is their different rate k_{21}. Cdc37 does not effect this transition, while it is reduced about 50 % within the fusion protein. It is likely that this transition is decelerated by sterical hindrance due to the tether. However, the rate is still the fastest observed.

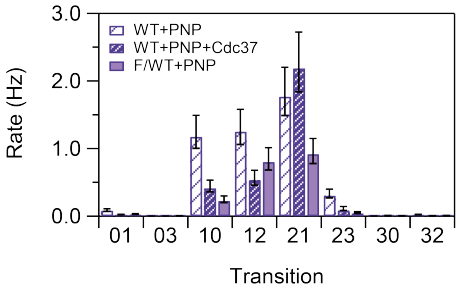

Figure C.2: The effect of 2 mM AMP-PNP on Hsp90's kinetics in presence of Cdc37 either in solution (+100 μM Cdc37) or as fusion protein (F/WT). Error bars represent the 95 % confidence interval.

C.4 Competition between Sba1 and Cdc37

An extension to the experiments presented in Fig. 3.41(A) and Fig. 3.41(B), where the effect of Sba1 or a second Cdc37 onto the binding between Cdc37 and Hsp90 is studied, is a study on their combined effect. This is shown in Fig. C.3. Their combined effect is not a linear combination of their effects observed separately. Instead, the binding of Cdc37N to Hsp90 attenuated by the second Cdc37 or Sba1, is not affected by the addition of Sb1 to the F/F construct comprising two Cdc37. The binding of Cdc37C to Hsp90, on the other hand, is increased. The unassigned high FRET population, only weakly affected by either Cdc37 or Sba1 in the separate experiments, is increased. This is further evidence that the high-FRET peak seen for the binding of Cdc37C to Hsp90 represents a complex conformation of Hsp90 with both co-chaperones.

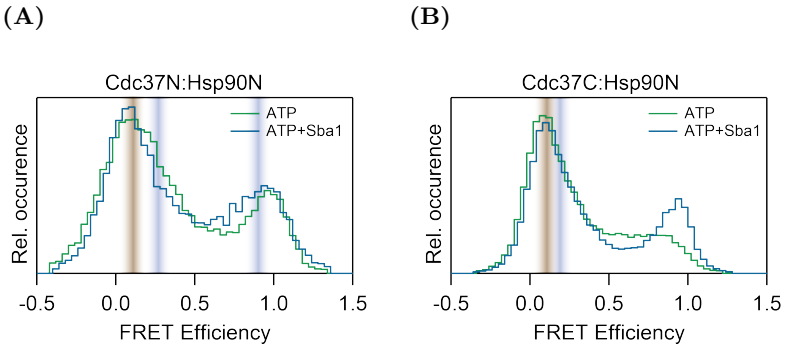

Figure C.3: The effect of a second Cdc37 on the competition between a labeled Cdc37 and Sba1 for binding to Hsp90. (A), Cdc37N and (A), Cdc37C binding to Hsp90N at 2 mM ATP.

C.5 Data statistics

C.5.1 Data sets

In Table C.1, the number of traces and the mean trace length for the two-color smFRET experiments are shown. In the indicated experiments the respective nucleotide is present at a concentration of 2 mM, Sba1 at 20 μM and Ste11 at 10 μM.

Table C.1: Statistics of the evaluated two-color smFRET data sets shown in the main text. Shown are the number of traces and the mean trace length (as bleaching rate τ_b). Construct are exchanges according to A/B, whereas WT refers to Hsp90 and F refers the fusion protein construct comprising Cdc37 and Hsp90 linked by a linker peptide. 61C and 385C refer to the respective aa position in the Hsp90 sequence that is labeled, 129 and 396 refer to the respective Cdc37 aa position that is labeled. In all constructs, labeling is achieved by cysteine-maleiimide coupling.

Construct	**Additive**	**n (traces)**	τ_b **(s)**
F61C/WT385C	ATP	76	30.3
F61C/WT385C	Apo	206	28.7
F61C/WT385C	AMP-PNP	105	24.4
WT61C/WT385C	AMP-PNP+Cdc37	141	34.4
WT61C/WT385C	AMP-PNP	116	30.5
WT61C/WT385C	ATP	96	38.2
F129C61C/WT	ATP	131	26.1
F129C61C/WT	ATP+Ste11	295	11.5
F129C61C/WT	ADP	124	24.9
F129C61C/WT	AMP-PNP	138	19.7
F129C61C/WT	ATP+Sba1	77	58.3
F129C61C/F	ATP	106	24.8
F129C61C/F	ATP+Sba1	88	23.9
F396C61C/WT	ATP	191	28.6
F396C61C/WT	ATP+Ste11	347	15.6
F396C61C/WT	ADP	217	23.6
F396C61C/WT	AMP-PNP	384	27.6
F396C61C/WT	ATP+Sba1	274	30.4
F396C61C/F	ATP	215	29.3
F396C61C/F	ATP+Sba1	214	34.8

C.5.2 Rates

Table C.2: HMM derived rates for state transitions for the Cdc37 constructs. Rates are given in s^{-1}. Nucleotides are present at 2 mM, in the wild-type construct+AMP-PNP/Cdc37 the latter is present at 100 μM. F/WT: F61C-Atto550/WT385C-Atto647N. F/F: F61C-Atto550/F385C-Atto647N. WT: WT61C-Atto550/WT385C-Atto647N. PNP: AMP-PNP.

Protein	Additive	01	03	10	12	21	23	30	32
F/WT	ATP	0.022	$5.0{\cdot}10^{-3}$	0.18	0.56	1.3	0.19	$6.7{\cdot}10^{-3}$	0.033
F/WT	-/-	0.02	$1.9{\cdot}10^{-3}$	0.13	0.40	0.96	0.070	$1.1{\cdot}10^{-3}$	$4.1{\cdot}10^{-3}$
F/WT	PNP	0.03	$4.6{\cdot}10^{-3}$	0.23	0.80	0.92	0.045	$5.4{\cdot}10^{-3}$	$8.3{\cdot}10^{-3}$
F/F	ATP	0.01	10^{-32}	0.095	0.41	1.7	0.19	$8.7{\cdot}10^{-3}$	0.03
WT	ATP	0.049	0	0.4	0.74	1.8	0.50	0	0.21
WT	PNP	0.086	0	1.2	1.3	1.77	0.30	0	0.022
WT	PNP/Cdc37	0.023	$1.4{\cdot}10^{-3}$	0.42	0.53	2.2	0.09	$1.0{\cdot}10^{-3}$	$6.2{\cdot}10^{-3}$

C.6 The effect of Cdc37 on the nucleotide binding and cooperativity

In Section 3.2 on page 67, the cooperative effect between the two nucleotide binding pockets of Hsp90 was shown, based on experiments with a fluorescent analogue of AMP-PNP. These experiments are extended to the fusion protein construct in order to study the effect of the co-chaperone Cdc37 on this cooperativity. The interaction of Hsp90 in the F/WT construct with nucleotides is characterized on the single molecule level with three-color smFRET experiments. This gives an insight into the molecular effects of Cdc37 on Hsp90's nucleotide binding affinities and on the previously characterized cooperativity in nucleotide binding. Furthermore, it enables a rough comparison with the effects of Aha1 and Sba1. Cdc37 had been characterized to have a slight influence on nucleotide binding affinity of Hsp90 by ensemble experiments, with different results for complexes of mixed homologues [80].

The two fluorophores Atto488 and Atto550 are attached to the Hsp90 amino acids 61_{90} and 385_{385} and report the conformation of Hsp90. As nucleotide reporter, AMP-PNP-γ-N-Atto647N is used at a concentration of 25 nM as in Section 3.2 (p. 67). The response of this system towards the addition of different unlabeled nucleotides at 250 μM concentration is compared to the results obtained in absence of Cdc37. Data are analyzed as described before.

The presence of Cdc37 does not change the binding affinity of Hsp90 to labeled AMP-PNP, as visible by an ensemble anisotropy experiment (Fig. C.4(A)). The cooperative effect is studied by a comparison of the average dwell time of the labeled nucleotide bound to Hsp90 and the effects of additional unlabeled nucleotides on it. The binding of labeled AMP-PNP is not changed, and the effect of additional AMP-PNP is not modified either, which is both consistent with the result from the ensemble experiment. However, the addition of ATP and ADP has an effect on the dwell time of the bound nucleotide. Each data set of F/WT consist of about 20 % of the data points present in the large data sets studied for wild-type Hsp90, which results in much larger errors. As an additional criterion, the tta is calculated from optimized HMM to verify findings from the dwell time analysis.

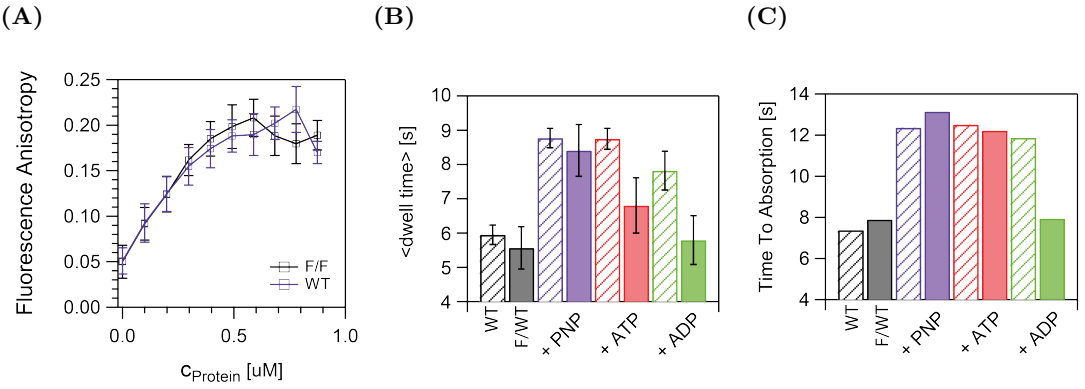

Figure C.4: Effects of Cdc37 on the binding to and dissociation from Hsp90 of labeled AMP-PNP. (A), equilibrium binding of labeled nucleotide (500 nM) to Hsp90, monitored by fluorescence anisotropy. (B), the mean dwell time of 25 nM labeled AMP-PNP on Hsp90 and effects of additional 250 μM unlabeled nucleotide, observed in three-color smFRET experiments. The shaded bars represent the experiments in absence, the filled bars the experiments in presence of Cdc37. (C), the time to absorption, calculated from the optimized HMM in the same data used for the dwell time calculation.

In general, this fits to the results from the two-color experiments on the fusion protein. Cdc37 interacts with Hsp90 mainly in presence of ADP and ATP, but only weakly with Hsp90 in the transition state, as induced by (two) AMP-PNP (c.f. Section 3.3.3). While the dwell time and the tta are not consistent in the ATP experiment, Cdc37 clearly modifies the effect of only ADP on the interaction between Hsp90 and AMP-PNP. In presence of Cdc37, ADP competes already with the first AMP-PNP for binding and does not increase the mean dwell time anymore. The modification of the affinity towards one nucleotide being the product of hydrolysis is usually assigned to the protein class of NEF. NEF have been described for the other main chaperone system present in cells, Hsp70 [196]. This experiment gives the first evidence for an Hsp90 co-chaperone fulfilling partly the role of an NEF.

C.7 Protein colokalization by DNA Tethers

An alternative to a fusion protein for colokalization of two interacting proteins to reach high apparent concentrations is tethering the proteins by DNA. Each protein is labeled with a DNA tether and the two DNA strand are complementary. Mixing the two conjugates results in a complex, whose stability only depends on the DNA duplex stability. The off-rate of DNA duplexes longer than 20 bp is high enough to enable long term observations of the complex at picomolar concentrations without dissociation - thus, a DNA tether also allows studies on low affinity interactions such as the one between Cdc37 and Hsp90.

Table C.3: DNA-tether sequences. dS, nucleotide backbone spacer; S, thiol; Bio, biotin. Complementary bases forming dsDNA are colored red.

DNA	Sequence
DNA1	S-5'-TCTCTCTCTC TTCTTCTTCT TTCTTTCTTT-dS-CTAATGCGCCGTCTCCATCA-3'-Bio
DNA2	5'-TGATGGAGACGGCGCATTAG-dS-CCCTCCCTCCCTCCTCCTCCTCTCTCTCTC-3'-S

A construct of each protein harboring an N-terminal (Cdc37) or C-terminal (Hsp90) ybbR-tag is cloned by PCR. Hsp90z 61C is labeled with Atto550-Maleiimide, Hsp90z ybbR is labeled with DNA1, yCdc37 ybbR 129C is first labeled with Atto647N-Maleiimide and then with DNA2. The DNA compositions are depicted in Table C.3. 20 nt of the two DNAs are complimentary, so that upon mixture they will form a double stranded helix. Covalent coupling of the thiol-DNA to the respective ybbR-tag is achieved by application of the SFP synthase (New England Biolabs, Ipswich, USA), following the kit manufacturer's protocol [135].

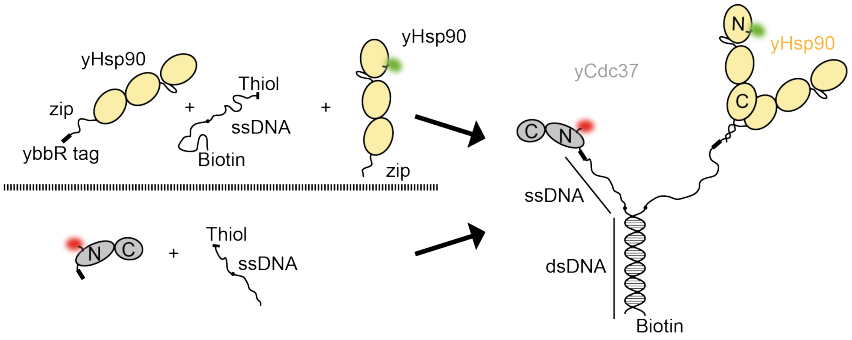

Figure C.5: Schematic view on the general work-flow for the construction of a dsDNA tethered macromolecule.

The two Hsp90 are exchanged by the standard monomer exchange protocol and subsequently mixed with the labeled Cdc37 construct. The complete construct, Cdc37-DNA2-DNA1-$Hsp90_2$ is then flushed into the TIRF chamber and specifically immobilized by biotin/Neutravidin interaction. The two proteins interact with each other in a nucleotide dependent interaction, shown in Fig. C.6. However, most traces do not exhibit an interaction. Thus, the used DNA construct results in a low local concentration of the two binding partners. The experiments are complicated by the weak reactivity of the single stranded DNA strands towards the proteins (< 1 %). An additional purification by chromatography (size exclusion or anion exchange) is not successful, but first approaches using mass weight cut-off concentrators for table top centrifuges (Vivaspin 500, MWCO 30 kDa, Sigma) are promising.

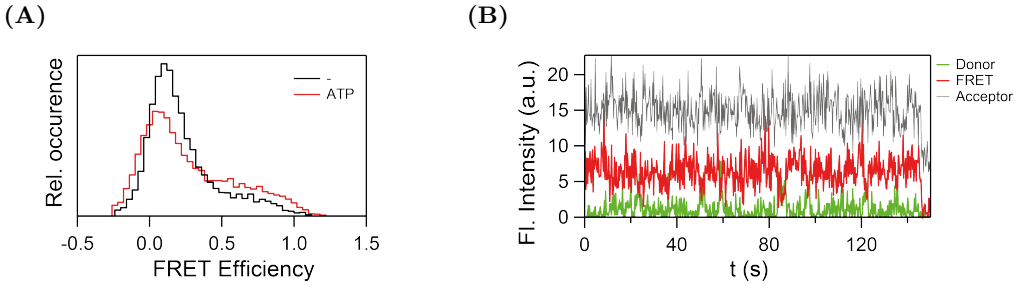

Figure C.6: smFRET on a DNA-tethered construct comprising Cdc37 and an Hsp90 dimer. (A), FRET E histogram of the construct measured in absence and in presence of 2 mM ATP ($n > 30$). (B), exemplary trace displaying dynamics between a low and a high FRET state, measured in presence of ATP.

D Results on the *in vivo* project

D.1 smFRET in the far red on DNA

A few smFRET experiments using the fluorophore Cy7 as DNA-conjugate have been published [98, 197]. As first *in vitro* experiment, smFRET is measured on a DNA double-helix. However, Cy7 is found to be rather unstable under oxidizing conditions – it bleaches very fast within a few seconds in absence of an oxygen scavenger system. Repeating the experiments in presence of an oxygen scavenging system results in long traces (> 1 min) before one of the fluorophores bleaches. The scavenger system GODCAT [198] was found to perform slightly better than PCA/PCD system [199, 200]. It was therefore applied in subsequent experiments, also on proteins. The result shown in Fig. D.1 demonstrates that the selected fluorophore pair for measuring smFRET at R/NIR wavelength, Atto647N and Cy7 indeed works.

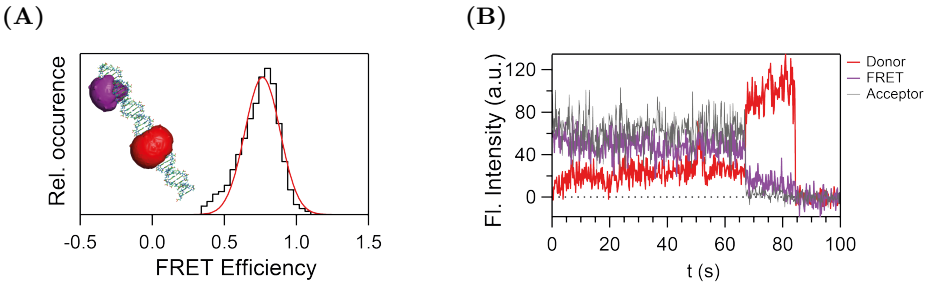

Figure D.1: smFRET between 647N and Cy7 on dsDNA. (A), FRET efficiency histogram of the labeled DNA measured in 1xPBS with GODCAT scavenger (n=21, 400 ms/frame, mean tracelength 144 s). The Gaussian fit results in the mean $E = 0.76$, with $E_{expected} = 0.071$ (at $R_0 = 73$ Å). The deviation arises from uncertain correction factors for a single FRET population. (B), an exemplary FRET E trace. The fluorescence of Donor (Atto647N) and Acceptor (Cy7) after donor excitation (FRET) and direct excitation (Acceptor) is shown.

D.2 smFRET in the far red on yeast Hsp90

So far, Cy7 has only been used in smFRET experiments as a DNA conjugate [98, 197]. Fluorescent dyes are sensitive to their environment and therefore may exhibit different properties depending on the macromolecule they are conjugated to (e.g. DNA or protein). Hence, it is necessary to test acceptor dyes on a protein as well.

smFRET on yeast Hsp90 as model protein is tested as well. As acceptor fluorophores I tested the dyes Cy7, Alexa750, LD750, Atto725 and Atto740. The results are listed in the following.

D.2.1 The FRET pair Atto647N-Cy7 exhibits much shorter trace lengths on the protein

At first, the FRET pair Atto647N/Cy7 found functional on DNA is tested on Hsp90, with both dyes coupled to aa 298. The experiment requires again an oxygen scavenger system, because bleaching is observed within a few frames (< 3 s) otherwise. However, the single protein traces bleach much faster than on the DNA sample at similar excitation intensities.

The mean trace length is found to be 35 s, compared to about 140 s on the DNA sample (both times measured in presence of GODCAT scavenging system). Additionally, the traces seem to suffer from fast photo-physics effects that result in an increased signal width.

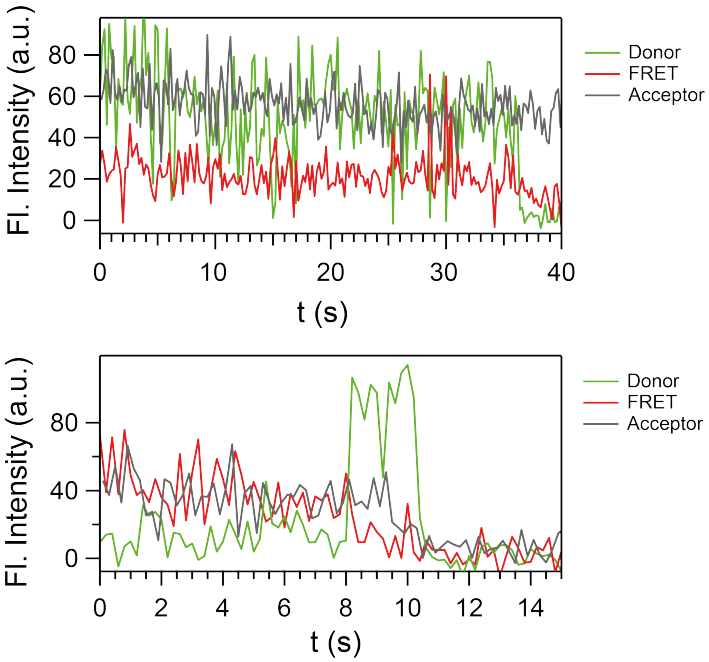

Figure D.2: Two exemplary traces of smFRET on Hsp90 between the fluorophores Atto647N and Cy7 measured in presence of 2 mM ATP. yHsp90 is labeled at the opposing aa 298 and aa 298 of the Hsp90 dimer with the dyes. Donor, Atto647N fluorescence; FRET, Cy7 fluorescence after donor excitation; Acceptor, Cy7 fluorescence after direct excitation.

In the single molecule traces Hsp90 populates two FRET states (c.f. Fig. D.2). The FRET histogram of Hsp90 with these dyes can be shifted towards the closed state of Hsp90 by the addition of AMP-PNP (c.f. Fig. D.3); nevertheless the traces are not well enough defined for a kinetic analysis.

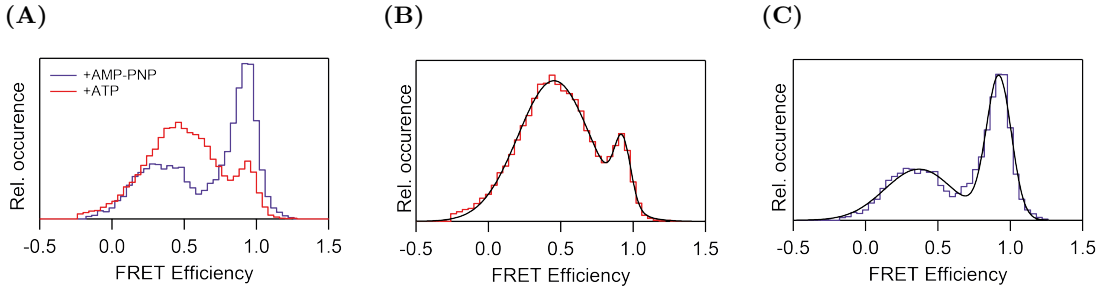

Figure D.3: FRET E histograms of yHsp90 labeled at aa 298 with Atto647N/Alexa750 in presence of 2 mM ATP and AMP-PNP (PNP). The histograms are each fitted by two Gaussians as shown in (B) and (C).

The FRET pair 298/298 was part the study on the dynamic structure of Hsp90, and from the found FRET-derived distances, the expected FRET E for the two FRET states Hsp90 populates can be calculated (with R_0(647N/Cy7) = 73 Å): E_O = 0.42 and E_C =0.87.

We find that the single molecule traces show not as much dynamic as usually observed in

experiments on yHsp90. Nevertheless, this could be caused by the decreased trace length. The equilibrium between the two FRET populations is successfully shifted by the addition of AMP-PNP, from 91 % open in presence of ATP to 50 % in presence of AMP-PNP. The two peaks are located at E = 0.45/0.42 and E = 0.93/0.92 in presence of ATP and AMP-PNP, which is close to the expected FRET E (fits shown in Fig. D.3).

D.2.2 The FRET pair Atto647N-Alexa750 displays a four-state model

Experiments with Alexa750 as acceptor dye (on aa 61) and Atto647N as donor (on aa 385) result in a reasonable signal and well defined traces (of a mean length of 40 s at the same excitation intensities), even though the γ-factor is lower than in the experiments with Cy7 (due to the lower quantum yield of Alexa750).

The kinetics in one data set are evaluated by SMACKS [113]. A cyclic, four state description describes the data the best, with rates similar to those found for the yeast Hsp90 labeled at aa 61 with Atto550 and at aa 385 with Atto647N. Hence, the dye Alexa750 does not interact specifically with Hsp90 (or in the same manner as Atto550). The FRET histogram, an exemplary fluorescence trace with the optimal viterbi path and the model selection are shown in Fig. D.4.

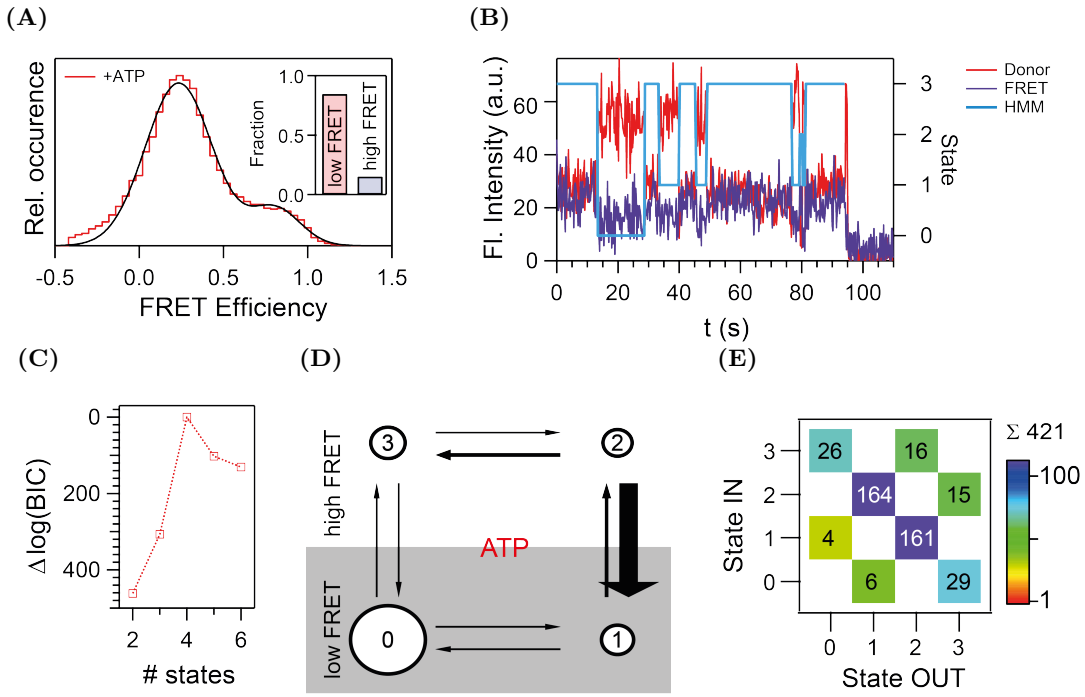

Figure D.4: smFRET on yHsp90z in presence of 2 mM ATP, labeled at one protomer's aa 61 with Alexa750 and at the other's aa 385 with Atto647N. (A), approx. 85 % of yHsp90 populates the low FRET peak (n = 206, mean tracelength 40 s). (B), an exemplary single molecule fluorescence trace (Donor, donor fluorescence; FRET, acceptor fluorescence after donor excitation) with the optimized viterbi path. For clarity, the fluorescence of the acceptor after direct excitation is not shown. (C), model evaluation by the bayesian information criterion clearly demonstrates that Hsp90 populates four states. (D), HMM analysis finds it fluctuating in a cycle with no directionality. (E), Transition occurrence plot of the optimal HMM model.

D.2.3 Characterization of further NIR acceptor dyes attached to Hsp90

The two fluorophores Atto740 and Atto725 were not found to produce a signal defined enough for smFRET and not further investigated.

The self-healing dye LD750 with a covalently bound triplet quenching agent [201] results in bright and long traces, but an additional FRET population with a deviating stoichiometry is found (c.f. Fig. D.5). Thus, it is likely to interact with the protein and this interaction results in dye quenching, affecting the γ-factor. LD750 is therefore not further considered for smFRET studies on Hsp90.

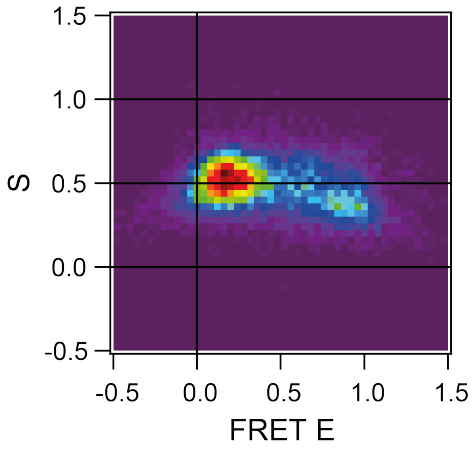

Figure D.5: smFRET on Hsp90 with Atto647N as donor and LD750 (both coupled to aa 298) as acceptor dye. The Stoichiometry vs FRETE plot reveals an additional population at high FRET E that deviates in its γ-factor from the other two. This indicates a specific interaction of LD750, enhancing its quantum yield. Therefore, LD750 was not further used in smFRET studies on Hsp90.

D.3 Fluorescence background in HeLa cells

To estimate the expected S/N ratio for smFRET experiments in living HeLa cells, the background fluorescence in a cell at excitation powers applied in the previous *in vitro* experiments is checked. The following findings are concluded from the experiment shown in Fig. D.6.

- The background in the red detection channel is much brighter than in the NIR channel.
- The background in a cell is not evenly distributed within the cell organelles. While the cell nucleus gives relatively weak background signal, much more is present in the cytosole.
- The background in the cytosole itself is not evenly distributed and suffers additionally from mobile bright spots, which are most likely transport vesicles.
- The background decays exponentially and rather fast.

Comparing the measured fluorescence intensities from smFRET experiments *in vitro* to the found background signal, we can conclude that smFRET experiments is possible in both, cell cytosole and nucleus. However, measurements in the cell nucleus are preferable, because the background is more homogenous and thus less impeding data evaluation.

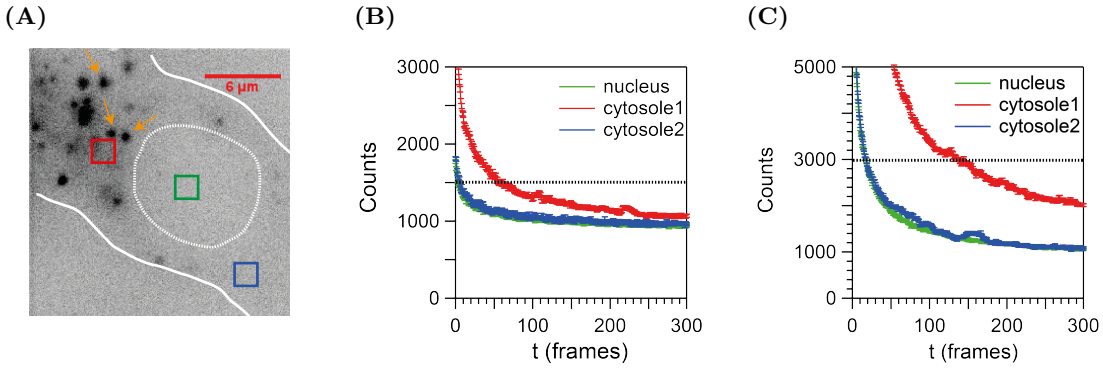

Figure D.6: Fluorescence background in a HeLa cell excited on the smFRET HILO setup at 635 ((B)) and 728 nm ((C)), with an integration time of 70 ms. (A), a HeLa cell on the setup, with the cell and its nucleus depicted. Orange arrows indicate mobile bright spots present in the cell cytosole that move during the movie and are most likely transport vesicles. Three areas of approx. 50 px x50 px are selected for background evaluation. The correspondent statistics (average counts and their s. d. are depicted in (B) and (C). The dashed line in the two graphs indicates the average count in the correspondent channel found with single fluorophores at the same excitation power.

D.4 GFP fluorescence in HeLa cells

HeLa cells expressing low level of GFP-actin fusion protein have been genetically engineered by Fernando Aprile-Garcia. The third excitation color at 458 nm is used to excite the GFP fluorescence in HILO mode, and the fluorescence is detected with the CCD camera (with EM switched off). Fig. D.7 demonstrates, that the imaging of GFP fluorescence works as sensitive substitute for bright-field imaging. However, the dynamic range of the camera is weak and has to be optimized for a better contrast, and the low level of GFP fluorescence have to be increased.

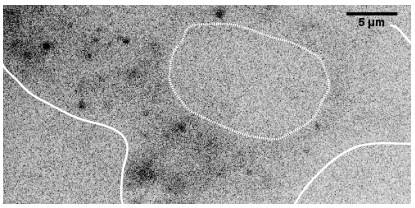

Figure D.7: Fluorescence of a HeLa cell expressing constantly the GFP-actin fusion protein upon excitation at 458 nm. The cell can be separated from the surrounding. The S/N ratio is worse than expected due to the weak expression level of the fusion protein.

D.5 Transfection experiments

Transfection of sDNA labeled with one Cy7 fluorophore is achieved using the Xfect protein transfection protocol (Clontech Laboratories, Mountain View, USA) according to the manufacturer's protocol (100 ng DNA are used), except that cells are washed five times with 1x PBS buffer and grown subsequently in Opti-MEM without phenol red (Thermo Fisher Scientific). The transfection is based on a cell-penetrating peptide that can shuffle proteins or DNA through the cell membrane, as shown in Fig. D.8.

No fluorescence is detected outside the cells. Movies at 70 ms excitation time with

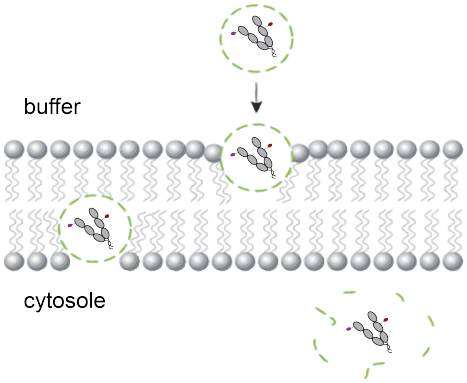

Figure D.8: Mechanism of the macromolecule transfection with a cell-penetrating peptide.

728 nm are recorded. Within these, single bright spots in the NIR detection are selected and evaluated. In Fig. D.9, further sm traces (indicated by a single bleaching step) are depicted.

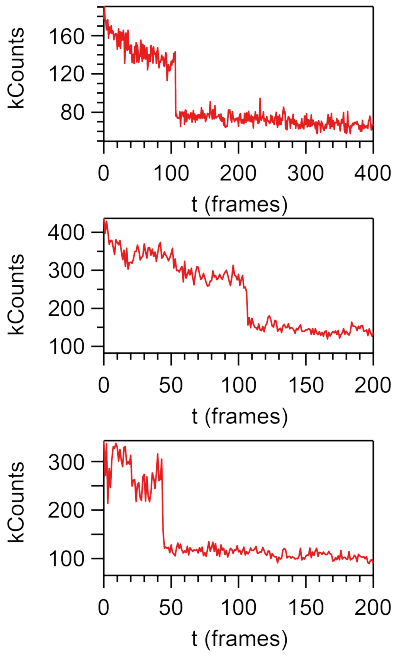

Figure D.9: Exemplary single molecule fluorescence traces of Cy7-labeled DNA successfully transfected into HeLa cells.

An additional, and optional idea is to add a cell penetrating peptide (CPP) at the C-terminus of the protein (detailed in Section 2.7.1 on page 40), which could work independently or in combination with the transfection agent.

While the transfection of DNA works, transfection with labeled (and optionally tagged) Hsp90 is much more difficult. This is mainly the case, because the labeled Hsp90 sticks much more to the cells, most likely to the membrane or proteins present at the cell surface. Therefore, it is difficult to discriminate protein inside and outside the cell, and additionally

the fluorescence background increases to levels that do not allow single molecule experiments. We visualized this by purification of the cellular proteins after following the transfection protocol and detecting the specific dye fluorescence on an SDS-gel. Exemplary shown in Fig. D.10 is the incubation of HeLa cells with 1 μM yeast Hsp90 labeled at aa 298 with Atto647N and either tagged with an NLS or a CPP. Both proteins are still present after washing the cells five times with 1x PBS. Appending a 1 min trypsin digest of the cells reduces the total cell amount, but does not clean the cells completely.

This experiment demonstrates that long incubation (30 min in this case, as cells are incubated according to the Xfect protocol) lead to binding of Hsp90 to the cell surface. Because the labeled DNA was not attached to the cells but appeared only on transfected cells, this effect must be caused by Hsp90 and not by the label.

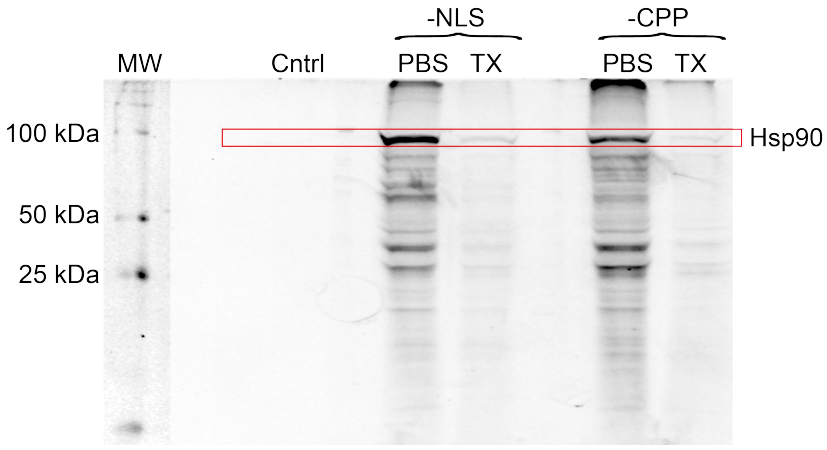

Figure D.10: 12 % SDS-gel from transfection test samples on the transfection/cell-sticking of labeled Hsp90.

We have by now started alternative transfection strategies. Namely, the rather old methods of glass bead shaking [202, 203], where cells are exposed briefly to glass beads in presence of the molecule that should be loaded into the cells and the application of Streptolysin O (SLO), a pore-forming toxin [183]. In first tests, especially the latter gives promising results, with negligible fluorescence in the control experiment and high intracellular fluorescence.

D.6 smFRET on human Hsp90 *in vitro*

For experiments that resemble the native system even further, human Hsp90 (hHsp90) should finally be studied in the live cell experiments in HeLa cells. Because the native cysteines in hHsp90 impede side-specific labeling, these are mutated to amino acids found at the aligned positions in homologues (or, according to the crystal structure to alanine or serine, depending on the presence or absence of H-bonds).

The protein (described in detail in Section 2.7.1) is successfully expressed in *e. coli* and purified by chromatography. The unlabeled protein has an ATPase activity of 0.37 min^{-1} at 30 °C. While the labeling procedure did not harm the protein, we found the monomer exchange to lead to complete aggregation of hHsp90. Therefore, hHsp90 labeled at position 405 with a mixture of Atto550 and Atto647N (and thus a FRET pair without the need for heating) is studied by smFRET. The aa 405 in hHsp90 is equivalent to aa 385 in yeast

Hsp90. Although this FRET pair is not optimal for characterization of Hsp90 due to the small AV and high anisotropy of the dye, the FRET E histogram can be shifted by nucleotides, as shown in Fig. D.11.

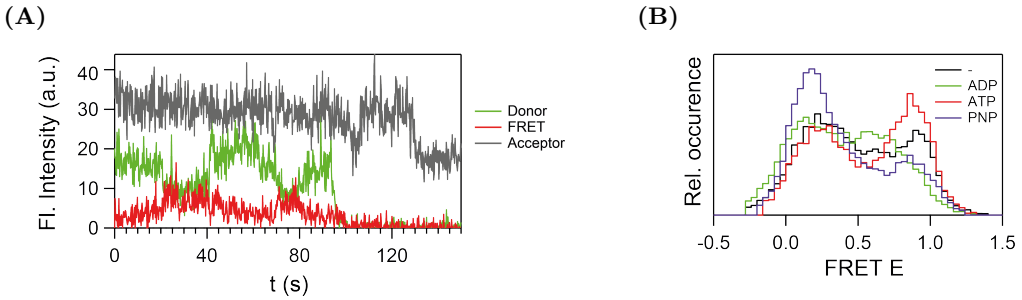

Figure D.11: smFRET on hHsp90. (A), example fluorescence trace of hHsp90z labeled at aa 405 with Atto550/Atto647N in presence of 2 mM ATP. Donor, donor fluorescence after donor excitation; FRET, acceptor fluorescence after donor excitation; Acceptor, acceptor fluorescence after acceptor excitation. (B), FRET E histograms obtained for > 50 traces in absence and in presence of the indicated nucleotide (2 mM).

Bibliography

1. Wortmann, Philipp, Markus Götz, and Thorsten Hugel: 'Cooperative nucleotide binding in Hsp90 and the underlying mechanisms'. *bioRxiv* (2017), vol. DOI:10.1101/113191.
2. Götz, Markus, Philipp. Wortmann, S. Schmid, and T. Hugel: 'A Multicolor Single-Molecule FRET Approach to Study Protein Dynamics and Interactions Simultaneously'. *Methods in enzymology* (2016), vol. 581: pp. 487–516.
3. Hellenkamp, Björn, Philipp Wortmann, Florian Kandzia, Martin Zacharias, and Thorsten Hugel: 'Multidomain structure and correlated dynamics determined by self-consistent FRET networks'. *Nature methods* (2017), vol. 14(2): pp. 174–180.
4. Hellenkamp, Björn, Philipp Wortmann, Florian Kandzia, Martin Zacharias, and Thorsten Hugel: 'Determination of structural ensembles and correlated dynamics of a multi-domain protein'. *Protocol Exchange* (2017), vol. DOI: 10.1038/protex.2016.078.
5. Levinthal, Cyrus: 'How to fold graciously'. *Mossbauer spectroscopy in biological systems* (1969), vol. 67: pp. 22–24.
6. Sali, Andrej, Eugene Shakhanovitch, and Martin Karplus: 'How does a protein fold?' *Nature* (1994), vol. 369: pp. 248–251.
7. Anfinsen, Christian B.: 'Principles that Govern the Folding of Protein Chains'. *Science* (1973), vol. 181: pp. 223–230.
8. Chiti, Fabrizio and Christopher M. Dobson: 'Protein misfolding, functional amyloid, and human disease'. *Annual review of biochemistry* (2006), vol. 75: pp. 333–366.
9. Hartl, F. Ulrich, Andreas Bracher, and Manajit Hayer-Hartl: 'Molecular chaperones in protein folding and proteostasis'. *Nature* (2011), vol. 475(7356): pp. 324–332.
10. Jego, Gaetan, Adonis Hazoume, Renaud Seigneuric, and Carmen Garrido: 'Targeting heat shock proteins in cancer'. *Cancer letters* (2013), vol. 332(2): pp. 275–285.
11. Jhaveri, Komal, Stefan O. Ochiana, Mark Ps Dunphy, John F. Gerecitano, Adriana D. Corben, Radu I. Peter, Yelena Y. Janjigian, Erica M. Gomes-DaGama, John 3rd Koren, Shanu Modi, and Gabriela Chiosis: 'Heat shock protein 90 inhibitors in the treatment of cancer: current status and future directions'. *Expert opinion on investigational drugs* (2014), vol. 23(5): pp. 611–628.
12. Borkovich, K. A., F. W. Farrelly, D. B. Finkelstein, J. Taulien, and S. Lindquist: 'hsp82 is an essential protein that is required in higher concentrations for growth of cells at higher temperatures'. *Molecular and Cellular Biology* (1989), vol. 9(9): pp. 3919–3930.

13. Koulov, Atanas V., Paul LaPointe, Bingwen Lu, Abbas Razvi, Judith Coppinger, Meng-Qiu Dong, Jeanne Matteson, Rob Laister, Cheryl Arrowsmith, John R. 3rd Yates, and William E. Balch: 'Biological and structural basis for Aha1 regulation of Hsp90 ATPase activity in maintaining proteostasis in the human disease cystic fibrosis'. *Molecular biology of the cell* (2010), vol. 21(6): pp. 871–884.

14. Milo, Ron: 'What is the total number of protein molecules per cell volume? A call to rethink some published values'. *BioEssays : news and reviews in molecular, cellular and developmental biology* (2013), vol. 35(12): pp. 1050–1055.

15. Taipale, Mikko, Daniel F. Jarosz, and Susan Lindquist: 'HSP90 at the hub of protein homeostasis: emerging mechanistic insights'. *Nature reviews. Molecular cell biology* (2010), vol. 11(7): pp. 515–528.

16. Langer, T.: 'Intracellular localization of the 90 kDA heat shock protein (HSP90alpha) determined by expression of a EGFP-HSP90alpha-fusion protein in unstressed and heat stressed 3T3 cells'. *Cell Biology International* (2003), vol. 27(1): pp. 47–52.

17. Ali, Adnan, Steven Bharadwaj, Ruth O'Carroll, and Nick Ovsenek: 'HSP90 Interacts with and Regulates the Activity of Heat Shock Factor 1 in Xenopus Oocytes'. *Molecular and Cellular Biology* (1998), vol. 18(9): pp. 4949–4960.

18. Ali, Maruf M. U., S. Mark Roe, Cara K. Vaughan, Phillipe Meyer, Barry Panaretou, Peter W. Piper, Chrisostomos Prodromou, and Laurence H. Pearl: 'Crystal structure of an Hsp90-nucleotide-p23/Sba1 closed chaperone complex'. *Nature* (2006), vol. 440(7087): pp. 1013–1017.

19. Pearl, Laurence H. and Chrisostomos Prodromou: 'Structure and mechanism of the Hsp90 molecular chaperone machinery'. *Annual review of biochemistry* (2006), vol. 75: pp. 271–294.

20. Richter, K., P. Muschler, O. Hainzl, and J. Buchner: 'Coordinated ATP hydrolysis by the Hsp90 dimer'. *The Journal of biological chemistry* (2001), vol. 276(36): pp. 33689–33696.

21. Jahn, Markus, Alexandra Rehn, Benjamin Pelz, Björn Hellenkamp, Klaus Richter, Matthias Rief, Johannes Buchner, and Thorsten Hugel: 'The charged linker of the molecular chaperone Hsp90 modulates domain contacts and biological function'. *Proceedings of the National Academy of Sciences* (2014), vol. 111(50): pp. 17881–17886.

22. Bergerat, A., B. de Massy, D. Gadelle, P. C. Varoutas, A. Nicolas, and P. Forterre: 'An atypical topoisomerase II from Archaea with implications for meiotic recombination'. *Nature* (1997), vol. 386(6623): pp. 414–417.

23. DUTTA, R. and M. INOUYE: 'GHKL, an emergent ATPase/kinase superfamily'. *Trends in biochemical sciences* (2000), vol. 25(1): pp. 24–28.

24. Dollins, D. Eric, Joshua J. Warren, Robert M. Immormino, and Daniel T. Gewirth: 'Structures of GRP94-Nucleotide Complexes Reveal Mechanistic Differences between the hsp90 Chaperones'. *Molecular cell* (2007), vol. 28(1): pp. 41–56.

25. Shiau, Andrew K., Seth F. Harris, Daniel R. Southworth, and David A. Agard: 'Structural Analysis of E. coli hsp90 Reveals Dramatic Nucleotide-Dependent Conformational Rearrangements'. *Cell* (2006), vol. 127(2): pp. 329–340.

26. Lavery, Laura A., James R. Partridge, Theresa A. Ramelot, Daniel Elnatan, Michael A. Kennedy, and David A. Agard: 'Structural asymmetry in the closed state of mitochondrial Hsp90 (TRAP1) supports a two-step ATP hydrolysis mechanism'. *Molecular cell* (2014), vol. 53(2): pp. 330–343.

27. Mickler, Moritz, Martin Hessling, Christoph Ratzke, Johannes Buchner, and Thorsten Hugel: 'The large conformational changes of Hsp90 are only weakly coupled to ATP hydrolysis'. *Nature structural & molecular biology* (2009), vol. 16(3): pp. 281–286.

28. Flynn, Julia M., Parul Mishra, and Daniel N. A. Bolon: 'Mechanistic Asymmetry in Hsp90 Dimers'. *Journal of molecular biology* (2015), vol. 427(18): pp. 2904–2911.

29. Mishra, Parul and Daniel N.A. Bolon: 'Designed Hsp90 Heterodimers Reveal an Asymmetric ATPase-Driven Mechanism In Vivo'. *Molecular cell* (2014), vol. 53(2): pp. 344–350.

30. Verba, Kliment A., Ray Yu-Ruei Wang, Akihiko Arakawa, Yanxin Liu, Mikako Shirouzu, Shigeyuki Yokoyama, and David A. Agard: 'Atomic structure of Hsp90-Cdc37-Cdk4 reveals that Hsp90 traps and stabilizes an unfolded kinase'. *Science (New York, N.Y.)* (2016), vol. 352(6293): pp. 1542–1547.

31. Southworth, Daniel R. and David A. Agard: 'Client-loading conformation of the Hsp90 molecular chaperone revealed in the cryo-EM structure of the human Hsp90:Hop complex'. *Molecular cell* (2011), vol. 42(6): pp. 771–781.

32. Retzlaff, Marco, Franz Hagn, Lars Mitschke, Martin Hessling, Frederik Gugel, Horst Kessler, Klaus Richter, and Johannes Buchner: 'Asymmetric activation of the hsp90 dimer by its cochaperone aha1'. *Molecular cell* (2010), vol. 37(3): pp. 344–354.

33. Schulze, Andrea, Gerti Beliu, Dominic A. Helmerich, Jonathan Schubert, Laurence H. Pearl, Chrisostomos Prodromou, and Hannes Neuweiler: 'Cooperation of local motions in the Hsp90 molecular chaperone ATPase mechanism'. *Nature chemical biology* (2016), vol.

34. Prodromou, Chrisostomos, James M. Nuttall, Stefan H. Millson, S. Mark Roe, Tiow-Suan Sim, Doreen Tan, Paul Workman, Laurence H. Pearl, and Peter W. Piper: 'Structural basis of the radicicol resistance displayed by a fungal hsp90'. *ACS chemical biology* (2009), vol. 4(4): pp. 289–297.

35. Richter, Klaus, Sandra Moser, Franz Hagn, Rainer Friedrich, Otmar Hainzl, Markus Heller, Sandra Schlee, Horst Kessler, Jochen Reinstein, and Johannes Buchner: 'Intrinsic inhibition of the Hsp90 ATPase activity'. *The Journal of biological chemistry* (2006), vol. 281(16): pp. 11301–11311.

36. Richter, K.: 'N-terminal Residues Regulate the Catalytic Efficiency of the Hsp90 ATPase Cycle'. *Journal of Biological Chemistry* (2002), vol. 277(47): pp. 44905–44910.

37. Tsutsumi, Shinji, Mehdi Mollapour, Christian Graf, Chung-Tien Lee, Bradley T. Scroggins, Wanping Xu, Lenka Haslerova, Martin Hessling, Anna A. Konstantinova, Jane B. Trepel, Barry Panaretou, Johannes Buchner, Matthias P. Mayer, Chrisostomos Prodromou, and Len Neckers: 'Hsp90 charged-linker truncation reverses the functional consequences of weakened hydrophobic contacts in the N domain'. *Nature structural & molecular biology* (2009), vol. 16(11): pp. 1141–1147.

38. Zhang, Huaqun, Chen Zhou, Wuyan Chen, Yechun Xu, Yanhong Shi, Yi Wen, and Naixia Zhang: 'A dynamic view of ATP-coupled functioning cycle of Hsp90 N-terminal domain'. *Scientific reports* (2015), vol. 5: p. 9542.

39. Prodromou, Chrisostomos, S.Mark Roe, Ronan O'Brien, John E. Ladbury, Peter W. Piper, and Laurence H. Pearl: 'Identification and Structural Characterization of the ATP/ADP-Binding Site in the Hsp90 Molecular Chaperone'. *Cell* (1997), vol. 90(1): pp. 65–75.

40. McLaughlin, Stephen H., Laure-Anne Ventouras, Bastiaan Lobbezoo, and Sophie E. Jackson: 'Independent ATPase activity of Hsp90 subunits creates a flexible assembly platform'. *Journal of molecular biology* (2004), vol. 344(3): pp. 813–826.

41. Prodromou, C., B. Panaretou, S. Chohan, G. Siligardi, R. O'Brien, J. E. Ladbury, S. M. Roe, P. W. Piper, and L. H. Pearl: 'The ATPase cycle of Hsp90 drives a molecular 'clamp' via transient dimerization of the N-terminal domains'. *The EMBO journal* (2000), vol. 19(16): pp. 4383–4392.

42. Leskovar, Adriane, Harald Wegele, Nicolas D. Werbeck, Johannes Buchner, and Jochen Reinstein: 'The ATPase cycle of the mitochondrial Hsp90 analog Trap1'. *The Journal of biological chemistry* (2008), vol. 283(17): pp. 11677–11688.

43. Panaretou, B., C. Prodromou, S. M. Roe, R. O'Brien, J. E. Ladbury, P. W. Piper, and L. H. Pearl: 'ATP binding and hydrolysis are essential to the function of the Hsp90 molecular chaperone in vivo'. *The EMBO journal* (1998), vol. 17(16): pp. 4829–4836.

44. Wiech, H., J. Buchner, R. Zimmermann, and U. Jakob: 'Hsp90 chaperones protein folding in vitro'. *Nature* (1992), vol. 358(6382): pp. 169–170.

45. Jakob, U., H. Lilie, I. Meyer, and J. Buchner: 'Transient interaction of Hsp90 with early unfolding intermediates of citrate synthase. Implications for heat shock in vivo'. *The Journal of biological chemistry* (1995), vol. 270(13): pp. 7288–7294.

46. Picard, D.: 'Heat-shock protein 90, a chaperone for folding and regulation'. *Cellular and Molecular Life Sciences* (2002), vol. 59(10): pp. 1640–1648.

47. Xu, Y. and S. Lindquist: 'Heat-shock protein hsp90 governs the activity of pp60v-src kinase'. *Proceedings of the National Academy of Sciences of the United States of America* (1993), vol. 90(15): pp. 7074–7078.

48. Stepanova, L., X. Leng, S. B. Parker, and J. W. Harper: 'Mammalian p50Cdc37 is a protein kinase-targeting subunit of Hsp90 that binds and stabilizes Cdk4'. *Genes & Development* (1996), vol. 10(12): pp. 1491–1502.

49. Young, J. C. and F. U. Hartl: 'Polypeptide release by Hsp90 involves ATP hydrolysis and is enhanced by the co-chaperone p23'. *The EMBO journal* (2000), vol. 19(21): pp. 5930–5940.

50. McLaughlin, Stephen H., Harvey W. Smith, and Sophie E. Jackson: 'Stimulation of the weak ATPase activity of human hsp90 by a client protein'. *Journal of molecular biology* (2002), vol. 315(4): pp. 787–798.

51. Zierer, Bettina K., Martin Rubbelke, Franziska Tippel, Tobias Madl, Florian H. Schopf, Daniel A. Rutz, Klaus Richter, Michael Sattler, and Johannes Buchner: 'Importance of cycle timing for the function of the molecular chaperone Hsp90'. *Nature structural & molecular biology* (2016), vol.

52. Karagöz, G. Elif and Stefan G. D. Rüdiger: 'Hsp90 interaction with clients'. *Trends in biochemical sciences* (2015), vol. 40(2): pp. 117–125.

53. Lorenz, Oliver Robin, Lee Freiburger, Daniel Andreas Rutz, Maike Krause, Bettina Karolina Zierer, Sara Alvira, Jorge Cuellar, Jose Maria Valpuesta, Tobias Madl, Michael Sattler, and Johannes Buchner: 'Modulation of the Hsp90 chaperone cycle by a stringent client protein'. *Molecular cell* (2014), vol. 53(6): pp. 941–953.

54. Kirschke, Elaine, Devrishi Goswami, Daniel Southworth, Patrick R. Griffin, and David A. Agard: 'Glucocorticoid receptor function regulated by coordinated action of the Hsp90 and Hsp70 chaperone cycles'. *Cell* (2014), vol. 157(7): pp. 1685–1697.

55. Wandinger, Sebastian Karl, Klaus Richter, and Johannes Buchner: 'The Hsp90 chaperone machinery'. *The Journal of biological chemistry* (2008), vol. 283(27): pp. 18473–18477.

56. Bohen, Sean P.: 'Genetic and Biochemical Analysis of p23 and Ansamycin Antibiotics in the Function of Hsp90-Dependent Signaling Proteins'. *Molecular and Cellular Biology* (1998), vol. 18(6): pp. 3330–3339.

57. Lee, Paul, Jie Rao, Albert Fliss, Emy Yang, Stephen Garrett, and Avrom J. Caplan: 'The Cdc37 protein kinase-binding domain is sufficient for protein kinase activity and cell viability'. *The Journal of cell biology* (2002), vol. 159(6): pp. 1051–1059.

58. Ghaemmaghami, Sina, Won-Ki Huh, Kiowa Bower, Russell W. Howson, Archana Belle, Noah Dephoure, Erin K. O'Shea, and Jonathan S. Weissman: 'Global analysis of protein expression in yeast'. *Nature* (2003), vol. 425(6959): pp. 737–741.

59. Bryan, Andrea K., Alexi Goranov, Angelika Amon, and Scott R. Manalis: 'Measurement of mass, density, and volume during the cell cycle of yeast'. *Proceedings of the National Academy of Sciences of the United States of America* (2010), vol. 107(3): pp. 999–1004.

60. Panaretou, Barry et al.: 'Activation of the ATPase Activity of Hsp90 by the Stress-Regulated Cochaperone Aha1'. *Molecular cell* (2002), vol. 10(6): pp. 1307–1318.

61. Siligardi, Giuliano, Bin Hu, Barry Panaretou, Peter W. Piper, Laurence H. Pearl, and Chrisostomos Prodromou: 'Co-chaperone regulation of conformational switching in the Hsp90 ATPase cycle'. *The Journal of biological chemistry* (2004), vol. 279(50): pp. 51989–51998.

62. Meyer, Philippe, Chrisostomos Prodromou, Chunyan Liao, Bin Hu, S. Mark Roe, Cara K. Vaughan, Ignacija Vlasic, Barry Panaretou, Peter W. Piper, and Laurence H. Pearl: 'Structural basis for recruitment of the ATPase activator Aha1 to the Hsp90 chaperone machinery'. *The EMBO journal* (2004), vol. 23(6): pp. 1402–1410.

63. Meyer, Philippe, Chrisostomos Prodromou, Bin Hu, Cara Vaughan, S. Mark Roe, Barry Panaretou, Peter W. Piper, and Laurence H. Pearl: 'Structural and Functional Analysis of the Middle Segment of Hsp90: Implications for ATP Hydrolysis and Client Protein and Cochaperone Interactions'. *Molecular cell* (2003), vol. 11(3): pp. 647–658.

64. Hessling, Martin, Klaus Richter, and Johannes Buchner: 'Dissection of the ATP-induced conformational cycle of the molecular chaperone Hsp90'. *Nature structural & molecular biology* (2009), vol. 16(3): pp. 287–293.

65. Picard, Didier: 'Intracellular dynamics of the Hsp90 co-chaperone p23 is dictated by Hsp90'. *Experimental cell research* (2006), vol. 312(2): pp. 198–204.

66. Richter, Klaus, Stefan Walter, and Johannes Buchner: 'The Co-chaperone Sba1 connects the ATPase reaction of Hsp90 to the progression of the chaperone cycle'. *Journal of molecular biology* (2004), vol. 342(5): pp. 1403–1413.

67. Graf, Christian, Chung-Tien Lee, L. Eva Meier-Andrejszki, Minh T. N. Nguyen, and Matthias P. Mayer: 'Differences in conformational dynamics within the Hsp90 chaperone family reveal mechanistic insights'. *Frontiers in molecular biosciences* (2014), vol. 1: p. 4.

68. McLaughlin, Stephen H., Frank Sobott, Zhong-ping Yao, Wei Zhang, Peter R. Nielsen, J. Gunter Grossmann, Ernest D. Laue, Carol V. Robinson, and Sophie E. Jackson: 'The co-chaperone p23 arrests the Hsp90 ATPase cycle to trap client proteins'. *Journal of molecular biology* (2006), vol. 356(3): pp. 746–758.

69. Chadli, A., I. Bouhouche, W. Sullivan, B. Stensgard, N. McMahon, M. G. Catelli, and D. O. Toft: 'Dimerization and N-terminal domain proximity underlie the function of the molecular chaperone heat shock protein 90'. *Proceedings of the National Academy of Sciences of the United States of America* (2000), vol. 97(23): pp. 12524–12529.

70. Bose, S., T. Weikl, H. Bugl, and J. Buchner: 'Chaperone function of Hsp90-associated proteins'. *Science (New York, N.Y.)* (1996), vol. 274(5293): pp. 1715–1717.

71. Freeman, B. C., D. O. Toft, and R. I. Morimoto: 'Molecular chaperone machines: chaperone activities of the cyclophilin Cyp-40 and the steroid aporeceptor-associated protein p23'. *Science (New York, N.Y.)* (1996), vol. 274(5293): pp. 1718–1720.

72. Weikl, T., K. Abelmann, and J. Buchner: 'An unstructured C-terminal region of the Hsp90 co-chaperone p23 is important for its chaperone function'. *Journal of molecular biology* (1999), vol. 293(3): pp. 685–691.

73. Kimura, Y., S. L. Rutherford, Y. Miyata, I. Yahara, B. C. Freeman, L. Yue, R. I. Morimoto, and S. Lindquist: 'Cdc37 is a molecular chaperone with specific functions in signal transduction'. *Genes & Development* (1997), vol. 11(14): pp. 1775–1785.

74. Reed, S. I.: 'The selection of amber mutations in genes required for completion of start, the controlling event of the cell division cycle of S. cerevisiae'. *Genetics* (1980), vol. 95(3): pp. 579–588.

75. Pearl, Laurence H.: 'Hsp90 and Cdc37 – a chaperone cancer conspiracy'. *Current opinion in genetics & development* (2005), vol. 15(1): pp. 55–61.

76. Taipale, Mikko, Irina Krykbaeva, Martina Koeva, Can Kayatekin, Kenneth D. Westover, Georgios I. Karras, and Susan Lindquist: 'Quantitative analysis of HSP90-client interactions reveals principles of substrate recognition'. *Cell* (2012), vol. 150(5): pp. 987–1001.

77. Gaiser, Andreas M., Anja Kretzschmar, and Klaus Richter: 'Cdc37-Hsp90 complexes are responsive to nucleotide-induced conformational changes and binding of further cofactors'. *The Journal of biological chemistry* (2010), vol. 285(52): pp. 40921–40932.

78. Siligardi, Giuliano, Barry Panaretou, Philippe Meyer, Shradha Singh, Derek N. Woolfson, Peter W. Piper, Laurence H. Pearl, and Chrisostomos Prodromou: 'Regulation of Hsp90 ATPase activity by the co-chaperone Cdc37p/p50cdc37'. *The Journal of biological chemistry* (2002), vol. 277(23): pp. 20151–20159.

79. Roe, S.Mark, Maruf M.U Ali, Philippe Meyer, Cara K. Vaughan, Barry Panaretou, Peter W. Piper, Chrisostomos Prodromou, and Laurence H. Pearl: 'The Mechanism of Hsp90 Regulation by the Protein Kinase-Specific Cochaperone p50cdc37'. *Cell* (2004), vol. 116(1): pp. 87–98.

80. Eckl, Julia M., Daniel A. Rutz, Veronika Haslbeck, Bettina K. Zierer, Jochen Reinstein, and Klaus Richter: 'Cdc37 (cell division cycle 37) restricts Hsp90 (heat shock protein 90) motility by interaction with N-terminal and middle domain binding sites'. *The Journal of biological chemistry* (2013), vol. 288(22): pp. 16032–16042.

81. Shao, J., N. Grammatikakis, B. T. Scroggins, S. Uma, W. Huang, J. J. Chen, S. D. Hartson, and R. L. Matts: 'Hsp90 regulates p50(cdc37) function during the biogenesis of the activeconformation of the heme-regulated eIF2 alpha kinase'. *The Journal of biological chemistry* (2001), vol. 276(1): pp. 206–214.

82. Caplan, Avrom J., Avi Ma'ayan, and Ian M. Willis: 'Multiple kinases and system robustness: a link between Cdc37 and genome integrity'. *Cell cycle (Georgetown, Tex.)* (2007), vol. 6(24): pp. 3145–3147.

83. Shao, Jieya, Thomas Prince, Steven D. Hartson, and Robert L. Matts: 'Phosphorylation of serine 13 is required for the proper function of the Hsp90 co-chaperone, Cdc37'. *The Journal of biological chemistry* (2003), vol. 278(40): pp. 38117–38120.

84. Vaughan, Cara K., Ulrich Gohlke, Frank Sobott, Valerie M. Good, Maruf M. U. Ali, Chrisostomos Prodromou, Carol V. Robinson, Helen R. Saibil, and Laurence H. Pearl: 'Structure of an Hsp90-Cdc37-Cdk4 complex'. *Molecular cell* (2006), vol. 23(5): pp. 697–707.

85. Keramisanou, Dimitra, Adam Aboalroub, Ziming Zhang, Wenjun Liu, Devon Marshall, Andrea Diviney, Randy W. Larsen, Ralf Landgraf, and Ioannis Gelis: 'Molecular Mechanism of Protein Kinase Recognition and Sorting by the Hsp90 Kinome-Specific Cochaperone Cdc37'. *Molecular cell* (2016), vol. 62(2): pp. 260–271.

86. Shao, Jieya, Angela Irwin, Steven D. Hartson, and Robert L. Matts: 'Functional dissection of cdc37: characterization of domain structure and amino acid residues critical for protein kinase binding'. *Biochemistry* (2003), vol. 42(43): pp. 12577–12588.

87. Harst, Anja, Hongying Lin, and Wolfgang M. J. Obermann: 'Aha1 competes with Hop, p50 and p23 for binding to the molecular chaperone Hsp90 and contributes to kinase and hormone receptor activation'. *The Biochemical journal* (2005), vol. 387(Pt 3): pp. 789–796.

88. Demtröder, Wolfgang: *Experimentalphysik 3: Atome, Moleküle und Festkörper*. 5. Aufl. 2016. Vol. 3. Springer-Lehrbuch. Berlin: Springer Berlin and Springer, 2016.

89. Lakowicz, Joseph R.: *Principles of fluorescence spectroscopy*. 3rd ed. New York: Springer, 2006.

90. Förster, Theodor: 'Zwischenmolekulare Energiewanderung und Fluoreszenz'. *Annalen der Physik* (1948), vol. 437(1-2): pp. 55–75.

91. Andrews, David L.: 'A unified theory of radiative and radiationless molecular energy transfer'. *Chemical Physics* (1989), vol. 135(2): pp. 195–201.

92. Andrews, David L. and David S. Bradshaw: 'Virtual photons, dipole fields and energy transfer: A quantum electrodynamical approach'. *European Journal of Physics* (2004), vol. 25(6): pp. 845–858.

93. Förster, Theodor: *Fluoreszenz organischer Verbindungen*. Göttingen: Vandenhoeck & Ruprecht, 1951.

94. Stryer, L.: 'Fluorescence energy transfer as a spectroscopic ruler'. *Annual review of biochemistry* (1978), vol. 47: pp. 819–846.

95. Hohng, Sungchul, Chirlmin Joo, and Taekjip Ha: 'Single-molecule three-color FRET'. *Biophysical journal* (2004), vol. 87(2): pp. 1328–1337.

96. Lee, Nam Ki, Achillefs N. Kapanidis, Hye Ran Koh, You Korlann, Sam On Ho, Younggyu Kim, Natalie Gassman, Seong Keun Kim, and Shimon Weiss: 'Three-color alternating-laser excitation of single molecules: monitoring multiple interactions and distances'. *Biophysical journal* (2007), vol. 92(1): pp. 303–312.

97. Person, Britta, Ingo H. Stein, Christian Steinhauer, Jan Vogelsang, and Philip Tinnefeld: 'Correlated movement and bending of nucleic acid structures visualized by multicolor single-molecule spectroscopy'. *Chemphyschem : a European journal of chemical physics and physical chemistry* (2009), vol. 10(9-10): pp. 1455–1460.

98. Lee, Jinwoo, Sanghwa Lee, Kaushik Ragunathan, Chirlmin Joo, Taekjip Ha, and Sungchul Hohng: 'Single-Molecule Four-Color FRET'. *Angewandte Chemie International Edition* (2010), vol. 49(51): pp. 9922–9925.

99. Ratzke, Christoph, Felix Berkemeier, and Thorsten Hugel: 'Heat shock protein 90's mechanochemical cycle is dominated by thermal fluctuations'. *Proceedings of the National Academy of Sciences of the United States of America* (2012), vol. 109(1): pp. 161–166.

100. Ratzke, C., B. Hellenkamp, and T. Hugel: 'Four-colour FRET reveals directionality in the Hsp90 multicomponent machinery'. *Nature Communications* (2014), vol. 5.

101. Laurence, Ted A., Xiangxu Kong, Marcus Jager, and Shimon Weiss: 'Probing structural heterogeneities and fluctuations of nucleic acids and denatured proteins'. *Proceedings of the National Academy of Sciences of the United States of America* (2005), vol. 102(48): pp. 17348–17353.

102. Ratzke, Christoph, Minh N. T. Nguyen, Matthias P. Mayer, and Thorsten Hugel: 'From a ratchet mechanism to random fluctuations evolution of Hsp90's mechanochemical cycle'. *Journal of molecular biology* (2012), vol. 423(3): pp. 462–471.

103. Tokunaga, Makio, Naoko Imamoto, and Kumiko Sakata-Sogawa: 'Highly inclined thin illumination enables clear single-molecule imaging in cells'. *Nature methods* (2008), vol. 5(2): pp. 159–161.

104. Lee, Nam Ki, Achillefs N. Kapanidis, You Wang, Xavier Michalet, Jayanta Mukhopadhyay, Richard H. Ebright, and Shimon Weiss: 'Accurate FRET measurements within single diffusing biomolecules using alternating-laser excitation'. *Biophysical journal* (2005), vol. 88(4): pp. 2939–2953.

105. Müller, Barbara K., Evgeny Zaychikov, Christoph Bräuchle, and Don C. Lamb: 'Pulsed Interleaved Excitation'. *Biophysical journal* (2005), vol. 89(5): pp. 3508–3522.

106. Kudryavtsev, Volodymyr, Martin Sikor, Stanislav Kalinin, Dejana Mokranjac, Claus A. M. Seidel, and Don C. Lamb: 'Combining MFD and PIE for accurate single-pair Forster resonance energy transfer measurements'. *Chemphyschem : a European journal of chemical physics and physical chemistry* (2012), vol. 13(4): pp. 1060–1078.

107. Hellenkamp, Björn: 'Dynamic Structure Of A Multi-Domain Protein: Uncovered Using Self-Consistent Fret Networks And Time-Correlated Distance Distributions'. PhD Thesis. Munich: Technische Universität München, 2016.

108. Kapanidis, Achillefs N., Ted A. Laurence, Nam Ki Lee, Emmanuel Margeat, Xiangxu Kong, and Shimon Weiss: 'Alternating-Laser Excitation of Single Molecules'. *Accounts of Chemical Research* (2005), vol. 38(7): pp. 523–533.

109. Kapanidis, Achillefs N., Nam Ki Lee, Ted A. Laurence, Soren Doose, Emmanuel Margeat, and Shimon Weiss: 'Fluorescence-aided molecule sorting: analysis of structure and interactions by alternating-laser excitation of single molecules'. *Proceedings of the National Academy of Sciences of the United States of America* (2004), vol. 101(24): pp. 8936–8941.

110. McKinney, Sean A., Chirlmin Joo, and Taekjip Ha: 'Analysis of Single-Molecule FRET Trajectories Using Hidden Markov Modeling'. *Biophysical journal* (2006), vol. 91(5): pp. 1941–1951.

111. Kahra, Dana, Michael Kovermann, Christian Low, Verena Hirschfeld, Caroline Haupt, Jochen Balbach, and Christian Gerhard Hubner: 'Conformational plasticity and dynamics in the generic protein folding catalyst SlyD unraveled by single-molecule FRET'. *Journal of molecular biology* (2011), vol. 411(4): pp. 781–790.

112. Santoso, Y., C. M. Joyce, O. Potapova, L. Le Reste, J. Hohlbein, J. P. Torella, N. D. F. Grindley, and A. N. Kapanidis: 'Conformational transitions in DNA polymerase I revealed by single-molecule FRET'. *Proceedings of the National Academy of Sciences* (2010), vol. 107(2): pp. 715–720.

113. Schmid, Sonja, Markus Götz, and Thorsten Hugel: 'Single-Molecule Analysis beyond Dwell Times: Demonstration and Assessment in and out of Equilibrium'. *Biophysical journal* (2016), vol. 111(7): pp. 1375–1384.

114. Fink, Gernot A.: *Markov models for pattern recognition: from theory to applications.* 2nd. Springer Science & Business Media, 2014.

115. Rabiner, L. R.: 'A tutorial on hidden Markov models and selected applications in speech recognition'. *Proceedings of the IEEE* (1989), vol. 77(2): pp. 257–286.

116. Schwarz, G.: 'Estimating the dimension of a model Ann Stat 6: 461–464'. *Find this article online* (1978), vol.

117. Giudici, P., T. Ryden, and P. Vandekerkhove: 'Likelihood-ratio tests for hidden Markov models'. *Biometrics* (2000), vol. 56(3): pp. 742–747.

118. Greenfeld, Max, Dmitri S. Pavlichin, Hideo Mabuchi, Daniel Herschlag, and Daniel J. Muller: 'Single Molecule Analysis Research Tool (SMART): An Integrated Approach for Analyzing Single Molecule Data'. *PloS one* (2012), vol. 7(2): e30024.

119. Grinstead, Charles M. and J. Laurie Snell: *Introduction to probability.* 2nd rev. ed. / Charles M. Grinstead, J. Laurie Snell. Providence, R.I.: American Mathematical Society, 1997.

120. SHAPIRO, S. S. and M. B. WILK: 'An analysis of variance test for normality (complete samples)'. *Biometrika* (1965), vol. 52(3-4): pp. 591–611.

121. Arnold, Taylor B. and John W. Emerson: 'Nonparametric goodness-of-fit tests for discrete null distributions'. *The R Journal* (2011), vol. 3(2): pp. 34–39.

122. Efron, B. and C. Stein: 'The Jackknife Estimate of Variance'. *Ann. Statist.* (1981), vol. 9(3): pp. 586–596.

123. Shao, Jun and C. F. J. Wu: 'A General Theory for Jackknife Variance Estimation'. *Ann. Statist.* (1989), vol. 17(3): pp. 1176–1197.

124. Davison, A. C. and D. V. Hinkley: *Bootstrap methods and their application*. Cambridge series on statistical and probablistic mathematics. Cambridge: Cambridge University Press, 1997.

125. Kalinin, Stanislav, Thomas Peulen, Simon Sindbert, Paul J. Rothwell, Sylvia Berger, Tobias Restle, Roger S. Goody, Holger Gohlke, and Claus A. M. Seidel: 'A toolkit and benchmark study for FRET-restrained high-precision structural modeling'. *Nature Methods* (2012), vol. 9(12): pp. 1218–1225.

126. Berman, Helen M. et al.: 'The Protein Data Bank'. *Acta crystallographica. Section D, Biological crystallography* (2002), vol. 58(Pt 6 No 1): pp. 899–907.

127. The UniProt Consortium: 'UniProt: a hub for protein information'. *Nucleic acids research* (2015), vol. 43(D1): pp. D204–D212.

128. Moritz Mickler: 'Der ATPase-Zyklus von Hsp90 in Einzelmolekül FRET Experimenten'. PhD thesis. Munich: Technische Universität München, 2008.

129. Panavas, T., C. Sanders, and T. R. Butt: 'SUMO fusion technology for enhanced protein production in prokaryotic and eukaryotic expression systems'. *Methods in molecular biology (Clifton, N.J.)* (2009), vol. 497: pp. 303–317.

130. Ashraf, S.Salman, R.Edward Benson, E.Sturgis Payne, Cale M. Halbleib, and Hanne Grøn: 'A novel multi-affinity tag system to produce high levels of soluble and biotinylated proteins in Escherichia coli'. *Protein Expression and Purification* (2004), vol. 33(2): pp. 238–245.

131. Kalderon, D., B. L. Roberts, W. D. Richardson, and A. E. Smith: 'A short amino acid sequence able to specify nuclear location'. *Cell* (1984), vol. 39(3 Pt 2): pp. 499–509.

132. Smith, A. E., D. Kalderon, B. L. Roberts, W. H. Colledge, M. Edge, P. Gillett, A. Markham, E. Paucha, and W. D. Richardson: 'The nuclear location signal'. *Proceedings of the Royal Society of London. Series B, Biological sciences* (1985), vol. 226(1242): pp. 43–58.

133. Raucher, Drazen and Jung Su Ryu: 'Cell-penetrating peptides: strategies for anticancer treatment'. *Trends in molecular medicine* (2015), vol. 21(9): pp. 560–570.

134. Vives, E., P. Brodin, and B. Lebleu: 'A Truncated HIV-1 Tat Protein Basic Domain Rapidly Translocates through the Plasma Membrane and Accumulates in the Cell Nucleus'. *Journal of Biological Chemistry* (1997), vol. 272(25): pp. 16010–16017.

135. Yin, Jun, Paul D. Straight, Shaun M. McLoughlin, Zhe Zhou, Alison J. Lin, David E. Golan, Neil L. Kelleher, Roberto Kolter, and Christopher T. Walsh: 'Genetically encoded short peptide tag for versatile protein labeling by Sfp phosphopantetheinyl transferase'. *Proceedings of the National Academy of Sciences of the United States of America* (2005), vol. 102(44): pp. 15815–15820.

136. Wilkins, M. R., E. Gasteiger, A. Bairoch, J. C. Sanchez, K. L. Williams, R. D. Appel, and D. F. Hochstrasser: 'Protein identification and analysis tools in the ExPASy server'. *Methods in molecular biology (Clifton, N.J.)* (1999), vol. 112: pp. 531–552.

137. Svergun, D., C. Barberato, and M. H. J. Koch: 'CRYSOL – a Program to Evaluate X-ray Solution Scattering of Biological Macromolecules from Atomic Coordinates'. *Journal of Applied Crystallography* (1995), vol. 28(6): pp. 768–773.

138. Di Svergun: 'Determination of the regularization parameter in indirect-transform methods using perceptual criteria'. *Journal of applied crystallography* (1992), vol. 25(4): pp. 495–503.

139. Drenth, Jan: *Principles of protein X-ray crystallography*. Springer Science & Business Media, 2007.

140. Abergel, Chantal: 'Molecular replacement: tricks and treats'. *Acta crystallographica. Section D, Biological crystallography* (2013), vol. 69(Pt 11): pp. 2167–2173.

141. Muschielok, Adam, Joanna Andrecka, Anass Jawhari, Florian Brückner, Patrick Cramer, and Jens Michaelis: 'A nano-positioning system for macromolecular structural analysis'. *Nature Methods* (2008), vol. 5(11): pp. 965–971.

142. Kalinin, Stanislav, Alessandro Valeri, Matthew Antonik, Suren Felekyan, and Claus A. M. Seidel: 'Detection of Structural Dynamics by FRET: A Photon Distribution and Fluorescence Lifetime Analysis of Systems with Multiple States'. *The Journal of Physical Chemistry B* (2010), vol. 114(23): pp. 7983–7995.

143. Gopich, I. V. and A. Szabo: 'Theory of the energy transfer efficiency and fluorescence lifetime distribution in single-molecule FRET'. *Proceedings of the National Academy of Sciences* (2012), vol. 109(20): pp. 7747–7752.

144. Krukenberg, Kristin A., Friedrich Forster, Luke M. Rice, Andrej Sali, and David A. Agard: 'Multiple conformations of E. coli Hsp90 in solution: insights into the conformational dynamics of Hsp90'. *Structure (London, England : 1993)* (2008), vol. 16(5): pp. 755–765.

145. Blanchet, Clement E. and Dmitri I. Svergun: 'Small-angle X-ray scattering on biological macromolecules and nanocomposites in solution'. *Annual review of physical chemistry* (2013), vol. 64: pp. 37–54.

146. Alexandrescu, A. T., C. Abeygunawardana, and D. Shortle: 'Structure and dynamics of a denatured 131-residue fragment of staphylococcal nuclease: a heteronuclear NMR study'. *Biochemistry* (1994), vol. 33(5): pp. 1063–1072.

147. Street, Timothy O., Laura A. Lavery, and David A. Agard: 'Substrate binding drives large-scale conformational changes in the Hsp90 molecular chaperone'. *Molecular cell* (2011), vol. 42(1): pp. 96–105.

148. Genest, Olivier, Michael Reidy, Timothy O. Street, Joel R. Hoskins, Jodi L. Camberg, David A. Agard, Daniel C. Masison, and Sue Wickner: 'Uncovering a region of heat shock protein 90 important for client binding in E. coli and chaperone function in yeast'. *Molecular cell* (2013), vol. 49(3): pp. 464–473.

149. Gupta, Amit J., Shubhasis Haldar, Goran Milicic, F. Ulrich Hartl, and Manajit Hayer-Hartl: 'Active cage mechanism of chaperonin-assisted protein folding demonstrated at single-molecule level'. *Journal of molecular biology* (2014), vol. 426(15): pp. 2739–2754.

150. Cunningham, Christian N., Kristin A. Krukenberg, and David A. Agard: 'Intra- and intermonomer interactions are required to synergistically facilitate ATP hydrolysis in Hsp90'. *The Journal of biological chemistry* (2008), vol. 283(30): pp. 21170–21178.

151. Obermann, W. M., H. Sondermann, A. A. Russo, N. P. Pavletich, and F. U. Hartl: 'In vivo function of Hsp90 is dependent on ATP binding and ATP hydrolysis'. *The Journal of cell biology* (1998), vol. 143(4): pp. 901–910.

152. Weikl, T., P. Muschler, K. Richter, T. Veit, J. Reinstein, and J. Buchner: 'C-terminal regions of Hsp90 are important for trapping the nucleotide during the ATPase cycle'. *Journal of molecular biology* (2000), vol. 303(4): pp. 583–592.

153. Halpin, Jackson C., Bin Huang, Ming Sun, and Timothy O. Street: 'Crowding Activates Heat Shock Protein 90'. *The Journal of biological chemistry* (2016), vol. 291(12): pp. 6447–6455.

154. Tamura, J. K., A. D. Bates, and M. Gellert: 'Slow interaction of 5'-adenylyl-beta,gamma-imidodiphosphate with Escherichia coli DNA gyrase. Evidence for cooperativity in nucleotide binding'. *The Journal of biological chemistry* (1992), vol. 267(13): pp. 9214–9222.

155. Li, Jing, Klaus Richter, Jochen Reinstein, and Johannes Buchner: 'Integration of the accelerator Aha1 in the Hsp90 co-chaperone cycle'. *Nature structural & molecular biology* (2013), vol. 20(3): pp. 326–331.

156. Cunningham, Christian N., Daniel R. Southworth, Kristin A. Krukenberg, and David A. Agard: 'The conserved arginine 380 of Hsp90 is not a catalytic residue, but stabilizes the closed conformation required for ATP hydrolysis'. *Protein science : a publication of the Protein Society* (2012), vol. 21(8): pp. 1162–1171.

157. Yount, Ralph G., Donner Babcock, William Ballantyne, and Deanna Ojala: 'Adenylyl imidiodiphosphate, an adenosine triphosphate analog containing a P-N-P linkage'. *Biochemistry* (1971), vol. 10(13): pp. 2484–2489.

158. Hunter, Christopher A. and Harry L. Anderson: 'What is cooperativity?' *Angewandte Chemie (International ed. in English)* (2009), vol. 48(41): pp. 7488–7499.

159. Whitty, Adrian: 'Cooperativity and biological complexity'. *Nature chemical biology* (2008), vol. 4(8): pp. 435–439.

160. Larkin, M. A., G. Blackshields, N. P. Brown, R. Chenna, P. A. McGettigan, H. McWilliam, F. Valentin, I. M. Wallace, A. Wilm, R. Lopez, J. D. Thompson, T. J. Gibson, and D. G. Higgins: 'Clustal W and Clustal X version 2.0'. *Bioinformatics (Oxford, England)* (2007), vol. 23(21): pp. 2947–2948.

161. Evers, Toon H., Elisabeth M. W. M. van Dongen, Alex C. Faesen, E. W. Meijer, and Maarten Merkx: 'Quantitative understanding of the energy transfer between fluorescent proteins connected via flexible peptide linkers'. *Biochemistry* (2006), vol. 45(44): pp. 13183–13192.

162. Arai, R., H. Ueda, A. Kitayama, N. Kamiya, and T. Nagamune: 'Design of the linkers which effectively separate domains of a bifunctional fusion protein'. *Protein engineering* (2001), vol. 14(8): pp. 529–532.

163. Williamson, M. P.: 'The structure and function of proline-rich regions in proteins'. *Biochemical Journal* (1994), vol. 297(2): pp. 249–260.

164. Zhang, Tao, Yanyan Li, Yanke Yu, Peng Zou, Yiqun Jiang, and Duxin Sun: 'Characterization of celastrol to inhibit hsp90 and cdc37 interaction'. *The Journal of biological chemistry* (2009), vol. 284(51): pp. 35381–35389.

165. Reece, R. J. and A. Maxwell: 'DNA gyrase: structure and function'. *Critical reviews in biochemistry and molecular biology* (1991), vol. 26(3-4): pp. 335–375.

166. Ban, C. and W. Yang: 'Crystal structure and ATPase activity of MutL: implications for DNA repair and mutagenesis'. *Cell* (1998), vol. 95(4): pp. 541–552.

167. Maxwell, A. and M. Gellert: 'The DNA dependence of the ATPase activity of DNA gyrase'. *The Journal of biological chemistry* (1984), vol. 259(23): pp. 14472–14480.

168. Spampinato, C.: 'The MutL ATPase Is Required for Mismatch Repair'. *Journal of Biological Chemistry* (2000), vol. 275(13): pp. 9863–9869.

169. Harkins, T. T., T. J. Lewis, and J. E. Lindsley: 'Pre-steady-state analysis of ATP hydrolysis by Saccharomyces cerevisiae DNA topoisomerase II. 2. Kinetic mechanism for the sequential hydrolysis of two ATP'. *Biochemistry* (1998), vol. 37(20): pp. 7299–7312.

170. Baird, C. L., T. T. Harkins, S. K. Morris, and J. E. Lindsley: 'Topoisomerase II drives DNA transport by hydrolyzing one ATP'. *Proceedings of the National Academy of Sciences* (1999), vol. 96(24): pp. 13685–13690.

171. Agrawal, Alka, Melanie Roue, Claus Spitzfaden, Stephanie Petrella, Alexandra Aubry, Michael Hann, Benjamin Bax, and Claudine Mayer: 'Mycobacterium tuberculosis DNA gyrase ATPase domain structures suggest a dissociative mechanism that explains how ATP hydrolysis is coupled to domain motion'. *The Biochemical journal* (2013), vol. 456(2): pp. 263–273.

172. Nadeau, K., A. Das, and C. T. Walsh: 'Hsp90 chaperonins possess ATPase activity and bind heat shock transcription factors and peptidyl prolyl isomerases'. *The Journal of biological chemistry* (1993), vol. 268(2): pp. 1479–1487.

173. Genest, Olivier, Joel R. Hoskins, Andrea N. Kravats, Shannon M. Doyle, and Sue Wickner: 'Hsp70 and Hsp90 of E. coli Directly Interact for Collaboration in Protein Remodeling'. *Journal of molecular biology* (2015), vol. 427(24): pp. 3877–3889.

174. Flaherty, K. M., C. DeLuca-Flaherty, and D. B. McKay: 'Three-dimensional structure of the ATPase fragment of a 70K heat-shock cognate protein'. *Nature* (1990), vol. 346(6285): pp. 623–628.

175. Mogk, Axel, Matthias P. Mayer, and Elke Deuerling: 'Mechanisms of Protein Folding: Molecular Chaperones and Their Application in Biotechnology'. *ChemBioChem* (2002), vol. 3(9): pp. 807–814.

176. Freeman, B. C. and R. I. Morimoto: 'The human cytosolic molecular chaperones hsp90, hsp70 (hsc70) and hdj-1 have distinct roles in recognition of a non-native protein and protein refolding'. *The EMBO journal* (1996), vol. 15(12): pp. 2969–2979.

177. Walerych, Dawid, Malgorzata Gutkowska, Marcin P. Klejman, Bartosz Wawrzynow, Zuzanna Tracz, Milena Wiech, Maciej Zylicz, and Alicja Zylicz: 'ATP binding to Hsp90 is sufficient for effective chaperoning of p53 protein'. *The Journal of biological chemistry* (2010), vol. 285(42): pp. 32020–32028.

178. Mayer, M. P. and B. Bukau: 'Hsp70 chaperones: cellular functions and molecular mechanism'. *Cellular and molecular life sciences : CMLS* (2005), vol. 62(6): pp. 670–684.

179. Georgakoudi, Irene, Brian C. Jacobson, Markus G. Muller, Ellen E. Sheets, Kamran Badizadegan, David L. Carr-Locke, Christopher P. Crum, Charles W. Boone, Ramachandra R. Dasari, Jacques van Dam, and Michael S. Feld: 'NAD(P)H and collagen as in vivo quantitative fluorescent biomarkers of epithelial precancerous changes'. *Cancer research* (2002), vol. 62(3): pp. 682–687.

180. Islam, Md Serajul, Masato Honma, Takakazu Nakabayashi, Masataka Kinjo, and Nobuhiro Ohta: 'pH dependence of the fluorescence lifetime of FAD in solution and in cells'. *International journal of molecular sciences* (2013), vol. 14(1): pp. 1952–1963.

181. Kolmakov, Kirill, Vladimir N. Belov, Jakob Bierwagen, Christian Ringemann, Veronika Muller, Christian Eggeling, and Stefan W. Hell: 'Red-emitting rhodamine dyes for fluorescence microscopy and nanoscopy'. *Chemistry (Weinheim an der Bergstrasse, Germany)* (2010), vol. 16(1): pp. 158–166.

182. Roy, Rahul, Sungchul Hohng, and Taekjip Ha: 'A practical guide to single-molecule FRET'. *Nature methods* (2008), vol. 5(6): pp. 507–516.

183. Teng, Kai Wen, Yuji Ishitsuka, Pin Ren, Yeoan Youn, Xiang Deng, Pinghua Ge, Andrew S. Belmont, Paul R. Selvin, and Richard Aldrich: 'Labeling proteins inside living cells using external fluorophores for microscopy'. *eLife* (2016), vol. 5: e20378.

184. Case, D. A., V. Babin, J. T. Berryman, R. M. Betz, Q. Cai, and D. S. Cerutti: 'AMBER 14 (Assisted Model Building with Energy Refinement)'. *University of California, San Francisco* (2014), vol.

185. Jorgensen, William L., Jayaraman Chandrasekhar, Jeffry D. Madura, Roger W. Impey, and Michael L. Klein: 'Comparison of simple potential functions for simulating liquid water'. *The Journal of chemical physics* (1983), vol. 79(2): pp. 926–935.

186. Maier, James A., Carmenza Martinez, Koushik Kasavajhala, Lauren Wickstrom, Kevin E. Hauser, and Carlos Simmerling: 'ff14SB: Improving the Accuracy of Protein Side Chain and Backbone Parameters from ff99SB'. *Journal of Chemical Theory and Computation* (2015), vol. 11(8): pp. 3696–3713.

187. Darden, Tom, Darrin York, and Lee Pedersen: 'Particle mesh Ewald: An N·log(N) method for Ewald sums in large systems'. *The Journal of Chemical Physics* (1993), vol. 98(12): p. 10089.

188. Shrake, A. and J. A. Rupley: 'Environment and exposure to solvent of protein atoms. Lysozyme and insulin'. *Journal of molecular biology* (1973), vol. 79(2): pp. 351–371.

189. Richter, Klaus, Paul Muschler, Otmar Hainzl, Jochen Reinstein, and Johannes Buchner: 'Sti1 is a non-competitive inhibitor of the Hsp90 ATPase. Binding prevents the N-terminal dimerization reaction during the atpase cycle'. *The Journal of biological chemistry* (2003), vol. 278(12): pp. 10328–10333.

190. Olesen, Sanne H., Donna J. Ingles, Jin-Yi Zhu, Mathew P. Martin, Stephane Betzi, Gunda I. Georg, Joseph S. Tash, and Ernst Schonbrunn: 'Stability of the human Hsp90-p50Cdc37 chaperone complex against nucleotides and Hsp90 inhibitors, and the influence of phosphorylation by casein kinase 2'. *Molecules (Basel, Switzerland)* (2015), vol. 20(1): pp. 1643–1660.

191. Sullivan, W., B. Stensgard, G. Caucutt, B. Bartha, N. McMahon, E. S. Alnemri, G. Litwack, and D. Toft: 'Nucleotides and Two Functional States of hsp90'. *Journal of Biological Chemistry* (1997), vol. 272(12): pp. 8007–8012.

192. Monod, J., J. Wyman, and J. P. Changeux: 'On The Nature Of Allosteric Transitions: A Plausible Model'. *Journal of molecular biology* (1965), vol. 12: pp. 88–118.

193. Stefan, Melanie I. and Nicolas Le Novere: 'Cooperative binding'. *PLoS computational biology* (2013), vol. 9(6): e1003106.

194. Schuler, Benjamin, Everett A. Lipman, Peter J. Steinbach, Michael Kumke, and William A. Eaton: 'Polyproline and the spectroscopic ruler revisited with single-molecule fluorescence'. *Proceedings of the National Academy of Sciences of the United States of America* (2005), vol. 102(8): pp. 2754–2759.

195. PAULING, L., R. B. COREY, and H. R. BRANSON: 'The structure of proteins; two hydrogen-bonded helical configurations of the polypeptide chain'. *Proceedings of the National Academy of Sciences of the United States of America* (1951), vol. 37(4): pp. 205–211.

196. Bracher, Andreas and Jacob Verghese: 'The nucleotide exchange factors of Hsp70 molecular chaperones'. *Frontiers in molecular biosciences* (2015), vol. 2: p. 10.

197. Lee, Sanghwa, Jinwoo Lee, and Sungchul Hohng: 'Single-molecule three-color FRET with both negligible spectral overlap and long observation time'. *PloS one* (2010), vol. 5(8): e12270.

198. Blanchard, Scott C., Harold D. Kim, Ruben L. Gonzalez JR, Joseph D. Puglisi, and Steven Chu: 'tRNA dynamics on the ribosome during translation'. *Proceedings of the National Academy of Sciences of the United States of America* (2004), vol. 101(35): pp. 12893–12898.

199. Aitken, Colin Echeverria, R. Andrew Marshall, and Joseph D. Puglisi: 'An oxygen scavenging system for improvement of dye stability in single-molecule fluorescence experiments'. *Biophysical journal* (2008), vol. 94(5): pp. 1826–1835.

200. Swoboda, Marko, Jorg Henig, Hsin-Mei Cheng, Dagmar Brugger, Dietmar Haltrich, Nicolas Plumere, and Michael Schlierf: 'Enzymatic oxygen scavenging for photostability without pH drop in single-molecule experiments'. *ACS Nano* (2012), vol. 6(7): pp. 6364–6369.

201. Altman, Roger B., Daniel S. Terry, Zhou Zhou, Qinsi Zheng, Peter Geggier, Rachel A. Kolster, Yongfang Zhao, Jonathan A. Javitch, J. David Warren, and Scott C. Blanchard: 'Cyanine fluorophore derivatives with enhanced photostability'. *Nature methods* (2011), vol. 9(1): pp. 68–71.

202. McNeil, P. L. and E. Warder: 'Glass beads load macromolecules into living cells'. *Journal of cell science* (1987), vol. 88 (Pt 5): pp. 669–678.

203. Matthews, Kathryn E. and Armand Keating: 'Bead transfection of adherent cells'. *Molecular Biotechnology* (1996), vol. 5(3): pp. 259–261.

Acknowledgments

I want to thank my supervisor Thorsten Hugel for giving me the opportunity to write my Ph.D. thesis in the fascinating field of single molecule biophysics and for his professional advise and guidance. I really appreciated the possibility to give all my scientific ideas a try.

Of course, this work would not have been possible without the support of a large number of people around me. A big thank goes to my office mates in Munich – Markus Jahn, Marco Grison, Christina Lumme and in Freiburg – Markus Götz for their company, coffee, help and of course for the various fruitful and vivid discussions. Special thanks also to Björn Hellenkamp for working together with me on the dynamic structure of Hsp90 – I will not forget the huge number of our endless, but nevertheless stimulating discussions. Furthermore, I would like to thank my colleague Sonja Schmid and our technician in Freiburg Jolanta Vorreiter for her help in the lab. I also want to mention here the other members of the Hugel group, as well as the Rief and Bausch groups in the TUM biophysics section in Garching. I really enjoyed the open and creative atmosphere in and outside the lab.

I would also like to thank my family for their spiritual support and my flat mates Stefan and Jakob for guiding me through the life in Freiburg as a 'studentische WG'.

Last, but not least, I want to thank Jana for surviving our long distance relationship lasting more than two years and for her assistance under all circumstances.